An investigation into the role of metastable states on excited populations of weakly ionized argon plasmas, with applications for optical diagnostics.

by

N Ivan Arnold

A dissertation submitted to the Graduate Faculty of
Auburn University
in partial fulfillment of the
requirements for the Degree of
Doctor of Philosophy

Auburn, Alabama
August 5th, 2017

Keywords: Impact Excitation, Dielectronic Recombination, Spectroscopic / Optical Diagnostics, Atomic Processes in Plasmas, Plasma Spectroscopy, Argon Plasma

Approved by

Edward Thomas, Chair, Professor of Physics
Stuart Loch, Associate Professor of Physics
Connor Ballance, Associate Professor of Physics
David Maurer, Associate Professor of Physics
Konrad Patkowski, Associate Professor of Physics
George Flowers, Dean of the Graduate School

Abstract

Performing spectroscopic measurements of emission lines in relatively cold laboratory plasmas is challenging because the plasma is often neutral-dominated and is not in thermal equilibrium. However, these types of plasma do offer a unique opportunity for benchmarking the finer details of atomic physics, helping researchers gain a better understanding of fundamental atomic processes in plasmas. In this thesis, we report on a new set of atomic data, from which rate coefficients for the electron-impact excitation of neutral argon, along with dielectronic recombination of Ar^{+} – Ar^{5+} are determined. This data is used to calculate synthetic emission spectra, which are compared to experimental measurements in the ALEXIS device. The goal is to identify emission lines that are sensitive to variations in temperature and density and to use this data to develop new optical density and temperature diagnostics for a low-temperature, neutral-dominated argon plasma. A key component of this is to first determine the metastable fraction in ALEXIS. It is likely that a lack of knowledge on the metastable fraction has been the main limiting factor in the general use of neutral Ar spectral diagnostics. A new spectroscopic method to measure the neutral argon metastable fractions is developed. We also present preliminary density and temperature diagnostics made using our atomic data, with comparisons to standard probe based measurement, and will discuss further efforts to improve and extend our models to other plasmas.

Acknowledgments

During my time here at Auburn University I have been fortunate to work with many wonderful people, without whom I would have failed miserably.

First and foremost I would like to thank Dr. Edward Thomas, who has been a mentor, friend, and benevolent dictator. In addition to paying my bills for the past four+ years, Ed has provided unwavering support and invaluable guidance and insight. Ed keeps the lights on in all Auburn University Plasma Sciences Laboratory (AUPSL) facilities through his tireless efforts, and none of us, his students, could continue to do our work without him.

I would be crazy not to mention the friendship and support of Dr. Stuart Loch. Stuart has been a wonderful friend, ally, and teacher during this entire process. I owe him for introducing me to atomic physics and its applications to plasma spectroscopy, and for the endless patience he displayed for what must have seemed an impossibly long list of questions with obvious (to him) answers. Thank you very much, Stuart, for never making me feel like an idiot, and for kindly explaining very complex things in very simple terms.

Dr. Connor Ballance has been an invaluable resource in all things computational. Having a world-renowned expert in R-Matrix theory in the office across the hall from me was a luxury made painfully clear after Connor left to work at Queen's University, Belfast. Without Connor's expertise and ability to translate complex computational methods into easily understandable language I would not have been able to tackle the tasks required to complete this journey.

There is a long list of staff, faculty, and fellow grad students that have made my time at AU much more enjoyable, and helped me finish the coursework and research required to write the thesis that follows. While I will probably manage to forget some of them, what follows is an attempt to thank, in no particular order, as many of them as I can remember.

Faculty: Dr. Michael Pindzola, Dr. James Hanson, Dr. David Maurer, Dr. Uwe Konopka, Dr. David Ennis, Dr. Greg Hartwell. Staff: Jennifer Morris, Freddie Killian, Max Cichon, Rick Springer, Darrick Artis, David Patrick. Fellow Students: Ami DuBois, Brian Lynch, Spencer LeBlanc, Csilla Czako, Taylor Hall, Jonathan Pearce, Stephen Williams, Daniel Smith.

Finally, I need to thank my loving and wonderful wife, Rachel Arnold, for putting up with this madness, my mother and fathe-in-law Mohammad and Helen Lahah for all their moral and financial support of our family throughout this process, my grandmother, Sophie Reed, and my Aunt Amy for showing me how to live right, my mom and two dads for all the moral support, and my beautiful baby boy Caiden James (TI) for providing me with the resolve to finish long after I felt like quitting.

To all of you, from the very bottom of my heart, THANK YOU!

Table of Contents

Abstract ii

Acknowledgments iii

List of Figures x

List of Tables xvi

1 Introduction, overview, theory, and methods. 1

1.1 Introduction 1

1.2 Complex atoms and selection rules 8

1.3 Atomic structure and wavefunctions. 8

1.3.1 Central Field Model 8

1.4 Addition of angular momenta / coupling schemes. 11

1.4.1 Russell-Saunders or LSJ coupling 11

1.4.2 jj coupling 13

1.4.3 jk coupling / Racah notation 14

1.5 Selection rules 15

1.6 Atomic processes 18

1.6.1 Radiative transitions 18

1.6.2 Dielectronic recombination 20

1.6.3 Electron-impact ionization 22

1.6.4 Equilibrium ionization balance 22

1.6.5 Electron-impact excitation 24

1.6.6 Population modeling 28

1.6.7 Local Thermodynamic Equilibrium 28

1.6.8 The Coronal Approximation 29

1.6.9 Collisional-Radiative Theory 30
1.6.10 Population Dependence on Electron Density 34
1.6.11 Electron Temperature Diagnostics 36
1.6.12 Electron Density Diagnostics 38
1.7 Computational Methods 39
1.7.1 R-matrix theory 39
1.7.2 Atomic Structure Calculations / R-matrix with PseudoStates (RMPS) 45
1.7.3 DR rate coefficients 47
1.8 The ALEXIS experiment. 50
1.8.1 Vacuum vessel 50
1.8.2 Electromagnet configuration 52
1.8.3 Magnetic Fields in ALEXIS. 53
1.8.4 Vacuum pumps and gas regulation. 57
1.8.5 Plasma generation 58
1.8.6 Data collection / diagnostics 58
1.8.7 Spectrometers 63
1.8.8 Data collection 63
1.9 Summary and overview 65
2 Electron impact excitation of neutral argon. 68
2.1 Introduction 68
2.2 Methods 70
2.2.1 Background 70
2.2.2 The atomic structure calculation. 70
2.2.3 RMPS Scattering Calculation 76
2.2.4 Optical methods / branching fractions 77
2.3 Results 79
2.3.1 Excitation from the ground state into the 2p manifold. 79

2.3.2 Excitation from metastable states. 84
2.4 Conclusion 88
3 Dielectronic recombination of low charge states of argon. 90
3.1 Introduction 90
3.2 Methods 92
3.2.1 Dielectronic Recombination: Theory 92
3.2.2 Calculation of atomic structure and rate coefficients. 93
3.3 Results 102
3.3.1 Maxwellian convolved rate coefficients. 102
3.4 Discussion 113
3.5 Summary and future work 115
4 Generalized collisional radiative modeling of metastable populations in neutral argon, benchmarked against ALEXIS. 117
4.1 Introduction. 117
4.2 Data Collection 117
4.2.1 Experimental determination of electron temperature/density. 117
4.2.2 Collecting spectral data. 123
4.3 Overview of observed spectral lines. 123
4.4 PEC's and QCD's 127
4.4.1 PEC's 127
4.4.2 QCD's. 128
4.4.3 Analysing metastable populations in low temperature argon plasmas. 130
4.4.4 Time dependence of relative metastable population densities. 132
4.4.5 Determining the metastable fraction in ALEXIS. 137
4.5 Development of a working temperature diagnostic using spectral line ratios. . 143
4.6 Dependence of metastable fraction on electron density. 146
4.7 Summary. 148

5 Conclusions, summary, future work. 149
5.1 Summary. 149
5.2 Conclusions: Electron impact excitation of neutral argon. 150
5.3 Conclusions: Dielectronic recombination of low charge states of argon. 150
5.4 Conclusions: A GCR Model for low temperature, neutral dominated argon plasmas. 152
5.5 Future work. 154
A Magnetic fields in ALEXIS. 165
A.1 Magnetic fields in ALEXIS 165
B DR Fitting Coefficients. 169
C Creating usable GCR Data. 171
D Chapter 2 Codes (ELEX). 176
E Chapter 3 Codes (DR). 180
F Chapter 4 Codes (GCR). 181
F.1 Foreword 181
F.2 pec_fits_dat.pro 182
F.3 pec_208.py 183
F.4 qcd_solver 185
F.4.1 qcd_reader 185
F.4.2 qcd_plotter 186
F.4.3 qcd_eq_solver 186
F.4.4 qcd_td_solver 186
F.4.5 Example script to demonstrate qcd_solver.py 187
F.5 Optical Emission Spectroscopy codes (OES_lib.py). 190
F.5.1 retrieve_ALEXIS_data 190
F.5.2 get_spect_ratio 191
F.5.3 get_meta_scale 191

F.5.4 Example script to demonstrate OES_lib.py 192

List of Figures

1.1 Energy level diagram for the ground and two metastable states of neutral argon. We label the ground and metastable states using Racah notation for the two metastables, and Russel-Saunders notation for the ground state. We also include Paschen notation (common among experimentalists) below the line for each state. For a detailed description of these notations see Section 1.4.3 4

1.2 Non-equilibrium (time dependent) ion abundance for neutral argon using typical densities and temperatures found in ALEXIS ($T_e = 2eV; N_e \approx 1 \times 10^{16} m^{-3}$). The dashed box indicates plausible residence times for ions. From this we can roughly estimate an ionization fraction for ALEXIS. 5

1.3 One electron orbitals for various systems and nl values. 10

1.4 Schematic of the argon energy levels discussed in this work. The Paschen designation is listed on the plot directly above the energy, while J-values are listed above the plot. Long-lived metastable levels are marked with an asterisk. 15

1.5 Sketch of the rough behavior of effective collision strengths for the three main types of transitions (arbitrary units). 27

1.6 Metastable fractions plotted as a function of electron temperature. The plot displays an overlay of line ratio vs. temperature plots for all 20 densities in the ADAS208 dataset. The lack of "blurriness" indicates a line ratio that is independent of density. There is a clear temperature dependence in the 1s5:1s3 metastable fraction. 38

1.7 R-Matrix theory in a nutshell. In the outer region the effects of the Coulomb potential of the nucleus on the impact electron is considered small. Inside the boundary these effects cannot be neglected. The energy values of the wavefunction at the boundary form the R-Matrix. Figure courtesy of AJK Pearce [65]. . 40

1.8 Energy distribution for the 749 levels in the atomic structure calculation. The black circles show low lying pseudostates. Pentagons (online color:yellow) represent spectroscopic levels below the ionization limit of 15.76 eV. Squares (online color:red) show the densely distributed pseudostates from about 15.8 – 43.5 eV. Embedded within this dense distribution are 20 spectroscopic levels that result from the configurations $3s3p^6$ [3d–5p] (triangles, online color:magenta). Diamonds (online color:cyan0) show the sparsely distributed pseudo-states with energy above 43.5 eV. 46

1.9 Our total ground-state DR rate coefficient for Ar^{5+}. We compare our results (dot-dashed; online color = red) to those presented in Abdel-Naby [1] (dashed; color = black 47

1.10 The effect of shifting energy terms to corresponding NIST energies on our DR rate coefficients. Rate coefficient shown is for Ar^{+}. The solid line (online color = blue) shows the unshifted rate coefficient. The dashed line is the shifted coefficient. Error bars (online color = red) represent the difference between a shifted and unshifted DR calculation. 49

1.11 ALEXIS has 5 main components The ANTENNA (Purple), the OUTER COILS (blue), the INNER COILS (orange), the MAIN CHAMBER (grey), and the DC FILAMENT PLASMA (clear). Viewports for optical and probe access are labeled 1-7. 51

1.12 A picture of the ALEXIS linear plasma device, taken from the same perspective as Figure 1.11. 51

1.13 Radial magnetic field profiles in ALEXIS at viewports 2, 4, and 6. The magnetic field is plotted on the Y-axis for three positions corresponding to the walls and center of the ALEXIS vacuum chamber. The "out of the page" direction points towards the RF antenna, while the "into the page" direction points towards the DC filament section of ALEXIS. 54

1.14 Magnetic field strengths at the radial center of the ALEXIS chamber for all measured values of current. We present data here for the viewports 2, 4, and 6. 55

1.15 Axial magnetic field profile of the ALEXIS electromagnetic coils, plotted at viewports 2 through 6. These measurements were taken at the center of the vacuum chamber. 56

1.16 A characteristic IV trace from a single Langmuir probe in ALEXIS. You can clearly see the floating potential V_f, the plasma potential V_p, the electron saturation region (starting at I_{se}, and the ion saturation region (I_{si}.)) 59

1.17 The ALEXIS double probe. 61

1.18 Typical ALEXIS double-probe trace. The deviation from an ideal trace is clearly seen in the saturation regions. 62

1.19 The StellarNet Black Comet spectrometer used to collect experimental spectra. 64

2.1 Schematic of the argon energy levels discussed in this work. The Paschen designation is listed on the plot directly above the energy, while J-values are listed above the plot. Long-lived metastable levels are marked with an asterisk. 72

2.2 Energy distribution for the 749 levels in the atomic structure calculation. Circles show low lying pseudostates. Pentagons (online color:yellow) represent spectroscopic levels below the ionization limit of 15.76 eV. Squares (online color:red) show the densely distributed pseudostates from about 15.8 – 43.5 eV. Embedded within this dense distribution are 20 spectroscopic levels that result from the configurations $3s3p^6$ [3d–5p] (triangles, online color:magenta). Diamonds (online color:cyan0) show the sparsely distributed pseudo-states with energy above 43.5 eV. 74

2.3 Direct cross-sections for excitation from the ground state of neutral argon ($1p0$ in Paschen notation) into the ten levels of the $2p$ manifold. The present work is shown as a solid blue line (online color only), circles represent the BSR-500 work of Zatsarinny *et al.* (online color: blue). Experimental cross-section data from Chilton *et al.* (black triangles), Filopović (green squares), and Chutjian and Cartwright (cyan diamonds) are also shown. 80

2.4 Direct cross-sections for excitations from the ground state of neutral argon ($1p0$ in Paschen notation). The present work is shown as a solid blue line (online color only), circles represent the BSR-500 work of Zatsarinny *et al.* (online color: blue). Experimental cross-section data from Filopović (green squares), Khakoo (magenta pentagons), Hoshino *et al.* (yellow stars), and Chutjian and Cartwright (cyan diamonds) are also shown. 82

2.5 Direct and cascade cross-sections for excitations from the ground state of neutral argon. Our direct cross-sections are shown as a solid blue line (online color only), while cascade cross-sections are shown in dashed green. The experimental results have been scaled to allow for a qualitative comparison. 83

2.6 Theoretical cross sections for excitation from the $1s5$ metastable state of neutral argon, compared with the 41 state R-Matrix calcualation of Bartschat and Zeman. The direct cross-section is shown as both circles (Bartschat and Zeman) and as a solid line (present work). The dashed line (online color:red) shows the apparent cross-section. The dot-dashed line (online color: green) shows the cascade contribution to the apparent cross-section. Where available, the experimental apparent cross-section measurements of Piech *et al.* are shown as cyan diamonds. 85

2.7 Theoretical cross sections for excitation from the $1s3$ metastable state of neutral argon, compared with the 41 state R-Matrix calcualation of Bartschat and Zeman. The direct cross-section is shown as both circles (Bartschat and Zeeman) and as a solid line (present work). The dashed line (online color:red) shows the apparent cross-section. The dot-dashed line (online color: green) shows the cascade contribution to the apparent cross-section. Where available, the experimental apparent cross-section measurements of Piech *et al.* are shown as cyan diamonds. 86

3.1 Our total ground-state DR rate coefficient for Ar^{5+}. We compare our results (dot-dashed; online color = red) to those presented in Abdel-Naby [1] (dashed; color = black) 98

3.2 The effect of shifting energy terms to corresponding NIST energies on our DR rate coefficients. Rate coefficient shown is for Ar^{+}. The solid line (online color = blue) shows the unshifted rate coefficient. The dashed line is the shifted coefficient. Error bars (online color = red) represent the difference between a shifted and unshifted DR calculation. 101

3.3 Maxwellian convolved DR rate coefficients for Ar^{+}. The upper left subplot shows the rate coefficient for $\Delta n = 0$, while the upper right shows the rate coefficient for $\Delta n = 1$. The bottom subplot shows their sum, super-imposed on a background displaying the Lorentzian resonance profiles. The ground level data are shown in red (dashed), nd the first excited metastable level is in blue (dot-dashed). 103

3.4 Maxwellian convolved DR rate coefficients for Ar^{2+}. The upper left subplot shows the rate coefficient for $\Delta n = 0$, while the upper right shows the rate coefficient for $\Delta n = 1$. The bottom subplot shows their sum, super-imposed on a background displaying the Lorentzian resonance profiles. The ground level data are shown in red (dashed), the first excited metastable level is in blue (dot-dashed), and the second excited metastable level is shown in green (dotted). 104

3.5 Maxwellian convolved DR rate coefficients for Ar^{3+}. The upper left subplot shows the rate coefficient for $\Delta n = 0$, while the upper right shows the rate coefficient for $\Delta n = 1$. The bottom subplot shows their sum, super-imposed on a background displaying the Lorentzian resonance profiles. The ground level data are shown in red (dashed). 105

3.6 Maxwellian convolved DR rate coefficients for Ar^{4+}. The upper left subplot shows the rate coefficient for $\Delta n = 0$, while the upper right shows the rate coefficient for $\Delta n = 1$. The bottom subplot shows their sum, super-imposed on a background displaying the Lorentzian resonance profiles. The ground level data are shown in red (dashed), the first excited metastable level is in blue (dot-dashed), and the second excited metastable level is shown in green (dotted). 106

3.7 Total ground state DR rate coefficients for all ion stages. Here we show Maxwellian convolved rate coefficients for Ar^{+} (∇, online color = black), Ar^{2+} (squares, online color = red), Ar $^{3+}$ ($\diamond$, online color = green), and Ar^{4+} (circles, online color = magenta). 107

3.8 Our rate coefficients for Ar^{+} compared with those of Loch [57] (triangles) and Mazzotta (+) [59]. We include rates for all levels within the ground term of each ion, in addition to the LS rate coefficient (purple, underscores). The ground level data are shown in red (dashed), and the first excited metastable level is in blue (dot-dashed). 109

3.9 Our rate coefficients for Ar^{2+} compared with those of Loch [57] (triamgles) and Mazzotta (+) [59]. We include rates for all levels within the ground term of each ion, in addition to the LS rate coefficient (purple, underscores). Ground state is shown in red (dashed), first excited metastable is in blue (dot-dashed), and the second excited metastable states is shown in green (dotted). 110

3.10 Our rate coefficients for Ar^{3+} compared with those of Loch [57] (triangles) and Mazzotta (+) [59]. We include rates for all levels within the ground term of each ion, in addition to the LS rate coefficient (purple, underscores). The ground level data are shown in red (dashed). 111

3.11 Our rate coefficients for Ar^{4+} compared with those of Loch [57] (triangles) and Mazzotta (+) [59]. We include rates for all levels within the ground term of each ion, in addition to the LS rate coefficient (purple, underscores). The ground state data are shown in red (dashed), the first excited metastable level is in blue (dot-dashed), and the second excited metastable level is shown in green (dotted). 112

3.12 Equilibrium ion fraction balance for Ar^{+}—Ar^{5+}. Solid lines represent the present work, dashed lines were generated using data from Mazzotta [59] 114

4.1 Radial electron temperature profiles for the 24 data runs at viewport 2 in the ALEXIS experiment. 120

4.2 Radial electron density profiles for the 24 data runs at viewport 2 in the ALEXIS experiment. 121

4.3 Spectral emission for the 24 data runs at viewport 2 in the ALEXIS experiment. The plot on the left shows an overlay of the 24 data runs collected at viewport 2 for the entire spectral range of the Black Comet spectrometer. On the right we focus on the wavelength range 760 – 860 nm and includes labels for the 4 distinct, strong lines given in Table 4.3. 124

4.4 Metastable population densities for neutral argon at equilibrium. 131

4.5 Time dependent metastable population densities for neutral argon at equilibrium. The dashed vertical line represents the limit for thermal neutral argon atoms to travel the radial distance of ≈ 4 cm from the center of the ALEXIS plasma to the plasma boundary. For this plot we choose $T_e \approx 5eV$; $N_e \approx 1 \times 10^{16} m^{-3}$. . . 134

4.6 The ratio of the ground to 1s3 metastable as a function of time. 135

4.7 The ratio of the 1s5 to 1s3 metastables as a function of time. 136

4.8 The theoretical *metastable fraction of best fit* is determined by looping over 300 possible metastable fractions, and comparing the resulting line ratio for experimental temperatures / line ratios observed in ALEXIS. 139

4.9 1s5:1s3 theoretically calculated metastable fractions for all 43 data runs in ALEXIS using the line at 852 nm, plotted vs. the experimentally measured line ratios. . 140

4.10 1s5:1s3 theoretically calculated metastable fractions for all 43 data runs in ALEXIS using the line at 826.1 nm, plotted vs. the experimentally measured line ratios. 141

4.11 Synthetic emission compared with experimental observations for the four strong, distinct lines observed in ALEXIS. 143

4.12 Experimental temperature measurements in ALEXIS, with error bars of 25 %. The orange stars are our predicted temperatures corresponding to the experimentally determined line ratios. The smooth curve is the result of a quadratic curve fit. 145

4.13 Metastable fraction vs electron density in ALEXIS fr all 43 data runs, separated by viewport and collection date. The top left plot displays data collected at viewport 2. The top right displays data from viewport 2 from a different collection date. The bottom left plot shows data collected from viewport 4. The bottom right plot is the data collected from viewport 6. 147

5.1 Benchmarking our results. The plot shown here displays experimental experimental measurement of the four strong lines in ALEXIS, with an overplot of their synthetic counterparts. The close agreement serves to validate our results. 153

C.1 Flow chart for creating GCR data from R-Matrix output. 175

List of Tables

1.1 L-S coupling for the $1s^2 2s2p$ configuration of neutral beryllium. 12

1.2 jj coupling for Be-like Xe. Notice the J-values are the same as before, but there are no total L and S quantum numbers. 13

1.3 The first few energy levels of neutral argon using **jk** coupling (Racah Notation). A superscript *o* indicates odd parity. 14

1.4 Selection rules for electric dipole, electric quadrupole, and magnetic dipole transitions. 16

1.5 Coil type and location of the nine electromagnetic coils used in the ALEXIS plasma column. 52

2.1 Paschen and Racah notation for all the energy levels referenced in the present work. 71

2.2 Comparison of energy levels from our atomic structure calculation with Zatsarinny and Bartschat [81] and the NIST database [51]. Average percent error with NIST values is shown for both the present work and for Z & B. 75

2.3 Einstein A_{ij} coefficients for selected strong dipole transitions, compared to NIST. For transitions involving radiative decays into the 1s3 and 1s5 metastables, we choose transitions corresponding to lines predicted to be good candidates for optical diagnostics. Average percent difference with NIST for all six lines is 14.5%. 76

3.1 Orbital type and scaling parameters for ion stages Ar^{+}-Ar^{4+}. These values were used in both our structure calculation and DR runs. TFDA indicates Thomas-Fermi-Dirac-Amaldi orbital potentials, which we used exclusively. Any λ_{nl} value not explicitly stated can be assumed to be the default value of 1.0000. 94

3.2 The first ten energy levels 94

3.3 Basis configurations for all four ion stages. The notation 4(s—f) is meant to represent the set of configurations that contain one electron in each of the 4s, 4p, 4d and 4f orbitals. 97

3.4 Potential metastable levels within the ground state configuration for each of the four ion stages presented. 99

4.1 Estimating error for the double probe. 118

4.2 Operating parameters for the 24 data runs conducted at viewport 2, and displayed in Figures 4.1 and 4.2. 122

4.3 Distinct lines in ALEXIS. Lower and upper levels are specified using Racah notation. Paschen notation (in parentheses) is given for the lower levels. The final column lists whether the transition involves a core change. 125

4.4 Atomic data for the spectral line at 696.543 nm. 125

4.5 Distinct, strong lines in ALEXIS, with Paschen notation included for the lower level. The final column shows whether the transition involves a core change. These lines are unblended and readily detectable with our spectrometer, making them good candidates for potential optical diagnostics. 126

A.1 The magnetic field in ALEXIS at viewport 2 in Gauss, as a function of the current in chamber and source power supplies. 166

A.2 The magnetic field in ALEXIS at viewport 4 in Gauss, as a function of the current in the chamber and source power supplies. 167

A.3 The magnetic field in ALEXIS at viewport 6 in Gauss, as a function of the current in the chamber and source power supplies. 168

B.1 Level-resolved fitting coefficients 169

Chapter 1

Introduction, overview, theory, and methods.

1.1 Introduction

This dissertation is primarily concerned with an ongoing effort to develop non-invasive diagnostics for low-temperature laboratory argon plasmas, focusing on the development of new spectroscopic techniques for diagnosing metastable fraction, electron temperature, and electron density. Low temperature argon plasmas are ubiquitous in basic research, industrial, and medical applications of plasmas. In all of these systems, the plasma is often weakly-ionized and dominated by the presence of neutral atoms. While in-situ probe techniques can often be used to diagnose these plasmas, it is highly desirable to have a remote, non-invasive technique from which we can obtain the plasma parameters.

For the work described in this dissertation, the scientific goal is to develop a non-invasive, optical emission spectroscopy-based diagnostic for measuring the density and electron temperature of a low temperature argon plasma. There are a variety of emission spectroscopy diagnostic techniques for high temperature plasma or very energetic plasmas [e.g., X-ray sources, astrophysical sources, etc.] [40, 68]. While there are also techniques that have been proposed for low temperature plasmas [17], it will be shown that these approaches were not applicable to the experiments performed as part of this study. As a result, a detailed study of the atomic properties of metastable argon had to be undertaken in order to understand the experimentally observed spectra - leading to the generation of new atomic data and a new understanding of atomic processes in low temperature plasmas.

High purity argon is readily available, and being a stable and inexpensive noble gas is an ideal candidate to conduct basic plasma research. As we will show, the low electron temperatures ($T_e < 5 \quad eV$) present in most basic argon plasma experiments leads to a plasma

that is neutral dominated. While these low temperature plasma are often in steady state, the plasma is neither in local thermodynamic equilibrium (LTE), nor can it be described by coronal approximations. This eliminates many current spectroscopic diagnostic techniques which rely on line-ratio methods that assume one of these two conditions and require the presence of adjacent ion species in populations large enough to be spectroscopically significant[40]. In the absence of LTE or coronal conditions, the appropriate method for analysing the spectral emission from these plasma is usually referred to as generalized collisional-radiative (GCR) theory [12]. The GCR method is an extension of the collisional radiative method [13], extended to include the role of metastable states in population modelling, and density dependence on electron density in the effective rate coefficients that connect the ground and metastable states [74]. The GCR approach is well established, and widely used in both the astrophysical and fusion plasma communities. Recently, efforts to apply this method to low-temperature laboratory plasmas have become more common [19].

One complication to the atomic picture of low temperature argon plasmas is the existence of two long lived metastable states that exist in neutral argon. These metastable states have radiation lifetimes greater than 1s, and provide an efficient channel for populating excited states of argon at temperatures significantly less than would be required by the ground state of neutral argon. As a result, excitations from argon metastable states tend to dominate the argon emission spectrum at low electron temperatures ($T_e \leq 10 \quad eV$). Thus, an analysis of metastable populations is essential for any spectral modeling. This is the main difficulty in developing spectral diagnostic tools for neutral argon emission: a lack of knowledge of the metastable populations. As shown in Figure 1.1, it is possible to excite from both metastable states of neutral argon at electron energies less than 2 eV. Contrast this with excitation from the ground state, which requires, at a minimum, energies greater than 12 eV. In the ALEXIS experiment a typical range for average Maxwellian electron temperatures is 2–7 eV, as measured using electromagnetic probes. As a result, excited states of neutral argon in ALEXIS plasmas are almost entirely populated by excitation from

one of the two metastable states. Any attempt to model the spectral emission from such a plasma must therefore include detailed knowledge of the relative fractional abundance of these metastables. This in turn is likely to depend on plasma conditions, vessel dimensions, and wall interactions.

It should be noted that the excitation that we discussed in the previous paragraph occurs almost entirely between states of neutral argon. As shown in Figure 1.1, excited states of neutral are effectively accessible only via excitation from the 1s3 and 1s5 metastables, due to the low electron temperature of the plasma. These low temperatures also mean that the emission spectrum of the plasma is dominated by the neutral atoms and the detection of argon ion emission lines is quite limited. As a result, our model of the spectral emission from the plasma will assume that almost all of the light that we detect will come from the metastable states. While we know that argon ions exist in these plasmas, the higher temperatures required to produce them lead to low ionization fractions, on the order of 1×10^{-4} or less. Residence times for argon ions swept along magnetic field lines in ALEXIS is estimated to be $\approx$ 5 ms, based on an estimate of their thermal speed. As can be seen in Figure 1.2, the amount of time required for ionized argon to reach a relative fraction, with respect to neutral argon, of even 1:1000 is on the the order of 1 s, while a ration of 1:100 does not occur until residence times are approximately 100 s. If we roughly estimate the residence time of ions in ALEXIS to be in the range 1 – 10 ms, as indicated by the dashed line box in Figure 1.2, we can see that expected ionization fractions in ALEXIS are $\approx 1 \times 10^{-6}$, leading us to conclude that very few ions are present.

We can now outline a basic algorithm for spectroscopic diagnostics of the types of plasmas under investigation. First, we must identify the dominant atomic processes that influence the detected spectroscopic emission. While excitation is obviously paramount among these processes, recombination processes, such as dielectronic recombination and radiative recombination, must also be considered to be confident that our analysis of the charge state distribution is correct. Next, we need access to accurate, level-resolved (i.e. J-resolved)

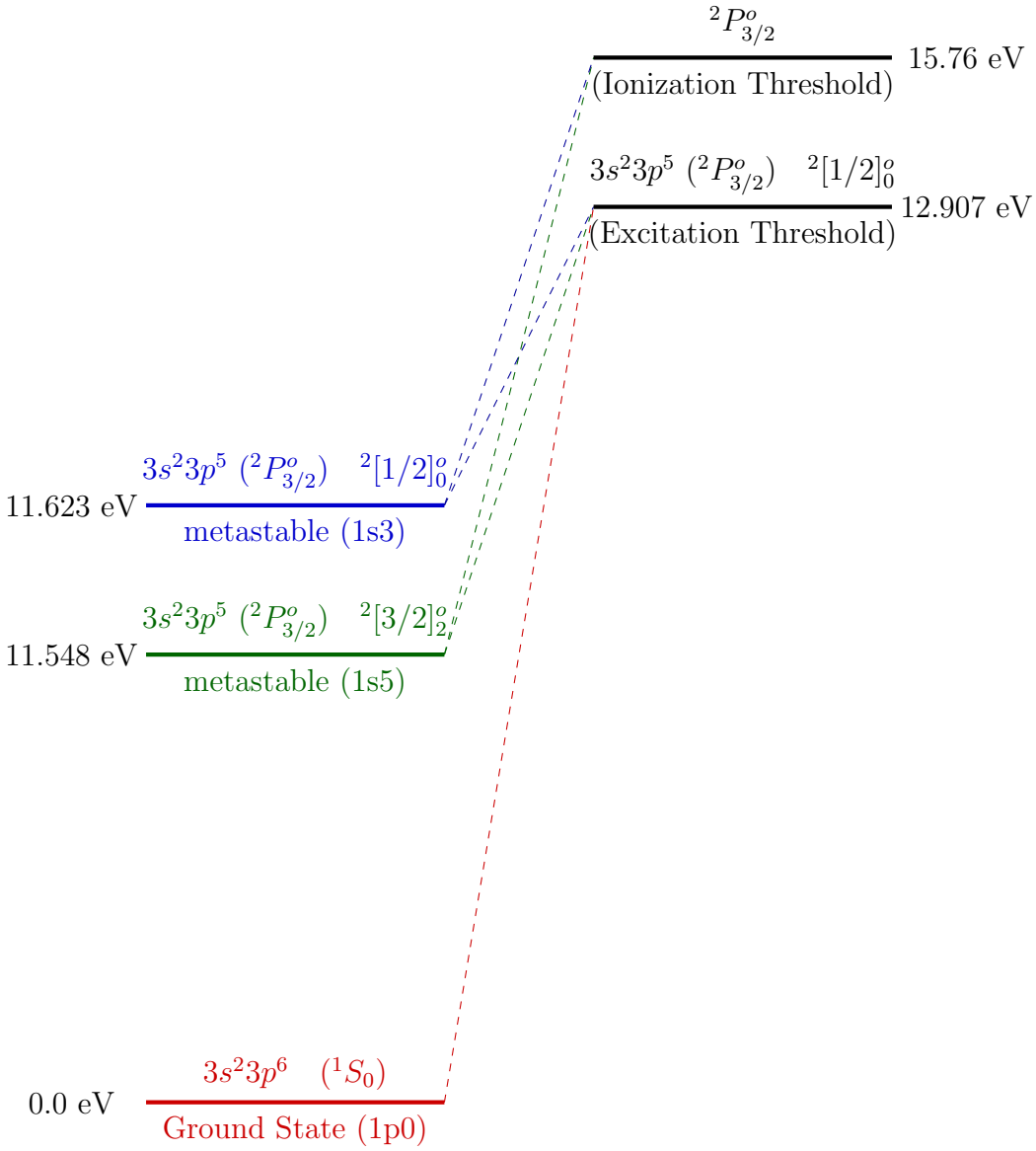

Figure 1.1: Energy level diagram for the ground and two metastable states of neutral argon. We label the ground and metastable states using Racah notation for the two metastables, and Russel-Saunders notation for the ground state. We also include Paschen notation (common among experimentalists) below the line for each state. For a detailed description of these notations see Section 1.4.3

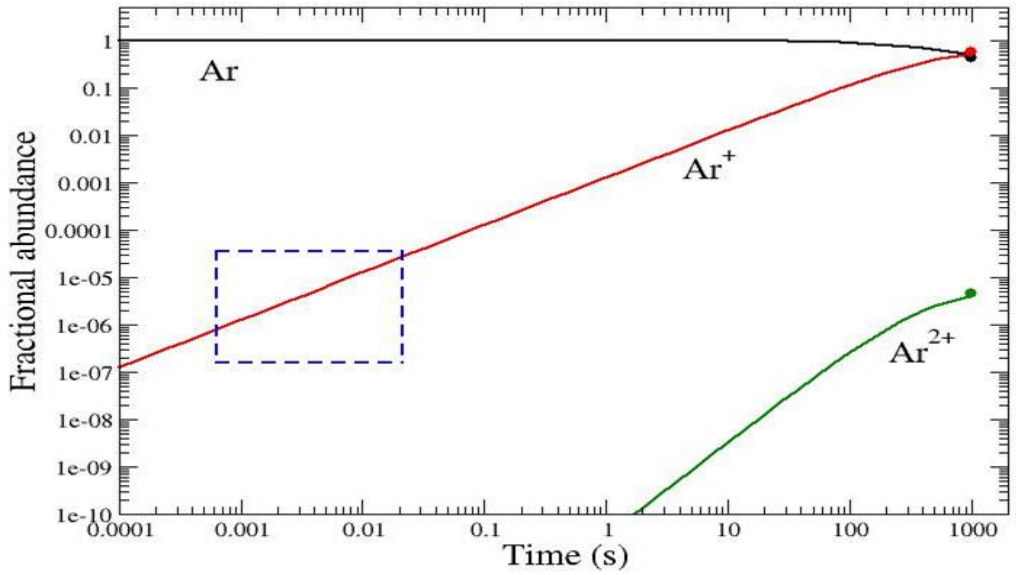

Figure 1.2: Non-equilibrium (time dependent) ion abundance for neutral argon using typical densities and temperatures found in ALEXIS ($T_e = 2eV; N_e \approx 1 \times 10^{16} m^{-3}$). The dashed box indicates plausible residence times for ions. From this we can roughly estimate an ionization fraction for ALEXIS.

atomic data for any relevant atomic processes, and this data must include detailed information of the role of the 1s3 and 1s5 metastables. Finally, we can use this metastable resolved atomic data within a GCR framework to model any spectral emission, and use standard methods, such as temperature and density sensitive line ratios, to predict experimentally measured plasma parameters. Comparison to experimental data from ALEXIS is used to provide a benchmark for our results. This is the main aim of this work, with the intention that the methods developed can then be applied to other argon plasmas.

At the time that we began our efforts, very little high quality, level resolved data for neutral argon existed. As we will detail in this dissertation, our first objective is to create the necessary level-resolved atomic data for neutral and low charge states of argon, and subsequently to benchmark that data against existing theoretical and experimental data when available. We will show that this goal has been met, and th at the atomic data we have calculated is both accurate and reasonably complete. Once this was completed we applied this new data to the development of new line ratio diagnostics for low temperature argon plasmas. Furthermore, at the outset of this project it was unclear just how much ionized argon was present in ALEXIS, and DR was deemed a potential contributor to atomic populations in ALEXIS. We now know that DR does not significantly impact atomic populations in most low-temperature argon plasmas, due to the absence of a significant population of ionized species from which to recombine..

Of the many atomic processes that can occur within low temperature plasmas, this thesis will focus on atomic data for only two, dielectronic recombination(DR) and electron impact excitation(ELEX). Many atomic processes (i.e. any ionizing processes) can be excluded from consideration in ALEXIS simply because the low electron temperatures do not supply the required energy for them to occur. Processes such as charge exchange rely on the presence of ionized argon and can also be excluded. For other processes, such as radiative recombination, reliable data already exists [36]. Electron-impact excitation should be the primary population mechanism for excited states of neutral argon, and therefore cannot be

ignored. The role of DR in low-temperature argon plasmas is largely unknown, due to the lack of reliable, level-resolved atomic data. However, DR is known to be an important, even dominant form of recombination in many types of plasmas [22] and should not be excluded without investigation into its role in low temperature argon plasmas.

This introductory chapter is intended to serve as an overview and guide to this work. It provides a necessary background for some of the collisional processes and underlying physics in the chapters that follow. This is required due to the chosen format for Chapters 2 and 3, which present work that has either already been published in a peer-reviewed journal, or is currently under preparation for publication. Chapter 4 will discuss the methods used to generate synthetic spectra and will benchmark those results against experimental measurements in the ALEXIS device. Chapter 5 will summarize the results presented in this work and present some concluding thoughts for future directions for this work.

Relevant Atomic Processes and Background Theory In the next few sections of this introduction we present a description of the relevant atomic processes discussed in this work.

1.2 Complex atoms and selection rules

Multi-electron systems All of the systems relevant atomic species under consideration in this work have more than one electron. In fact, most of the atomic processes relevant to modelling low-temperature argon plasmas occur within neutral argon (18 electrons), or singly ionized argon (17 electrons), though in Chapter 2 we present data for Ar^{2+}, Ar^{3+}, Ar^{4+}, and Ar^{5+} to complete the atomic dataset for DR currently available through the DR project [5], and for comparison with previously published work. In such *multi-electron* systems, the Hamiltonian is given by:

$$H = \sum_{i=1}^{N} \left(\underbrace{\frac{-\hbar^2}{2m_e}\nabla_i^2}_{KE} - \underbrace{\frac{Ze^2}{4\pi\varepsilon_o r_i}}_{PE} \right) + \sum_{i=1}^{N-1} \sum_{j=i+1}^{N} \underbrace{\frac{e^2}{4\pi\varepsilon_o |\vec{r_i} - \vec{r_j}|}}_{correlation} \tag{1.1}$$

This equation explicitly contains the Coulomb interaction between electrons in the final term, and is usually not possible to solve the time-independent Schrödinger equation analytically. A numerical method must be employed to extract meaningful solutions for the eigenvalues and eigenvectors. Additional relativistic terms are also added to improve accuracy (i.e. spin-orbit interaction, relativistic mass and velocity). This makes analytic solutions even less feasible. The relativistic terms will not be shown on the following pages, to allow the main ideas to be more clearly presented.

1.3 Atomic structure and wavefunctions.

1.3.1 Central Field Model

A common and extremely powerful approximation in atomic structure calculations is to assume that the N electrons surrounding the nucleus can be treated separately. Each is

assumed to be well approximated by a central potential due to the nucleus combined with an *average* potential from the combination of all the other electrons. This is called the *central field model*. Using this assumption we can rewrite equation 1.1:

$$H = \underbrace{\frac{-\hbar^2}{2m_e}\nabla_i^2}_{KE} \underbrace{- \frac{Ze^2}{4\pi\varepsilon_o r_i} + \sum_{j\neq i} \frac{e^2}{4\pi\varepsilon_o |\vec{r_i} - \vec{r_j}|}}_{V_{effective}} \tag{1.2}$$

where we have labeled the sum of the potential energy and the interaction of electron N with all of its neighbors as $V_{effective} = V_i(r_i) = \frac{-Ze^2}{4\pi\varepsilon_o r_i} + \sum_{j\neq i} \frac{e^2}{4\pi\varepsilon_o |\vec{r_i} - \vec{r_j}|}$. The first term of $V_{effective}$ is the central potential due to the nucleus, the second represents the interaction of electron N with its neighbors.

We can insert $V_{effective}$ into Schrödinger's equation, and rewrite it thus:

$$\hat{H} R_i(r) = \left[\frac{-\hbar^2}{2m_e}\nabla_i^2 + \frac{l_i(l_i+1)\hbar^2}{2mr^2} + V_i(r_i) \right] R_i(r) = E_i R_i(r) \tag{1.3}$$

The solutions of this equation are almost always numerical, and are usually called *orbitals* ($R(r)$). Figure 1.3 shows examples of orbitals calculated from the atomic physics code AUTOSTRUCTURE [6]; the same code is used to calculate all of the atomic structure in Chapters 2 and 3, and the DR rate coefficients in Chapter 2. The angular part of $\Psi(r)$; $Y_{l_i m_i}(\theta_i, \phi_i)$, are known as *spherical harmonics*. The radial part $R_{n_i l_i}(r_i)$ is not the same as the hydrogenic radial wavefunctions, but can still be labeled with using the principal orbital quantum number n and angular momentum quantum number l.

$$\Psi(\vec{r_i}) = R_{n_i l_i}(r_i) Y_{l_i m_i}(\theta_i, R_i) \tag{1.4}$$

Thus, any multi-electron wavefunction for an N-electron system can be written as:

$$\psi(\vec{r_1}, \vec{r_2}, \vec{r_3}, \ldots, \vec{r_N}) = \phi_1(\vec{r_1})\phi_2(\vec{r_2})\phi_3(\vec{r_3}) \ldots \phi_N(\vec{r_N}) \tag{1.5}$$

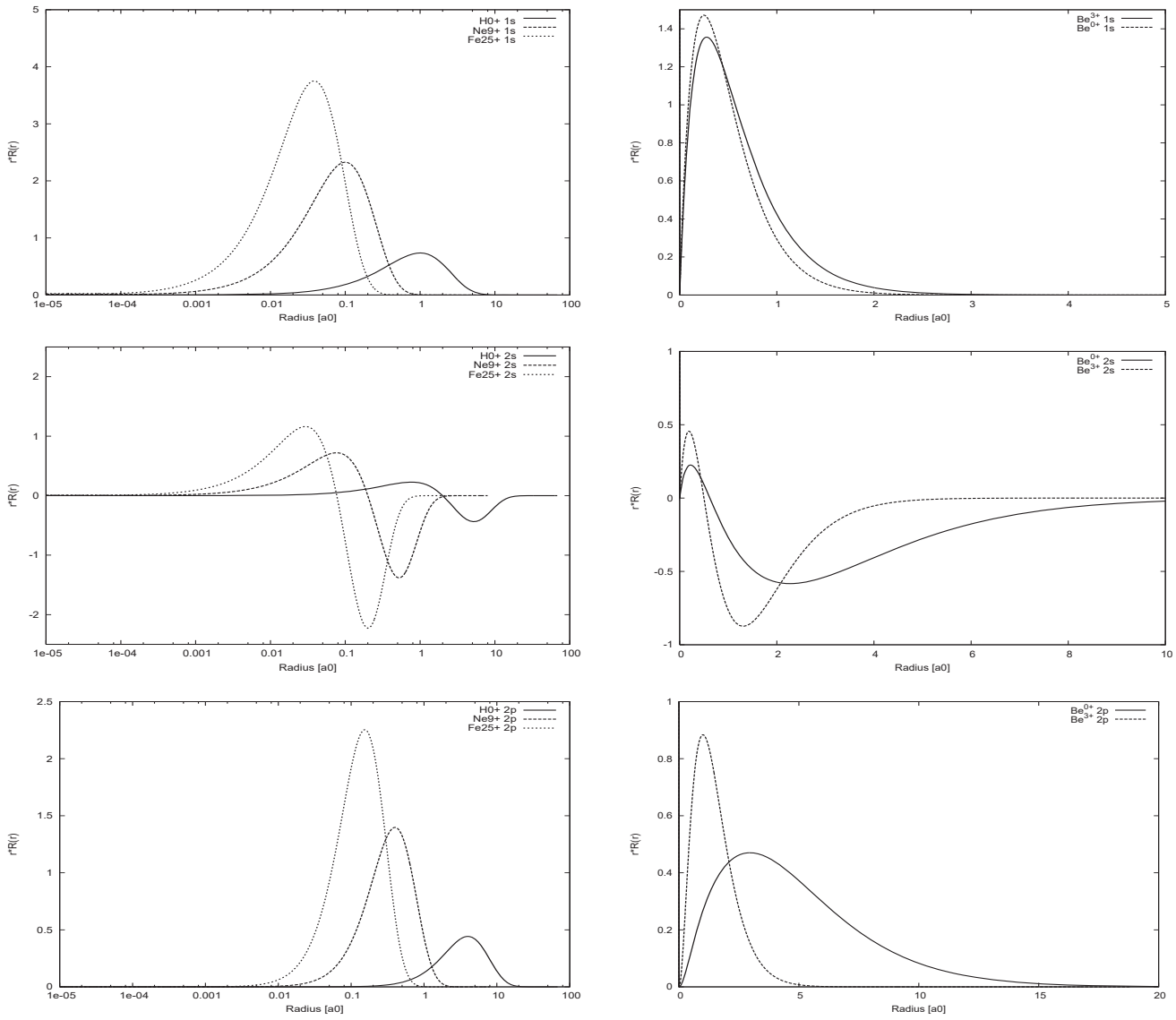

Figure 1.3: One electron orbitals for various systems and nl values.

Once the condition that the wavefunction must be antisymmetric upon the exchange of any two electrons is included, the total wavefunction for the system is given by a linear combination of the products of the orbitals. This is referred to as a Slater determinant.

Spin It is observed that electrons have a magnetic field similar to that of a charged spinning body. This contribution to the total angular momentum of an electron is called the electron's "spin", and is an intrinsic property. Spin does not arise from Schrödinger's equation, though other formulations (i.e. the Dirac equation) do include spin explicitly. Thus, each orbital

will also have a spin-coordinate with associated quantum numbers $s = \frac{1}{2}; m_s = \pm\frac{1}{2}$, which must be included in the total wavefunction.

$$\Phi = R_{nl}(r)Y_{lm}(\theta, \phi)\sigma_{sm} \tag{1.6}$$

1.4 Addition of angular momenta / coupling schemes.

For system of n atomic orbitals with i electrons, each with orbital angular momentum l_i and spin s_i, the primary conserved quantity of interest for each electron is the total angular momentum j. Depending on the atomic properties of the system under investigation, this quantity is determined using a variety of different methods, called *angular coupling schemes*. In brief, different coupling schemes utilize different methods for combining or "coupling" the quantum numbers that appropriately describe the system. These sets of appropriate numbers are known as "good" quantum numbers for the system. It is important when evaluating any atomic system to use an appropriate coupling scheme, as "good" quantum numbers for one system may not accurately describe another. As an example, consider neutral argon. By far, the most widely used set of quantum numbers used to describe atomic systems are l and s, the quantum numbers for orbital angular momentum and spin. This type of coupling is known as Russell-Saunders, or LSJ coupling. For most systems, these l and s quantum numbers can be combined to arrive at a distinct set of total L, S, and J values to describe the atomic states. However, for most neutral systems, including neutral argon, the actual atomic states exist as a superposition of L, S, J states. The terms described by the LS coupling scheme do not accurately or uniquely identify the states in a neutral system.

In this section, we describe various coupling / labeling schemes for atomic systems.

1.4.1 Russell-Saunders or LSJ coupling

Russell-Saunders coupling is probably the most common, and works well for light systems. It is accomplished with the following steps.

LSJ Coupling

1. First couple the l_i values to determine the total orbital angular momentum $\vec{L}$: $\vec{L} = \sum_i \vec{l_i}$
2. Then couple the s_i values to arrive at a total spin angular momentum $\vec{S}$: $\vec{S} = \sum_i \vec{s_i}$
3. Then couple $\vec{L}$ and $\vec{S}$ to get the total angular momentum, $\vec{J}$: $\vec{J} = \vec{L} + \vec{S}$

It is often useful to retain the L and S quantum numbers, as these are approximately conserved quantities for light species. Also, for light systems, the J-values within an LS term are close to degenerate.

The resulting L, S, and J values are written in the form ${}^{2S+1}L_J$, where the historical convention $L = 0, 1, 2, 3, 4, 5... = S, P, D, F, G, H...$ is used.

The L, S, and J summations obey the triangle inequality:

$$|l_1 - l_2 - l_3 \dots l_i| \leq L \leq l_1 + l_2 + l_3 \dots l_i \tag{1.7}$$

$$|s_1 - s_2 - s_3 \dots s_i| \leq S \leq s_1 + s_2 + s_3 \dots s_i \tag{1.8}$$

$$|L - S| \leq J \leq |L + S| \tag{1.9}$$

Example: Beryllium $1s^2 2s2p$

Table 1.1: L-S coupling for the $1s^2 2s2p$ configuration of neutral beryllium.

l_1	l_2	L	s_1	s_2	S	J
0	1	1	$\frac{1}{2}$	$\frac{1}{2}$	0	1
					1	2, 1, 0

For the example shown in Table 1.1, we can write the configuration as $1s^2 2s2p$ and the four Russell-Saunders determined levels as $(^1P_1)$ and $(^3P_{2,1,0})$. Thus there are two ^{2S+1}L terms in this configuration with 4 $^{2S+1}L_J$ levels.

1.4.2 jj coupling

For sufficiently heavy systems, the L and S quantum numbers are not "good" quantum numbers. In this case, the *j-j coupling scheme* is more appropriate.

(jj coupling)

1. First couple the l_i and s_i values: $\vec{j_i} = \vec{l_i} + \vec{s_i}$
2. Then couple the $\vec{j_i}$ values: $\vec{J} = \sum_i \vec{j_i}$

This gives the same J-values as L-S coupling.

Example: Beryllium-like Xenon (Xe^{50+}) $1s^2 2s2p$

Table 1.2: jj coupling for Be-like Xe. Notice the J-values are the same as before, but there are no total L and S quantum numbers.

l_1	s_1	j_1	l_2	s_2	j_2	J
0	$\frac{1}{2}$	$\frac{1}{2}$	1	$\frac{1}{2}$	$\frac{1}{2}$	$1, 0$
		$\frac{1}{2}$			$\frac{3}{2}$	$2, 1$

For light species, the J levels within a term are close to degenerate, while for heavier elements and for high charge states the splitting of the levels within a term becomes large and LS coupling is a less useful coupling scheme. Each J has a magnetic quantum number M_J associated with it.

$$-J \leq M_J \leq J \tag{1.10}$$

These are almost always degenerate in energy, unless a magnetic field is applied.

1.4.3 jk coupling / Racah notation

Finally, an alternative coupling scheme is often employed for neutral systems, where the atom is divided into a "core" plus an outermost electron. The core is evaluated using standard LSJ coupling to arrive at a "parent" J_1, which is then coupled with the outermost electron to arrive at a value K. The total angular momentum J is then determined by coupling K and the spin of the outermost electron; $J = K \pm \frac{1}{2}$. This is the method most widely used for neutral argon. The first few levels, from the NIST data base are given below. In most literature, values for the core are excluded when referring to the energy levels. The resulting notation $nl[k]_j$ is referred to as *Racah notation.*

For the first two rows in this table, we see that the core has a J of 3/2, which is coupled with an electron with orbital angular momentum $l = 0$ to arrive at a K of $\frac{3}{2}$ (in brackets). The total angular momentum is then $J = \frac{3}{2} \pm \frac{1}{2}$, leading to a J of 2 (first row) and a J of 1 (second row).

Table 1.3: The first few energy levels of neutral argon using **jk** coupling (Racah Notation). A superscript o indicates odd parity.

Core	$nl\,[K]_j$	NIST Energy (eV)
$3s^2 3p^5 (^2P^o_{3/2})$	$4s[3/2]^o_{(2)}$	11.548
$3s^2 3p^5 (^2P^o_{3/2})$	$4s[3/2]^o_{(1)}$	11.623
$3s^2 3p^5 (^2P^o_{1/2})$	$4s[1/2]^o_{(0)}$	11.723
$3s^2 3p^5 (^2P^o_{1/2})$	$4s[1/2]^o_{(1)}$	11.828
$3s^2 3p^5 (^2P^o_{3/2})$	$4p[1/2]_{(1)}$	12.907
$3s^2 3p^5 (^2P^o_{3/2})$	$4p[5/2]_{(3)}$	13.075
$3s^2 3p^5 (^2P^o_{3/2})$	$4p[5/2]_{(2)}$	13.095

Paschen notation Though not a coupling scheme, another method for labeling energy levels in atomic systems, common in experimental physics, is called *Paschen notation.* It is important to note that Paschen notation does not reflect any one coupling scheme. Instead, it labels energy levels by energy order with respect to the ionization potential. For example, in neutral argon the levels in the first excited configuration are labeled $1s5$, $1s4$, $1s3$, $1s2$,

indicating that these are electrons that belong to the first excited configuration with an orbital angular momentum s. The energy order is with respect to the ionization potential, not the energy of the ground state, which can lead to confusion since typical NIST values are ordered using the reverse convention. See Figure 1.4 for the first two excited configurations of neutral argon, including Paschen notation for the levels within these configurations.

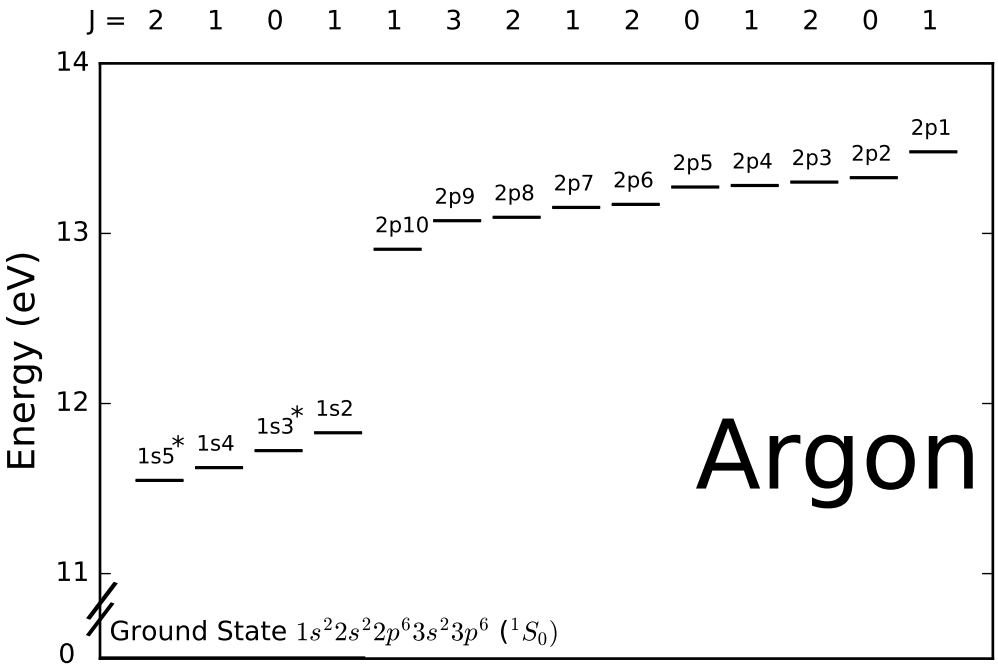

Figure 1.4: Schematic of the argon energy levels discussed in this work. The Paschen designation is listed on the plot directly above the energy, while J-values are listed above the plot. Long-lived metastable levels are marked with an asterisk.

1.5 Selection rules

If one includes the variation of the electric and magnetic fields across the dimensions of the atom, one can derive expressions and selection rules for electric and magnetic quadrupole transitions. The selection rules can be defined for systems with more than one electron, with rules for the total L, S and J.

Table 1.4: Selection rules for electric dipole, electric quadrupole, and magnetic dipole transitions.

		E-dipole	E-quadrupole	M-dipole
Rigorous rules	1	$\Delta J = 0, \pm 1$ (not 0-0)	$\Delta J = 0, \pm 1, \pm 2$ (not 0-0, 1/2-1/2, 0-1)	$\Delta J = 0, \pm 1$ (not 0-1)
	2	$\Delta M_J = 0, \pm 1$	$\Delta M_J = 0, \pm 1, \pm 2$	$\Delta M_J = 0, \pm 1$
	3	parity changes	parity unchanged	parity unchanged
Propensity rules	4	$\Delta S = 0$	$\Delta S = 0$	$\Delta S = 0$
	5	One electron jumps	One of no-electron jumps	No electron jumps
		$\Delta n = any$	$\Delta n = any$	$\Delta n = 0$
		$\Delta l = \pm 1$	$\Delta l = 0, \pm 2$	$\Delta l = 0$
	6	$\Delta L = 0, \pm 1$ (not 0-0)	$\Delta L = 0, \pm 1, \pm 2$ (not 0-0, 0-1)	$\Delta L = 0$

Table 1.4 shows the selection rules for three transition types. The rules are always valid for hydrogenic systems. For multi-electron systems only the rigorous rules are always obeyed. As the propensity rules involve L and S quantum numbers, which are no longer conserved quantities, these rules can be broken. Since the total angular momentum is a conserved quantity, the rules on J are rigorously obeyed. For the purpose of our work this is the most important, and often the only, consideration, as L and S are not good quantum numbers for neutral systems.

If an excited state has no allowed dipole transitions to the ground (or to any levels below) it is likely to be a *metastable*, and can have a large long lived population. The lifetime of an excited state is given by:

$$\tau_i \sim \frac{1}{\sum_{j<i} A_{i\to j} + N_e \sum_{j\neq i} q_{i\to j}} \tag{1.11}$$

where $A_{i\to j}$ are the spontaneous emission rates, and $q_{i\to j}$ represents the electron collisional rate coefficients. Thus, in plasmas with few collisions $\tau_i \sim 1/\sum_j A_{i\to j}$. Very approximately these lifetimes are:

Typical lifetimes for light atomic species.

- Levels that can electric-dipole decay $\tau \sim 1 \times 10^{-8} s$
- Levels that can only magnetic dipole decay $\tau \sim 1 \times 10^{-3} s$
- Levels that can only quadrupole decay $\tau \sim 1 s$

Excited population modeling Until this point we have been mostly focusing on atomic structure and isolated atoms. To understand the line spectra emitted from plasmas, we need to know all of the atomic processes that can change the energy of the bound electrons. While there are many possible processes, in most plasmas electron collisions form the dominant populating mechanism. In the next several sections we will look at the main electron-impact processes that occur in a plasma. Since these processes depend upon the properties of free electrons, this provides a means of diagnosing the electron temperature and density.

We will first describe the radiative processes that can occur, then look at mechanisms that can change the ionization state of the atom. This will allow us to model the "ionization balance" of the elements in the plasmas. We will then describe electron-impact excitation, allowing us to model the distribution of electrons in the excited states. To do this we will use what is known as *generalized collisional-radiative theory* (GCR).

Our atomic model for neutral argon uses GCR to create synthetic spectra to model the emission from the ALEXIS plasma, which we then compare to experimental spectra as a benchmark for our methods. Synthetic line ratios are used to predict the metastable fractional abundance of the ALEXIS plasma, as well as electron density and temperature using spectral line ratios sensitive to these two parameters. These are compared to experimental probe-based measurements of temperature and density in order to verify the accuracy of our methods.

1.6 Atomic processes

1.6.1 Radiative transitions

We have already covered the selection rules for spontaneous emission. The process would be:

$$X^{+z}(i) \longrightarrow X^{+z}(j) + h\tilde{\nu} \tag{1.12}$$

The rate of spontaneous emission is given by the Einstein A-coefficient. For electric dipole radiation this is given by:

$$A_{i\to j} = \frac{w_{ij}^3}{3\pi c^3 \hbar \varepsilon_o} | < \psi_j | D | \psi_i > |^2. \tag{1.13}$$

where D is the electric dipole operator, ($D = e\vec{r}$), i is the initial level of the bound electron and j is the final level of the electron. The photon that is given off has an angular frequency of ω_{ij}.

The stimulated emission coefficient can be related to the photoabsorption and simulated emission via the detailed balance relationships. This produces the following expressions for the stimulated emission

$$B_{i\to j} = \frac{c^3}{8\pi h \nu^3} A_{i\to j} \tag{1.14}$$

and the photoabsorption coefficient is given by:

$$B_{i\to j} = \frac{w_j}{w_i} B_{j\to i} \tag{1.15}$$

where w_i and w_j are statistical weights.

Of course, electrons can also transition from bound to free states. Consider first *photoionization*:

$$X^{+Z}(i) + h\tilde{\nu} \longrightarrow X^{+Z+1}(k) + e \tag{1.16}$$

The number of photoionizations in cm^3/s is:

$$N_i a(\tilde{\nu}) \frac{c}{h\tilde{\nu}} u(\tilde{\nu}) d\tilde{\nu} \tag{1.17}$$

where $a(\tilde{\nu})$ is the photoionization cross subsection and $u(\tilde{\nu})$ is the radiation field density.

The inverse process is **radiative recombination**:

$$X^{+Z+1}(k) + e \longrightarrow X^{+Z}(i) + h\tilde{\nu} \tag{1.18}$$

with an associated capture cross subsection $Q_c(\tilde{\nu})$. There is also *stimulated recombination*:

$$X^{+z+1} + e + h\tilde{\nu} \longrightarrow X^{+z}(i) + h\tilde{\nu} + h\tilde{\nu} \tag{1.19}$$

with an induced radiation parameter: $\sigma(\tilde{\nu})$. Detailed balance relates these cross subsections:

$$\sigma(\tilde{\nu}) = \frac{c^3}{8\pi h\tilde{\nu}^3} Q_c(\tilde{\nu}) \tag{1.20}$$

$$Q_c(\tilde{\nu}) = \left(\frac{h\tilde{\nu}}{m_e v c}\right)^2 \frac{w_i}{w_+} a(\tilde{\nu}) \tag{1.21}$$

The expression for $Q_c(\tilde{\nu})$ is called the **Milne Relation**.

In a real plasma it is the rates of the processes that are most important, rather than the cross-sections. To describe this, we need to know the free electron energy distribution function (EDF). Often this is a thermal distribution, and can be modelled as a Maxwellian. However, investigating the potential for non-Maxwellian energy distributions is considered

an avenue for future projects, and we have begun discussions with other research groups about how this could be implemented in our model, and tested experimentally.

The classic expression for a Maxwellian energy distribution is given by:

$$f(\vec{v}, T_e) = 4\pi \left(\frac{m}{2\pi k T_e} \right)^{3/2} e^{\frac{-m}{2kT_e}\vec{v}^2} \tag{1.22}$$

Using this energy distribution, the radiative recombination bound-free rate coefficient is:

$$\alpha_i(T_e) = \sqrt{\frac{2}{\pi}} \frac{1}{c^2} \left(m_e k T_e\right)^{-\frac{3}{2}} \frac{w_i}{w_+} e^{\frac{I_i}{kT_e}} \int_{I_i}^{\infty} a\left(\tilde{\nu}\right) \left(h\tilde{\nu}\right)^2 e^{\frac{-h\tilde{\nu}}{kT_e}} d\left(h\tilde{\nu}\right) \tag{1.23}$$

Where I_i is the ionization potential. At lower temperatures, $\alpha_i(T_e)$ falls off as $\sqrt{\frac{1}{T_e}}$. At higher temperatures, $\alpha_i(T_e)$ falls off as $\sqrt{\frac{1}{T_e^3}}$. Due to this rapid decrease with temperature, radiative recombination is not usually the dominant recombination mechanism in a plasma. However, for low temperature laboratory plasmas it can still play a significant role.

1.6.2 Dielectronic recombination

This process was thought to be unimportant, but in the 1960s it was found to be the dominant recombination mechanism for many plasmas and was essential in describing the spectral emission from the solar corona [22].

This is a two-step process:

i. **Resonance Capture**:

$$A^{+Z+1}(i) + e \longleftrightarrow A^{+Z}(j, nl)$$

The free electron 'collides' with the bound electron. The bound electron gains some energy and the free electron loses energy and is captured into nl. This happens at a precise energy for each nl. The reverse process is called Auger breakup and is very fast.

ii. **Radiative Stabilization**:

$$\begin{aligned} A^{+Z}(j,nl) &\longrightarrow A^{+Z}(i,nl) + h\tilde{\nu}(TypeI) \\ &\longrightarrow A^{+Z}(j,n'l') + h\tilde{\nu}(TypeII) \end{aligned} \tag{1.24}$$

The recombination process is only complete if the ion ends up in a bound state. The type I radiative transition produces a photon called a "satellite line". This photon is very slightly shifted from the emission of:

$$A^{+Z+1}(j) \longrightarrow A^{+Z+1}(i) + h\tilde{\nu} \tag{1.25}$$

These satellite lines can provide useful diagnostics.

The DR resonance positions are approximately given by:

$$E^{res}(n) \approx E_s - \underbrace{R\frac{Z_1^2}{n^2}}_{Hydrogenic} \tag{1.26}$$

Where R is the Rydberg constant. The total dielectronic recombination Maxwellian rate coefficient is given by:

$$\alpha^{DR}(T_e) = 2\frac{v_a}{\sqrt{\pi}}\sqrt{\frac{I_H}{kT_e}}\int_0^\infty \frac{\epsilon}{kT_e}\overbrace{\sigma^{DR}(\epsilon)}^{DR\ cross-section} e^{\frac{-\epsilon}{kT_e}} d\left(\frac{\epsilon}{kT_e}\right) \tag{1.27}$$

where v_a is $2.188 \times 10^8 cm/s$, σ^{DR} is the dielectronic recombination cross subsection, and ϵ is the electron energy [eV]

Note that although the selection rules do not hold for dielectronic capture, they still give a reasonable indication of which core excitation will have the largest rate coefficient (i.e. $\Delta n = 0$, dipole allowed excitations).

The strength of the resonances are given by $\frac{A_i^a A_i^r}{\sum A^a + \sum A^r}$. A_i^a is the dielectronic capture into i and A_i^r is the radiative stabilization of i.

Some useful databases for DR rate coefficients are:

DR databases

1. Mazzotta et al., Astronomy & Astrophysics Supplement Series. **133** : 403 (1998).
2. Arnaud and Rothenflug, Astronomy & Astrophysics Supplement Series. **60** : 425 (1985).
3. The DR project (Badnell) `http://amdpp.phys.strath.ac.uk/tamoc/DATA/`

1.6.3 Electron-impact ionization

This process is:

$$A^{+Z}(i) + e(\epsilon_i) \longleftrightarrow A^{+Z+1}(j) + e + e \tag{1.28}$$

If one compares the ionization and total $(DR + RR)$ recombination rate coefficient for a typical ion, it is clear that ionization rates become bigger than recombination rates at temperatures significantly below the ionization potential for that ion. This is particularly pronounced for near neutral ion stages.

One can obtain ionization rates at temperatures below the ionization potential due to electrons in the high energy tail of the Maxwellian free electron distribution.

1.6.4 Equilibrium ionization balance

Given ionization and recombination rate coefficients, one can work out the temperature at which each ion stage of an element will form.

Consider an element with three ion stages, including the bare nucleus. Let α , β , γ be the ground states of the four ion stages. We will consider only connections between adjacent ion stages.

$$\begin{aligned}
\frac{dN_\alpha}{dt} &= -S_{\alpha\to\beta}N_\alpha N_e + R_{\beta\to\alpha}N_\beta N_e + 0\ N_\gamma N_e \\
\frac{dN_\beta}{dt} &= S_{\alpha\to\beta}N_\alpha N_e - \left(R_{\beta\to\alpha} + S_{\beta\to\alpha}\right) N_\beta N_e + R_{\gamma\to\beta}N_\gamma N_e \\
\frac{dN_\gamma}{dt} &= 0\ N_\alpha N_e + S_{\beta\to\gamma}N_\beta N_e - R_{\gamma\to\beta}N_\gamma N_e
\end{aligned} \tag{1.29}$$

Which can be written as:

$$\begin{bmatrix} dN_\alpha/dt \\ dN_\beta/dt \\ dN_\gamma/dt \end{bmatrix} = \begin{bmatrix} C_{\alpha\alpha} & C_{\alpha\beta} & C_{\alpha\gamma} \\ C_{\beta\alpha} & C_{\beta\beta} & C_{\beta\gamma} \\ C_{\gamma\alpha} & C_{\gamma\beta} & C_{\gamma\gamma} \end{bmatrix} \begin{bmatrix} N_\alpha \\ N_\beta \\ N_\gamma \end{bmatrix} \tag{1.30}$$

Note that this is not really three equations with three unknowns. Due to the fact that each gain rate goes in elsewhere as a loss rate, this is really an under determined equation. Thus, we require one other equation to use in the solution. We use particle conservation:

$$N^{TOT} = N_\alpha + N_\beta + N_\gamma \tag{1.31}$$

We can then solve for the equilibrium populations by setting dN/dt=0. We replace the first equation with the one for N^{TOT}.

$$\begin{bmatrix} N^{TOT} \\ 0 \\ 0 \end{bmatrix} = \begin{bmatrix} 1 & 1 & 1 \\ C_{\beta\alpha} & C_{\beta\beta} & C_{\beta\gamma} \\ C_{\gamma\alpha} & C_{\gamma\beta} & C_{\gamma\gamma} \end{bmatrix} \begin{bmatrix} N_\alpha \\ N_\beta \\ N_\gamma \end{bmatrix} \tag{1.32}$$

Which we can then solve for the fractional abundances.

$$\begin{bmatrix} N_\alpha/N^{TOT} \\ N_\beta/N^{TOT} \\ N_\gamma/N^{TOT} \end{bmatrix} = \begin{bmatrix} 1 & 1 & 1 \\ C_{\beta\alpha} & C_{\beta\beta} & C_{\beta\gamma} \\ C_{\gamma\alpha} & C_{\gamma\beta} & C_{\gamma\gamma} \end{bmatrix}^{-1} \begin{bmatrix} 1 \\ 0 \\ 0 \end{bmatrix} \tag{1.33}$$

This can, of course, be generalized for a system of N ion stages and solved numerically.

Note that the matrix coefficients and, hence, the fractional abundances are only a function of electron temperature. Later, we will generalize these equations to include excited states. The results will also be *density dependent*.

Thus, seeing emission from a given ion stage immediately gives us a range of temperatures that the plasma can have.

Some useful ionization databases are:

Useful ionization databases

1. Mazzotta et al., Astronomy & Astrophysics Supplement Series. **133** : 403 (1998).
2. Arnaud and Rothenflug, Astronomy & Astrophysics Supplement Series. **60** : 425 (1985).
3. Dere, Astronomy and Astrophysics. **466** : 771 (2007).
4. Mattioli et al., Journal of Physics B. **40** : 3569 (2007).

1.6.5 Electron-impact excitation

In most plasmas, the excited state populations depend strongly on the electron impact excitation rate coefficients.

$$X^{+Z}(i) + e(\epsilon_i) \longrightarrow X^{+Z}(j) + e(\epsilon_j) \tag{1.34}$$

Energy is conserved. Thus, $\Delta E_{ij} = \epsilon_i - \epsilon_j$. The excitation cross section $\sigma_{i\to j}(\epsilon_i)$ (in cm^2) describes the process.

We define a dimensionless threshold-scaled energy, $X = \frac{\epsilon_i}{\delta E_{ij}}$ for $X \in [1, \infty]$ and a dimensionless quantity called the *collision strength* that is related to the cross subsection.

$$\begin{aligned} \Omega_{ij} &= w_i \left(\frac{\epsilon_i}{I_H}\right) \frac{\sigma_{i\to j}\left(\epsilon_i\right)}{\pi a_o^2} \\ &= w_j \left(\frac{\epsilon_j}{I_H}\right) \frac{\sigma_{j\to i}\left(\epsilon_j\right)}{\pi a_o^2} \end{aligned} \tag{1.35}$$

Ω_{ij} is symmetric between initial and final states.

The Maxwellian excitation rate coefficient is:

$$q_{i\to j} = 4\pi \left(\frac{m_e}{2\pi k T_e}\right)^{3/2} \int_0^\infty v_i e^{-\frac{\epsilon_i}{kT_e}} \sigma_{i\to j}\left(\epsilon_i\right) v_i^2 dv_i \tag{1.36}$$

$$= 2\sqrt{\pi}\alpha c a_o^2 \left(\frac{I_H}{kT_e}\right)^{1/2} \frac{1}{w_i} e^{-\frac{\Delta E_{ij}}{kT_e}} \int_0^\infty \Omega_{ij}(\epsilon_j) e^{-\frac{\epsilon_j}{kT_e}} d\left(\frac{\epsilon_j}{kT_e}\right) \tag{1.37}$$

where $\pi a_o^2 = 8.7972 \times 10^{-17}\ cm^2$.

We also define an *effective collision strength*, Υ_{ij} (Upsilon)

$$\Upsilon_{ij}(T_e) = \int_0^\infty \Omega_{ij}(\epsilon_i) e^{-\frac{\epsilon_j}{kT_e}} d\left(\frac{\epsilon_j}{kT_e}\right) \tag{1.38}$$

$$\begin{aligned} q_{j\to i}(T_e) &= \frac{w_i}{w_j} e^{\frac{\Delta E_{ij}}{kT_e}} q_{i\to j}(T_e) \\ &= 2\sqrt{\pi}\alpha c a_o^2 \frac{1}{w_j} \left(\frac{I_H}{kT_e}\right)^{1/2} \Upsilon_{ij} \end{aligned} \tag{1.39}$$

The effective collision strengths are easily interpolated. Note that different excitations show characteristic behavior as shown below.

Let us consider the case of singly ionized argon, and the means of exciting from the ground term to an excited term. Note that one can have *direct excitation*:

$$Ar^{+}(3s^{2}3p^{5}) + e \longrightarrow Ar(3s^{2}3p^{4}\ nl) + e$$

and *resonant excitation*, where the electron is absorbed into a bound state of neutral argon whose energy lies above the ionization threshold:

$$Ar^{+}(3s^{2}3p^{5}) + e \longleftrightarrow \underbrace{Ar(3s^{2}3p^{5}\ n'l')}_{Auger}$$

which can then decay into an excited term of singly ionized argon:

$$Ar(3s^{2}3p^{5}\ n'l' \longleftrightarrow Ar^{+}(3s^{2}3p^{4}\ nl) + e$$

In this example both processes end up in the same final state.
Note that because of the large number of possible nl states, there will be a whole series of resonances attached to each possible core excitation, we have just considered the 1s-3p core excitation here. This means that the excitation cross section has a smooth background that corresponds to the direct ionization process, on top of this is the indirect excitation (resonant excitation), which consists of a large number of usually very narrow resonances.

Resonance contributions have the largest effect on transitions with weak backgrounds, such as the non-dipole excitations. Also, note that while the dipole selection rules that we showed earlier are just for photon transitions, they also give a good indication of which electron-impact processes will be strong.

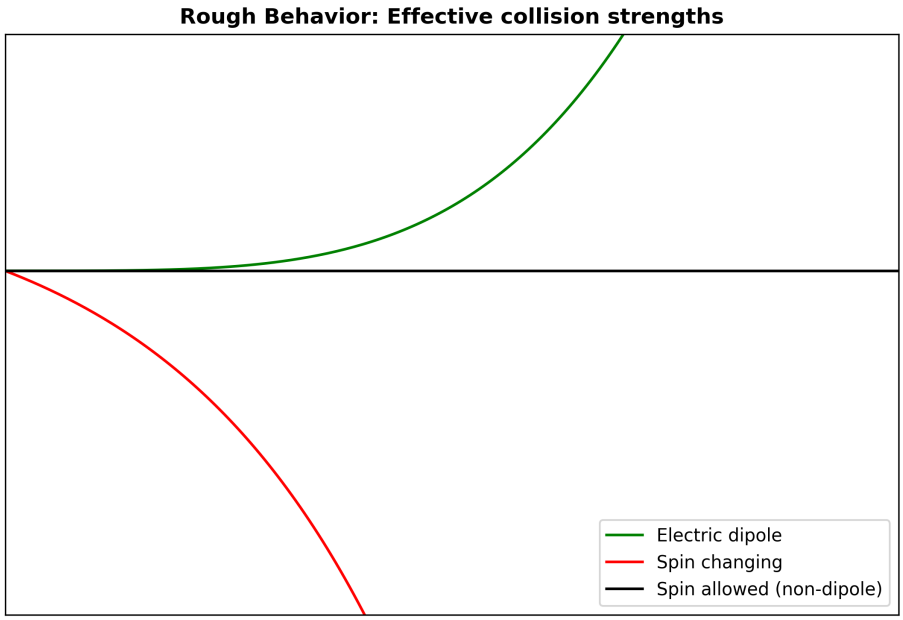

Figure 1.5: Sketch of the rough behavior of effective collision strengths for the three main types of transitions (arbitrary units).

1.6.6 Population modeling

In the following subsections we will look at different approximations that are used to model the excited populations (and hence the spectra) of atoms. In the first approximation we will evaluate the populations in Local Thermodynamic Equilibrium (LTE), valid for black body plasmas or plasmas at high densities. In the second approximation, valid at low densities, we use the Coronal approximation. In the last method, we use collisional-radiative theory, which is valid at all densities.

1.6.7 Local Thermodynamic Equilibrium

If a plasma is in thermodynamic equilibrium, then all of its physical characteristics are determined by the temperature.

The radiation field is given by a Plank distribution:

$$u(\nu) = \frac{8\pi h\nu^3}{c^3}\frac{1}{e^{\frac{h\nu}{kT}} - 1} \tag{1.40}$$

The free electrons have a Maxwellian distribution:

$$f(v) = 4\pi \left(\frac{m}{2\pi kT_e}\right)^{3/2} e^{-\frac{mv^2}{2kT_e}} v^2 \tag{1.41}$$

The bound states have a Boltzmann distribution:

$$\frac{N_i}{N_j} = \frac{\omega_i}{\omega_j} e^{-\frac{E_i - E_j}{kT_e}} \tag{1.42}$$

alternatively they can be modeled with a Saha-Boltzmann distribution if one knows information about the ion, N_+.

$$N_i = N_e N_+ \left(\frac{h^2}{2\pi mkT_e}\right)^{3/2} \frac{\omega_i}{2\omega_+} e^{\frac{I_i}{kT_e}} \tag{1.43}$$

A plasma can be in *local* thermodynamic equilibrium (LTE) if collision timescales are sufficiently faster than radiative timescales, i.e. collisional-redistribution happens before radiative losses drive the system out of thermodynamic equilibrium. If a system is in LTE, the above equations hold.

To check if the collisional rates for a given excited state (N_i) will dominate over the radiative rates, one can evaluate the following ratio

$$\frac{\sum_{j<i} A_{i\to j}}{N_e \sum_{i\neq j} q_{i\to j}} \tag{1.44}$$

whenever this is less than one, the collisional rates will be greater than the radiative rates. The collisional-rates would have to dominate by a large factor to drive the populations to LTE. Note that one can either work out a critical N_e at which the populations are driven to LTE, or a critical n-shell at which they become LTE.

1.6.8 The Coronal Approximation

In practice, the free electrons often have a Maxwellian or nearly Maxwellian distribution. The ground and metastable states vary on a timescale similar to the plasma dynamics and must be modeled as part of the plasma evolution. The autoionizing and excited states very quickly come into equilibrium with the ground and metastable states. This is called the *quasi-static equilibrium* approximation.

Before considering this we will consider the low density limit, the *coronal approximation*. This assumes that:

- The only mechanism to populate the excited states is collisional excitation from the ground.
- The only depopulating mechanism for excited states is radiative decay.

Thus, an excited state population is given by

$$\frac{dN_i}{dt} = N_1 N_e q_{1\to i} - N_i \sum_{j<i} A_{i\to j} \tag{1.45}$$

We set the $dN/dt = 0$ as the excited populations are likely to be in equilibrium with the ground

$$N_i = \frac{N_1 N_e q_{1\to i}}{\sum_{j<i} A_{i\to j}} \tag{1.46}$$

A line intensity ratio in the coronal approximation is given by:

$$\frac{I_{i\to j}}{I_{k\to l}} = \left(\frac{q_{1\to i}(T_e)}{\sum_{j'<i} A_{i\to j'}}\right)\left(\frac{\sum_{l'<k} A_{k\to l'}}{q_{1\to k}(T_e)}\right)\left(\frac{A_{i\to j}}{A_{k\to l}}\right) \tag{1.47}$$

Note that this isn't quite the full picture, as it does not allow for radiative cascades from higher levels, something that is permitted in the coronal approximation. However, in most cases this gives a reasonably accurate representation of the coronal results.

1.6.9 Collisional-Radiative Theory

All excited populations should become coronal at low electron densities and LTE at high electron densities. However, the majority of plasmas lie in between these two regimes, and are well-described by neither. This is almost universally the case for low-temperature laboratory plasmas. The regime in between the coronal and LTE limits is called the *Generalized Collisional-Radiative* (GCR) regime. It should be noted that a GCR description is appropriate for both coronal and LTE plasmas, but not vice versa.

We consider the set of linear differential equations describing the rate of change of the populations of the ground and excited states. We are simply balancing the rates involving all of the atomic processes that we considered earlier in this section. While we could consider rate equations for all of the ion stages at once, in practice it is sufficient just to consider one ion stage and the ground of the next ion stage up. This is the same as saying that

an excited state is overwhelmingly populated via excitation within the current ion stage, or recombination from the next ion stage. So, in practice, we are often omitting ionization from previous ion stage as an important population mechanism (it can be included in principle).

$$
\begin{aligned}
\frac{dN_1}{dt} &= -N_e(\sum_{j\neq 1} q^e_{1\to j} + S_1)N_1 + (A_{2\to 1} + N_e q_{2\to 1})N_2 + ...(A_{n\to 1} + N_e q_{n\to 1})N_n + \\
&\quad N_e R_{+\to 1} N_+ \\
\frac{dN_2}{dt} &= N_e q_{1\to 2} N_1 - (A_{2\to 1} + N_e(\sum_{j\neq 2} q^e_{2\to j} + S_2))N_2 + ...(A_{n\to 2} + N_e q_{n\to 2})N_n + \\
&\quad N_e R_{+\to 2} N_+ \\
\frac{dN_3}{dt} &= N_e q_{1\to 3} N_1 + N_e q_{2\to 3} N_2 - (\sum_{j<3} A_{3\to j} + N_e(\sum_{j\neq 3} q^e_{3\to j} + S_3))N_3 + ... \\
&\quad +(A_{n\to 3} + N_e q_{n\to 3})N_n + N_e R_{+\to 3} N_+ \\
.... &\quad ..... \\
.... &\quad ..... \\
\frac{dN_n}{dt} &= N_e q_{1\to n} N_1 + N_e q_{2\to n} N_2 + N_e q_{3\to n} N_3 + ... - (\sum_{j<n} A_{n\to j} + N_e(\sum_{j<n} q^e_{n\to j} + S_n))N_n \\
&\quad +N_e R_{+\to n} N_+ \\
\frac{dN_+}{dt} &= N_e S_1 N_1 + N_e S_2 N_2 + N_e S_3 N_3 ..... + N_e S_n N_n - N e N_+ \sum_j R_{+\to j}
\end{aligned}
\tag{1.48}
$$

(1.49)

This can be written in matrix form, using C to represent the total atomic rates in each matrix element.

$$\begin{bmatrix} dN_1/dt \\ dN_2/dt \\ dN_3/dt \\ .... \\ .... \\ dN_n/dt \\ dN_+/dt \end{bmatrix} = \begin{bmatrix} C_{11} & C_{12} & C_{13} & .. & .. & C_{1n} & R_1 \\ C_{21} & C_{22} & C_{23} & .. & .. & C_{2n} & R_2 \\ C_{31} & C_{32} & C_{33} & .. & .. & C_{3n} & R_3 \\ ... & ... & ... & .. & .. & ... & .. \\ ... & ... & ... & .. & .. & ... & .. \\ C_{n1} & C_{n2} & C_{n3} & .. & .. & C_{nn} & R_n \\ N_eS_{1+} & N_eS_1 & N_eS_2 & .. & .. & N_eS_n & -\sum_n R_n \end{bmatrix} \begin{bmatrix} N_1 \\ N_2 \\ N_3 \\ .. \\ .. \\ N_n \\ N_+ \end{bmatrix} \tag{1.50}$$

The excited states are in equilibrium with the ground, so we can set the $dN/dt = 0$ for the excited states.

$$\begin{bmatrix} dN_1/dt \\ 0 \\ 0 \\ 0 \\ 0 \\ 0 \\ dN_+/dt \end{bmatrix} = \begin{bmatrix} C_{11} & C_{12} & C_{13} & .. & .. & C_{1n} & R_1 \\ C_{21} & C_{22} & C_{23} & .. & .. & C_{2n} & R_2 \\ C_{31} & C_{32} & C_{33} & .. & .. & C_{3n} & R_3 \\ ... & ... & ... & .. & .. & ... & .. \\ ... & ... & ... & .. & .. & ... & .. \\ C_{n1} & C_{n2} & C_{n3} & .. & .. & C_{nn} & R_n \\ N_eS_{1+} & N_eS_1 & N_eS_2 & .. & .. & N_eS_n & -\sum_n R_n \end{bmatrix} \begin{bmatrix} N_1 \\ N_2 \\ N_3 \\ .. \\ .. \\ N_n \\ N_+ \end{bmatrix} \tag{1.51}$$

We cannot set the dN/dt for the ground (and metastable) states, because the plasma conditions can change on a timescale quicker than the equilibrium timescale for those levels. Normally we solve the time-dependence of the ground and metastable levels using some form of plasma modeling code. However, it is still possible to isolate the atomic physics from

the plasma physics and evaluate the excited populations as a function of the ground and metastable populations. These are sometimes called their "driving populations".

To proceed, we eliminate the first and last rows. Considering the matrix on the right hand side, we can move the first and last contribution to the left hand side of the equation.

$$\begin{bmatrix} -C_{21}N_1 - R_2N_+ \\ -C_{31}N_1 - R_3N_+ \\ \dots - \dots \\ \dots - \dots \\ -C_{n1}N_1 - R_nN_+ \end{bmatrix} = \begin{bmatrix} C_{22} & C_{23} & .. & .. & C_{2n} \\ C_{32} & C_{33} & .. & .. & C_{3n} \\ \dots & \dots & .. & .. & \dots \\ & \dots & \dots & .. & .. & \dots \\ C_{n2} & C_{n3} & .. & .. & C_{nn} \end{bmatrix} \begin{bmatrix} N_2 \\ N_3 \\ .. \\ .. \\ N_n \end{bmatrix} \tag{1.52}$$

We can then solve for the excited populations with a matrix inversion:

$$\begin{bmatrix} N_2 \\ N_3 \\ .. \\ .. \\ N_n \end{bmatrix} = \begin{bmatrix} C_{22} & C_{23} & .. & .. & C_{2n} \\ C_{32} & C_{33} & .. & .. & C_{3n} \\ \dots & \dots & .. & .. & \dots \\ \dots & \dots & .. & .. & \dots \\ C_{n2} & C_{n3} & .. & .. & C_{nn} \end{bmatrix}^{-1} \begin{bmatrix} -C_{21}N_1 - R_2N_+ \\ -C_{31}N_1 - R_3N_+ \\ \dots - \dots \\ \dots - \dots \\ -C_{n1}N_1 - R_nN_+ \end{bmatrix} = \tag{1.53}$$

If we call the matrix that we are to invert on the RHS, the *reduced collisional-radiative matrix C'*, then we have:

$$\begin{bmatrix} N_2 \\ N_3 \\ .. \\ .. \\ N_n \end{bmatrix} = \left[C'\right]^{-1} \begin{bmatrix} -C_{21}N_1 - R_2N_+ \\ -C_{31}N_1 - R_3N_+ \\ \dots - \dots \\ \dots - \dots \\ -C_{n1}N_1 - R_nN_+ \end{bmatrix} \tag{1.54}$$

Or, written in terms of the individual matrix elements we have:

$$N_2 = -\sum_j {C'_{2j}}^{-1} C_{j1} N_1 - N_e \sum_j {C'_{2j}}^{-1} R_j N_+ \tag{1.55}$$

with the general level being given by:

$$N_i = -N_1 \Big(\underbrace{\sum_j {C'_{ij}}^{-1} C_{j1}}_{Excitation\ contribution} \Big) - N_e N_+ \Big(\underbrace{\sum_j {C'_{ij}}^{-1} R_j N_+}_{Recombination\ contribution} \Big) \tag{1.56}$$

This can be further generalized for σ metastable states in the ion (or neutral) and ρ metastables in the plus ion stage.

$$N_i = -\sum_\sigma N_\sigma \sum_j {C'_{ij}}^{-1} C_{j\sigma} - N_e \sum_\rho N_\rho^+ \sum_j {C'_{ij}}^{-1} R_{j\rho} \tag{1.57}$$

This system of equations is easily solved numerically. Note that one can archive the contributions from N_σ and N_ρ^+ on a T_e, N_e grid for later use, once we know the fractional abundances of these ground and metastable states. For our purposes, we can assume that N_ρ^+ is small compared to N_σ, and neglect the second term on the RHS of equation 1.57. The matrix represented by the $\sum_j {C'_{ij}}^{-1} R_{j\rho}$ factor is determined theoretically using ADAS208. For the factor $\sum N_\sigma$, we will show in the following sections that is sufficient to know the relative metastable fractions in order to calculate synthetic spectral line ratios. We detail the method by which we determine these relative metastable fractions in Chapter 4.

1.6.10 Population Dependence on Electron Density

It is useful to have a physical expectation of how the populations will change as a function of density and temperature. Fortunately we can use the coronal and LTE conditions to guide

our thinking. Consider the ratio of the excited population i to the product of the ground population times the electron density. We will consider the case here with no metastables.

$$\frac{N_i}{N_1 N_e} \tag{1.58}$$

At low electron densities, coronal conditions hold:

$$\frac{N_i}{N_1 N_e} = \frac{q_{1\to i}(T_e)}{\sum_{j<i} A_{i\to j}} \tag{1.59}$$

This ratio is constant for a given electron temperature. At high electron densities, LTE conditions hold:

$$\frac{N_i}{N_1} = \frac{\omega_i}{\omega_1} e^{-(E_i - E_1)/kT} \tag{1.60}$$

$$\frac{N_i}{N_1 N_e} = \frac{1}{N_e}\frac{\omega_i}{\omega_1} e^{-(E_i - E_1)/kT} \tag{1.61}$$

$$\tag{1.62}$$

The ratio has a slope of $1/N_e$. We will usually consider plots of $\log_{10}$ of $\frac{N_i}{N_1 N_e}$ vs $\log_{10}$, in this case the slope will be -1. That is, for a given excited level i, the graph will be a constant at low N_e and have a slope of $1/N_e$ at high desities. Remember that the region in between these two extremes is called the *collisional-radiative* regime and one needs to solve the GCR equations to know how the populations will behave. Knowledge of the atomic processes can guide our thinking in this regime, but it is more difficult to know how the populations will behave.

1.6.11 Electron Temperature Diagnostics

The primary tool we employ for spectral line analysis is ADAS208, which uses the following definition for the emissivity of the spectral line $j \rightarrow k$.

$$\epsilon_{j\rightarrow k} = A_{j\rightarrow k}\left[\sum_{\sigma=1}^{M} \mathscr{F}_{j\sigma}^{exc} N_e N_\sigma + \sum_{\nu'=1}^{M+1} \mathscr{F}_{j\nu'}^{rec} N_e N_{\nu'}^{+} + \sum_{\nu'=1}^{M_{Z+1}} \mathscr{F}_{j\nu'}^{CX} N_H N_{\nu'}^{+} + \sum_{\mu'=1}^{M_{Z-1}} \mathscr{F}_{j\mu'}^{ion} N_e N_{\mu}^{\prime -}\right] \tag{1.63}$$

Where $A_{i\rightarrow j}$ is the Einstein A coefficient, N_e is the electron density, M is the number of metastables, and the coefficients $\mathscr{F}_{j\sigma}^{exc}$), $\mathscr{F}_{j\nu'}^{rec}$, $\mathscr{F}_{j\nu'}^{CX}$, $\mathscr{F}_{j\mu'}^{ion}$ are the effective contributions to the excited populations from excitation from the metastables, from free electron capture by parent metastables, from charge exchange recombination from neutral hydrogen by parent metastables and due to ionization from the lower charge states respectively.

In order to determine these emissivities, ADAS208 calculates *photon emissivity coefficients*, defined as:

$$\mathscr{PEC}_{\sigma,j\rightarrow k} = A_{j\rightarrow k}\mathscr{F}_{\sigma} \tag{1.64}$$

For our purposes, we can discount the last three terms in Equation 1.63, as the ionization fraction in our plasmas of interest is extremely low ($\approx 1 \times 10^{-4}$ or lower). This leads to a relatively lower number of ions compared to neutral, making the effective contribution of recombination, ionization, and charge exchange small compared to the contributions from collisional processes. For our plasmas of interest, we can define a spectral line ratio in terms of PEC's as:

$$\frac{I_{j\rightarrow k}}{I_{j'\rightarrow k'}} = \frac{\sum_{\sigma=1}^{M} \mathscr{PEC}_{\sigma,j\rightarrow k}^{exc} N_\sigma}{\sum_{\sigma=1}^{M} \mathscr{PEC}_{\sigma,j'\rightarrow k'}^{exc} N_\sigma} \tag{1.65}$$

For a system with three metastables, such as neutral argon, this can be written:

$$\frac{I_{j\to k}}{I_{j'\to k'}} = \frac{\mathscr{PEC}^{exc}_{1,j\to k} + \mathscr{PEC}^{exc}_{2,j\to k}\frac{N_2}{N_1} + \mathscr{PEC}^{exc}_{3,j\to k}\frac{N_3}{N_1}}{\mathscr{PEC}^{exc}_{1,j'\to k'} + \mathscr{PEC}^{exc}_{2,j'\to k'}\frac{N_2}{N_1} + \mathscr{PEC}^{exc}_{35,j'\to k'}\frac{N_3}{N_1}} \tag{1.66}$$

Where we have written the metastable populations in terms of the relative metastable density populations (or simply *metastable fractions*) $\frac{N_2}{N_1}$, $\frac{N_3}{N_1}$. The weighting is arbitrary; any of the three states can be chosen as the normalization parameter.

ADAS208 calculates PEC's as a function of temperature and density. In order to create an electron temperature diagnostic, we need to find a ratio of two spectral lines that is dependent upon electron temperature, but not upon electron density. This can be determined theoretically by looking at plots of PEC's created as a function of temperature and density, and remembering that a temperature sensitive PEC for a given wavelength would indicate a temperature sensitive line at that wavelength.

In practice, we overlay the theoretical PEC plots for a given spectral as a function of temperature for all densities in our ADAS208 dataset. Density dependence then shows up as "blurriness". This can be seen in Figure 1.6, which displays 20 density overlay plots of PEC ratios as a function of electron temperature, normalized to the 1s3 metastable for the lines located at 763.5 and 852.1 nm. As can be seen , there is little density dependence (or "blurriness"), in the figure, but there is strong temperature dependence.

Finding lines that are sensitive to temperature variations independently of changes in density is only part of the story. If we look back to Equation 1.66 we can see that without some knowledge of the metastable fractions we are still unable to predict line ratios in any meaningful way. Thus, much of our work has been spent trying to determine the relevant metastable fractions in neutral argon, specifically in the ALEXIS plasma. These efforts are detailed in Chapter 4.

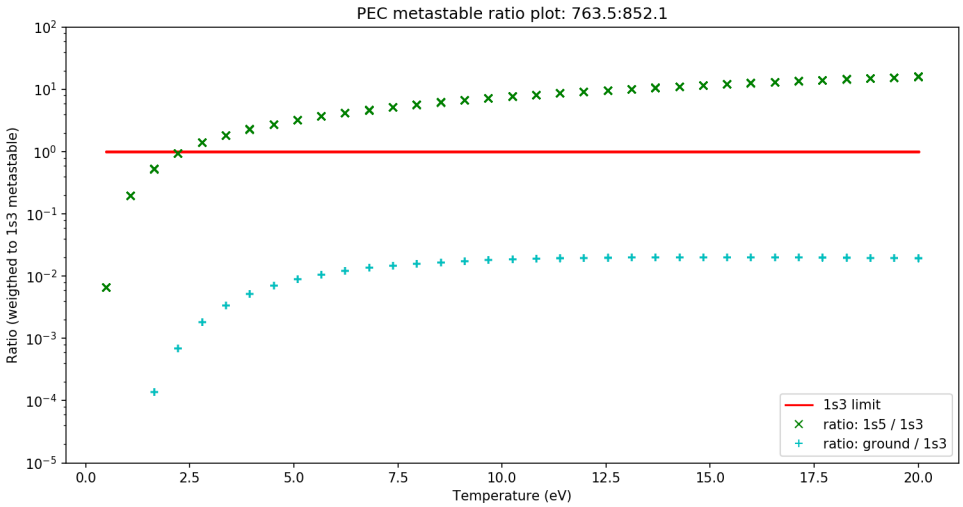

Figure 1.6: Metastable fractions plotted as a function of electron temperature. The plot displays an overlay of line ratio vs. temperature plots for all 20 densities in the ADAS208 dataset. The lack of "blurriness" indicates a line ratio that is independent of density. There is a clear temperature dependence in the 1s5:1s3 metastable fraction.

1.6.12 Electron Density Diagnostics

In principle, electron density diagnostics are achievable in neutral argon by simply repeating the analysis in the previous subsection, replacing the phrase "temperature" with "density". However, in practice we have found that spectral lines that are sensitive to changes in electron density, but not temperature, are harder to find. It seems that, at least in neutral argon, the temperature response in a spectral line ratio is driven by the varying rates of change in the populations of the metastable states with respect to one another, and that this is less likely to happen as a function of density. We have not been able to determine any lines that are detectable with our spectrometers that we feel are candidates for a density diagnostic at this time. We do believe that such lines exist, but detecting these lines is beyond the limitations of our current experimental resources.

1.7 Computational Methods

In this section we describe some of the computational methods employed for calculating atomic collision data in this work.

1.7.1 R-matrix theory

R-Matrix theory was introduced by Wigner and Eisenbud in 1946 and 1947 [79] for applications in nuclear resonance reactions. It was later realized that the same method could be applied to the resonance processes in electron-atom/ion collisions. This was formalized by Burke [24] in 1976. A comprehensive overview of R-Matrix theory can be found in the text by Burke and Berrington [23].

The basic idea of R-Matrix theory as applied to electron scattering problems is the partitioning of space in the vicinity of an atom or ion into two loosely defined regions: "outer" and "inner". Though we say loosely defined, any real problem would need to decide an exact boundary where the transition between these two regions occurs. For electron-ion collisions, this boundary is usually taken to be the radial extent of the most diffuse bound orbital, which effectively sets the boundary so that all bound electrons are inside. In the outer region, the incoming electron can be considered distinguishable from those bound to the target atom (or ion). This greatly simplifies the problem, as the interaction between electrons can be safely ignored, and exact solutions to the radial wavefunctions are possible. Indeed, the problem in this outer region becomes that of an electron moving in a central nuclear multipole field.

However, as the incoming electron crosses the R-Matrix boundary it loses this distinguishability, and electron-electron correlation effects can no longer be neglected. A large scale calculation, one which accounts for all the interactions between all the electrons in the system is now required. To ensure continuity of the wavefunction, we match the solutions

to the inner and outer region to each other at the boundary. The energy eigenvalues at the boundary form the elements of the R-matrix. See Figure 1.7 for an overview.

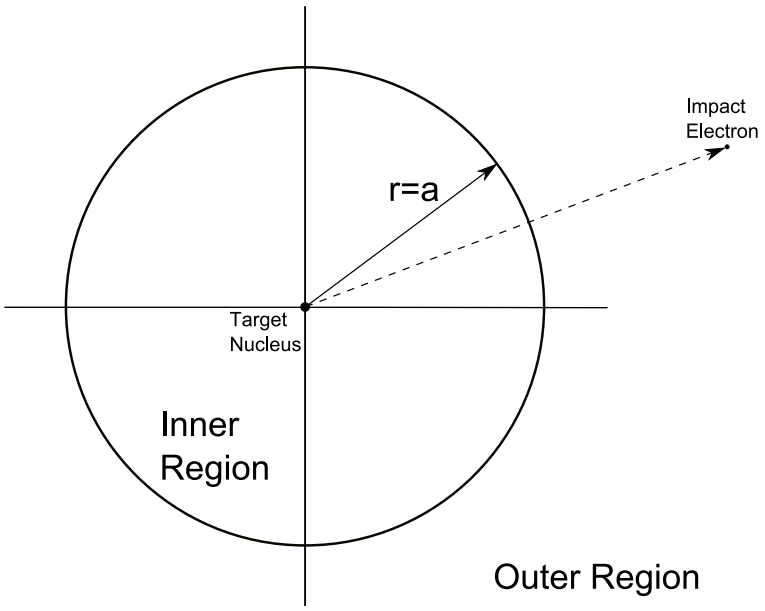

Figure 1.7: R-Matrix theory in a nutshell. In the outer region the effects of the Coulomb potential of the nucleus on the impact electron is considered small. Inside the boundary these effects cannot be neglected. The energy values of the wavefunction at the boundary form the R-Matrix. Figure courtesy of AJK Pearce [65].

Brief derivation of *R*-Matrix theory. We begin by partitioning configuration space at a radius of $r = a_0$, where r is the radial distance of the scattering electron from the nucleus, and a_0 is chosen such that the charge distribution of the target ion is contained within the sphere. This choice for a_0 is by definition the same as selecting a radius equal to the size of the target ion's most diffuse bound orbital. Critically, the $(N+1)$-electron system behaves in a way similar to a bound state and these states are described by a configuration interaction (CI) basis expansion of the total wavefunctions, analogous to that used in many bound state calculations.

For scattering of an electron by a light atom of N electrons, the time-independent Schrödinger equation describing the interaction is:

$$H_{N+1}\Psi = E\Psi \tag{1.67}$$

where E is the total energy and the non-relativistic Hamiltonian is defined by:

$$H_{N+1} = \sum_{i=1}^{N+1}(-\frac{1}{2}\nabla_i^2 - \frac{Z}{r_i}) + \sum_{i>j=1}^{N+1}\frac{1}{r_{ij}} \tag{1.68}$$

where Z is the effective nuclear charge (not necessarily an integer) and $r_{ij} = |r_i - r_j|$, r_i and r_j are the vector coordinates of electrons i and j relative to an origin placed at the target nucleus, which is assumed to have infinite mass.

To solve equation 1.67, we first create the eigenstates Φ_i of the target using:

$$\langle\Phi_i|H_N|\Phi_j\rangle = \omega_i\delta_{ij} \tag{1.69}$$

where ω_i is the eigenenergy of state i and H_N is the Hamiltonian of the target, which has the same form as equation 1.68 using N instead of $N+1$. These eigenstates are written as a CI expansion in terms of some basis configurations ϕ_i by

$$\Phi_i(x_1...x_N) = \sum_j \phi_j(x_1...x_N)c_{ji} \tag{1.70}$$

where $x_i \equiv r_i\sigma_i$ represents the space and spin coordinates of the ith electron and the coefficients c_{ji} are determined by diagonalizing the target Hamiltonian. For our work we use the atomic structure package AUTOSTRUCTURE [6] to generate the spectroscopic radial orbitals.

The basis states that provide the solution to Equation 1.67 applied to the inner region have the form:

$$\psi_k^{N+1} = A \sum_{i,j} a_{ijk} \psi_i^{N+1} \frac{u_{ij}(r_{N+1})}{r_{N+1}} + \sum_i b_{ik} \chi_i^{N+1} \tag{1.71}$$

where A is an antisymmetrization operator, ψ_i^{N+1} are channel functions obtained by coupling N-electron target states with the angular and spin functions of the scattered electron, $u_{ij}(r)$ are radial continuum basis functions. The square integrable functions χ_i^{N+1} represent bound states included to account for electron correlation effects, to ensure completeness of the total wavefunction. Given that they are constructed solely from target orbitals, they will have negligible values on the R-matrix boundary. The continuum basis orbitals $u_{ij}(r)$ are only defined over the range $0 \leq r \leq a_0$, as they are solutions to the radial part of the Hamiltonian. These orbitals represent the radial motion of the scattered electron in the internal region, thus they must vanish at the origin and are typically chosen such that they are non-zero at the R-matrix boundary, $r = a_0$, to provide a link between the solutions to the internal and external regions. Finally, the coefficients a_{ijk} and b_{ik} are determined by diagonalization of the $(N + 1)$-electron Hamiltonian.

The resulting eigenfunctions and eigenvectors are used to form the R-matrix:

$$R_{ij}(E) = \frac{1}{2a} \sum_k \frac{\omega_{ik}\omega_{jk}}{E_k - E} \tag{1.72}$$

where E_k are the eigenvalues of the $(N + 1)$-Hamiltonian and ω_{ik} are surface amplitudes given by

$$\omega_{ik} = \sum_j u_{if} c_{ijk}|_{r=a_0} \tag{1.73}$$

where the c_{ijk} correspond to the eigenvectors of the Hamiltonian.

The R-matrix relates the reduced radial wavefunction $F_i(r)$, which describes the radial motion of the scattered electron in the ith channel, to its derivative on the R-matrix boundary ($r = a_0$). The reduced radial wavefunctions satisfy:

$$F_i(r = a_0) = \sum_j R_{ij}(E)(a\frac{dF_j}{dr} - bF_j)_{r=a_0} \tag{1.74}$$

In the external region, the total wavefunction is expanded without antisymmetrization, because the scattered and target electrons no longer occupy the same region of the configuration space. The external wavefunction is of the form:

$$\Psi^{N+1} = \sum_i \psi_i^{N+1} \frac{F_i(r_{N+1})}{r_{N+1}} \tag{1.75}$$

where the channel functions ψ_i are the same as those used in the inner region. Applying this to equation 1.67 yields:

$$(\frac{d^2}{dr^2} - \frac{l_i(l_i+1)}{r^2} + \frac{2Z}{r} + k_i^2)F_i(r) = 2\sum_{j=1}^{n} V_{ij}(r)F_j(r) \tag{1.76}$$

where both i and j sum over the n coupled channels of the close-coupled expression, l_i are the channel angular momenta, and k_i^2 are the channel energies, defined terms of the eigenenergies E_i by:

$$k_i^2 = 2(E - E_i) \tag{1.77}$$

The potential matrix V_{ij} is defined by:

$$V_{ij} = \langle \psi_i^{N+1} | \sum_k^N \frac{1}{r_{kN}} | \psi_j^{N+1} \rangle \tag{1.78}$$

where the integration is carried out over all coordinates except those of the impact electron. To solve for the elements V_{ij} of the potential matrix, we use the expansion

$$\sum_{k}^{N} \frac{1}{r_{kN}} = \sum_{\lambda=0}^{\infty} \sum_{k=1}^{N} r_k^{\lambda} P_{\lambda}(cos\theta_{kN+1}) \tag{1.79}$$

where in practice, we keep only the dipole and quadrapole Legendre Polynomial terms. The elements V_{ij} can be expressed in terms of a finite inverse power series in the radial coordinate,

$$V_{ij}(r) = \sum_{\lambda=0}^{\lambda_m} \frac{C_{ij}^{(\lambda)}}{r^{\lambda+1}} \tag{1.80}$$

where $C_i j^{(\lambda)}$ are the long-range potential coefficients. From the form of this expansion, it is apparent that the primary contribution for V_{ij} comes from the region $r < a_0$, which allows us to construct the element V_{ij} from the target N-electron dipole matrix elements. The $n \times n$ R-matrix can thus be related to the asymptotic form $n \times n$ K or S matrices. The final cross section in the LSπ coupling scheme for the transition from state $\alpha_i L_i S_i$ to state $\alpha_j L_j S_j$ is given by:

$$\sigma_{i \to j} = \frac{\pi}{k_i^2} \sum_{l_i, l_j} \frac{(2L+1)(2S+1)}{(2L_i+1)(2S_i+1)} \delta_{ij} - \delta_{ij}^2 \tag{1.81}$$

For our work, R-Matrix calculations are performed with a set of parallel R-matrix programs which are extensively modified versions of the serial RMATRIX I programs [15], developed by Connor Ballance (Queen's Belfast) in conjuction with the Belfast computational research group.

Finally, our R-Matrix calculation depends heavily on our ability to represent the N+1 target orbitals, high-lying Rydberg states, and continuum as a set of discrete states. For this, we rely on the atomic structure code AUTOSTRUCTURE [4].

1.7.2 Atomic Structure Calculations / *R*-matrix with PseudoStates (RMPS)

The standard R-matrix method treats the scattering (N+1)-electron system as a bound state. For our work, we need a method of representing high-lying Rydberg states, and a way to represent the continuum that allows for their interaction with bound states. To accomplish this, we use a large number of pseudostates to represent both, as introduced by Gorczyca and Badnell, et al [39]. In this scheme, we represent the target with the spectroscopic states outlined above and by using non-orthogonal Laguerre pseudo-orbitals to represent both the higher Rydberg states and the continuum. These pseudo-orbitals are subsequently orthogonalized to each other and to the spectroscopic states. These pseudo-orbitals do not have spectroscopic eigenvalues and only agree with their spectroscopic counterparts in having the same number of radial nodes. The eigenenergies of the pseudostates range from just below the ionization limit to far above and can thus be used to discretize the continuum. It should be noted that the pseudostate complex only serves as a computational representation of the continuum. Individual pseudostates have no physical significance.

Our atomic structure calculation is an extension of the term resolved calculations presented by Ballance and Griffin [9]. The radial functions for the spectroscopic and pseudo states were determined using the atomic structure code AUTOSTRUCTURE. In order to facilitate the number of structure calculations performed before the final target structure was achieved we used the Graphical AUTOSTRUCTURE Package (GASP), which is a Java front end to AUTOSTRUCTURE.

For our work with neutral argon, the high-lying Rydberg states and the target continuum were represented using non-orthogonal Laguerre pseudo orbitals for all subshells from 5d to 14g; they were subsequently orthogonalized to the spectroscopic orbitals and to each other. A total of 749 levels arising from the $3s^2 3p^6$; $3s^2 3p^5$ nl ; $3s 3p^6$ nl configurations were included in the intermediate coupled Configuration Interaction (CI) expansion of the target. Of these, 400 levels were below the ionization limit of 15.76 eV. The remaining levels were above this limit, with 259 levels densely distributed in the energy range of about 15.8 –

43.5 eV. The remaining 90 levels were sparsely distributed in the range of about 43.5 – 88.6 eV. Embedded within the dense distribution of pseudo states with energy of 15.8 – 43.5 eV were 20 levels resulting from the core-excited spectroscopic configurations $3s3p^6$ [3d–5p]. This large pseudo-state basis not only allows us to include the effects of continuum coupling within the scattering calculation, it also has a pronounced effect on the quality of the target structure. In addition to including the effects of configuration interaction, it corrects for the variation of the orbitals with LS term dependence, which is quite large in argon. This distribution of states is detailed in Figure 1.8.

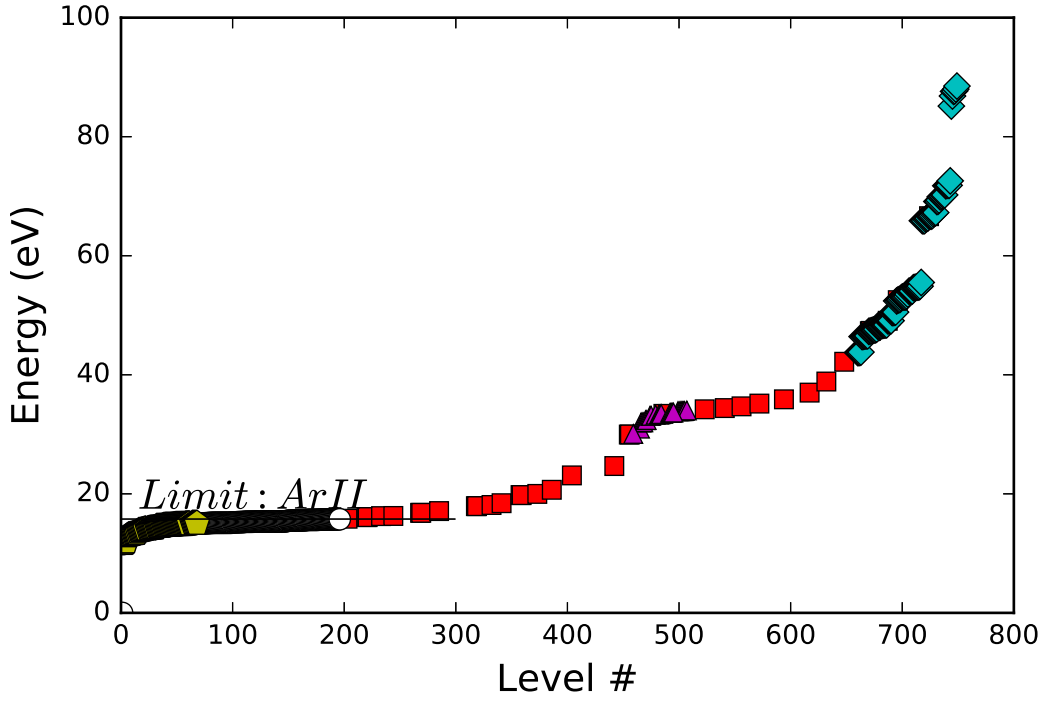

Figure 1.8: Energy distribution for the 749 levels in the atomic structure calculation. The black circles show low lying pseudostates. Pentagons (online color:yellow) represent spectroscopic levels below the ionization limit of 15.76 eV. Squares (online color:red) show the densely distributed pseudostates from about 15.8 – 43.5 eV. Embedded within this dense distribution are 20 spectroscopic levels that result from the configurations $3s3p^6$ [3d–5p] (triangles, online color:magenta). Diamonds (online color:cyan0) show the sparsely distributed pseudo-states with energy above 43.5 eV.

1.7.3 DR rate coefficients

We use AUTOSTRUCTURE to perform LS-coupling and (Breit-Pauli) intermediate coupling calculations of DR rate coefficients and cross sections for Ar^{+}—Ar^{4+}. In addition, we also calculate rate coefficients for Ar^{5+} (aluminum like argon) in order to compare with the previously published level-resolved calculations of Abdel-Naby (Abdel-Naby et al. 2012); this comparison is shown in Figure 3.10.

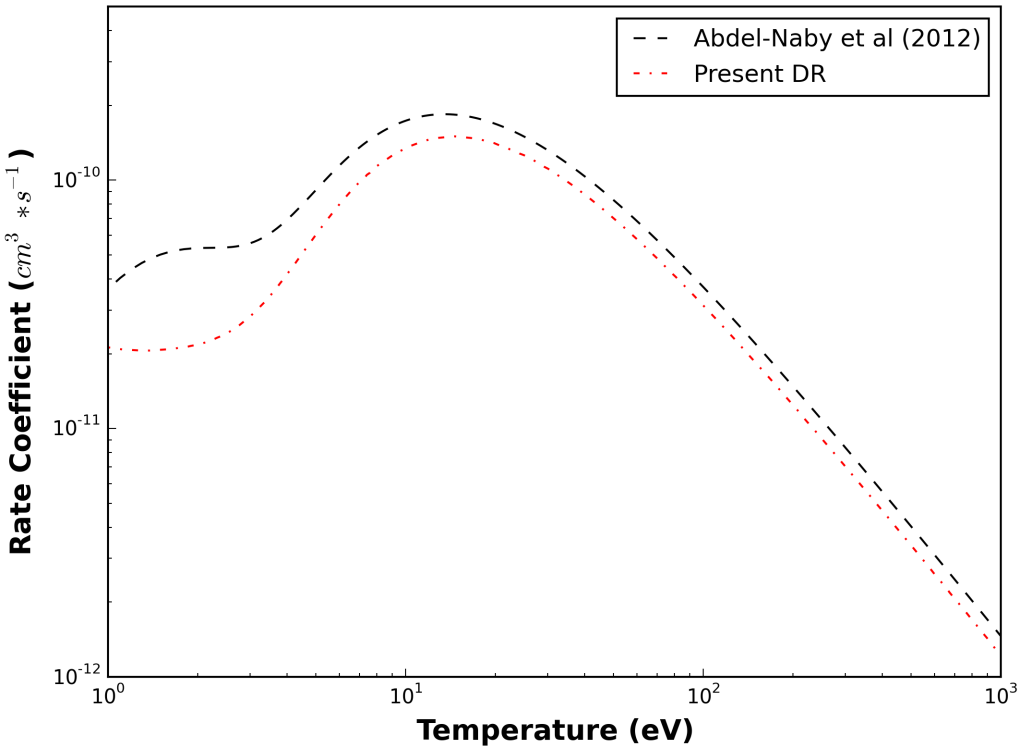

Figure 1.9: Our total ground-state DR rate coefficient for Ar^{5+}. We compare our results (dot-dashed; online color = red) to those presented in Abdel-Naby [1] (dashed; color = black

For each ion stage Ar^{+}—Ar^{4+}, we calculate cross-sections and rate coefficients for all ground and metastable levels within the ground state configuration of the initial ion. The appropriate metastable set can then be chosen for the particular plasma conditions. For the case of Ar^{+} this leads to two separate rates, one each for the ground level ($^2P^o_{3/2}$) and

first excited metastable level ($^2P^o_{1/2}$). In addition to level-resolved rate coefficients, we have calculated term resolved DR rate coefficients for each ion.

For all ion stages, we account for both dipole and quadrupole radiative transitions, though we expect the contributions from the quadrupole transitions to be small. Rydberg-Rydberg hydrogenic radiative rates are calculated during post-processing. For the Rydberg electron, we explicitly calculate n = 5—15 and l = 0—9. We employ a simple interpolated approximation to the cross section to account for the higher Rydberg resonances from n = 15—200. The energy mesh for all five ion stages spans from 0 eV through 130 eV. For our level-resolved calculations we have generated Maxwellian convolved rate coefficients for core excitations from $\Delta n = 0$, $\Delta n = 1$, and a total rate coefficient ($\Delta n = 0$, 1) for each of the metastable states within the ground configuration, where Δn refers to the excitation of the core electron. Due to heavy computational cost, we do not calculate $\Delta n = 2$ core excitations for our level resolved data. However, we have conducted configuration-averaged distorted-wave calculations using AUTOSTRUCTURE to estimate the contribution from $\Delta n = 2$ excitations, and found them negligible. Specifically, for all ion stages considered here, the contribution to the rate coefficient from $\Delta n = 2$ core excitations ($n = 3$ to $n = 5$), as determined from our configuration-averaged calculations, is 3 to 4 orders of magnitude less than the combined contribution from $\Delta n = 0$ and $\Delta n = 1$ core excitations. All of our Maxwellian rate coefficient data files are in the standard *adf09* format employed by the Atomic Data and Analysis Structure (ADAS) database (Summers 2004).

Prior to the generation of our Maxwellian resolved rate coefficients, the N+1 resonance energies were shifted to NIST values, with respect to the core excited energies of the N electron system, in order to better match the observed values. Figure 2 illustrates the impact of shifting the level energies from the atomic structure calculation to NIST values for the two metastable states in the Ar^+ground state. The difference between the shifted and unshifted calculations can be used to provide a measure of the uncertainty in our results.

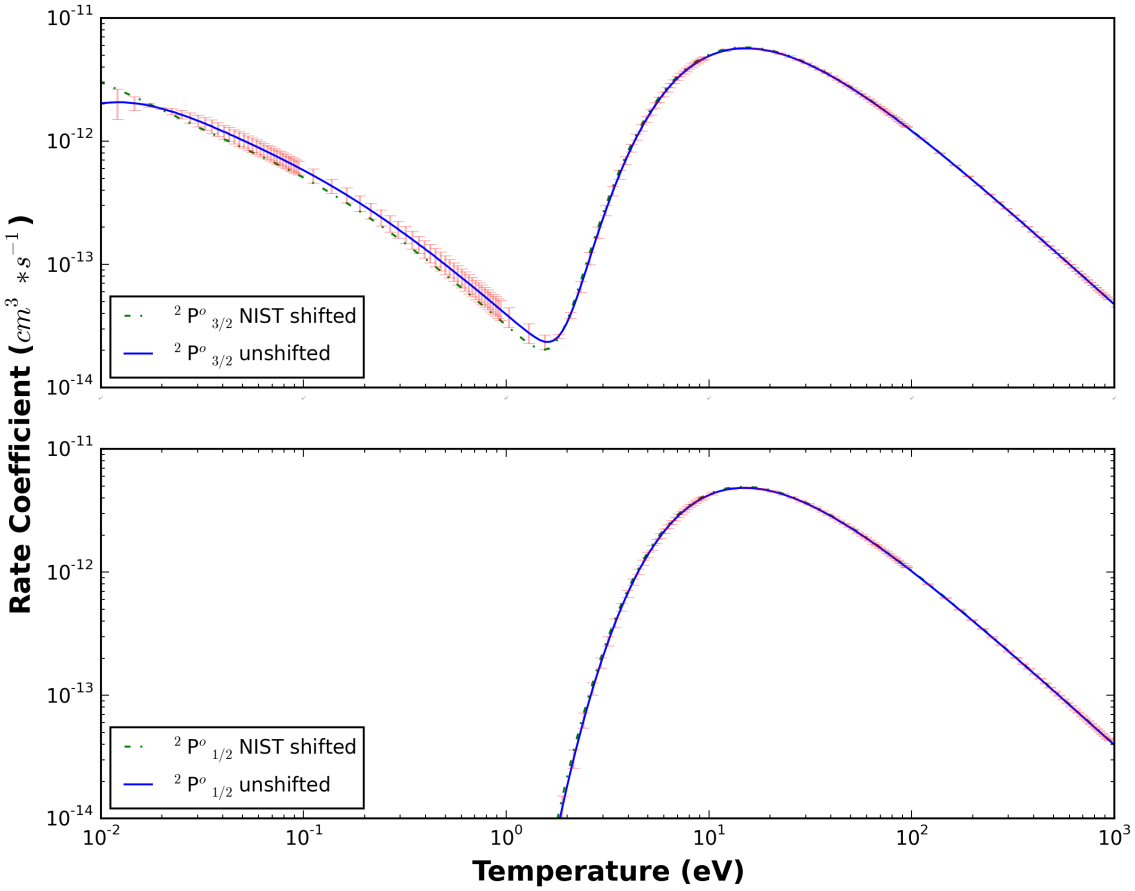

Figure 1.10: The effect of shifting energy terms to corresponding NIST energies on our DR rate coefficients. Rate coefficient shown is for Ar^+. The solid line (online color = blue) shows the unshifted rate coefficient. The dashed line is the shifted coefficient. Error bars (online color = red) represent the difference between a shifted and unshifted DR calculation.

1.8 The ALEXIS experiment.

In order to benchmark our atomic data, we compare our theoretical results and predictions with a variety of experimental and theoretical data available in the literature. We also make use of the Auburn Linear eXperiment for Instability Studies (ALEXIS). The ALEXIS device is used to study a wide variety of plasma instabilities generated by transverse shear flows in magnetized plasmas [75, 33, 31]. For our purposes, ALEXIS is reconfigured to generate a homogeneous argon plasma, from which we then collect line-of-sight averaged spectra for comparison to our theoretical data.

In this section, we will detail the basic capabilities and design of ALEXIS, and describe the data collection and analysis process. The original design of the ALEXIS chamber has been described extensively in papers by Walllace [77] and Eadon [34] with its most recent upgrades described in a paper by DuBois [30]. Therefore, only a brief summary of the ALEXIS configuration required for these studies is given below.

1.8.1 Vacuum vessel

Originally, the basic chamber design for ALEXIS was a 170 cm long, 10 cm diameter vacuum vessel constructed from ISO-100 compatible vacuum components [77]. This design has been extended to approximately 200 cm in length to accommodate an additional electromagnetic coil (we will discuss these in more detail shortly). A schematic of the experiment is shown in Figure 1.11. In this schematic you can clearly see the five main components of the experiment. 1) The RF antenna 2) the source electromagnetic coils (in blue) 3) the main chamber coils (in orange), 4) the main vacuum chamber (in grey) and 5) the DC filament plasma source (in white). Two important changes were made to the experiment for our purposes. First, the DC plasma source was completely disconnected, as its primary purpose is to create shear flows by generating an internally biased DC plasma within the main RF

plasma column. Second, the last electromagnetic coil was disconnected, and consequently it is not shown in the Figure 1.11.

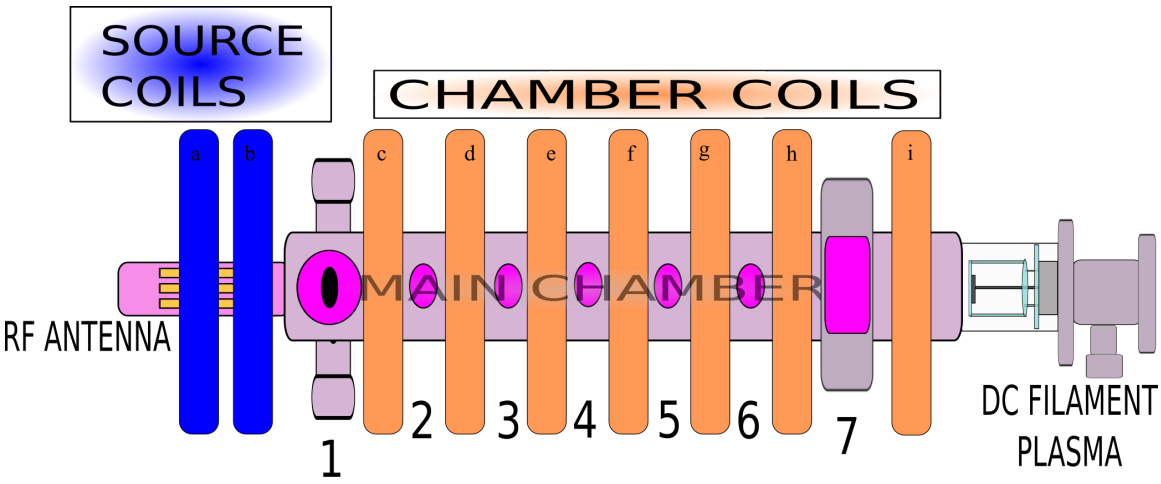

Figure 1.11: ALEXIS has 5 main components The ANTENNA (Purple), the OUTER COILS (blue), the INNER COILS (orange), the MAIN CHAMBER (grey), and the DC FILAMENT PLASMA (clear). Viewports for optical and probe access are labeled 1-7.

Figure 1.12 is a picture of the ALEXIS linear plasma device, taken from the same perspective as Figure 1.11.

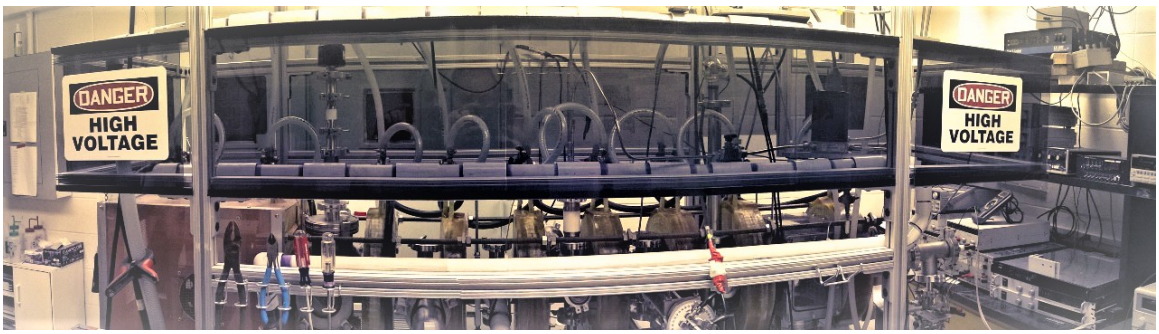

Figure 1.12: A picture of the ALEXIS linear plasma device, taken from the same perspective as Figure 1.11.

For these studies, the primary plasma source is the RF antenna, which is a single, slotted copper band, approximately 10 cm in length, circling a 5 cm diameter, 25 cm long

glass dome. The power source for the plasma is a variable (up to 300 Watts), 13.56 MHz RF power supply that is connected to an auto-matching LC network. The RF antenna section is connected to an ISO-100 (100 mm) stainless steel six-way cross (also indicated by the port labelled 1 in Figure 1.11). The two axial ports of the 6-way cross connect to the antenna and the main chamber. The four radial ports are used for viewing the plasma and in-situ diagnostics. The other four ports on this 6-way cross are used for viewing and diagnostics.

The main chamber is 91 cm long with a diameter of 10 cm, with ISO-100 flanges at the ends of the chamber. At 18.3 cm intervals there are four QF-40 flanged ports (for a total of 20), used for spectroscopic and probe-based diagnostics, gas feed, vacuum pumps, and pressure gauges. At section 7 of the chamber, is a custom designed optical box which allows multiple views of the plasma through large, square acrylic windows. On the bottom of this optical access region is the diffusion pump.

1.8.2 Electromagnet configuration

ALEXIS uses a series of electromagnetic coils to generate an axial magnetic field to confine the linear plasma column and help collisionally excite the noble gas used to create the plasma. For our work, we used nine coils that are distributed along the length of the vacuum chamber at the locations indicated in Table 1.6. Because of the uneven spacing between coil locations (a consequence of the chamber being designed and fabricated in several stages over a decade long period) - the coils were fabricated with several winding configurations in order to ensure that a uniform axial magnetic field could be generated in ALEXIS. As manufactured by Everson Tesla Incorporated, the coil types were: type 1 has 48 turns, type 2 has 50 turns, and type 3 has 59 turns. The coil types are also listed in Table 1.5.

Table 1.5: Coil type and location of the nine electromagnetic coils used in the ALEXIS plasma column.

Electromagnetic Coil	a	b	c	d	e	f	g	h	i
Axial Location (cm)	0	18.3	44.3	62.6	80.9	99.2	117.5	135.8	167.8
Configuration Type	1	1	3	1	2	2	1	3	1

Each coil is constructed from inside diameter 0.36 cm hollow copper tubing, to allow for water cooling. This tubing is wound into a basic solenoid shape, using different numbers of turns as described in the previous paragraph. The coils are then encased in an epoxy resin. As a result, the nine coils all have an inner diameter of 20 cm, outer diameter of 33 cm, and an axial length of 6.4 cm.

The electromagnetic coils on ALEXIS are powered using two large Power Ten DC power supplies. The "source" coils (a and b) are powered with a Power Ten 6.6 kW, 10 Volt, 330 Amp supply. The "chamber" coils (c through i) are powered with a Power Ten 13 kW, 40 Volt, 330 Amp supply. For other experiments, up to three Power Ten supplies can be wired in various coil configurations.

1.8.3 Magnetic Fields in ALEXIS.

The magnetic field in ALEXIS is generated by sending current from the Power Ten DC power supplies through the electromagnetic coils. It is similar to a solenoid field, being almost entirely axial (in the $\hat{z}$ direction) and very close to uniform. It is stronger at the coils' centers (in the $\hat{z}$ direction) and has local minima at the midway points. All of our measurements are taken at the viewports 2, 4, and 6 as pictured in Figure 1.11.

In order to determine the magnetic field strength as a function of the current in the electromagnetic coils, we measured the field generated by each power supply individually at each of the viewports 2 through 6, at currents of 20, 30, 40 ,50 60, 70, 80, 90, 100, 120, 140, 160, 80, 200, 225, and 250 Amps. The total field is the sum of the fields generated by each of the power supplies. To test the radial homogeneity of the magnetic field we measured the field at the center and close to each edge of the chamber diameter. In Figure 1.13 we show radial magnetic field cross-sections for various magnetic fields in the range 0 to 1000 Gauss at viewports 2, 4, and 6. All data presented in this work was collected at one of these three ports. As can be seen in the figure, radial magnetic field profiles are smooth and close to uniform across the diameter of the chamber.

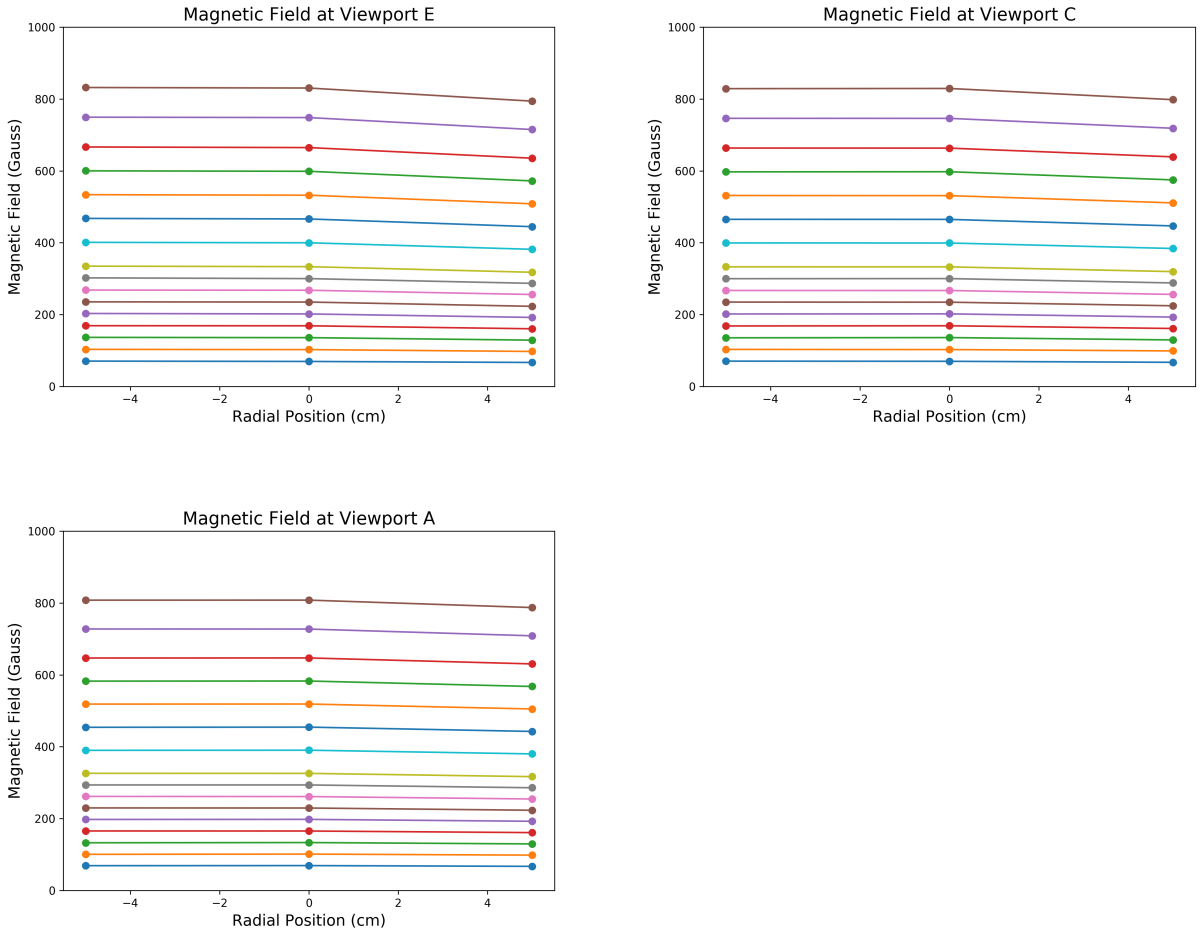

Figure 1.13: Radial magnetic field profiles in ALEXIS at viewports 2, 4, and 6. The magnetic field is plotted on the Y-axis for three positions corresponding to the walls and center of the ALEXIS vacuum chamber. The "out of the page" direction points towards the RF antenna, while the "into the page" direction points towards the DC filament section of ALEXIS.

Figure 1.14 shows a 3D surface plot of all magnetic fields measured across a range of 0 – 250 Amps of current on both the chamber and source magnets, measured at viewports 2, 4, and 6. As can be seen in the figure, the magnetic field in ALEXIS is highly dependent on the current in the chamber magnet, and weakly dependent on the source magnet current.

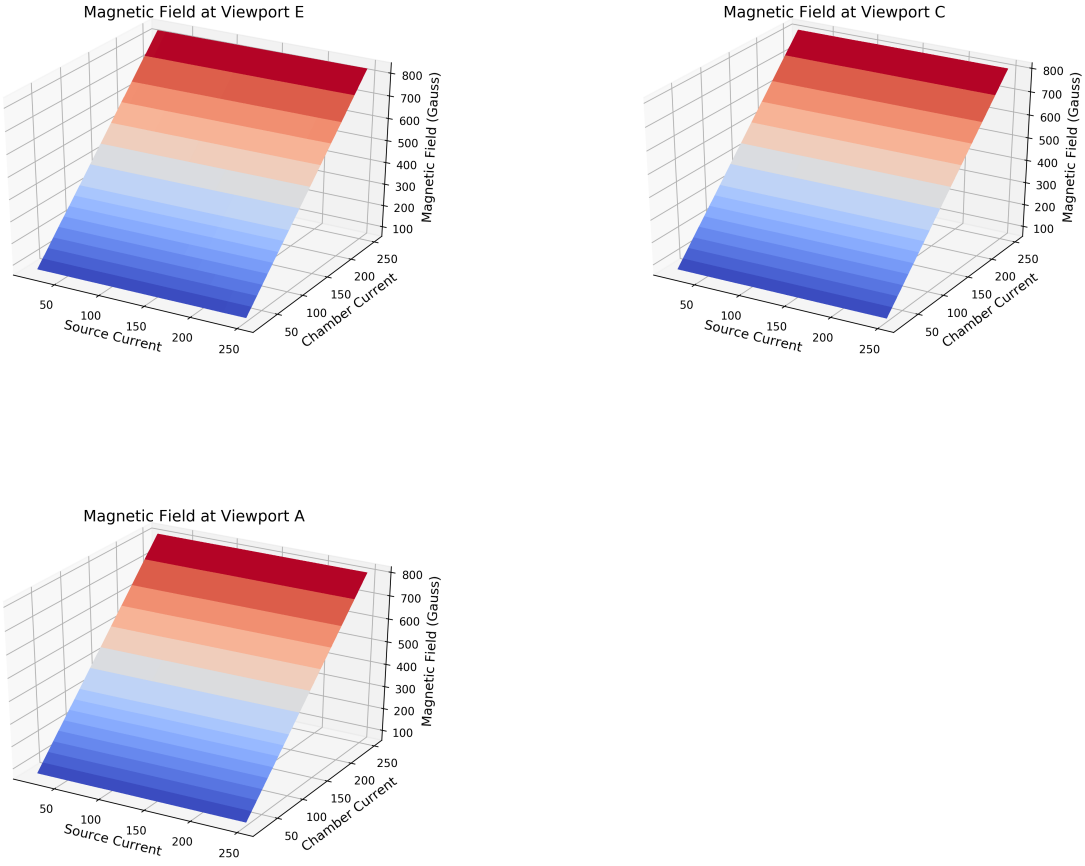

Figure 1.14: Magnetic field strengths at the radial center of the ALEXIS chamber for all measured values of current. We present data here for the viewports 2, 4, and 6.

Finally, in Figure 1.15, we present an axial magnetic profile of the magnetic field at all viewports. This plot clearly shows the uniform axial magnetic field profile in ALEXIS.

The raw data for viewports 2, 4, and 6 is made available in Appendix A.1.

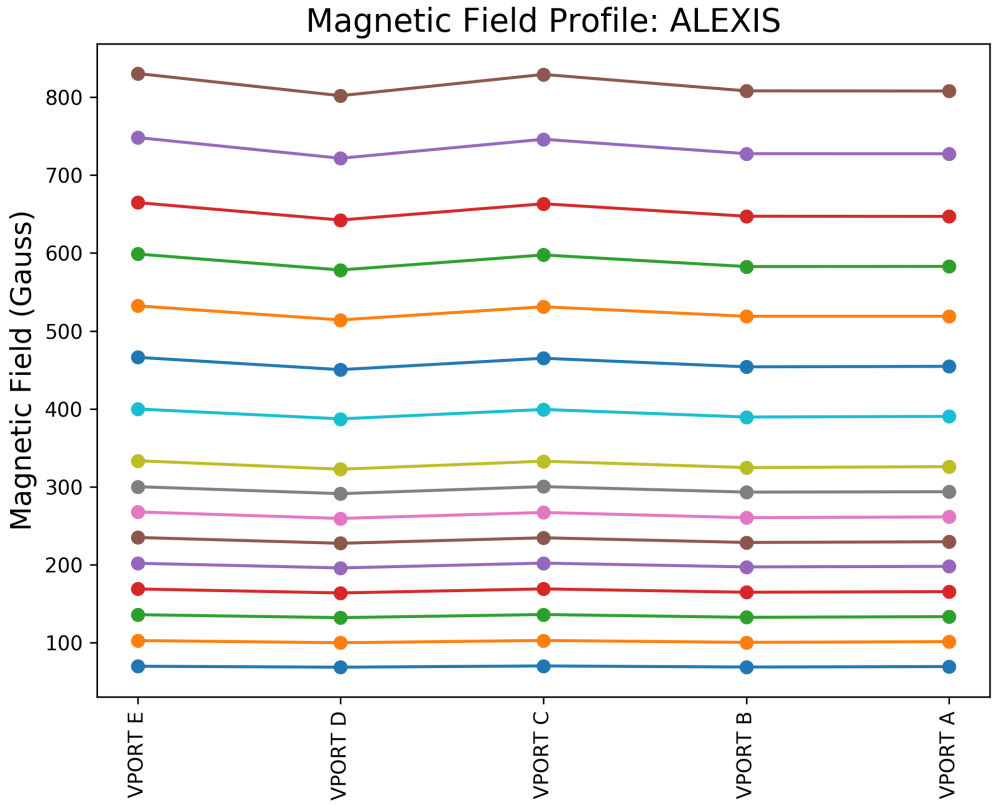

Figure 1.15: Axial magnetic field profile of the ALEXIS electromagnetic coils, plotted at viewports 2 through 6. These measurements were taken at the center of the vacuum chamber.

1.8.4 Vacuum pumps and gas regulation.

ALEXIS typically operates with a base pressure in the 10^{-6} Torr range. During actual data collection, after the argon gas has been introduced, typical operating pressure are 5×10^{-4} Torr (0.5 mTorr). Vacuum is maintained in ALEXIS using a combination of a 2.8 liter per second roughing pump, capable of achieving pressures of about 10 mTorr, and an Edwards Diffstak 100/300c , 300 liters per second diffusion pump.

Gas flow is regulated using a MKS Instruments model 1179A mass flow controller (MFC). All experiments described in this work will be performed using a gas fill of high purity argon (i.e. Argon 6.0 grade with $< 0.0001\%$ impurities from the source bottle). The MFC is controlled via an MKS Instruments type 327 controller, integrated into our data acquisition system via LabVIEW. This allows for the computerized regulation of the system and reproducible plasma conditions.

Pressure is monitored using several gauges. Two thermocouple pressure gauges and a Bayerd-Alpert (BA) ionization gauge are monitored using a Kurt Lesker KJL 4500 ionization guage controller. Thermocouple 1 is used to monitor the base pressure of the roughing pump during pump-down procedures, and is installed where the roughing pump attaches to the main chamber. Thermocouple 2 is installed between the roughing and diffusion pumps, and is used to monitor backing pressure once the system is switched over to the diffusion pump. The BA gauge is mounted on the top of the chamber at port 2 (as described in Figure 1.11), and monitors main chamber pressure. The BA gauge is monitored in LabVIEW using the ionization gauge controller. During data runs this pressure information is stored in a `{.fits}` data file. [1] In addition the aforementioned gauges, a LESKER 943 cold cathode gauge is used to monitor pressure near the RF antenna end of the experiment. This gauge is used primarily to verify that pressure on both ends are in agreement. The data from this gauge is not stored.

[1] The FITS - Flexible Image Transport System (FITS) - file format is a public domain, open source file storage format. It is commonly used in astronomy for storing images, but it can also be used as a compact method for storing a wide variety of digital data.

1.8.5 Plasma generation

The RF plasma source is RF-VII model RF-3-XIII 300 Watt RF generator operating at 13.56 MHz. Experiments in ALEXIS are typically performed using RF powers in the 10 – 100 Watt range. In order to minimize reflected power, the RF generator is paired with an ATN 5 capacitive autotuning network, also manufactures by RF-VII. RF power settings for ALEXIS are managed remotely using LabVIEW.

1.8.6 Data collection / diagnostics

ALEXIS uses a variety of probe-based diagnostics, including single and double tipped Langmuir probes, emissive probes, b-dot probes, and "k" probes to measure electron temperature and density, plasma potential, and wavenumber of shear driven instabilities [32, 31]. In previous studies it has used laser-induced fluorescence (LIF) to measure ion-flows [35]. In the experiments performed for this work, a double-tipped, in-situ Langmuir probe is used to make local measurements of the electron density and electron temperature. These localized measurements will be used to benchmark against the optical measurements that are being developed in this work. In the following section, a descriptions of the operation and model of the single and double-tipped Langmuir probe are given.

H. M. Mott-Smith and I. Langmuir first described the properties of the current-voltage (I-V) characteristic of an in-situ plasma probe, first in a series of reports in 1924 [53] and summarized in an article in Physical Review in 1926 [63]. The simplest version of a Langmuir probe is simply a conducting object (often a metal wire or sphere), that is inserted into a plasma and subjected to an externally applied bias voltage. This configuration is the *single Langmuir probe*. It has several prominent features that allow us to characterize a plasma. The bias voltage is swept through an appropriate range, and the resulting current, as a function of applied voltage, is recorded. The voltage at which no current is drawn is referred as the *floating potential*. The voltage at which electrons begin to saturate the probe, corresponding to the greatest amount of positive current, is in most cases roughly equal to

the plasma's *space potential*, which is often called simply the *plasma potential*. The region that corresponds to the greatest negative current, when the probe is saturated with ions, is called the *ion saturation region*.

When plotted, the resulting I-V trace is referred to as a *characteristic I-V trace*. A sample characteristic I-V trace, taken in ALEXIS with a single tipped Langmuir probe [33], is shown in Figure 1.16. In the figure, you can clearly see the floating potential V_f, the plasma space potential V_p, the electron saturation region (starting at I_{se}), and the ion saturation region (I_{si}). The transition region occurs in between V_f and V_p. The trace in Figure 1.16 is very near to an ideal theoretical Langmuir probe trace (an ideal trace would be flat in both saturation regions). This is almost never the case in an RF laboratory plasma, as distortion from RF feedback combines with geometric and sheath effects to distort the IV trace and give erroneous temperature measurements.

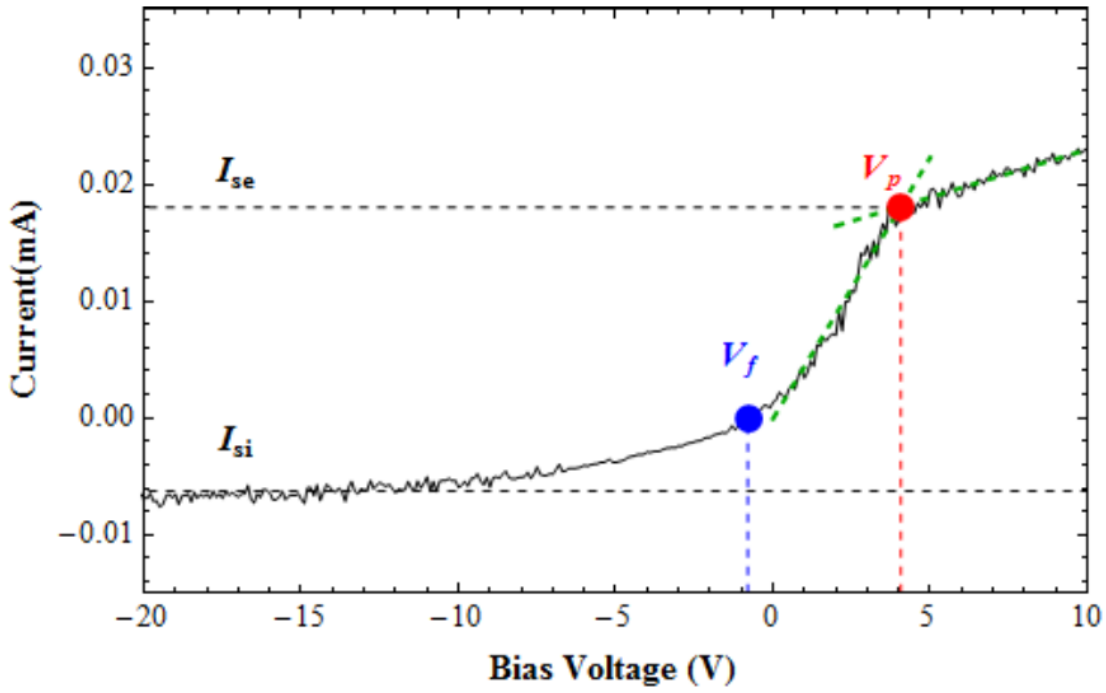

Figure 1.16: A characteristic IV trace from a single Langmuir probe in ALEXIS. You can clearly see the floating potential V_f, the plasma potential V_p, the electron saturation region (starting at I_{se}, and the ion saturation region (I_{si}.))

To minimize the impact of the RF sheath fluctuations, the electron temperature and density measurements in ALEXIS are taken using a *double Langmuir probe*. A double probe measures the ion saturation current as it flow between two metal tips, which are located in close proximity to one another in the plasma. This current is measured as function of bias voltage, swept between the two tips, and again plotted as an I-V trace.

The double probe used in ALEXIS is shown in Figure 1.18. This probe has two stainless steel tips. Each tip is 2 mm in diameter and protrudes 2 mm from the ceramic housing. They are situated 2.5 mm apart, and have a surface area of 0.157 cm^2. Bias voltage is swept between these two tips using a Keithley 2400 sourcemeter operating as a four-quadrant source for both current and voltage and which is controlled via LabVIEW. Electron temperature and density can be derived from the characteristic probe trace. A standard formula, found in many sources [46, 26] is given in equation 1.82.

$$I = I_{si} tanh \frac{eV}{2T_e} \tag{1.82}$$

where I is the collected current, I_{si} is the ion saturation current, e is the electron charge, V is the voltage between the two tips, and T_e is the electron temperature. This basic formula allows us to determine T_e from an IV trace. It is then simple to calculate electron density from the following expression:

$$n_e = \frac{I_{si}}{eA}\sqrt{\frac{m_i}{T_e}} \tag{1.83}$$

where n_e is the electron density, I_{si} is the ion saturation current, e is the electron charge, A is the area of each probe tip, m_i is the ion mass, and T_e is the electron temperature in eV.

A complication in many laboratory plasmas is the distortion of the IV trace due to geometric and sheath effects. Furthermore, any deviation in the electron distribution from an ideal Maxwellian can also lead to error in measured temperatures/densities. This can be seen in Figure 1.17 on a typical IV-trace from ALEXIS. It is clear that both saturation

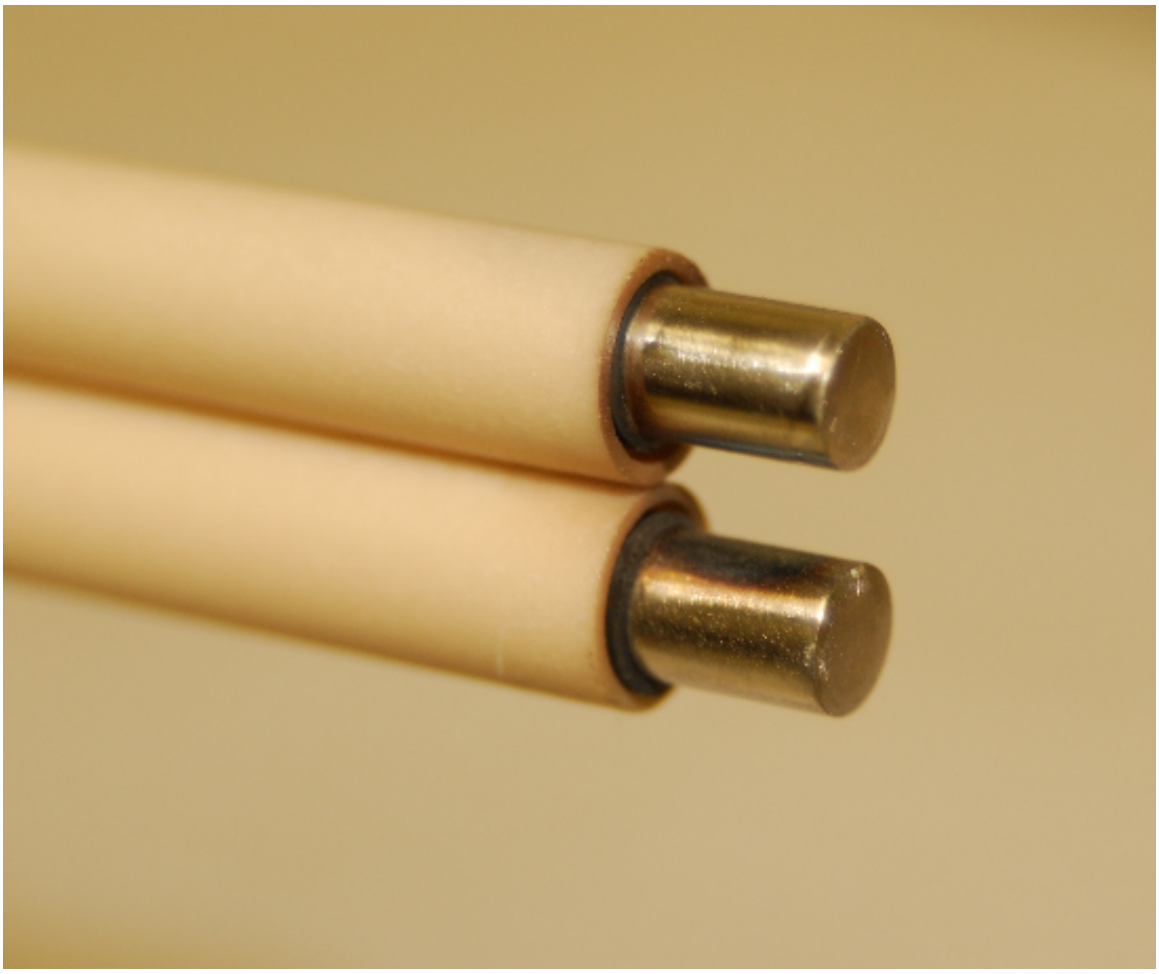

Figure 1.17: The ALEXIS double probe.

regions are fsubject to perturbations that cause the ion current to deviate from saturation. To compensate for these distortions, a modified version of equation 1.82 is used. This modified fit was developed in conjunction with Tejero at the Naval Research Laboratory (NRL), and is given in equation 1.84.

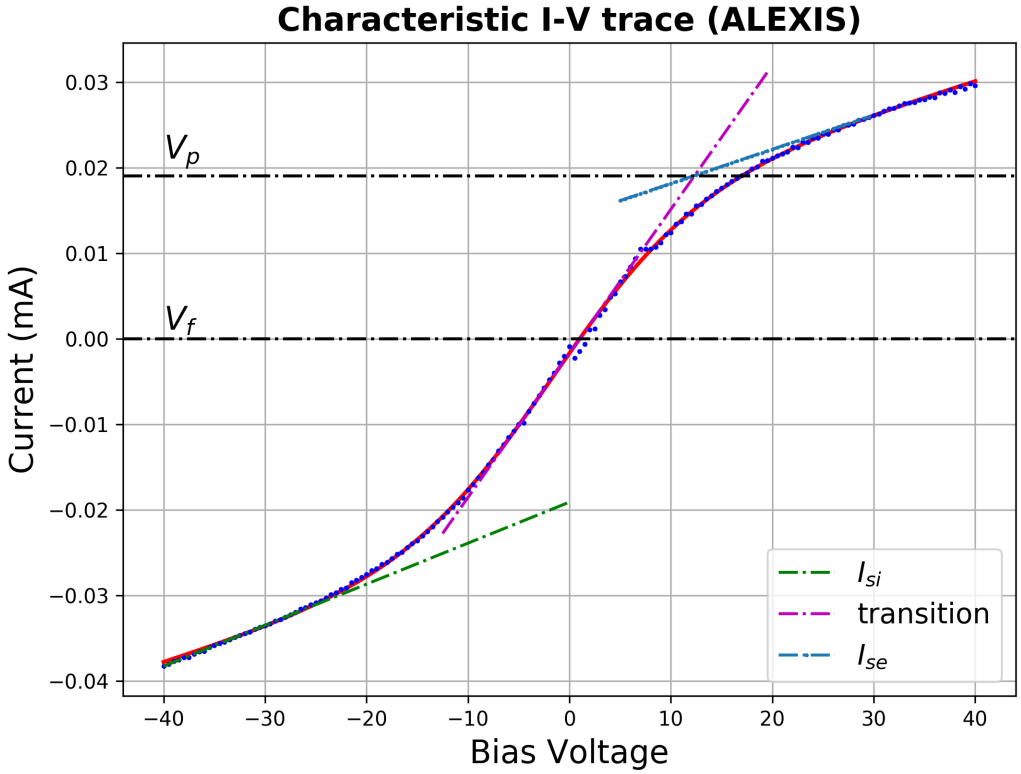

Figure 1.18: Typical ALEXIS double-probe trace. The deviation from an ideal trace is clearly seen in the saturation regions.

$$I(V) = a_0(V - a_1) + a_2 * tanh\frac{V - a_1}{a_3} + a_4 \tag{1.84}$$

where a_0 is the slope of a linear fit in the transition region, a_1 is the voltage offset of the floating potential (V_f), a_2 is the ion saturation current, a_3 is a fitting parameter with units

of Volts, and a_4 is the current offset. This model can be fitted using standard regression techniques, and electron temperature and density then calculated:

$$T_e = \frac{I_{si}}{2 * dI/dV_{V=0}} = \frac{I_{si}}{2 * \left(a_0 + \frac{a_2}{cosh^2(\frac{a_1}{a_3})} \right)} \tag{1.85}$$

$$n_e = \frac{I_{si}}{eA}\sqrt{\frac{m_i}{T_e}} = \frac{a_2}{eA}\sqrt{\frac{m_i}{T_e}} \tag{1.86}$$

These two equations are the basis for all experimental, probe-based electron temperature and density measurements in ALEXIS.

1.8.7 Spectrometers

While the double probe is the basic tool used to benchmark electron temperature or density predictions made using our atomic data, we still need some way to collect experimental spectra. We accomplish this using a standard Charge Coupled Device (CCD) USB powered Black Comet spectrometer, manufactured by StellarNet. This spectrometer is shown in Figure 1.19. It is capable of taking measurements is the 200-1100 nm range. The spectrometer was irradiance calibrated by StellarNet using a NIST traceable standard source. This allows for absolute irradiance measurements, though all the techniques described in this work rely solely on relative line techniques. The collection optics used are a 1 m, 1000 micron fiber optic cable coupled to a StellarNet CR2 cosine receptor; both were included in the factory calibration. The use of the cosine receptor eliminates any angular dependence in the collected spectra.

1.8.8 Data collection

In order to create a radial temperature and density map of the ALEXIS plasma, we insert the double probe into the center of the experiment and record an IV-Trace, sweeping the bias voltage from -40 V to +40 V in steps of 0.5 Volts. We then move the probe towards

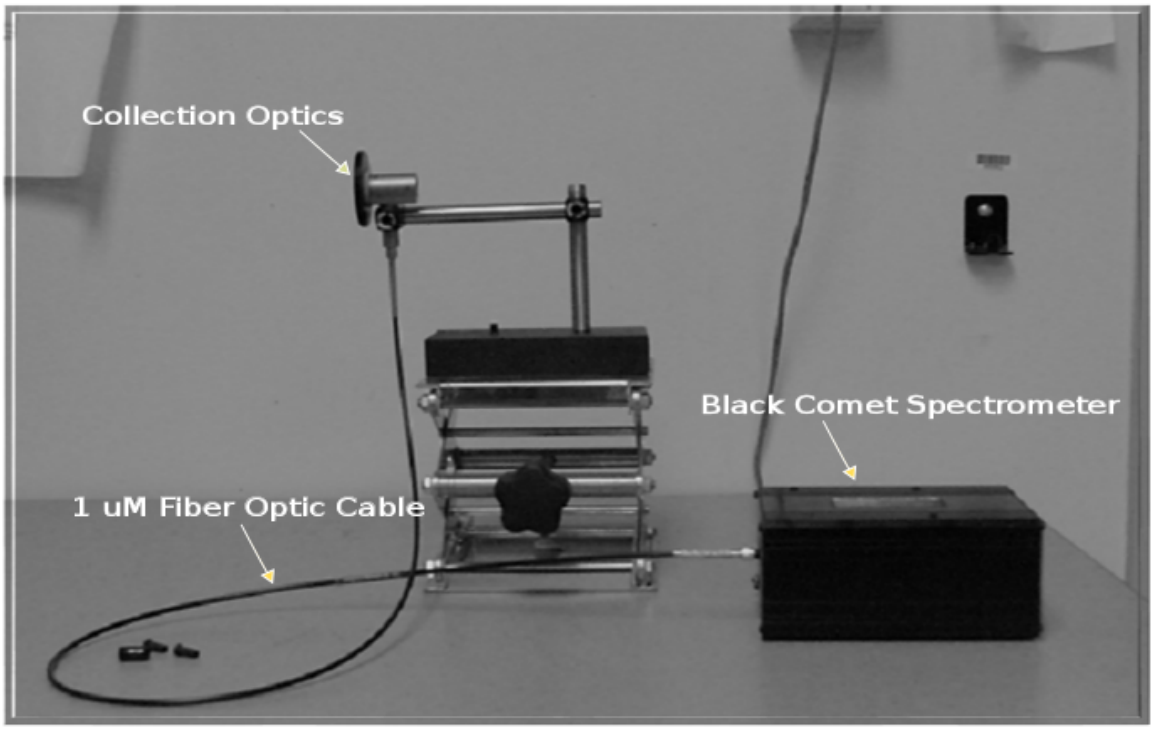

Figure 1.19: The StellarNet Black Comet spectrometer used to collect experimental spectra.

the chamber wall by 2mm and repeat. This is continued until the probe reaches the plasma boundary / chamber wall, allowing us to calculate a temperature and density at each swept location for a total of 26 data points from r = 0 to r= 50 mm. It is assumed that the ALEXIS plasma is sufficiently radially symmetric that this radial temperature and density profile can be extended to include the entire diameter. Earlier measurements have demonstrated the azimuthal symmetry of the ALEXIS plasma.

During the first 15 data collection intervals, we take a sample spectra and check the maximum value of the spectral array to ensure that it is both sufficiently high as to provide a signal to noise ratio (SNR) $>$ 10 dB, and below the 16 bit saturation threshold of the spectrometer. If the array maximum is outside these limits, the integration time is adjusted either up or down by $\approx 5\%$ and the data collection process is repeated until a suitable SNR is achieved. During the last 10 data collection intervals we record spectra at this optimized integration time. This allows us to capture spectra when the least amount of the probe shaft

is inserted in the plasma, in order to minimize any distortive effects from the presence of the probe.

Thus, for each data run we collect 26 temperature measurements, and 10 spectra. We collect data for a variety of plasma conditions by varying RF power, chamber and source magnet current, and MFC voltage (neutral pressure). A total of 46 data runs were ultimately deemed suitable for post-processing. These data runs were performed at viewports 1, 3, and 5. The resulting data is stored in the standard `{.fits}` file format. All data acquisition and storage is automated using LabVIEW.

The collected data was then modeled using a combination of the ADAS atomic code suite and new code developed specifically to analyze these results. This is further detailed in chapter 4.

1.9 Summary and overview

This introductory chapter has provided a brief but reasonably complete overview of the research contained within this dissertation. The remainder of this document is organized as follows:

Chapter 2: Metastable resolved electron impact excitation of neutral argon. Electron-impact excitation is expected to be the primary population mechanism in low temperature plasmas. In this chapter we detail our calculation of metastable resolved impact excitation cross-sections for neutral argon, and compare our results with previous theoretical calculations and experimental observations where possible. To our knowledge this is the first metastable resolved theoretical calculation to date. Our calculations rely heavily on parallel R-Matrix methods developed by Connor Ballance while at Auburn University in conjunction with collaborators at Rollins College (FL), Strathclyde University (Glasgow, UK), and Queen's University (Belfast, UK). We also present what is, to our knowledge, the

first calculation of metastable and level resolved cascade cross-sections for neutral argon, using code developed specifically for this project.

Chapter 3: Calculation of dielectronic recombination rate coefficients for low charge states of argon. The role of dielectronic recombination (DR) in low temperature argon plasmas is largely unknown, due to the lack of reliable atomic data [3]. In this chapter we present work published in the Journal of Atomic Physics (J. Phys. B.) in July of 2015. We present DR rate coefficients calculated using methods developed by Nigel Badnell at Strathclyde University (Glasgow, UK), using the AUTOSTRUCTURE code package developed by the same. Experimental measurements of these rate coefficients do not, to our knowledge, presently exist. Instead, we present comparisons to previously published semi-empirical and configuration-averaged rate coefficients, and discuss the implications we expect our results to have on various types of plasmas.

Chapter 4: Generalized collisional radiative modeling for low temperature neutral argon plasmas, with case study of the ALEXIS plasma. In this chapter we apply the atomic data from previous chapters toward a generalized collisional radiative model for low-temperature neutral argon. We detail our development of this model using a combination of Atomic Data and Analysis Structure (ADAS) and independently developed codes. Using these methods we are able to successfully determine metastable fractions in low temperature argon plasmas, and we present these results and discuss their time dependence. We also demonstrate a working electron temperature diagnostic, utilizing temperature sensitive line ratios, for the ALEXIS plasma, and describe methods that we feel can lead to a successful electron density diagnostic, but are outside our current abilities due to the hardware limitations of our spectrometer.

Chapter 5: Conclusions and discussion of future work. Here we discuss the broader implications of our work, and present several tasks that can be accomplished in the future.

For the atomic data calculated in chapters 2 and 3 we discuss the potential impact on plasmas beyond those considered in this thesis, including astrophysical and fusion plasmas. In discussing chapter 4 we focus on the application of our GCR model to other low temperature neutral dominated plasmas, including the Magnetized Dusty Plasma eXperiment (MDPX) and the ongoing work on laboratory studies of particle acceleration and double layers with applications to space plasmas performed by researchers at West Virginia University (WVU). We also discuss potential future applications for our GCR model, focusing on the development of future plasmas diagnostics.

Chapter 2

Electron impact excitation of neutral argon.

2.1 Introduction

The study of atomic processes in plasmas has long been an important diagnostic tool for laboratory[16], fusion [47], industrial, and astrophysical plasmas[70, 55]. Atomic processes can be used to obtain insights on the density, temperature, charge state, and transport of charged and neutral atoms in the plasma. However, in order to use atomic processes as a plasma diagnostic, it is necessary to have reliable rate coefficients for these processes. As an example, consider the low temperature regions of fusion plasmas. The hot "core" plasma is coupled to the material "first wall" through a lower temperature edge region. Because of the strong coupling between the edge region and core plasma, it is possible to manipulate the conditions of the edge plasma to affect and possibly control the conditions of the core plasma. One example of this type of control mechanism is massive gas injection (MGI), which has been proposed as a leading candidate for the mitigation of disruptions in large scale tokamak fusion reactors, such as ITER [54]. MGI is being studied at several facilities worldwide, including Alcator C-Mod [78], DIII-D [44], MAST [76], JET [54], TEXTOR [20], ASDEX [64], and NTSX-U [69]. In MGI, neutral noble gas is injected into a plasma during a disruption. These gases are subject to extreme temperature gradients, and progress from neutral to fully ionized on timescales less than 10 ms [69, 71]. These drastic temperature gradients, coupled with the rapid ionization of noble gas, lead to the formation of a highly non-equilibrium plasma. Without accurate rate coefficients to describe the population of atomic states, any attempt to model a process such as MGI would be daunting at best.

Argon is a leading candidate for MGI [54, 20, 71, 44], and is also one of the leading gases used to produce research and industrial plasmas. Line ratios of argon can be used to

diagnose, among other things, the electron temperature of both laboratory plasmas[16] and planetary nebulae [49], and the elemental abundance of argon in the sun [58]. In a previous work [3] we focused on the dielectronic recombination of low charge states of argon (Ar^{+} – Ar^{4+}). Here we present new level-resolved atomic data for the electron impact excitation of neutral argon, including excitation from long-lived metastable states, using a parallel Breit-Pauli R-Matrix with PseudoStates (BPRMPS) method. The existence of these long lived metastables has a significant impact on computational models of low-temperature argon plasmas, as the energy required to excite from these metastables to higher levels is ≈11.5 eV less than excitation from the ground state. Peak values of cross-sections for excitation from these metastable states can be two or even three orders of magnitude more than those from the ground state, often leading to situations where excitation from metastables is the dominant form of excitation within the plasma. While previous authors have published theoretical metastable resolved excitation data for neutral argon [11], to our knowledge ours is the first calculation to include large numbers of pseudo-states to represent both Rydberg states with energy close to the ionization limit and the target continuum. In addition, the large number of final states in our calculation allows us to include cascade effects in our theoretical cross-sections for excitation out of both ground and metastable states, via the determination of branching fractions for all final spectroscopic states. This in turn allows, for the first time, a direct comparison to experimentally measured apparent cross-sections for neutral argon [18, 66, 28, 48].

The remainder of this paper is structured as follows: In the next section we present a brief overview of the underlying R-matrix theory used to calculate our impact excitation data, and describe our method for calculating cross sections and branching ratios from this data. In Section 2.2 we present a comparison of our cross sections to results from previous literature. Section 2.3 presents a discussion of the results and an analysis of their implications, along with a brief summary.

2.2 Methods

2.2.1 Background

Neutral systems are described using several different notations depending on the needs of the author. It should be noted that the L-S coupling scheme used in Russel-Saunders notation does not accurately describe neutral systems, as most levels are a superposition of L-S states (i.e. L and S are generally not "good" quantum numbers). Generally, one of two notations is employed. Paschen notation is commonly used to describe neutral systems, particularly in those papers that deal with the experimental measurement of cross-sections, and is a quick and effective way to identify levels and their respective energy order within an excited configuration. Much of the theoretical literature, including the NIST atomic database, prefer to use variations of Racah notation $nl\,[K]_j$, which provides a unique set of quantum numbers for each state. We will use Paschen notation throughout this work, as our results are compared primarily with experimental literature that uses the same. Table 2.1 shows the notations in both schemes, along with the associated energies, for the first three excited configurations of neutral argon.

In this work we focus on the excitation of neutral argon via impact with free electrons from the $1s$ manifold into the $2p$ manifold. Figure 2.1 shows the energy distribution of these levels.

2.2.2 The atomic structure calculation.

Our atomic structure calculation is an extension of the term resolved calculations presented by Ballance and Griffin [9]. The radial functions for the spectroscopic and pseudo states were determined using the atomic structure code AUTOSTRUCTURE. In order to facilitate the number of structure calculations performed before the final target structure was achieved we used the Graphical AutoStructure Package (GASP), which is a Java front end to AUTOSTRUCTURE. Thomas-Fermi-Dirac-Amaldi orbitals were used for the 1s, 2s, 2p,

Table 2.1: Paschen and Racah notation for all the energy levels referenced in the present work.

Paschen	$nl\,[K]_j$	NIST Energy (eV)
1s5	$4s\ ^2[3/2]^o_{(2)}$	11.548
1s4	$4s\ ^2[3/2]^o_{(1)}$	11.623
1s3	$4s\ ^2[1/2]^o_{(0)}$	11.723
1s2	$4s\ ^2[1/2]^o_{(1)}$	11.828
2p10	$4p\ ^2[1/2]_{(1)}$	12.907
2p9	$4p\ ^2[5/2]_{(3)}$	13.075
2p8	$4p\ ^2[5/2]_{(2)}$	13.095
2p7	$4p\ ^2[3/2]_{(1)}$	13.153
2p6	$4p\ ^2[3/2]_{(2)}$	13.171
2p5	$4p\ ^2[1/2]_{(0)}$	13.273
2p4	$4p\ ^2[3/2]_{(1)}$	13.282
2p3	$4p\ ^2[3/2]_{(2)}$	13.302
2p2	$4p\ ^2[1/2]_{(1)}$	13.328
2p1	$4p\ ^2[1/2]_{(0)}$	13.480
3d6	$5p\ ^2[1/2]_{(1)}$	14.464
3d5	$5p\ ^2[5/2]_{(3)}$	14.499
3d3	$5p\ ^2[5/2]_{(2)}$	14.506
3d4′	$5p\ ^2[3/2]_{(1)}$	14.525
3d4	$5p\ ^2[3/2]_{(2)}$	14.529
3d1′	$5p\ ^2[1/2]_{(0)}$	14.576
2s5	$5p\ ^2[3/2]_{(1)}$	14.680
2s4	$5p\ ^2[1/2]_{(1)}$	14.687
3d1″	$5p\ ^2[3/2]_{(2)}$	14.688
3d2	$5p\ ^2[1/2]_{(0)}$	14.738

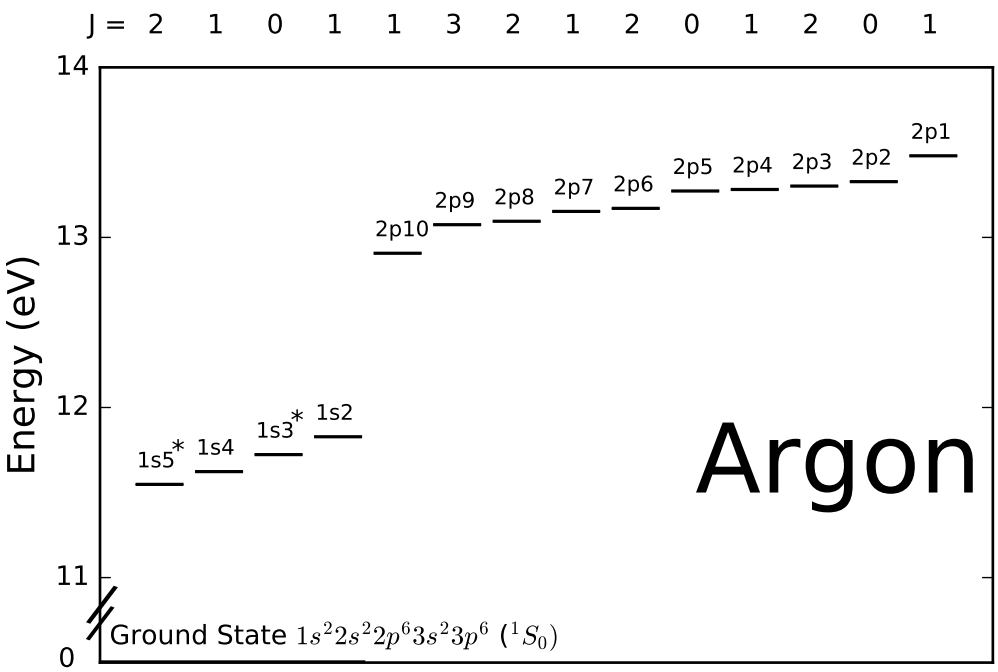

Figure 2.1: Schematic of the argon energy levels discussed in this work. The Paschen designation is listed on the plot directly above the energy, while J-values are listed above the plot. Long-lived metastable levels are marked with an asterisk.

3s, 3p, 3d, 4s, 4p, 4d, 4f, 5s, and 5p subshells with the associated scaling parameters 1.00000, 1.00000, 1.00000, 1.09980, 1.07743, 1.01500, 1.07410, 1.01900, 0.97000, 1.00000, 0.99000, and 0.96000.

The higher Rydberg states and the target continuum were represented using non-orthogonal Laguerre pseudo orbitals for all subshells from 5d to 14g; they were subsequently orthogonalized to the spectroscopic orbitals and to each other. A total of 749 levels arising from the $3s^2 3p^6$; $3s^2 3p^5$ nl ; $3s3p^6$ nl configurations were included in the intermediate coupled CI expansion of the target. Of these, 57 spectroscopic and 140 pseudo states were below the ionization limit of 15.76 eV. The remaining levels were above this limit, with 442 pseudo and 20 spectroscopic levels (resulting from the core-excited spectroscopic configurations $3s3p^6$ [3d–5p]) distributed in the energy range of about 15.8 – 43.5 eV. The remaining 90 levels were sparsely distributed in the range of about 43.5 – 88.6 eV. The distribution of energy levels is shown in Figure 2.3. This large pseudo-state basis has a pronounced effect on the quality of the target structure. In addition to including the effects of configuration interaction, it corrects for the variation of the orbitals with LS term dependence, which is quite large in argon.

In order to check the accuracy of the target states, we used the same set of orbitals to perform an intermediate coupling Breit-Pauli calculation of the energy levels of argon. The results for the lowest 24 levels, which except for the ground level are specified in jK-coupling notation, are shown in Table 2.2 in comparison to the experimental energies from the NIST data base [23]. We also compare our results with those of Zatsarinny and Bartschat [16], which were obtained from a non-orthogonal basis set structure calculation followed by a B-spline R-matrix calculation; the use of non-orthogonal valence orbitals allows for a great deal of freedom with respect to the determination of the bound states, and this most likely represents the most accurate theoretical target structure for argon. However, as can be seen, the present results are also in excellent agreement with the experimental energies. The

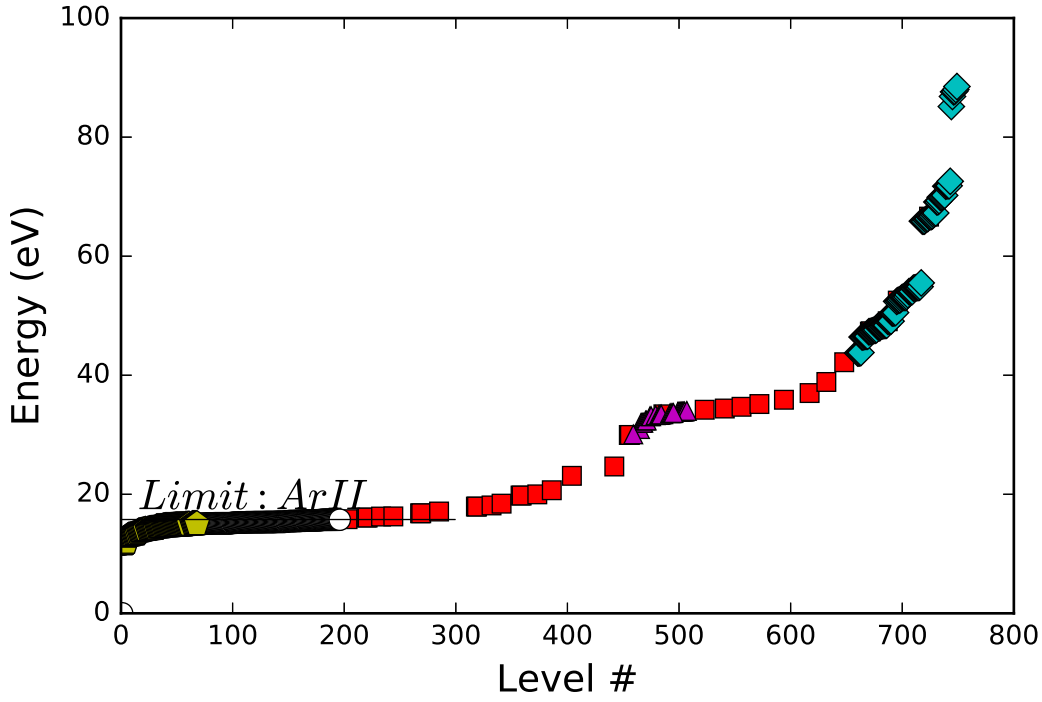

Figure 2.2: Energy distribution for the 749 levels in the atomic structure calculation. Circles show low lying pseudostates. Pentagons (online color:yellow) represent spectroscopic levels below the ionization limit of 15.76 eV. Squares (online color:red) show the densely distributed pseudostates from about 15.8 – 43.5 eV. Embedded within this dense distribution are 20 spectroscopic levels that result from the configurations $3s3p^6$ [3d–5p] (triangles, online color:magenta). Diamonds (online color:cyan0) show the sparsely distributed pseudo-states with energy above 43.5 eV.

average percentage error is only 0.26%, compared to an average percentage difference of 0.21% for the energies of Zatsarinny and Bartschat [16].

As an additional benchmark of our structure calculation we have compared Einstein A-values from our work with the accepted values from the NIST database for selected dipole transitions. For those involving radiative decay into a metastable state we have chosen transitions that correspond to lines that we predict to be good candidates for optical diagnostics. These results are shown in Table 2.3.

Table 2.2: Comparison of energy levels from our atomic structure calculation with Zatsarinny and Bartschat [81] and the NIST database [51]. Average percent error with NIST values is shown for both the present work and for Z & B.

Level	Paschen	NIST (eV)	Present (eV)	% Error	Z&B (eV)	% Error
1	1s5	11.548	11.537	0.1	11.628	0.69
2	1s4	11.624	11.638	0.13	11.700	0.66
3	1s3	11.723	11.759	0.3	11.798	0.64
4	1s2	11.827	11.923	0.8	11.898	0.60
5	2p10	12.907	12.923	0.12	12.907	0.00
6	2p9	13.076	13.061	0.11	13.083	0.05
7	2p8	13.095	13.087	0.06	13.105	0.07
8	2p7	13.153	13.15	0.02	13.141	0.08
9	2p6	13.172	13.167	0.03	13.159	0.10
10	2p5	13.273	13.294	0.16	13.252	0.16
11	2p4	13.282	13.317	0.26	13.273	0.08
12	2p3	13.302	13.339	0.27	13.294	0.06
13	2p2	13.327	13.365	0.28	13.298	0.22
14	2p1	13.48	13.593	0.84	13.472	0.06
15	3p10	13.845	13.784	0.44	13.901	0.40
16	3p9	13.864	13.807	0.41	13.917	0.38
17	3p8	13.904	13.856	0.34	13.949	0.33
18	3p7	13.978	13.894	0.61	14.019	0.28
19	3p6	14.013	13.939	0.53	14.041	0.20
20	3p5	14.063	14.004	0.42	14.042	0.14
21	3p4	14.068	14.045	0.17	14.061	0.05
22	3p3	14.09	14.061	0.21	14.079	0.08
23	3p2	14.099	14.057	0.30	14.093	0.03
24	3p1	14.153	14.109	0.31	14.125	0.20
			Avg. % Err	0.26	Avg. % Err	0.23

Table 2.3: Einstein A_{ij} coefficients for selected strong dipole transitions, compared to NIST. For transitions involving radiative decays into the 1s3 and 1s5 metastables, we choose transitions corresponding to lines predicted to be good candidates for optical diagnostics. Average percent difference with NIST for all six lines is 14.5%.

NIST Wavelength (nm)	Upper Level	Lower Level	Present Work (A_{ij})	NIST (A_ij)
Ground state				
104.8	4s $^2[3/2]^o(1)$	$^1S_0$	5.23e08	5.10e08
106.7	4s $^2[1/2]^o(1)$	$^1S_0$	9.76e07	1.19e08
1s5 metastable				
763.5	4p $^2[3/2](2)$	4s $^2[3/2]^o(2)$	2.93e07	2.45e07
772.4	4p $^2[3/2](1)$	4s $^2[3/2]^o(2)$	6.29e06	5.18e06
1s3 metastable				
826.5	4p $^2[1/2](1)$	4s $^2[1/2]^o(0)$	1.70e07	1.53e07
852.1	4p $^2[3/2](1)$	4s $^2[1/2]^o(0)$	1.24e07	1.39e07

2.2.3 RMPS Scattering Calculation

An R-Matrix calculation that included all 749 levels associated with the 397 terms in the previous, term-resolved RMPS scattering calculation [9] is extremely computationally intensive, even on the largest massively parallel computers. Therefore, we have focused on target energies below 30 eV, reducing the number of orbitals from 749 levels to 450 for the close-coupling expansion.

In our implementation of the RMPS method, the basis used to represent the (N+1)-electron continuum was made orthogonal to the pseudo orbitals using a method developed by Gorczyca and Badnell [39]. The scattering calculation was performed with our set of parallel R-matrix programs which are extensively modified versions of the serial RMATRIX I programs [15]. The R-matrix box had a radius of 84.2 Bohr radii and we employed 50 basis orbitals to represent the (N+1)-electron continuum per angular momentum. For the total cross section calculations, we employed a variety of energy meshes. With the lower $LS\pi$ partial waves from $L = 0$ to $L = 12$, in the energy range from the first excitation threshold at approximately 11.56 eV up to an energy of about 15.76 eV, we employed 932 energy mesh points. For the higher partial waves from$L = 13$ to $L = 50$, we employed 200 mesh points over the same energy range. Finally, in the energy range from 15.76 eV to a maximum energy of

31.29 eV, we employed an additional 100 mesh points for all partial waves. The contributions from higher partial waves above $L = 50$ were then estimated for dipole transitions using the method originally described by Burgess [21], and for the non-dipole transitions assuming a geometric series in L, using energy ratios.

The excitation cross sections were determined using the methods described in Griffin et al. [41]. They included the contributions from all K-matrices up to $L = 12$, which we determined was sufficient to achieve convergence at these energies.

The previous work of Ballance and Griffin [9] investigated the effects of coupling to the target continuum on electron-impact excitation in Ar, using LS coupling. Our calculations are fully level resolved, using intermediate coupling, allowing for a direct comparison with previous level-to-level theoretical and experimental cross-sections.

2.2.4 Optical methods / branching fractions

Much of the available experimentally determined impact excitation cross-sections for neutral argon make use of what is known as the optical method, for which we will provide a brief description. A more detailed theoretical treatment, along with a description of a typical laboratory setup, can be obtained from Fillipelli et al. [37].

For the optical method, a mono-energetic beam of electrons is directed toward a target of atoms in steady-state that are in the ground or some excited metastable state, exciting them into an atomic state i. These atoms may then decay into some lower state j and the resulting fluorescence is detected. The resulting measurement, if possible, is of the *optical emission cross-section* for the $i \rightarrow j$ transition, defined as:

$$Q_{ij}^{opt} = \frac{\Phi_{ij}}{n_0(I/e)} \tag{2.1}$$

where Φ_{ji} is the number of photons per second per unit beam length, n_0 is the target gas number density, I is the electron beam current, and e is the charge of the electron. It is understood that the index i refers to a higher energy state, and the index j to a lower state.

In real laboratory settings the level i can radiate to multiple lower levels j, however, the level i can be populated from many other levels and isolating a single direct excitation cross section is often impossible from the spectrum. For this reason, most experiments do not measure optical emission cross-sections. Instead they measure the *apparent cross-section*, which is the sum of all optical emission cross-sections out of level i to lower levels j.

$$Q_i^{app} = \sum_{j<i} Q_{ij} \tag{2.2}$$

mendely The apparent cross-sections contain contributions from both the *direct excitation cross-section* and the *cascade contribution*, which is the sum of optical emission cross-sections into level i from levels above.

$$Q_i^{app} = Q_i^{dir} + \sum_{k>i} Q_{ki}^{opt} \tag{2.3}$$

From an experimental perspective, it is necessary to know the cascade contribution to determine the direct excitation cross-section. From a theoretical viewpoint, the cascade contribution from a single higher level k to a level i can be obtained by multiplying the $k \rightarrow i$ optical emission cross-section by the corresponding *branching fraction*. The branching fraction can be determined experimentally, or theoretically using Einstein A-values. The total cascade contribution is then a simple sum:

$$Q_i^{cas} = \sum_{k>i} (Br * Q^{opt})_{ki} \tag{2.4}$$

We have used AUTOSTRUCTURE to calculate A-Values for the 1596 transitions between the 57 spectroscopic levels of neutral argon that fall below the ionization limit. From these A-Values we have calculated branching fractions for all 57 levels. We are able to extract direct excitation cross-sections for transitions between all levels of neutral argon with $nl < 5p$ from our RMPS calculation. We can also determine the cascade contribution for low-lying excited states, as peak values for cross-sections are known to decrease rapidly with increasing

n and our RMPS calculation includes all excitations up to 5p. A direct comparison is then possible for experimental measurements, including cascade effects, that involve excitation from the ground state, the $1s3$ metastable state, or the $1s5$ metastable state, both of which are know to have lifetimes greater than 1.3 s [66]. To our knowledge this is the first time such a direct comparison with apparent cross section measurements has been performed.

2.3 Results

In the following section we compare our work to other theoretical results, primarily involving B-Spline R-matrix calculations from the group at Drake University (Bartschat, Zatsarinny, Zeman, Wang) and the experimental work of the group at Wisconsin (Boffard, Chilton. Piech, Lin *et al.*). The Drake group produces accurate atomic data using a B-Spline R-Matrix method, and have presented many articles concerning the excitation of neutral argon from both ground and metastable states [80, 11]. The Wisconsin group have published some of the only measurements of excitation cross-sections from metastable states of argon, along with detailed excitation functions for both ground and metastable states.

2.3.1 Excitation from the ground state into the 2p manifold.

In Figure 2.3 we show our results for direct excitation cross-sections from the $^1S_0$ ground state of neutral argon into all ten levels of the of the $2p$ manifold. W have compared our theoretical results with the theoretical results of Zatsarinny *et al.* [82], and experimental data from Chilton *et al.* [27], Filopović [38], and Chutjian and Cartwright [29]. Zatsarinny's data is the result of a 500 state B-Spline R-Matrix calculation (BSR-500). Error bars on the experimental data have been omitted for clarity, but are usually $\approx 35\%$ and result from a combination of statistical error and error in the absolute calibration of the experimental apparatus. Calibration error is normally the dominant source of error in these measurements; statistical error can often be neglected.

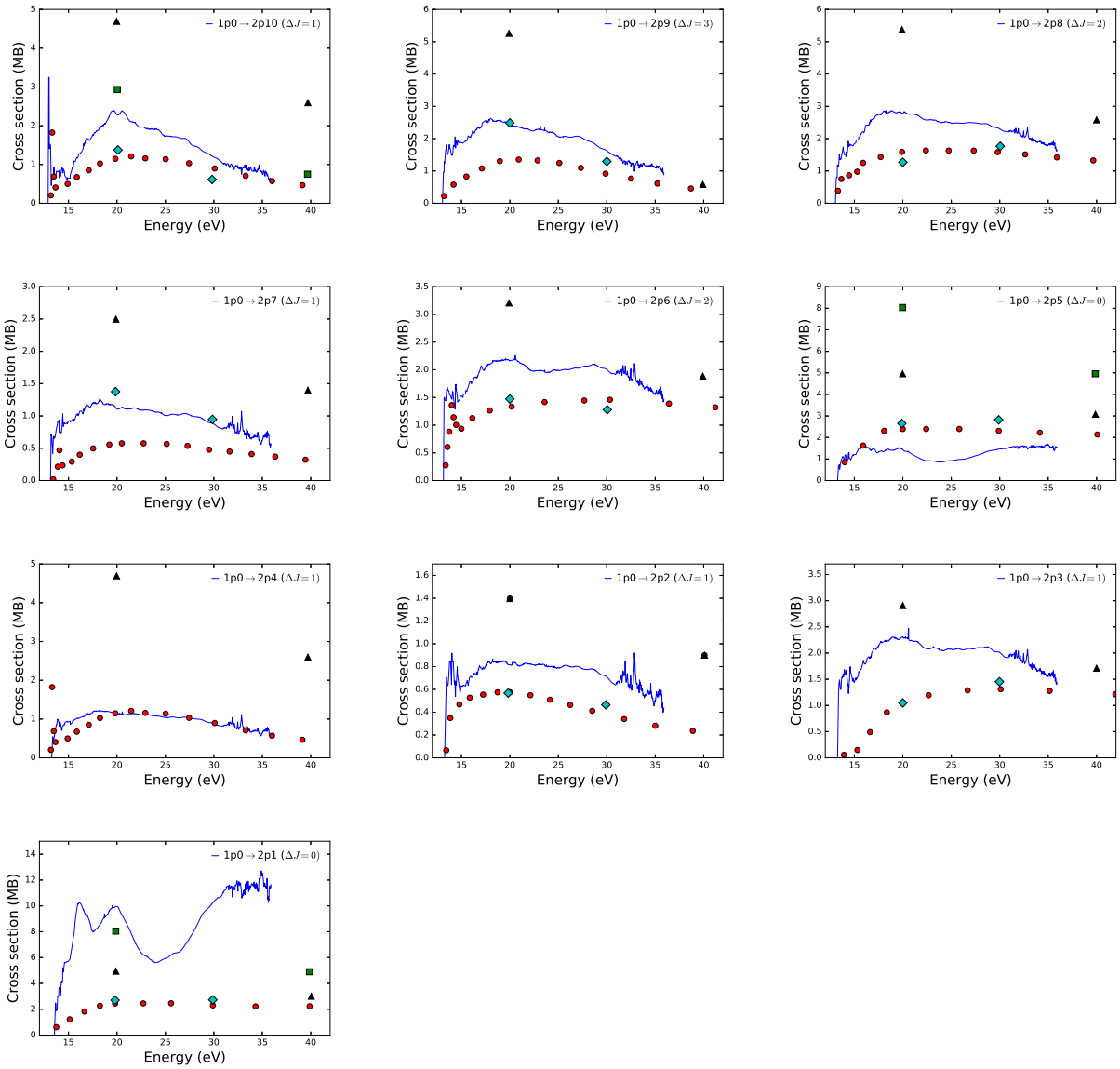

Figure 2.3: Direct cross-sections for excitation from the ground state of neutral argon ($1p0$ in Paschen notation) into the ten levels of the $2p$ manifold. The present work is shown as a solid blue line (online color only), circles represent the BSR-500 work of Zatsarinny *et al.* (online color: blue). Experimental cross-section data from Chilton *et al.* (black triangles), Filopović (green squares), and Chutjian and Cartwright (cyan diamonds) are also shown.

As can be seen, there is a general agreement with existing theoretical results for most of the transitions. The experimental data displays a large variance, but in general our results most closely match the experimental measururements of Chutjian and Cartwright. This is the same trend noted by Zatsarinny in his analysis of existing experimental data.

We repeat our analysis in Figure 2.4 for the four levels of the $1s$ manifold. We again compare with the BSR-500 results of Zatsarinny, as well as the experimental data from Chutjian and Cartwright, and Filopović. We also compare with the experimental results of Khakoo *et al.* [50] and Hoshino *et al.* [45]. In general, our results show good agreement with previous theoretical calculations, and again most closely match Chujtian and Cartwright, though we also show excellent agreement with the newer measurements provided by Hoshino *et al.*. To our knowledge, no experimental cascade data or detailed excitation functions are available for these levels.

As noted by other authors [82, 50], the measurements made by Chilton *et al.* tend to overestimate the excitation cross-sections beyond the limits of the error bars described in their paper ($\approx$35%), possibly due to an error in the absolute calibration of their equipment. However, the excitation functions presented by Chilton for all levels of the $2p$ manifold are the most detailed to date, and separate the direct contribution from the contribution due to radiative cascades. This allows for direct, qualitative comparison between theoretical and experimental measurements of cascade effects, and of the ratio of the cascade contribution to the direct and apparent cross-sections.

When scaled to account for any potential calibration error, the experimental excitation functions presented by Chilton can be qualitatively compared to our theoretical results. We present this comparison in Figure 2.5. Our results seem to match the trend of the experimental data well in all but one or two cases, specifically the dipole forbidden transitions $1p0 \rightarrow 2p1$ and $1p0 \rightarrow 2p5$. In all other cases we can predict whether cascades will dominate over direct contributions, and at what approximate energy this will occur. This serves to validate the accuracy of our cascade cross-section data for these levels.

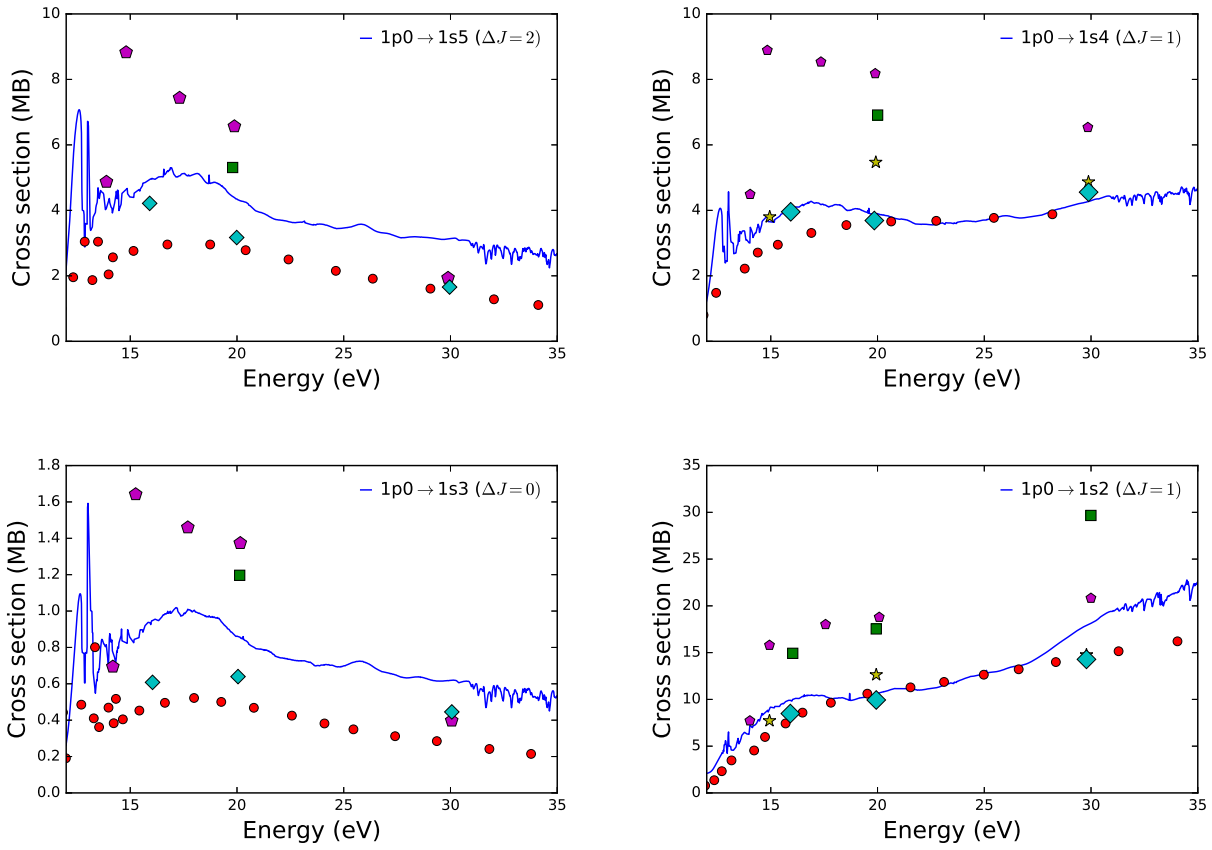

Figure 2.4: Direct cross-sections for excitations from the ground state of neutral argon ($1p0$ in Paschen notation). The present work is shown as a solid blue line (online color only), circles represent the BSR-500 work of Zatsarinny *et al.* (online color: blue). Experimental cross-section data from Filopović (green squares), Khakoo (magenta pentagons), Hoshino *et al.* (yellow stars), and Chutjian and Cartwright (cyan diamonds) are also shown.

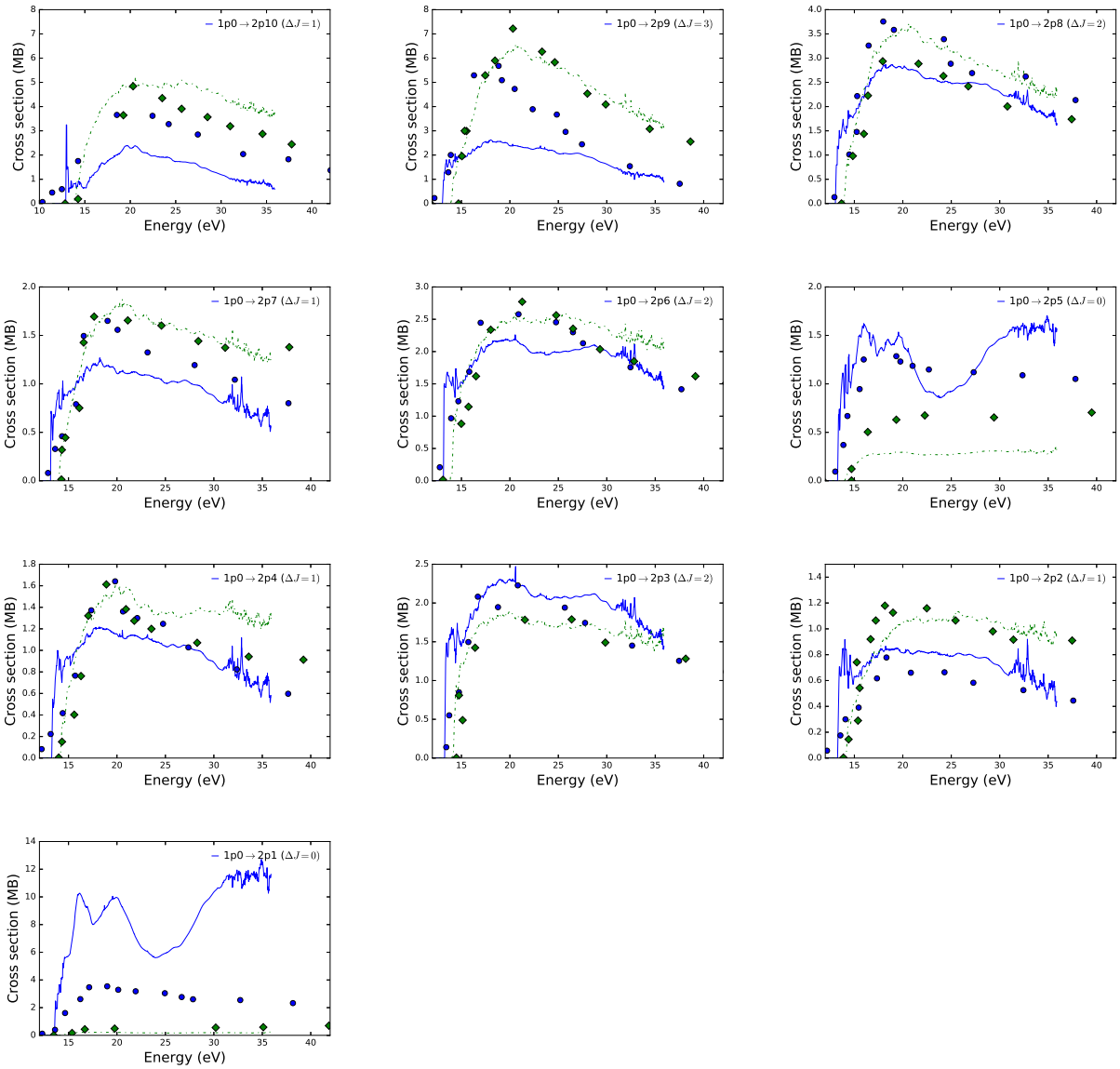

Figure 2.5: Direct and cascade cross-sections for excitations from the ground state of neutral argon. Our direct cross-sections are shown as a solid blue line (online color only), while cascade cross-sections are shown in dashed green. The experimental results have been scaled to allow for a qualitative comparison.

2.3.2 Excitation from metastable states.

In this section we extend our analysis to excitation from the long-lived $1s5$ and $1s3$ metastable states. Even though the relative population of these states is usually low, on the order of $\approx 1\times10^{-4}$ when compared with the ground state population, excitation from these states can dominate the emission of low-temperature argon plasmas, due to the low excitation threshold of transitions from these states. Less than 2 eV is required to excite either metastable state into the $2p$ manifold; more than 11 eV is required for the ground state. Given the proliferation of basic plasma experiments that both use argon and have electron temperatures less than 10 eV, a detailed knowledge of emission from metastable states is critical. The extent of currently available theoretical data is limited, and to our knowledge this is the first fully level-resolved theoretical calculation to examine the role of radiative cascades in the apparent cross-sections resulting from metastable excitation.

In Figures 2.6 and 2.7 we present theoretical direct excitation cross-sections from both the $1s5$ and $1s3$ metastable states. We show the direct cross-section, the cross-section resulting from radiative cascades, and their sum, the apparent cross-section. For comparison, we also show the theoretically calculated 41 state R-Matrix (RM41) direct cross-sections from Bartschat and Zeman [11]. Experimental data from Piech *et al.* [66], as presented in the paper by Bartschat and Zeman, is also shown. It should be noted that the Piech *et al.* data is for the *apparent* cross-section. Piech *et al.* used both a thermal beam and a fast beam apparatus to obtain data. Error bars are again omitted for clarity, but are of the same order as the Chilton data ($\approx 35\%$) and again dominated by error in absolute calibration.

Overall, a comparison of our direct cross-sections with those of Bartschat and Zeman shows excellent agreement. They note that their data tends to overestimate the cross-sections for core changing ($^2P_{3/2} \rightarrow^2 P_{1/2}$) transitions, specifically $1s5 \rightarrow 2p4$, $1s5 \rightarrow 2p3$, $1s5 \rightarrow 2p2$. In the first case, our direct cross-sections are significantly smaller than Bartschat and Zeman's, and seem to match the experimental data more closely. However, in the second

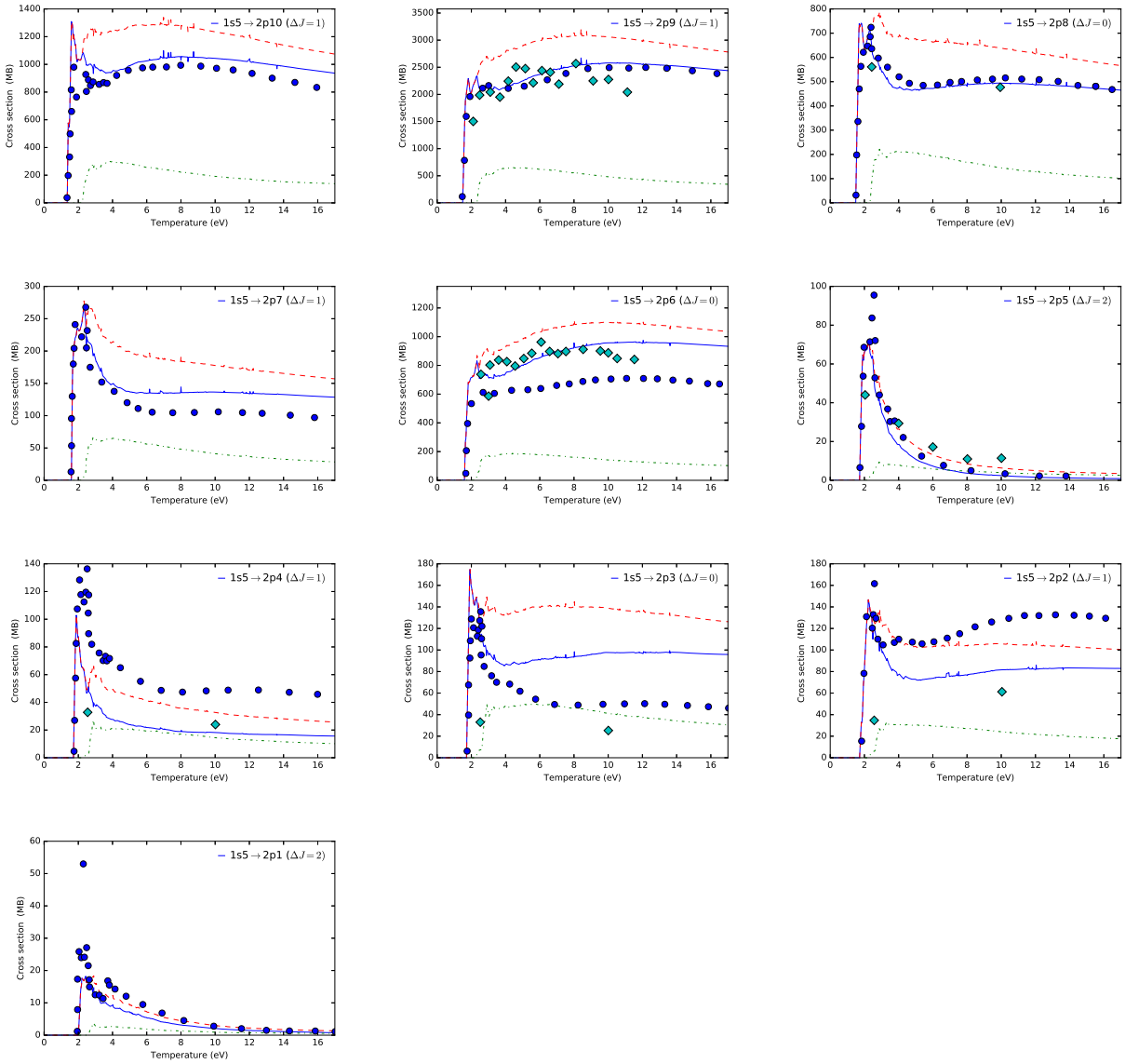

Figure 2.6: Theoretical cross sections for excitation from the $1s5$ metastable state of neutral argon, compared with the 41 state R-Matrix calcualation of Bartschat and Zeman. The direct cross-section is shown as both circles (Bartschat and Zeman) and as a solid line (present work). The dashed line (online color:red) shows the apparent cross-section. The dot-dashed line (online color: green) shows the cascade contribution to the apparent cross-section. Where available, the experimental apparent cross-section measurements of Piech *et al.* are shown as cyan diamonds.

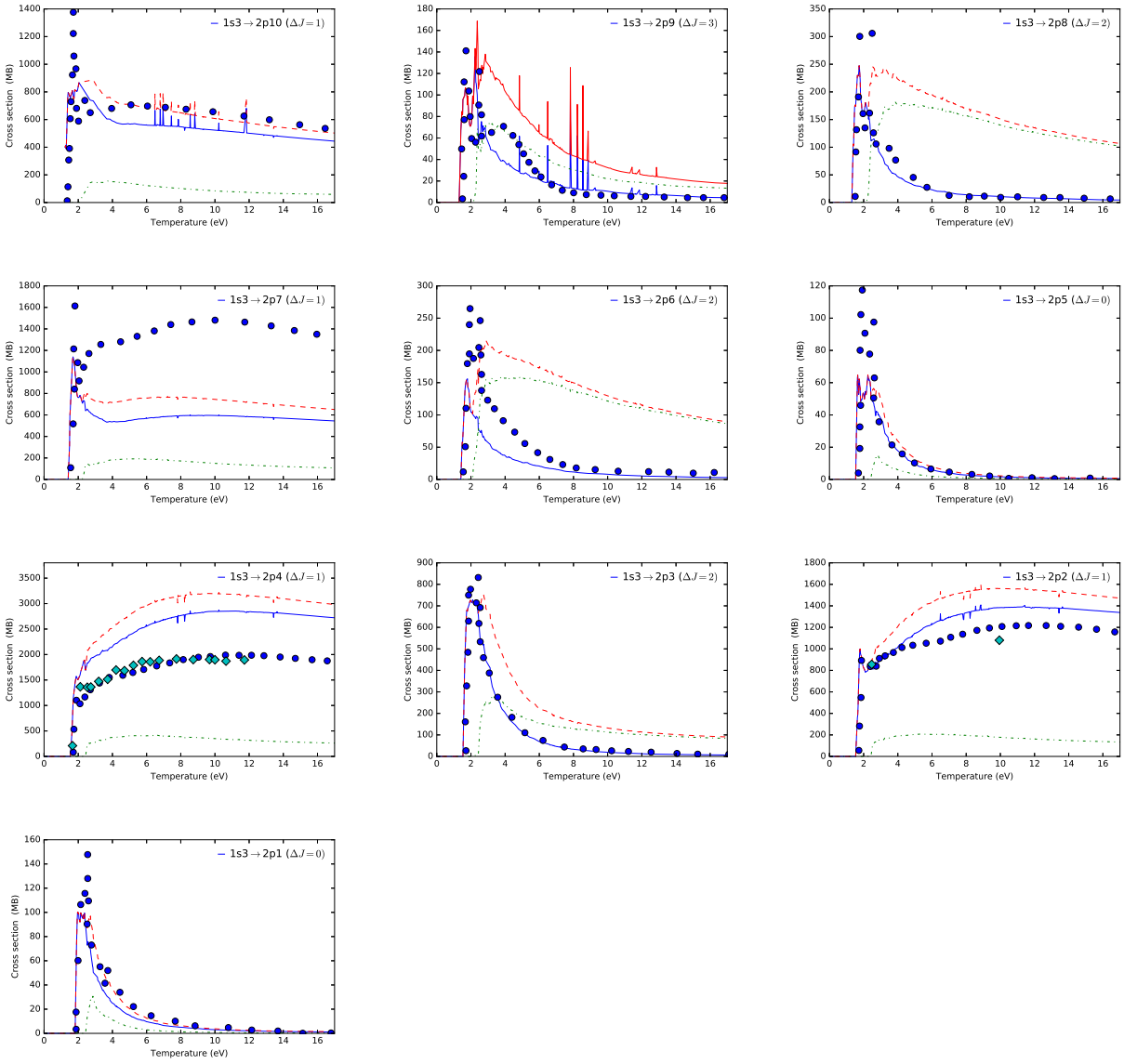

Figure 2.7: Theoretical cross sections for excitation from the $1s3$ metastable state of neutral argon, compared with the 41 state R-Matrix calcualation of Bartschat and Zeman. The direct cross-section is shown as both circles (Bartschat and Zeeman) and as a solid line (present work). The dashed line (online color:red) shows the apparent cross-section. The dot-dashed line (online color: green) shows the cascade contribution to the apparent cross-section. Where available, the experimental apparent cross-section measurements of Piech *et al.* are shown as cyan diamonds.

case our data is significantly higher, and shows worse agreement. In the final case, our data matches Bartschat and Zeman's closely, and no experimental data is available.

Comparing our data to the experimental cross-sections of Piech *et al.* is less straightforward. First, it must be noted that the Piech *et al.* data is a measurement of the *apparent* cross-section, and includes contributions from radiative cascades. Consequently, it should be compared to our theoretically calculated apparent cross-sections, represented in Figures 2.6 and 2.7 as dot-dashed lines (online color:red). However, it is clear from these figures that the Piech *et al.* apparent cross-sections most closely match the *direct* cross-sections from both Bartschat and Zeman (circles, online color:blue) and the present work (solid blue line). Previously this was seen as a validation of the claim by the Wisconsin group that the cascade contribution for excitation from metastable states into all levels in the $2p$ manifold was small, which implies that the direct and apparent cross-sections are effectively identical. To arrive at this conclusion the Wisconsin group measured the fluorescence from just two transitions. The first measurement was of the $1s5 \rightarrow 2p9$ transition, for which the cascade contribution to the resulting apparent cross-section was determined to be less than 20%. The second measurement was of the $1s5 \rightarrow 2p6$ cascade contribution, determined to be less than 10%. The cascade contribution for all other apparent cross-sections in the $2p$ manifold was deemed similarly small by extension.

Our theoretical data tend to disagree with this assessment. In most cases our results predict that the cascade contribution to the apparent cross-section is greater than 20%. In some extreme instances involving excitation from the $1s3$ metastable, cascade contributions dominate at higher energies. The Wisconsin group made no measurements of cascade contributions involving direct excitations from the $1s3$ level. While our results seem to confirm the claim that the $1s5 \rightarrow 2p9$ cascade contribution is larger than the $1s5 \rightarrow 2p6$, one of our calculated cascade cross-sections are larger than the upper bounds imposed by the measurements of the Wisconsin group. All of this would tend to indicate that cascade cross-sections

contribute to apparent metastable cross-sections in neutral argon more significantly than previously predicted.

While we have no conclusive explanation for these discrepancies, we can propose some potential scenarios that might account for them. We note that in all cases the experimental data underestimates our theoretical predictions, and that the experimental apparatus has the same potential for calibration error that was present in the Chilton ground state excitation data. In this case, scaling the experimental data by an appropriate factor would solve most problems. It is also possible that our data, along with the data presented by Bartschat and Zeman, overestimates the cross-sections, which could also be addressed by the introduction of some scaling parameter. Finally, it is possible that our calculation of the contribution of radiative cascades is simply wrong, and overestimates the cascade contribution significantly. On this last point we would note the success of our methods to accurately model most of the qualitative behavior of the ground-state cross-sections of Chilton *et al.*

2.4 Conclusion

We have calculated direct, cascade, and apparent cross-sections for excitation from the ground and long-lived metastable states of neutral argon into all levels of the $2p$ manifold. We focus on the $2p$ manifold because of the ready availability of experimental data for comparison, but it should be noted that it is possible to calculate direct cross-sections for all transitions in our dataset, which includes spectroscopic levels up to $5p$ (not a Paschen designation, here we mean $n = 5, l = 1$), and cascade and apparent cross-sections for any transition whose cascade contribution can be well approximated by radiation from the remaining levels in our dataset above its upper level.

The agreement between our data and the data of previous authors is generally very good. Our ground-state data tends to agree well with the ground-state excitation data of Chutjian and Cartwright, and Hoshino et al. We also are able to predict many of the qualitative features of the direct and cascade cross-sections described by Chilton et al. We

concur with previous authors that the Chilton data may overestimate the peak values of the cross-sections, potentially due to errors in the absolute calibration of their equipment.

We also show excellent agreement with the direct theoretical metastable cross-sections of Bartschat and Zeman. While our data tends to agree with the general shape and qualitative features of the experimental metastable apparent cross-section data of Piech *et al.*, our data disagrees with the Piech *et al.* estimation of the cascade contribution. We find that the contribution from radiative cascades to the apparent cross-section is much greater than previously estimated.

In Chapter 4 we will to use the results from this calculation to model line emission from low-temperature (< 10 eV) argon plasmas, in an effort to develop new non-invasive spectroscopic plasma diagnostics capable of measuring electron temperature and density. This can be extended to consider plasmas operating under high magnetic fields, where standard probe-based diagnostics behave erratically. This data could also prove useful to researchers needing detailed information of the role of metastable states in neutral argon plasmas.

Chapter 3

Dielectronic recombination of low charge states of argon.

3.1 Introduction

The study of atomic processes in plasmas has long been an important diagnostic tool for laboratory, fusion [47], industrial, and astrophysical plasmas [70, 55]. Atomic processes can be used to obtain insights on the density, temperature, charge state, and transport of charged and neutral atoms in the plasma. However, in order to use atomic processes as a plasma diagnostic, it is necessary to have reliable models of rate coefficients for these processes. The focus of this paper is on the dielectronic recombination (DR) data for argon. Fully level resolved DR rate coefficients are available for higher charge states ($> Ar^{4+}$), where the system is ionized to the point that electron-electron interactions can be neglected or approximated. Such data has been calculated as part of the DR Project [7, 14, 2, 62, 2, 81, 1], and using the Flexible Atomic Code (FAC) [43]. However, for the lower charge states of argon, many challenges remain, and the available data for Ar^{+}—Ar^{4+} is not fully level resolved.

Beyond the applications to basic and industrial plasmas, understanding atomic processes in the low temperature regions of fusion plasmas is also critical. The hot "core" plasma is coupled to the material, "first wall", through a lower temperature edge region. Because of the strong coupling between the edge region and core plasma, it is possible to manipulate the conditions of the edge plasma to affect and possibly control the conditions of the core plasma. For example, massive gas injection (MGI) has been proposed as a leading candidate for the mitigation of disruptions in large scale tokamak fusion reactors, such as ITER [54]. MGI is being studied at several facilities worldwide, including Alcator C-Mod [78], DIII-D [44], MAST [76], JET [54], TEXTOR [20], ASDEX [64], and NTSX-U [69]. In MGI, neutral noble gas is injected into a plasma during a disruption. These gases are subject to extreme

temperature gradients, and progress from neutral to fully ionized on timescales less than 10 ms [69, 71]. These drastic temperature gradients, coupled with the rapid ionization of noble gas, lead to the formation of a highly non-equilibrium plasma. Argon is a leading candidate for MGI [54, 20, 71, 44], and the accurate determination of ionization and recombination rate coefficients for the low charge states of argon is critical for MGI applications.

The low charge states of argon are also commonly observed in astrophysical systems, such as solar spectra [58] and H II regions [49]. The recombination rate coefficients for low charge states of argon are key in determining elemental abundances in such plasmas [58]. As will be shown below, DR rate coefficients for these low charge states of argon are currently not well known.

In light of these observations, for a wide range of plasma applications, there is a critical need for accurate atomic rate coefficients for low charge states of argon. Dielectronic recombination is often the dominant recombination process in photoionized and electron-collisional plasmas [22, 8]. Unfortunately, accurate, comprehensive level-resolved DR rates for low charge states of argon, those below Ar^{5+}, are missing from the literature. Currently, the most comprehensive available data for these ion stages is the configuration-averaged distorted wave (CADW) rates presented by Loch [57], and the rate coefficients presented by Mazzotta [59], based on the empirical formula of Burgess [22]. Mazzotta's rates are still in widespread use in the astrophysical and plasma modelling community, even though these rate coefficients are known to be accurate only at high temperatures (Savin et al. 2006). Our goal is to present fully level-resolved partial and total DR rates for low charge states of argon in order to fill the gap in the currently available atomic data. This is necessary in order to accurately model relevant atomic processes (i.e. ion fractional abundance) in non-equilibrium argon plasmas, which can be dominated by neutral and near-neutral ion stages.

The remainder of this paper is structured as follows: In the next section we describe our method for calculating DR rate coefficients and present our atomic structure results. In

Section 3 we present our rate coefficients and a comparison to results from previous literature. Section 4 presents a discussion of the results and an analysis of the implications our new rates can have on equilibrium fractional abundances. In Section 5 we present a summary and discuss future efforts.

3.2 Methods

3.2.1 Dielectronic Recombination: Theory

For our results, the methodology for the calculation of DR rate coefficients follows the procedure detailed by Badnell[8]. What follows is a summary. We calculate DR rate coefficients with AUTOSTRUCTURE [6], which makes use of the Independent-Processes and Isolated-Resonances using Distorted Waves (IPIRDW) method, the validity of which is detailed by Pindzola [67]. The role DR plays in photoionized and collisional plasmas has been thoroughly discussed in the literature [22, 60, 59, 5].

DR occurs when a continuum electron combines with an ion to form an intermediate doubly excited state.

$$X^{+(z+1)}(nl) + e^- \leftrightarrow [X^{+z}(n'l'; n''l'')] \rightarrow X^{+z}(n'''l'''; n''l'') + h\nu \tag{3.1}$$

$$\rightarrow X^{+z}(n'l'; n'''l''') + h\nu \tag{3.2}$$

The intermediate term $[X^{+z}(n'l'; n''l'')]$ in Equation 3.2 represents the capture of a free electron into a doubly excited resonance. Note that the first process (3.1) is a radiative decay of a core (excited) electron, and the second (3.2) is a decay of the valence (captured) electron.

The partial DR cross section from an initial metastable state v of an ion $X^{+(z+1)}$, through an autoionizing state j, into a final state f of an ion X^{+z} is given by Badnell [5] as:

$$\sigma^{j}_{f\nu} = \hat{\sigma}^{j}_{f\nu} L^{j}(E)_{j} \tag{3.3}$$

where:

$$L^{j}(E)_{j} = \frac{\Gamma_{j}/2\pi}{(E - E_{j}) + \Gamma^{2}/4} \tag{3.4}$$

is the Lorentzian line shape of position E_j and width Γ_j, and:

$$\hat{\sigma}^{j}_{f\nu} = \frac{(2\pi a_0 I_H)^2}{E_c} \frac{\omega_j}{2\omega_\nu} \tau_0 \frac{\sum_l A^a{}_{j\to\nu,E_c l} A^r_{j\to f}}{\sum_h A^r_{j\to h} A^u_{j\to m,E_c l}} \tag{3.5}$$

is the integrated partial DR cross section, where ω_j is the statistical weight of the doubly-excited resonance state j of the $N+1$ electron, ω_v is the statistical weight of the N electron initial state, and the auto-ionization and recombination rates (A^a) and (A^r) are given in s^{-1}. E_c is the energy of the continuum electron of orbital angular momentum l. I_H is the standard ionization energy of the hydrogen atom, in the same units as E_c, and $2\pi a_0 \tau_0 \equiv 2.6741 \cdot 10^{-32}\ \ cm^2 \cdot s$.

Equation 3.3 allows an analytic integration over the appropriate resonance profiles, as opposed to a numerical integration as required by R-matrix and other methods. This is a primary strength of the IPIRDW method.

3.2.2 Calculation of atomic structure and rate coefficients.

Atomic structure calculation

Accurate atomic structure is the foundation of any dielectronic recombination calculation. Using the Graphical AUTOSTRUCTURE Package (GASP) [10], we adjusted the orbital

scaling parameters for AUTOSTRUCTURE to improve the agreement between the calculated energies and NIST energies [51] for the recombining ion. In Table 3.1 we list our orbital scaling parameters for each of the argon ions considered here. For the recombined ion we will shift our core-excited energies to NIST values prior to post-processing the AUTOSTRUCTURE data. Table 3.2 shows the first ten energy levels for the recombining ion, for all ion stages, compared with their NIST values. In general, agreement is good, with average percent difference relative to the accepted NIST energy over the first ten levels at or below 6.34% for each ion. Since we shift our core-excited energies to NIST values, the percent difference given in Table 3.2 provides a measure of the shifts we employed. Table 3.3 lists the basis set of configurations used for all ion stages.

Table 3.1: Orbital type and scaling parameters for ion stages Ar^{+}-Ar^{4+}. These values were used in both our structure calculation and DR runs. TFDA indicates Thomas-Fermi-Dirac-Amaldi orbital potentials, which we used exclusively. Any λ_{nl} value not explicitly stated can be assumed to be the default value of 1.0000.

Ion Stage	Orbital Type	λ_1	λ_2	λ_3	λ_4	λ_5	λ_6	λ_7
Ar^{+}	TFDA	1.0000	1.0000	1.1092	1.1200	1.1500	1.0000	1.0000
Ar^{2+}	TFDA	1.0000	1.0000	1.1760	1.0700	1.1100	1.0000	1.0000
Ar^{3+}	TFDA	1.0000	1.1000	1.0500	1.1175	1.0700	1.1100	0.9000
Ar^{4+}	TFDA	1.0000	1.0000	1.0300	1.0873	1.1400	1.0000	1.0000

Table 3.2: The first ten energy levels above the ground state for each ion stage presented, compared to their corresponding NIST standard values. Percent differences are shown relative to NIST values. All energies are in eV.

Ar^{+}	Present Work	NIST Energy	% Difference
$3s^2 3p^5\ (^2P^o_{1/2})$	0.231914	0.177493	30.7
$3s3p^6\ (^2S_{1/2})$	14.025105	13.479520	4.04
$3s^2 3p^4 3d\ (^2D_{7/2})$	16.533358	16.406501	0.77
$3s^2 3p^4 3d\ (^2D_{5/2})$	16.554746	16.425575	0.79
$3s^2 3p^4 3d\ (^2D_{3/2})$	16.577074	16.444113	0.81
$3s^2 3p^4 3d\ (^2D_{1/2})$	16.593795	16.457377	0.83

$3s^2 3p^4 4s\ (^4P_{5/2})$	17.600721	16.644233	5.75
$3s^2 3p^4 4s\ (^4P_{5/2})$	17.717950	16.748528	5.79
$3s^2 3p^4 4s\ (^4P_{5/2})$	17.793009	16.812471	7.69
$3s^2 3p^4 4s\ (^2P_{3/2})$	18.031237	17.140026	5.12
		Average Difference	6.23

Ar^{2+}	Present Work	NIST Energy	% Difference
$3s^2 3p^4\ (^3P_1)$	0.141657	0.137891	2.73
$3s^2 3p^4\ (^3P_0)$	0.201049	0.194684	3.27
$3s^2 3p^4\ (^1D_2)$	1.952476	1.737109	12.40
$3s^2 3p^4\ (^1s_0)$	4.320608	4.124420	4.76
$3s3p^5\ (^3P_2^o)$	14.680730	14.109466	4.05
$3s3p^5\ (^3P_1^o)$	14.808724	14.233061	4.04
$3s3p^5\ (^3P_0^o)$	14.875263	14.298849	4.03
$3s3p^5\ (^1P_1^o)$	19.083367	17.856499	6.87
$3s^2 3p^3 3d\ (^5D_1^o)$	19.184392	17.963507	6.80
$3s^2 3p^3 3d\ (^5D_2^o)$	19.185140	17.964154	6.80
		Average Difference	6.34

Ar^{3+}	Present Work	NIST Energy	% Difference
$3s^2 3p^3\ (^2D_{3/2}^o)$	2.977781	2.614940	13.9
$3s^2 3p^3\ (^2D_{5/2}^o)$	2.992544	2.630920	13.7
$3s^2 3p^3\ (^2P_{1/2}^o)$	4.758861	4.321142	10.1
$3s^2 3p^3\ (^2P_{3/2}^o)$	4.775964	4.343460	9.95
$3s3p^4\ (^4P_{5/2})$	14.750822	14.576000	1.20
$3s3p^4\ (^4P_{3/2})$	14.862745	14.694070	1.15
$3s3p^4\ (^4P_{1/2})$	14.926407	14.759460	1.13
$3s3p^4\ (^2D_{5/2})$	18.787736	18.091920	3.84

$3s3p^4\ (^2D_{3/2})$	18.796049	18.10162	3.84
$3s^23p^23d\ (^2P_{3/2})$	21.569795	20.62556	4.58
		Average Difference	5.58

Ar^{4+}	Present Work	NIST Energy	% Difference
$3s^23p^2\ (^3P_1)$	0.102616	0.094629	8.44
$3s^23p^2\ (^3P_2)$	0.273426	0.251534	8.70
$3s^23p^2\ (^1D_2)$	2.319142	2.020776	14.8
$3s^23p^2\ (^1S_0)$	4.857763	4.700540	3.24
$3s3p^3\ (^5S_2^o)$	10.155219	10.427940	2.62
$3s3p^3\ (^3D_1^o)$	15.102034	15.080040	0.14
$3s3p^3\ (^3D_2^o)$	15.008098	15.085780	0.52
$3s3p^3\ (^3D_3^o)$	15.124864	15.101660	0.15
$3s3p^3\ (^3P_2^o)$	17.657050	17.576320	0.45
$3s3p^3\ (^3P_1^o)$	17.658696	17.577300	0.46
		Average Difference	3.96

Table 3.3: Basis configurations for all four ion stages. The notation 4(s—f) is meant to represent the set of configurations that contain one electron in each of the 4s, 4p, 4d and 4f orbitals.

Ion Stage	Basis Configurations
Ar^{+}	$3s^2 3p^5$; $3s^2 3p^4 3d$; $3s^2 3p^4 4(s—f)$
16 configurations	$3s 3p^5 3d$; $3s^2 3p^3 3d^2$; $3s^3 p^5 4(s—f)$
	$3s 3p^6$; $3p^6 3d$; $3p^5 3d^2$; $3s 3p^4 3d^2$
Ar^{2+}	$3s^2 3p^4$; $3s^2 3p^3 3d$; $3s^2 3p^3 4(s—d)$
15 configurations	$3s 3p^5$; $3s 3p^4 3d$; $3p^4 3d^2$; $3s 3p^3 3d^2$
	$3s 3p^4 4(s—d)$; $3p^6$; $3p^5 3d$; $3s^2 3p^2 3d^2$
Ar^{3+}	$3s^2 3p^3$; $3s^2 3p^2 3d$; $3s^2 3p^2 4(s—f)$; $3s 3p^4$
24 configurations	$3s 3p^3 3d$; $3s 3p^3 4(s—f)$; $3s^2 3p 3d^2$; $3s^2 3p 3d 4s$
	$3s^2 3p 4s^2$; $3s 3p^2 3d^2$; $3s 3p^2 3d 4s$; $3s 3p^2 4s^2$
	$3p^5$; $3p^4 3d$; $3p^4 4s$; $3p^3 3d^2$; $3p^3 3d 4s$; $3p^3 4s^2$
Ar^{4+}	$3s^2 3p^2$; $3s^2 3p 3d$; $3s^2 3p 4(s—f)$; $3s^2 3d^2$
24 configurations	$3s^2 3d 4(s—f)$; $3s^2 4s 4(p—f)$; $3s^2 4p 4(d—f)$
	$3s 3p^2 3d$; $3s 3p^2 4(s—p)$; $3s 3p^3$; $3s 3p 3d^2$
	$3s 3p 3d 4d$; $3p^4$; $3p^3 3d$

Calculation of DR rate coefficients

We use AUTOSTRUCTURE to perform LS-coupling and (Breit-Pauli) intermediate coupling calculations of DR rate coefficients and cross sections for Ar^{+}—Ar^{4+}. In addition, we also calculate rate coefficients for Ar^{5+} (aluminium like argon) in order to compare with the previously published level-resolved calculations of Abdel-Naby [1]; this comparison is shown in Figure 3.1. The previous work used similar methods, and serves as a benchmark for our calculations, though there are some important differences in our methodology. Note that we used a different set of basis configurations, and different orbital scaling parameters. We also used Thomas-Fermi-Dirac-Amaldi (TFDA) orbital potentials; the previous work exclusively used Slater type orbital potentials. Furthermore, the previous work did not shift energy values to NIST standards prior to post-processing. Even with these differences in our approach, we match the previously published rate coefficient with an average percent difference of approximately 10% from peak through tail. By way of comparison, we will show

in later sections that differences between our rate coefficients and configuration-averaged, distorted wave (CADW) or semi-empirical methods can vary by more than an order of magnitude.

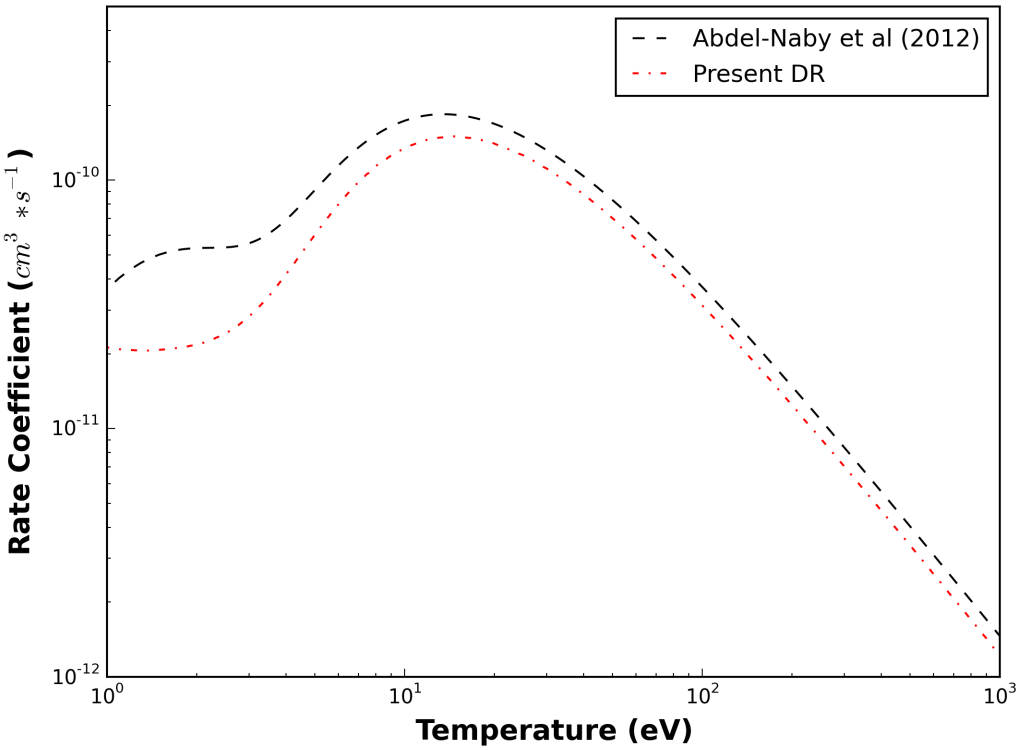

Figure 3.1: Our total ground-state DR rate coefficient for Ar^{5+}. We compare our results (dot-dashed; online color = red) to those presented in Abdel-Naby [1] (dashed; color = black)

For each ion stage Ar^{+}—Ar^{4+}, we calculate cross-sections and rate coefficients for all ground and metastable levels within the ground state configuration of the initial ion. The appropriate metastable set can then be chosen for the particular plasma conditions. For the case of Ar^{+}, this leads to two separate rates, one each for the ground level ($^2P^o_{3/2}$) and first excited metastable level ($^2P^o_{1/2}$). The number of rates for each ion stage is summarized in Table 3.4. In addition to level-resolved rate coefficients, we have calculated term resolved DR rate coefficients for each ion.

Table 3.4: Potential metastable levels within the ground state configuration for each of the four ion stages presented.

Ar^{+} *(2 levels)*	Ar^{2+} *(5 levels)*	Ar^{3+} *(5 levels)*	Ar^{4+} *(5 levels)*
$3s^2 3p^5\ (^2P^o_{3/2})$	$3s^2 3p^4\ (^3P_2)$	$3s^2 3p^3\ (^4S^o_{3/2})$	$3s^2 3p^2\ (^3P_0)$
$3s^2 3p^5\ (^2P^o_{1/2})$	$3s^2 3p^4\ (^3P_1)$	$3s^2 3p^3\ (^2D^o_{3/2})$	$3s^2 3p^2\ (^3P_1)$
	$3s^2 3p^4\ (^3P_0)$	$3s^2 3p^3\ (^2D^o_{5/2})$	$3s^2 3p^2\ (^3P_2)$
	$3s^2 3p^4\ (^1D_2)$	$3s^2 3p^3\ (^2P^o_{1/2})$	$3s^2 3p^2\ (^1D_2)$
	$3s^2 3p^4\ (^1S_0)$	$3s^2 3p^3\ (^2P^o_{3/2})$	$3s^2 3p^2\ ^1S_0$

The basis configurations from our atomic structure run, listed in Table 3.3, become our target configurations for the purpose of the DR calculation. It is implicit that either an additional Rydberg orbital or a continuum orbital of varying l shall be attached to these basis configurations. In addition, we account for a set of allowed final configurations. These configurations are obtained by allowing the captured and excited electrons to radiate into subshells with n = 3,4.

For all ion stages, we account for both dipole and quadrupole radiative transitions, though we expect the contributions from the quadrupole transitions to be small. Rydberg-Rydberg hydrogenic radiative rates are calculated during post-processing. For the Rydberg electron, we explicitly calculate n = 5—15 and l = 0—9. We employ a simple interpolated approximation to the cross section to account for the higher Rydberg resonances from n = 15—200. The energy mesh for all five ion stages spans from 0 eV through 130 eV. For our level-resolved calculations, we have generated Maxwellian convolved rate coefficients for core excitations from $\Delta n = 0$, $\Delta n = 1$, and a total rate coefficient ($\Delta n = 0$, 1) for each of the metastable states within the ground configuration, where Δn refers to the excitation of the core electron. Due to heavy computational cost, we do not calculate $\Delta n = 2$ core excitations for our level resolved data. However, we have conducted configuration-averaged distorted-wave calculations using AUTOSTRUCTURE to estimate the contribution from $\Delta n = 2$ excitations, and found them negligible. Specifically, for all ion stages considered here, the contribution to the rate coefficient from $\Delta n = 2$ core excitations ($n = 3$ to $n = 5$),

as determined from our configuration-averaged calculations, is 3 to 4 orders of magnitude less than the combined contribution from $\Delta n = 0$ and $\Delta n = 1$ core excitations. All of our Maxwellian rate coefficient data files are in the standard *adf09* format employed by the Atomic Data and Analysis Structure (ADAS) database [74].

Prior to the generation of our Maxwellian resolved rate coefficients, the N+1 resonance energies were shifted to NIST values, with respect to the core excited energies of the N electron system, in order to better match the observed values. Figure 3.2 illustrates the impact of shifting the level energies from the atomic structure calculation to NIST values for the two metastable states in the Ar^+ground state. The difference between the shifted and unshifted calculations can be used to provide a measure of the uncertainty in our results. A suitable error bar is the residual between a pure theoretical DR calculation and one whose energy levels have been shifted to NIST standards. For illustration, we have super-imposed this error bar on the unshifted rate coefficient of Ar^+ in Figure 3.2. We note that below $\approx 10^{-2}$ eV our error becomes large, effectively setting a lower bound for our rate coefficients.

Fitting Coefficients

In addition to Maxwellian rate coefficients, we have calculated net level-resolved DR fitting coefficients for all metastable levels within the ground configuration, in accordance with the formula:

$$\hat{\alpha}_d = \frac{1}{T^{3/2}} \sum_i c_i \exp(\frac{E_i}{T}) \qquad (cm^3 s^{-1}) \tag{3.6}$$

$\hat{\alpha}_d$ is the Maxwellian convolved rate coefficient, T is the temperature in eV, and c_i and E_i are given in Appendix A.

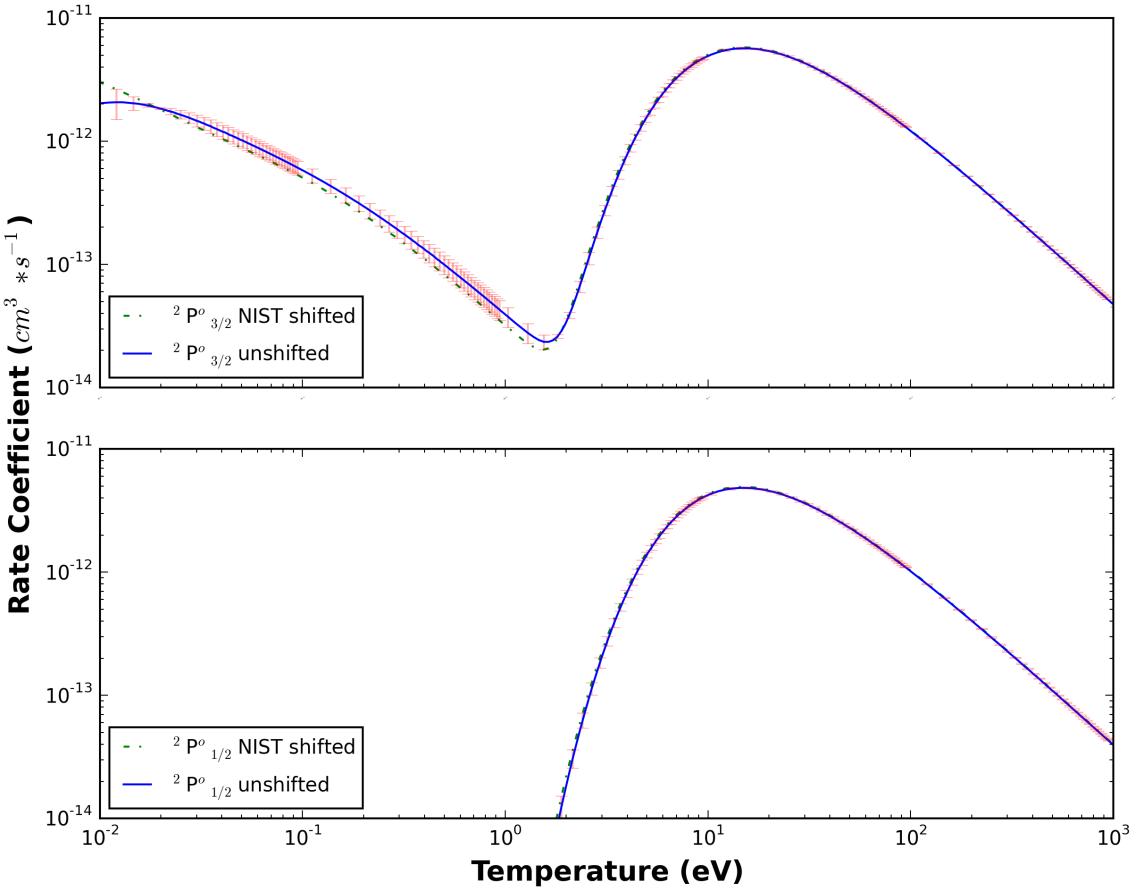

Figure 3.2: The effect of shifting energy terms to corresponding NIST energies on our DR rate coefficients. Rate coefficient shown is for Ar^+. The solid line (online color = blue) shows the unshifted rate coefficient. The dashed line is the shifted coefficient. Error bars (online color = red) represent the difference between a shifted and unshifted DR calculation.

3.3 Results

3.3.1 Maxwellian convolved rate coefficients.

In Figures 3.3—3.6 we present our Maxwellian convolved rate coefficients for ground and metastable levels within the ground LS term. We note that the fitting coefficients in Appendix A cover all possible metastable states within the ground configuration. The rate coefficient for core excitations with $\Delta n = 0$, $\Delta n = 1$, and the total DR rate coefficient ($\Delta n = 0$, 1) are shown separately for each of the four ion stages Ar^{+}—Ar^{4+}. The total rate coefficient (bottom plot in each subplot) is displayed superimposed on the background Lorentzian line resonance profiles, in order to provide an intuitive glimpse of the resonance features contributing to the total DR. For electron collisional plasmas, it should be noted that the peak abundance coincides roughly with the high T peak of the rate coefficient, roughly between 10 and 20 eV for all ion stages presented. Note that we show total ground state DR resonances only.

We present a summary of our new rates in Figure 3.7, which shows total ground level DR rate coefficients for all ion stages (Ar^{+}—Ar^{4+}).

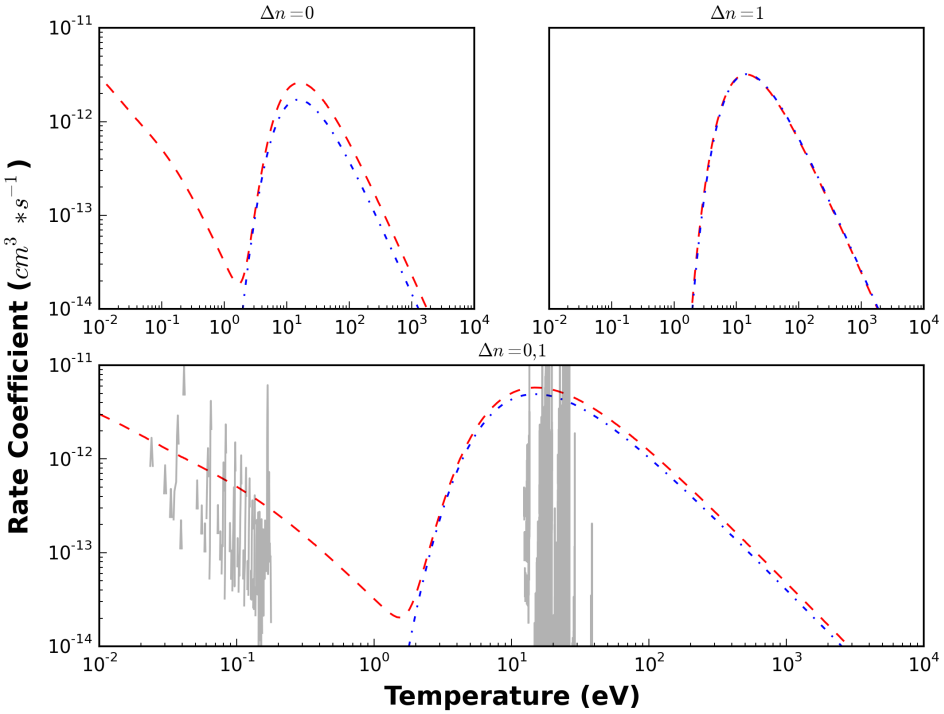

Figure 3.3: Maxwellian convolved DR rate coefficients for Ar^+. The upper left subplot shows the rate coefficient for $\Delta n = 0$, while the upper right shows the rate coefficient for $\Delta n = 1$. The bottom subplot shows their sum, super-imposed on a background displaying the Lorentzian resonance profiles. The ground level data are shown in red (dashed), nd the first excited metastable level is in blue (dot-dashed).

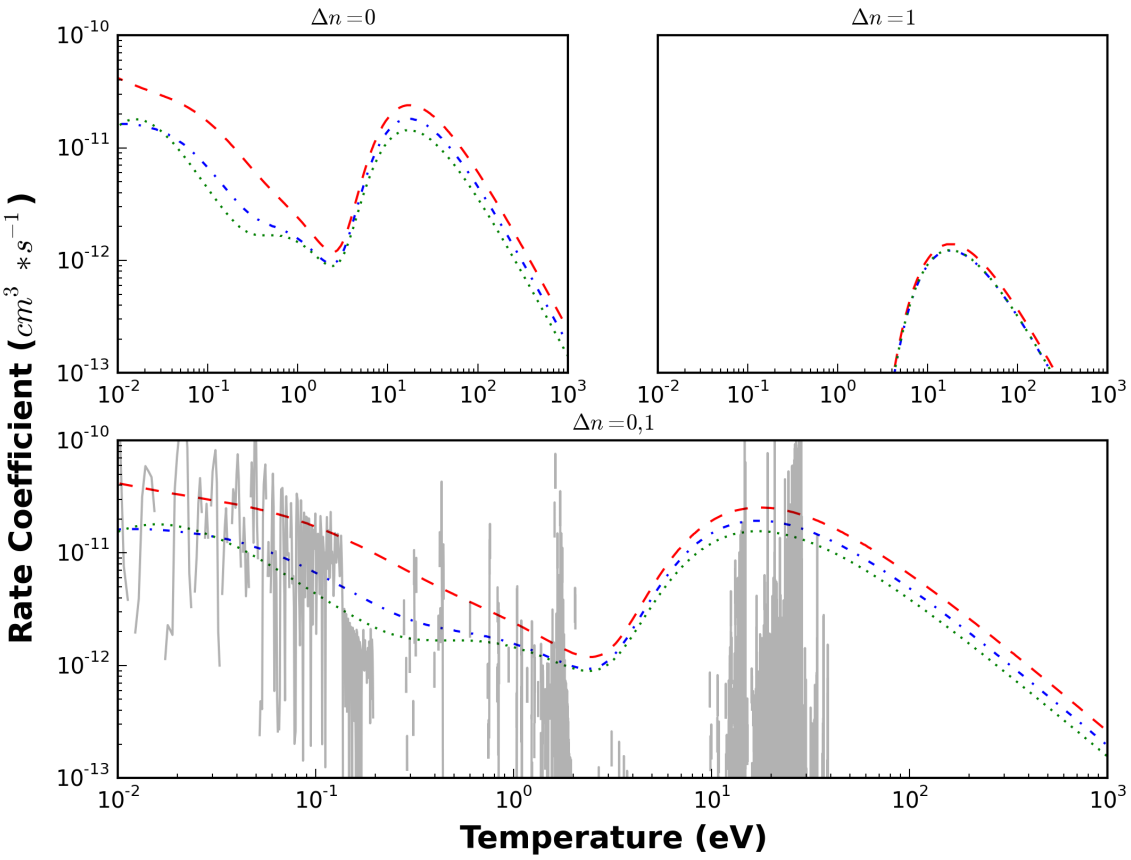

Figure 3.4: Maxwellian convolved DR rate coefficients for Ar^{2+}. The upper left subplot shows the rate coefficient for $\Delta n = 0$, while the upper right shows the rate coefficient for $\Delta n = 1$. The bottom subplot shows their sum, super-imposed on a background displaying the Lorentzian resonance profiles. The ground level data are shown in red (dashed), the first excited metastable level is in blue (dot-dashed), and the second excited metastable level is shown in green (dotted).

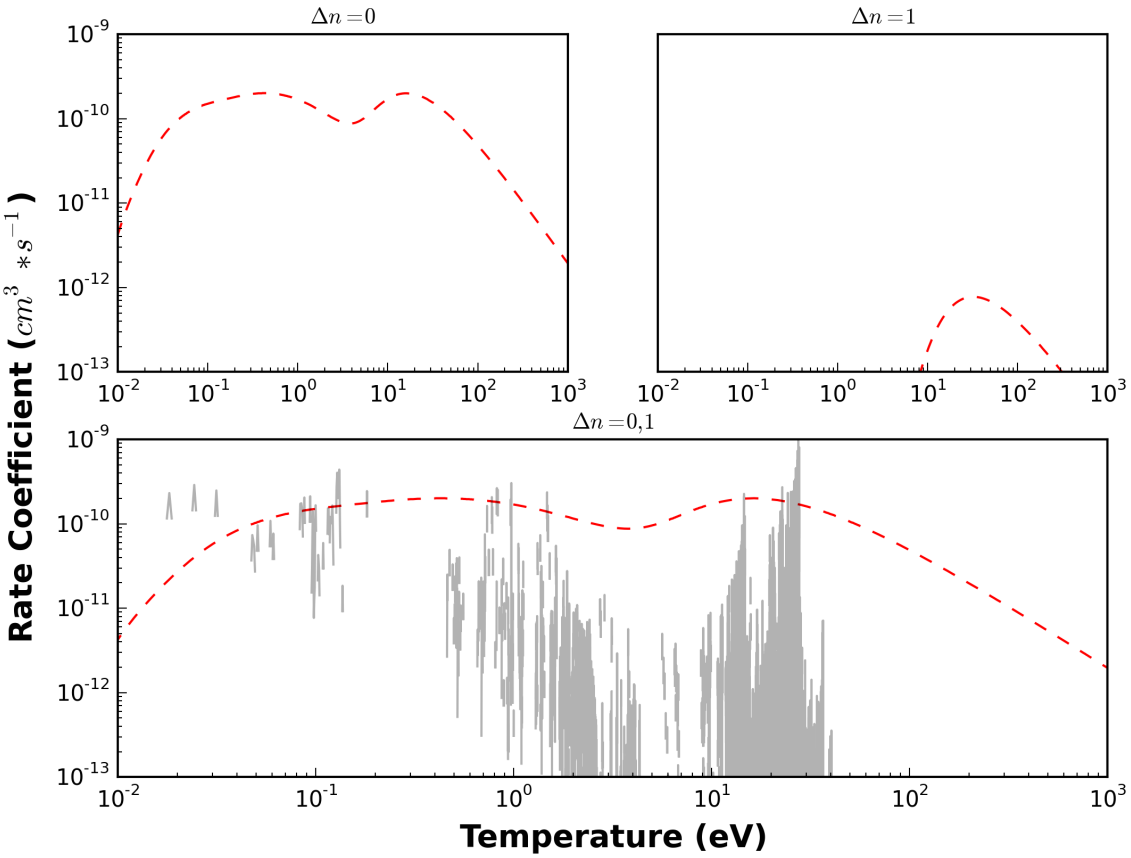

Figure 3.5: Maxwellian convolved DR rate coefficients for Ar^{3+}. The upper left subplot shows the rate coefficient for $\Delta n = 0$, while the upper right shows the rate coefficient for $\Delta n = 1$. The bottom subplot shows their sum, super-imposed on a background displaying the Lorentzian resonance profiles. The ground level data are shown in red (dashed).

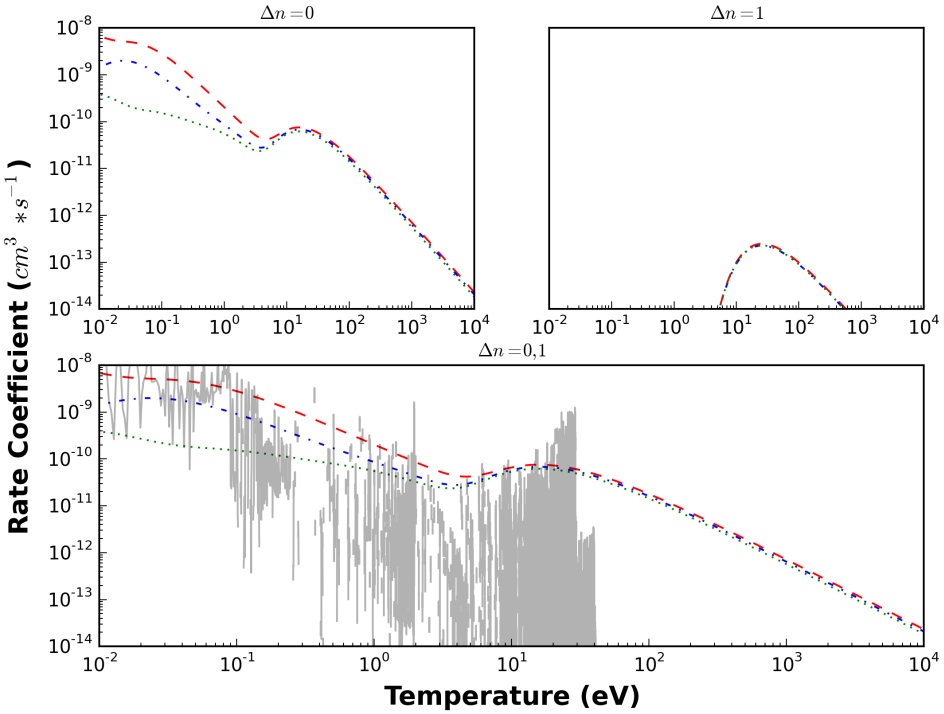

Figure 3.6: Maxwellian convolved DR rate coefficients for Ar^{4+}. The upper left subplot shows the rate coefficient for $\Delta n = 0$, while the upper right shows the rate coefficient for $\Delta n = 1$. The bottom subplot shows their sum, super-imposed on a background displaying the Lorentzian resonance profiles. The ground level data are shown in red (dashed), the first excited metastable level is in blue (dot-dashed), and the second excited metastable level is shown in green (dotted).

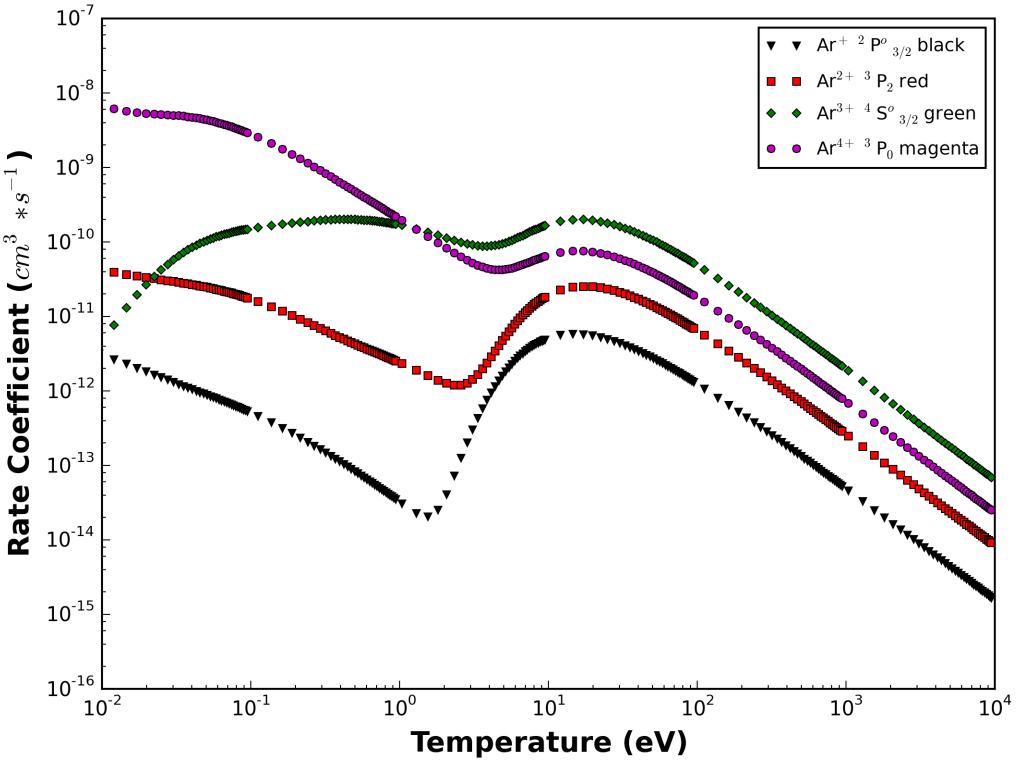

Figure 3.7: Total ground state DR rate coefficients for all ion stages. Here we show Maxwellian convolved rate coefficients for Ar^{+} (∇, online color = black), Ar^{2+} (squares, online color = red), Ar $^{3+}$ ($\diamond$, online color = green), and Ar^{4+} (circles, online color = magenta).

Comparison with previous work.

In addition to comparing our DR rate coefficients for Ar^{5+} with the previous work of Abdel-Naby [1], we have compared all of our results with the configuration-averaged, distorted wave (CADW) rates of Loch [57], and the semi-empirical rates given in Mazzotta [59]. This comparison is shown in Figures 3.8—3.11. For systems beyond Mg-like, Mazzota uses the DR rate coefficients from a range of sources, including the rates of Landini anf Fossi [52], Shull and Van Steenburg [72], and the modified Burgess-Merts rates provided by Merts [61]. The CADW rates of Loch et al. represent, to our knowledge, the most comprehensive set of data to date for near-neutral argon DR. The rates presented in Mazzotta et al. are still in widespread use in the astrophysical/plasma modelling community.

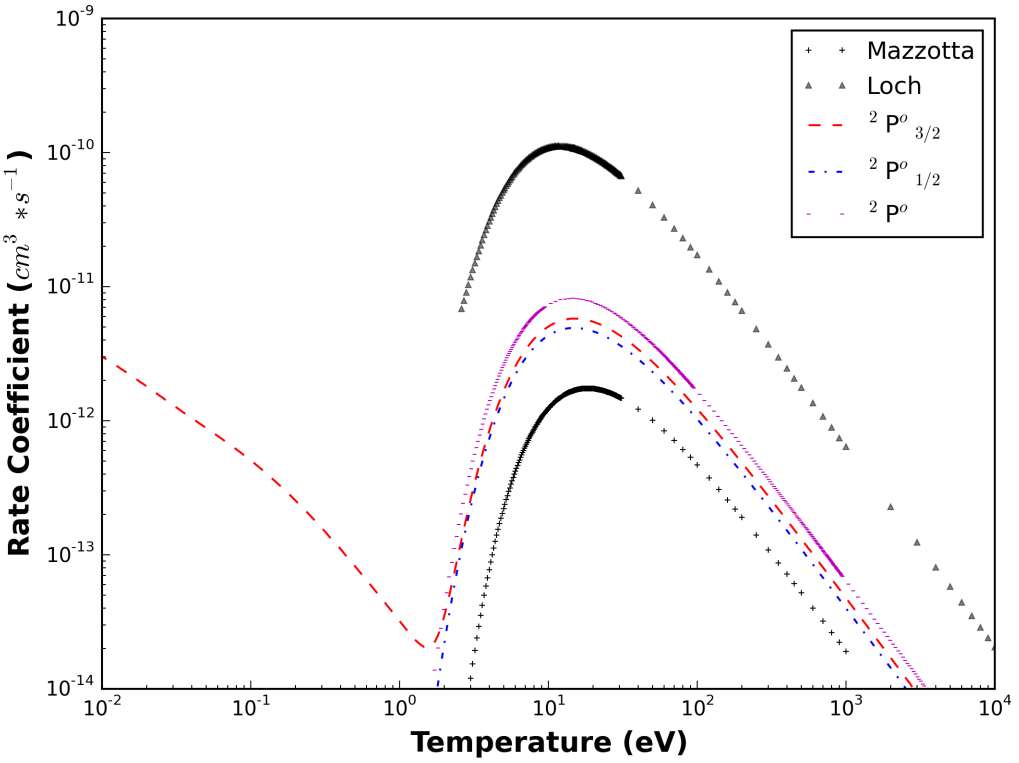

Figure 3.8: Our rate coefficients for Ar^+ compared with those of Loch [57] (triangles) and Mazzotta (+) [59]. We include rates for all levels within the ground term of each ion, in addition to the LS rate coefficient (purple, underscores). The ground level data are shown in red (dashed), and the first excited metastable level is in blue (dot-dashed).

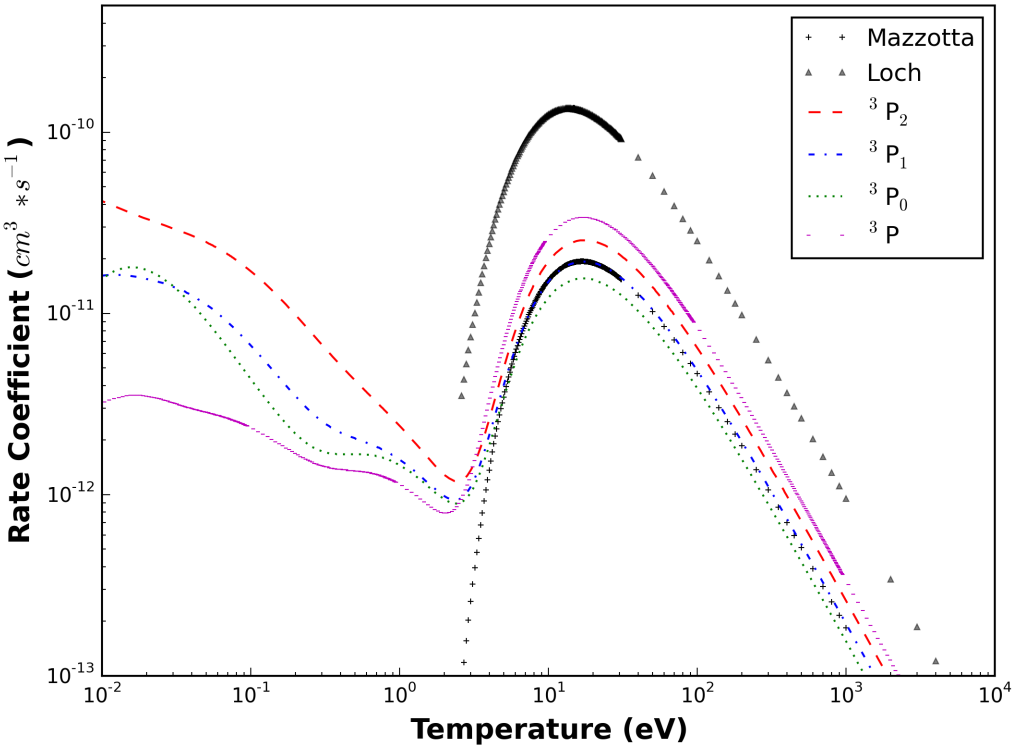

Figure 3.9: Our rate coefficients for Ar^{2+} compared with those of Loch [57] (triamgles) and Mazzotta (+) [59]. We include rates for all levels within the ground term of each ion, in addition to the LS rate coefficient (purple, underscores). Ground state is shown in red (dashed), first excited metastable is in blue (dot-dashed), and the second excited metastable states is shown in green (dotted).

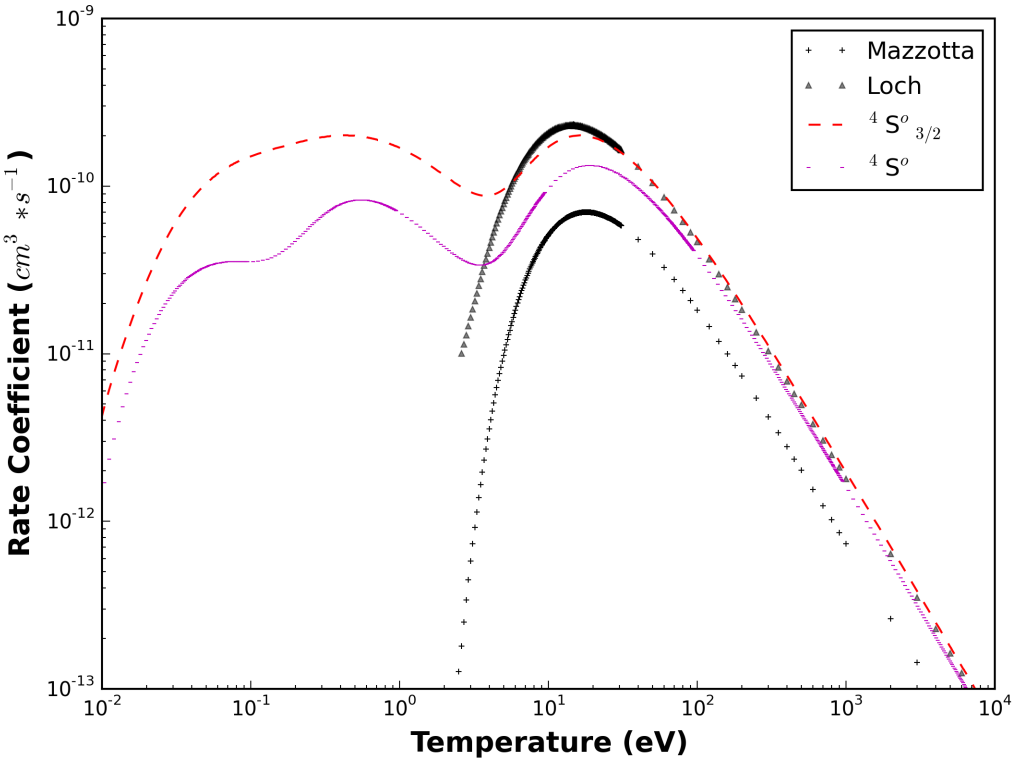

Figure 3.10: Our rate coefficients for Ar^{3+} compared with those of Loch [57] (triangles) and Mazzotta (+) [59]. We include rates for all levels within the ground term of each ion, in addition to the LS rate coefficient (purple, underscores). The ground level data are shown in red (dashed).

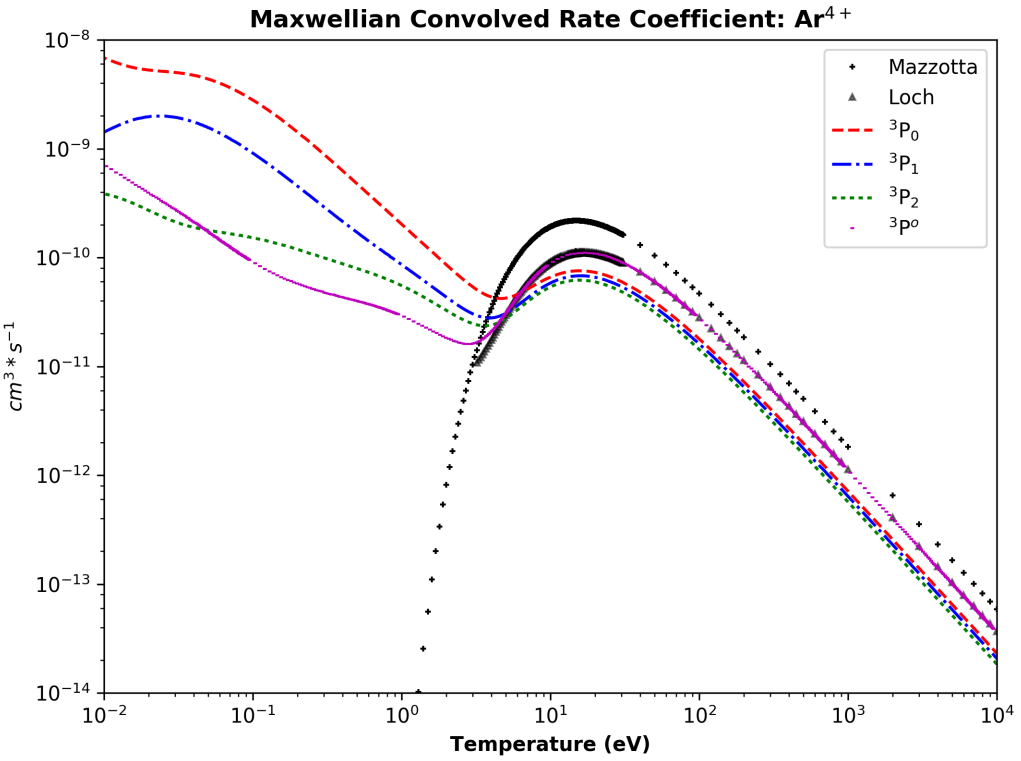

Figure 3.11: Our rate coefficients for Ar^{4+} compared with those of Loch [57] (triangles) and Mazzotta (+) [59]. We include rates for all levels within the ground term of each ion, in addition to the LS rate coefficient (purple, underscores). The ground state data are shown in red (dashed), the first excited metastable level is in blue (dot-dashed), and the second excited metastable level is shown in green (dotted).

3.4 Discussion

In general, we observe significant differences between our DR data and previously published, non-level-resolved rates. For higher temperatures ($>$ 10 eV), and low charge states (i.e. Ar^{+}, Ar^{2+}), our rates are almost an order of magnitude greater than those of Mazzotta, and one to two orders of magnitude less than the CADW results of Loch [57]. For more highly charged systems (i.e. $Ar^{3+}$and above), across the same energy range, our rates agree more closely with those previously published, though significant differences still exist. The higher results produced by the CADW method have been observed before in Li-like systems for cases where the autoionization and radiative rates for a given nl are close in magnitude [42]. Due to the largely semi-empirical nature of Mazzotta's data, the current discrepancies are not unexpected.

Also of interest in our data are the results for metastable initial levels in the recombining ion. For example, for the case of Ar^{+}, the ground level DR rate coefficient contains a sizeable fine-structure DR contribution at low temperatures, while the metastable rate coefficient does not, dropping off dramatically at low temperature. All ions presented here display some fine-structure contribution to the total DR rate coefficient.

As a brief example of the impact these new, level-resolved, coefficients can have on atomic processes, we present Figure 3.12, which shows an equilibrium fractional abundance calculation using only ground state data (i.e. no metastables). This calculation was performed using the ADAS atomic software [73]. The ionization data for all ion stages are from Loch et al. [57]. The bold lines represent ion fraction abundances calculated using our level-resolved DR data, while dashed lines represent abundances calculated using the semi-empirical DR rates presented in Mazzotta [59]. Differences are significant across the entire temperature range, shown in eV. The largest differences are seen in the case of Ar^{3+}, due to differences in the level-resolved rate coefficients for Ar^{3+} and Ar^{4+}. For Ar^{3+} our fractional abundance peak value is more than 30% lower than obtained using the DR data

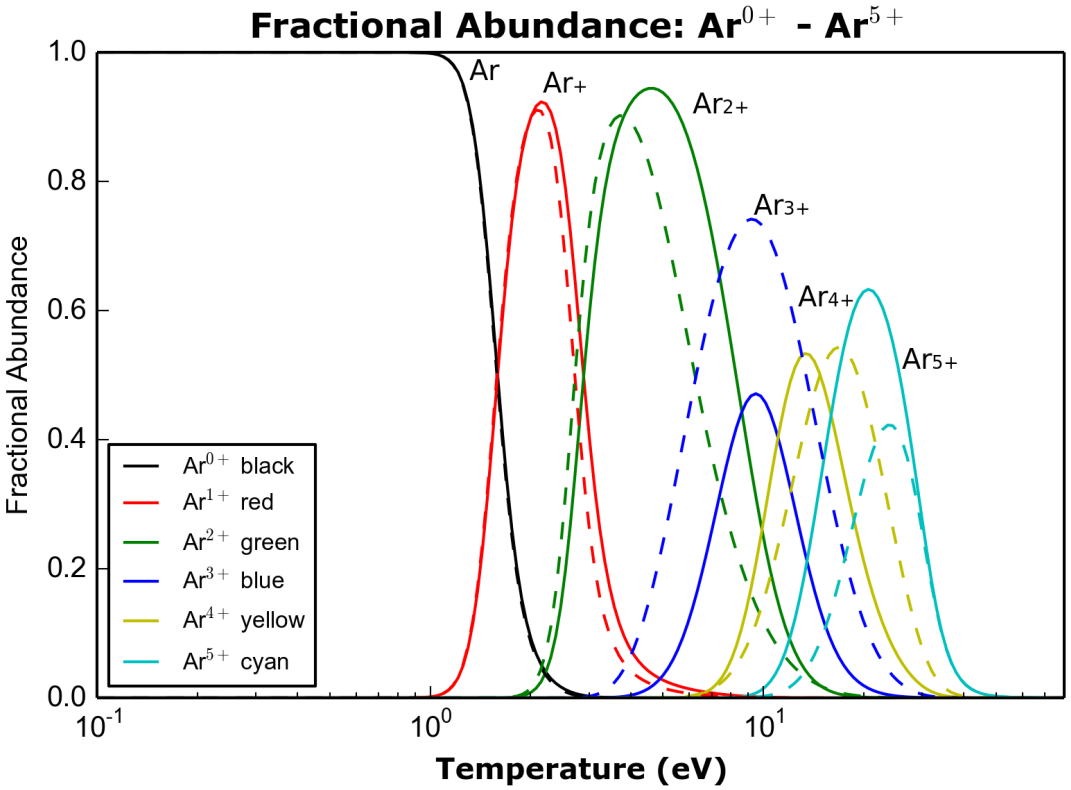

Figure 3.12: Equilibrium ion fraction balance for Ar^{+}—Ar^{5+}. Solid lines represent the present work, dashed lines were generated using data from Mazzotta [59]

from Mazzotta [59]. Reviewing the rate coefficients from Figure **??**, we see that our DR rate coefficients for Ar^{4+} recombining into Ar^{3+} are significantly lower than Mazzotta's, while our coefficients for Ar^{3+} are significantly higher. Therefore, according to our new data, Ar^{3+} depopulates into the lower ion stages more rapidly than previously predicted, while at the same time populating less rapidly from higher ion stages, leading to the dramatic decrease in the fractional abundance shown in Figure 3.12. Ar^{3+} spectral emission is observed in planetary nebulae, where it is used to measure electron temperature and density [49]. Our new results have implications for Argon elemental abundance diagnostics in a range of astrophysical plasmas, including those found in H II regions and the solar atmosphere [58]. If Ar^{3+} lines are used to measure elemental abundances, the difference in the Ar^{3+} fractional abundance will carry through linearly to differences in the diagnosed astrophysical abundance of argon relative to hydrogen.

3.5 Summary and future work

In response to a need for fully-level resolved DR rate coefficients in the fusion, astrophysical, laboratory, and industrial plasma modelling community, we have performed LS-coupling and (Breit-Pauli) intermediate coupling calculations of DR rate coefficients and cross sections for Ar^{+}—Ar^{4+}. We anticipate that these new rates could be used in conjunction with results from the DR Project data [4] to provide a comprehensive set of accurate rate coefficients for argon (Ar^{+}—Ar^{17+}). This is especially appropriate for use with massive gas injection (MGI) experiments, currently being investigated as a primary method for the safe mitigation of dangerous plasma disruptions in large scale fusion reactors such as ITER and JET [54]. A complete, comprehensive set of rate coefficients is necessary for MGI, where it is expected that a noble gas such as argon will become fully ionized in less than 10 ms [69, 71]. These coefficients will also be useful in the modelling of plasma that are dominated by neutrals or low charge species of argon, as can arise from numerous environments where the temperature and/or density is low, or the confinement time is short.

We have tabulated our results in the form of both ADAS standard *adf09* data files and fitting coefficients in the style of Mazzotta [59], listed in Appendix A. We plan to submit our DR rate coefficients for inclusion in the DR project, as well as the ADAS database [73]. To our knowledge, our new rates represent the only level resolved DR rate coefficients for Ar^{+}—Ar^{4+} to date, and therefore offer a significant improvement to rates published previously, and should be the best rates for these ion stages currently available. The DR data in the *adf09* files are also final state and metastable resolved, allowing generalised collisional-radiative modelling to be performed.

Using our new DR rates, we have calculated the equilibrium fractional abundance of argon for the first five ion stages of argon. We have compared this result to that calculated from rates published in previous works, and found significant differences.

In addition to these new DR rates, we are currently in the process of calculating a new set of level-resolved electron impact excitation atomic cross sections for neutral argon. We plan to combine this new excitation data with the DR rates presented here, along with existing radiative recombination (RR) rates to aid in the development a generalized collisional-radiative (GCR) model for neutral and singly-ionized argon. This is of particular interest to local research at Auburn University, aimed at the development of new optical diagnostics for low temperature and density argon plasmas. Future work will also focus on the impact of this GCR model on relevant atomic processes.

Chapter 4

Generalized collisional radiative modeling of metastable populations in neutral argon, benchmarked against ALEXIS.

4.1 Introduction.

In this section we detail our efforts to develop plasma diagnostics from our metastable resolved atomic data. The first step is to determine relative metastable population densities or *metastable fractions* of the plasma. Once these metastable fractions have been determined, we can build synthetic spectra from our atomic data. Without these metastable fractions, however, the contribution from each metastable to the theoretical line heights in our spectra is unknown. Knowing these metastable fractions also sheds insight on time dependent phenomena within the plasma, as these metastable fractions depend on the resident time of the excited neutral in the plasma bulk.

Once we have the information required to build synthetic emission spectra, we can measure theoretical line ratios. We predict that at least some of these will be temperature dependent, and determining that temperature dependence will allow us to predict electron temperatures within the ALEXIS plasma. These can be compared to experimentally measured electron temperatures, serving to benchmark our dataset and validate our methods.

4.2 Data Collection

4.2.1 Experimental determination of electron temperature/density.

As discussed in detail in Section 1.8.6, the double-tipped Langmuir probe is used to make measurements of the plasma electron density and electron temperature in the ALEXIS device. This data is then used to benchmark against the calculated temperature and densities from

the optical spectral analysis. One aspect that was not discussed previously was the estimate of errors in the experimental measurements. In this section, the methods used to estimate the errors in the experimental measurements is discussed.

Error analysis: Double probe density and temperature measurements, spectral line heights. Typical error estimates of temperature and density measurement range from ≈ 10 % [56] to over 100 % [25]. Contributions to double probe error include non-Maxwellian electron energy distributions, incorrect assumptions concerning sheath geometry, spatial variations in the RF discharge, and large stray capacitance to ground.

To illustrate the variations that can occur in probe measurements, consider electron temperature measurements performed using the double probe on the same day and using the same operating parameters. The results are shown in Table 4.1. From the data in the table, we can see that the deviation of each individual temperature measurement from the average of these measurements is 15 % ; 25 %, and 6 %, respectively. We set our error bar for average temperature measurements in ALEXIS equal to the largest of these, at 25 %. We should also note that the error in these temperature measurements seems unpredictable.

Table 4.1: Estimating error for the double probe.

RF Power	**MFC Voltage**	**Magnetic Field (Gauss)**	**Average Temp (eV)**
30 Watts	0.5 Volts	330 Gauss	5.81 eV
30 Watts	0.5 Volts	330 Gauss	4.05 eV
30 Watts	0.5 Volts	330 Gauss	5.39 eV
		Average =	5.08 eV

By contrast, the factory calibrated Black Comet spectrometer has an error of ≤ 10 %, as listed by StellarNet, in absolute intensity and line height for the entire 200 – 1100 nm spectral range. In the "visible" region, which StellarNet lists as 400 – 900 nm, this error is less, at ≈ 5 %. Furthermore, line height measurements in the ALEXIS plasma are reproducible, meaning that similar plasma operating conditions optical emission spectra that are qualitatively and quantitatively reproducible.

Temperature and density profiles in ALEXIS

All of our spectral data from ALEXIS are line-of-sight averaged. We collect spectra along a radial line of the plasma at one the viewports labelled 2, 4, or 6 in Figure 1.11, and infer general properties of the bulk from this data. For this to be valid, we must assume that the plasma is relatively homogeneous and symmetric along the radial axis. One way we can verify this assumption is to examine radial temperature and density profiles in ALEXIS for a variety of plasma conditions. Figures 4.1 and 4.2 show radial temperature and density profiles for all 24 data runs collected at viewport 2 in ALEXIS. The corresponding experimental operating parameters are displayed in Table 4.2. These data runs were performed at varying magnetic fields and magnetic field configurations (by varying the coil currents in the source and chamber regions), and varying neutral gas pressure (by varying the voltage on the MFC). RF power was held constant at 30 Watts.

At first glance, it might appear that there are two band of temperature and density profiles, but this can be explained by examining the operating parameters shown in Table 4.2. From the table, a disproportionate number of data runs were performed at a magnetic field strength of ≈ 85 Gauss, corresponding to a chamber magnet current of 25 Amps. With these low magnetic field settings, the ALEXIS plasma occupies most of the vacuum chamber, and has a particularly flat density profile, as can be seen in the radial density profiles shown in Figure 4.2. The density profiles resulting from low magnetic field settings appear clustered around an electron density of $\approx 0.5 \times 10^{-15}\ m^{-3}$. These flat density profiles are particularly suited for line-of-sight spectral emission measurements.

As can be seen in the Figures 4.1 and 4.2, ALEXIS has radial temperature and density profiles that are both smooth and relatively flat. As a result, line of sight averaged spectra should reasonably approximate the electron temperature and density of the bulk along a radial slice of the plasma, and can be compared to experimentally measured, radially averaged temperature and density.

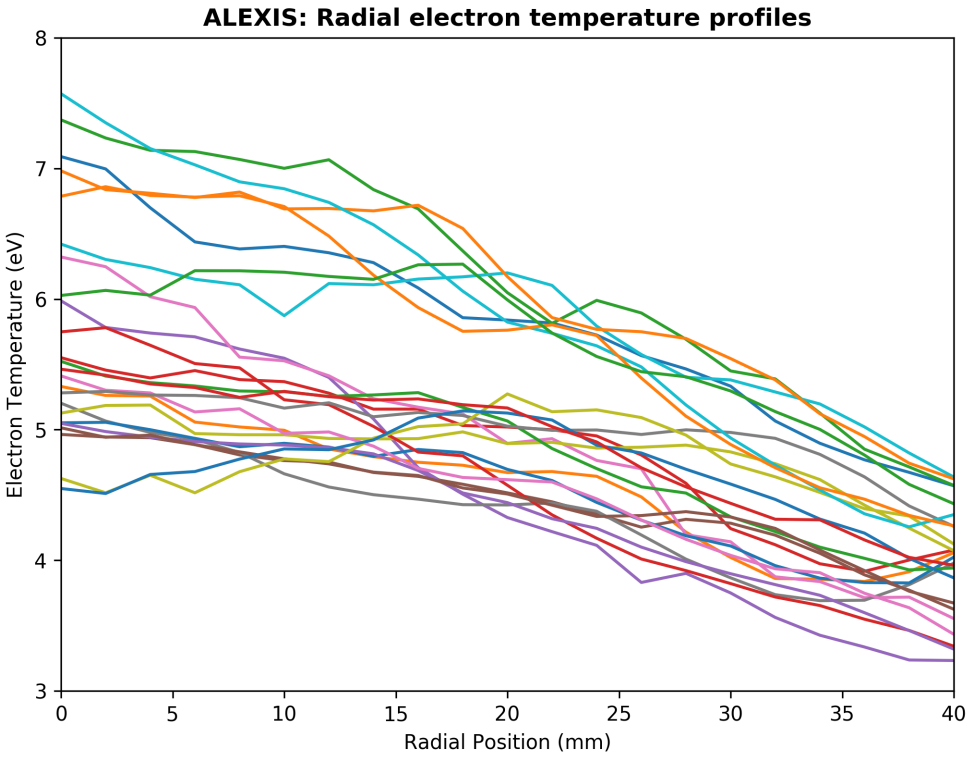

Figure 4.1: Radial electron temperature profiles for the 24 data runs at viewport 2 in the ALEXIS experiment.

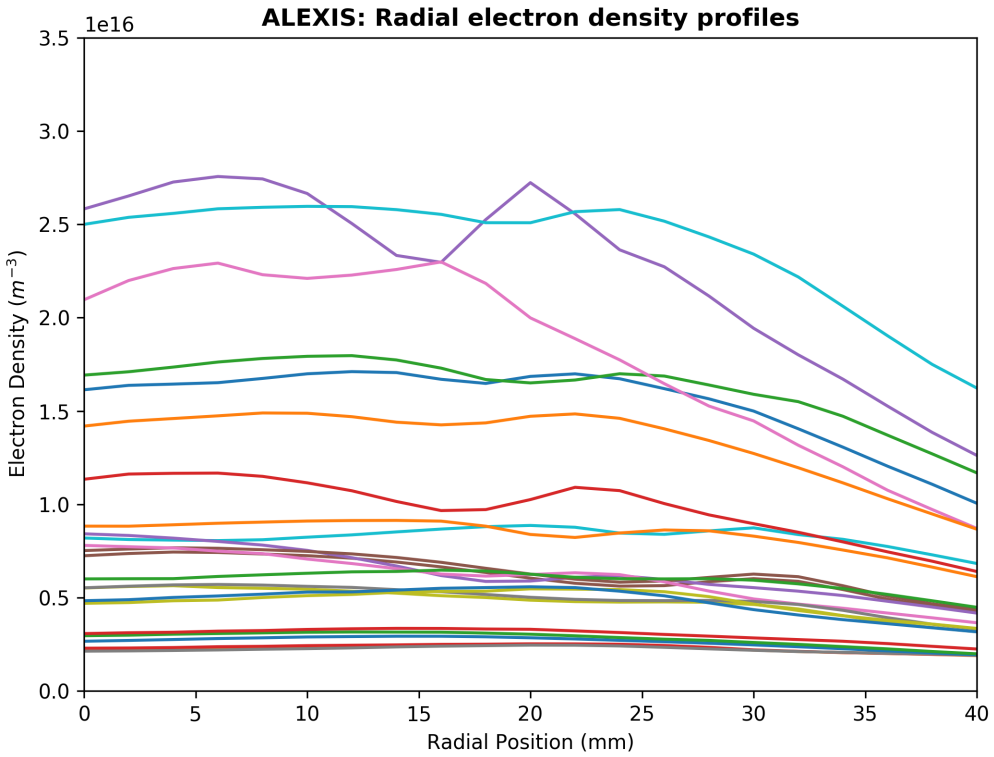

Figure 4.2: Radial electron density profiles for the 24 data runs at viewport 2 in the ALEXIS experiment.

Table 4.2: Operating parameters for the 24 data runs conducted at viewport 2, and displayed in Figures 4.1 and 4.2.

Coll. Date	Coll. Time	RF Power (Watts)	Neutral Press. (mTorr)	Mag. Field (Gauss)
11.11.2016	12:25	30	0.7	85
11.11.2016	12:47	30	0.5	85
11.11.2016	13:09	30	0.4	85
11.11.2016	12:04	30	0.9	85
11.11.2016	13:26	30	0.3	85
11.11.2016	13:46	30	0.9	85
11.11.2016	14:06	30	0.7	85
11.11.2016	14:25	30	0.5	85
11.11.2016	14:43	30	0.4	85
11.11.2016	16:26	30	0.3	85
11.11.2016	16:44	30	0.3	85
11.15.2016	10:47	30	0.8	333
11.15.2016	11:03	30	0.6	333
11.15.2016	11:19	30	0.5	333
11.15.2016	11:42	30	0.4	333
11.15.2016	12:00	30	0.8	250
11.15.2016	12:17	30	0.6	250
11.15.2016	12:35	30	0.5	170
11.15.2016	12:52	30	0.5	85
11.15.2016	14:10	30	0.3	85
11.15.2016	14:33	30	0.8	333
11.15.2016	15:32	30	0.7	250
11.15.2016	15:45	30	0.7	170
11.15.2016	16:02	30	0.7	85

4.2.2 Collecting spectral data.

For more details on spectral data collection see Section 1.8.8 in the introduction. We collect spectral data using a StellarNet Black Comet extended range UV-VIS CCD spectrometer. This spectrometer is capable of recording spectra in the 200-1100 nm range. We record ten spectra at optimized integration times during each radial sweep of the double probe. These spectra are recorded during the last ten radial data collection intervals, when the probe is furthest from the center of the plasma, in order to minimize the disturbance of the plasma by the presence of the probe. These ten spectra are then stored in the same data file as the I-V trace probe data, and stored for post-processing.

4.3 Overview of observed spectral lines.

In the range covered by our Black Comet spectrometer (200 – 100 nm), neutral argon emits strongly in the range loosely defined by 650 – 950 nm. This can be seen in Figure 4.3, which is an overlay plot of the 24 data runs collected at viewport 2. It is in this range that we choose to focus our search for temperature and density sensitive emission lines. Fortunately, our atomic dataset covers all transitions with an upper level less than $nl = 5\text{p}$, which includes most lines in this wavelength range.

We are further restricted by the rather broad instrument resolution of the Black Comet spectrometer. Though listed by StellarNet as having a spectral resolution of 0.7 nm, the actual effective resolution of the instrument is closer to 1.7 nm, meaning that many of the lines that we see are a blend of two or more corresponding lines in the NIST database. Our estimate of the spectrometers resolution is based on the observation that it cannot resolve the spectral lines at 842.86 and 840.82 nm, which are 1.64 nm apart. We exclude these "blended" or "combination" lines from our analysis.

Table 4.3 contains relevant atomic data for the 13 distinct lines detected by our spectrometer in the range 650 – 950 nm that correspond to PEC's in our atomic dataset and are

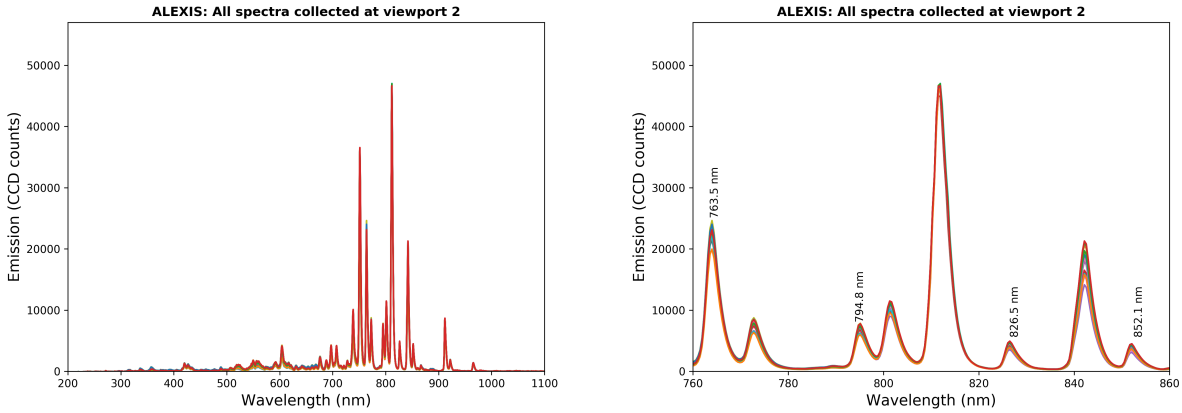

Figure 4.3: Spectral emission for the 24 data runs at viewport 2 in the ALEXIS experiment. The plot on the left shows an overlay of the 24 data runs collected at viewport 2 for the entire spectral range of the Black Comet spectrometer. On the right we focus on the wavelength range 760 – 860 nm and includes labels for the 4 distinct, strong lines given in Table 4.3.

more than 1.7 nm apart. We would add a word of caution about the relevance of the "NIST relative strength" values. These should not be assumed to translate in any precise manner to the ALEXIS plasma. The relative intensities given by NIST are those listed in Reader et al. and come from a wide variety of sources. The details of the original experiments used to calculate these intensities are not provided, and it is stated on the NIST website that these are intended only for a rough estimate of the general shape of the spectra. As a result, these numbers are useful for separating strong lines from weak, and that is all.

The atomic transitions that define these lines often involve a core change (i.e, a change in the total angular momentum of the core). For neutral atomic systems, standard Russel-Saunders ($^{2S+1}L_J$) notation is often not used, as L and S are not generally "good" quantum numbers in this context. Most states in neutral systems are actually superpositions of different $[L, S]$ states, and therefore some variation of Racah notation is usually employed, which utilizes quantum numbers n, l, k, and j (with k being the total angular momentum quantum number for the core configuration and j being the total angular momentum once the outer electron is included). Each state can then be described by combining the quantum numbers of the outermost electron with information about the core configuration, as shown

Table 4.3: Distinct lines in ALEXIS. Lower and upper levels are specified using Racah notation. Paschen notation (in parentheses) is given for the lower levels. The final column lists whether the transition involves a core change.

NIST WL	REL STR	LOWER LEVEL	UPPER LEVEL	CC?
696.5431	10000	4s $^2[3/2]^o$ 2 (1s5)	4p $^2[1/2]$ 1	Y
706.7218	10000	4s $^2[3/2]^o$ 2 (1s5)	4p $^2[3/2]$ 2	N
714.7042	1000	4s $^2[3/2]^o$ 2 (1s5)	4p $^2[3/2]$ 1	Y
727.2935	2000	4s $^2[3/2]^o$ 1 (1s4)	4p $^2[1/2]$ 1	Y
763.5105	25000	4s $^2[3/2]^o$ 2 (1s5)	4p $^2[3/2]$ 2	N
794.8176	20000	4s $^2[1/2]^o$ 0 (1s3)	4p $^2[3/2]$ 1	N
826.4521	10000	4s $^2[1/2]^o$ 1 (1s2)	4p $^2[1/2]$ 1	N
852.1441	15000	4s $^2[1/2]^o$ 1 (1s2)	4p $^2[3/2]$ 1	N
866.7943	4500	4s $^2[1/2]^o$ 0 (1s3)	4p $^2[3/2]$ 1	Y
912.2967	35000	4s $^2[3/2]^o$ 2 (1s5)	4p $^2[1/2]$ 1	N
919.4638	550	4p $^2[1/2]$ 1 (2p10)	5s $^2[1/2]^o$ 2	Y
922.4498	15000	4s $^2[1/2]^o$ 1 (1s2)	4p $^2[3/2]$ 2	Y

by the following excerpt from the NIST database for the transition leading to the spectral line at 696.543 nm:

Table 4.4: Atomic data for the spectral line at 696.543 nm.

Wavelength	**Lower Configuration**	**Term**	j	**Upper Configuration**	**Term**	j
696.543	$3s^2 3p^5 (^2P^o_{3/2}) 4s$	$^2[3/2]^o$	2	$3s^2 3p^5 (^2P^o_{1/2}) 4p$	$^2[1/2]^o$	1

In the example given in Table 4.3, the core configuration for the lower level is given by $(^2P^o_{3/2})$ (hence k=[3/2]), and the upper level has a $(^2P^o_{1/2})$ core (hence k=[1/2]). Due to the rules governing the selection of s, l and j, these two cores are the only possible $^{2S+1}L_J$ combinations arising from the $3s^2 3p^5$ core configuration of neutral argon. Any transition that involves a change in this core configuration, such as the one listed above, is described as *core changing*. The outermost electron is then described by the n, l, k, and j values in the remainder of the configuration and term entries. For the lower level of the above example this would be given by $4s^2[3/2]^o_2 \quad (J = 2)$, where $n = 4$, $l = 0$, $k = 3/2$, and $j = 2$. Note that the k quantum number is the total angular momentum of the core. This then couples to the angular momentum of the outer electron to give the total angular momentum (j). Finally, it has been noted by some authors that core-changing transitions are more challenging to

calculate than non-core changing transitions. It is then possible that lines arising from core changing transitions could have larger uncertainties in our synthetic spectrum and may be less reliable for diagnostic purposes.

It should be noted that all theoretical lines need to be shifted by 0.2 nm to match observations, in order to correct for the difference in the refractive indices of vacuum and air.

Of the 13 lines listed in Table 4.3, the lines located at 696.5, 706.7, 714.7, 727.3, 866.8, and 919.5 nm are only weakly or partially observed. In addition, the line at 912.3 is blended with emission from neutral carbon, which emits at 911.2 nm with a transition energy of just 1.32 eV. This reduces Table 4.3 to just 4 lines, which we list in Table 4.4. Note that none of them involve a core changing transition. For the remainder of this work, our search for temperature and density sensitive lines will focus on these four lines.

Table 4.5: Distinct, strong lines in ALEXIS, with Paschen notation included for the lower level. The final column shows whether the transition involves a core change. These lines are unblended and readily detectable with our spectrometer, making them good candidates for potential optical diagnostics.

NIST WL	REL STR	LOWER LEVEL	UPPER LEVEL	CC?
763.5105	25000	4s $^2[3/2]^o$ 2 (1s5)	4p $^2[3/2]$ 2	N
794.8176	20000	4s $^2[1/2]^o$ 0 (1s3)	4p $^2[3/2]$ 1	N
826.4521	10000	4s $^2[1/2]^o$ 1 (1s2)	4p $^2[1/2]$ 1	N
852.1441	15000	4s $^2[1/2]^o$ 1 (1s2)	4p $^2[3/2]$ 1	N

Finally, we would comment that there are many more lines than the 4 presented in Table 4.5 available for analysis. Modeling these lines, however, would require one of the following: 1) A more robust model, capable of separating the individual contributions from the PEC's contributing to the lines that are too close for our spectrometer to resolve. 2) Acquiring a spectrometer with better resolution, capable of resolving blended lines. 3) Acquiring a more sensitive spectrometer, capable of detecting weak lines. We think that meeting any of these three requirements would open up opportunities for future work.

4.4 PEC's and QCD's

To calculate synthetic spectra, and for quantitative analysis of metastable populations for neutral argon, we use ADAS 208. ADAS 208 generates multiple type of coefficients for a variety of purposes, but the two which we use for our calculations are *photon emissivity coefficients* (PEC's), and *metastable coupling coefficients* (QCD's). PEC's are used primarily to generate synthetic spectra from the rate coefficients contained in our ADF04 data file. QCD's are used to determine the relative populations of the metastable states, and how these populations evolve in time.

We calculate PEC's and QCD's on a predetermined temperature and density grid that contains 36 electron temperatures and 20 electron densities. Box 4.4 shows the grid of densities. Temperatures are dispersed linearly from 0.5 – 20 eV, while densities are placed on a custom grid that focuses primarily on the densities of order 1×10^{10} cm^{-3}. Temperature parameters are chosen to cover a range suitable for most low-temperature argon plasma. Densities are chosen to match observations in ALEXIS.

Density grid for PEC's and QCD's

Densities (m^{-3}): 1.00e+08 , 5.10e+09 , 1.01e+10 , 1.51e+10 , 2.01e+10 , 2.51e+10 , 3.01e+10 , 3.51e+10 , 4.01e+10 , 4.51e+10 , 5.00e+10 , 5.50e+10 , 6.00e+10 , 6.50e+10 , 7.00e+10 , 7.50e+10 , 8.00e+10 , 8.50e+10 , 9.00e+10 , 9.50e+10

4.4.1 PEC's

Synthetic line heights in ALEXIS are determined using ADAS 208. The code creates *photon emissivity coefficients* (PEC's) for the 50 strongest observed transitions, using the rate information contained in an ADF04 data file. PEC's allow us to determine the emissivity of a given transition, and since the emissivity is directly proportional to the height of the corresponding spectral line, they are often thought of as direct analogues to line heights.

Using these PEC's, the emissivity of a spectral line with upper level i and lower level j can be written:

$$\epsilon_{i\to j} = \sum_k PEC_{\sigma_k, i\to j} N_e N_{\sigma_k}. \tag{4.1}$$

Where the summation is over the metastable states (k). For neutral argon this becomes:

$$\epsilon_{i\to j} = PEC_{\sigma_1, i\to j} N_e N_{\sigma_1} + PEC_{\sigma_2, i\to j} N_e N_{\sigma_2} + PEC_{\sigma_3, i\to j} N_e N_{\sigma_3} \tag{4.2}$$

since there are only three metastables (including the ground state). Dividing through by $\frac{1}{N_{\sigma_1}}$ yields:

$$\epsilon_{i\to j} = PEC_{\sigma_1, i\to j} N_e + PEC_{\sigma_2, i\to j} N_e \frac{N_{\sigma_2}}{N_{\sigma_1}} + PEC_{\sigma_3, i\to j} N_e \frac{N_{\sigma_3}}{N_{\sigma_1}} \tag{4.3}$$

from which we can easily see that the relative metastable population $\frac{N_{\sigma_k}}{N_{\sigma_1}}$ is of primary importance to our ability to predict the emissivity, and thus the height, of any given spectral line. In fact, this relative metastable population, or *metastable fraction*, is the only quantity in Equation 4.3 that is not directly calculated by ADAS 208, and without this quantity we cannot accurately determine the height of any one line. Therefore, before we can make any attempt to model spectral emission from ALEXIS, we must determine the appropriate metastable fractions.

4.4.2 QCD's.

In order to calculate PEC's, ADAS 208 needs any relevant rate coefficients for the atomic processes that can occur in the plasma under investigation. These rate coefficients will end up as the partitioned matrix elements in the generalized collisional radiative (GCR) matrix (see Section 1.6.9) and are known as the *generalized collisional-radiative coefficients*. We list these coefficients in Box 4.4.2.

Generalized collisional radiative coefficients.

- Ionization coefficients:

$$S_{CD,\sigma\to\nu} = \mathscr{S}_{\sigma\nu} - \sum_j \mathscr{S}_{\nu j} \sum_i \mathscr{C}^{-1}_{ji}\mathscr{C}_{i\sigma}$$

- Free electron recombination coefficients:

$$\alpha_{CD,\nu'\to\rho} = \mathscr{R}_{\rho\nu'} + \sum_j \mathscr{C}_{\rho j} \sum_i \mathscr{C}^{-1}_{ji}\mathscr{R}_{i\nu'}$$

- Metastable cross-coupling coefficients:

$$X_{CD,\sigma\to\rho} = \mathscr{C}_{\rho\sigma} + \sum_j \mathscr{C}_{\rho j} \sum_i \mathscr{C}^{-1}_{ji}\mathscr{C}_{i\sigma}$$

- Parent metastable cross-coupling coefficients:

$$Q_{CD,\nu'\to\nu} = \sum_j \mathscr{C}_{\rho j} \sum_i \mathscr{C}^{-1}_{ji}\mathscr{C}_{i\sigma}$$

Of these, we take particular interest in the metastable cross-coupling coefficients (QCD's), which govern the rate at which metastable states become populated/depopulated, and can be used to determine how quickly the metastable populations of ion or neutral species reach a steady state population. We would like to determine the relative population densities of the ground and metastable states in low-temperature argon, for use in Equation 4.3. We can do this by using the rates in the relevant output file from ADAS 208 ("qcd208.pass") which contains both XCD and QCD data. Note that for ALEXIS conditions, the SCD, ACD,

and XCD coefficients will be negligibly small (due to the low temperature and small Ar^+ fraction). Thus, the QCD rates are used to solve the GCR matrix defined as:

$$\begin{bmatrix} 1 \\ 0 \\ 0 \end{bmatrix} = \begin{bmatrix} 1 & 1 & 1 \\ N_e Q_{12} & N_e(Q_{12}+Q_{23}) & N_e Q_{32} \\ N_e Q_{13} & N_e(Q_{23}+Q_{23}) & N_e(Q_{31}+Q_{32}) \end{bmatrix} \begin{bmatrix} \frac{N_1}{N_{TOT}} \\ \frac{N_2}{N_{TOT}} \\ \frac{N_3}{N_{TOT}} \end{bmatrix} \tag{4.4}$$

The matrix in Equation 4.4 is populated from the qcd208.pass data file output from the same run of ADAS 208 that creates our PEC data. It is solved in Python using standard inversion routines available in numpy. The results are used in the sections that follow to determine metastable relative population densities in ALEXIS.

Finally, we note that the relative population densities in Equation 4.3 can be weighted to any of the three metastables in neutral argon. For the rest of this work, we choose to weight all PEC's, and by extension any synthetic line ratios and spectra, to the 1s3 metastable. We make this choice to allow for easy comparison to the experimentally observed metastable fractions presented in Piech et al., which use the same convention.

4.4.3 Analysing metastable populations in low temperature argon plasmas.

Equilibrium metastable populations.

To accomplish this, we perform a *steady-state metastable balance* calculation, where we solve the GCR matrix for neutral argon, assuming that the relative metastable population densities are in equilibrium with each other. This initially seemed like a reasonable assumption, as time scales for metastables to reach relative equilibrium are generally accepted to be a few tenths of a second to a couple of seconds, and the neutral argon residence time is much longer (approximately 5 – 20 seconds). The result of our calculation is shown in Figure 4.4. This figure plots metastable fractions relative to the ground state at equilibrium, as a function of temperature, for all 36 temperatures in our dataset. It also flattens our data along the

density axis, so that we are looking at 20 stacked layers of line ratio vs. temperature plots, for all 20 densities in our PEC dataset. This has the following effect on our plot data; any density dependence of the metastable fractions would show up as "blurriness".

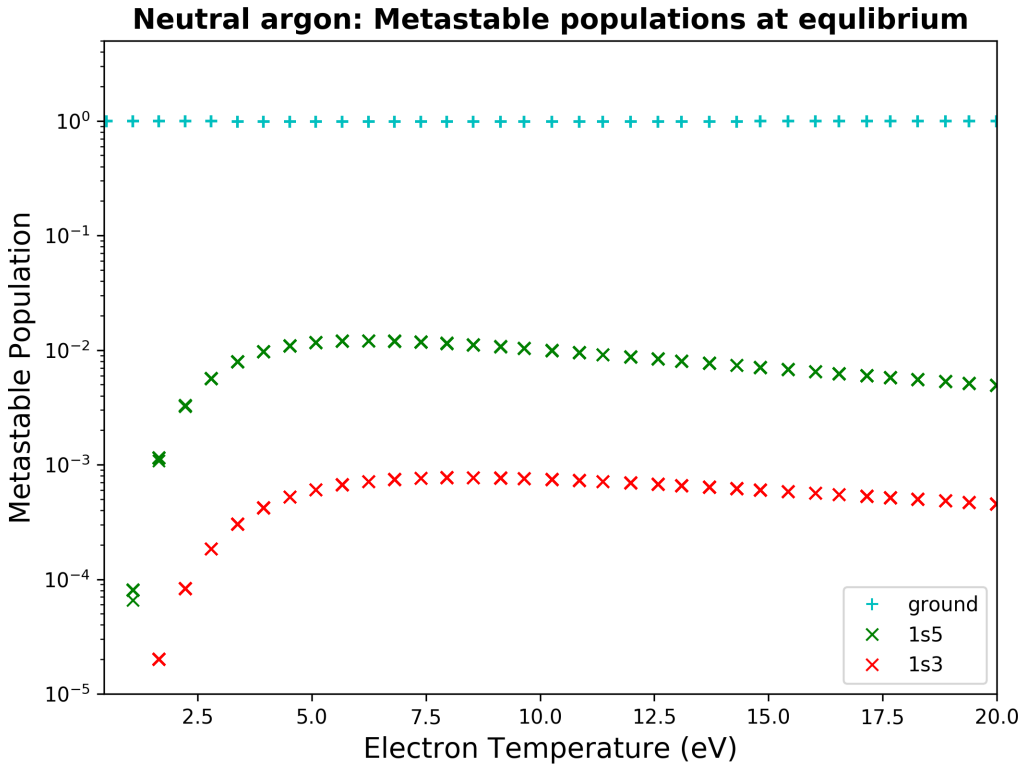

Figure 4.4: Metastable population densities for neutral argon at equilibrium.

From the plots in Figure 4.4, we can draw the following conclusions for temperatures and densities in our atomic dataset:

Conclusions: Equilibrium metastable fractions in ALEXIS

1. Equilibrium metastable fractions for neutral argon (and by extension in ALEXIS) vary significantly as a function of temperature.
2. Equilibrium metastable fractions in neutral argon do not vary significantly as a function of density.
3. For the 1s5 metastable, the equilibrium ratio of the ground state to the 1s5 metastable is of the order 100:1 for temperatures relevant to ALEXIS ($\approx 2 - 7$ eV).
4. For the 1s3 metastable, this ratio is of the order 1000:1

To our knowledge, this represents the first theoretical calculation of metastable populations in low-temperature neutral argon that is capable of including the plasma's response to variations in temperature and density.

4.4.4 Time dependence of relative metastable population densities.

From the previous section we see that the equilibrium populations of the 1s3 and 1s5 metastables vary significantly with respect to each other as a function of temperature. We also know the energy required to excite neutral argon from the ground state is not available in low temperature laboratory plasmas, leading to the conclusion that most of the atomic transitions occurring in the plasma (and by extension most of the observed spectral lines) are the result of excitation from one of the two excited metastables.

It would seem, then, that the dynamics of the 1s3 and 1s5 metastables, with respect to temperature, density, and time, would be of primary importance in any attempt to model low temperature plasmas like ALEXIS. In this subsection we investigate the time-dependent properties of metastable populations in neutral argon. We accomplish this by calculating a

time dependent metastable population calculation. We note that the relevant rate coefficients (QCD's) are functions of electron temperature and density. By fixing temperature and density at values appropriate for ALEXIS we can set up the GCR matrix at $t = 0$ along with an initial population distribution, and propagate the ground and metastable populations forward in time on an appropriate grid. We also make the assumption that argon is entirely in the ground state as it enters the ALEXIS vacuum chamber, leading to a percent population of ground:1s5:1s3 metastables of 100%:0%:0%, respectively.

The results of our time dependent analysis are shown in Figure 4.5. We fixed the electron temperature at 5.08 eV. The electron density was held constant at $2 \times 10^{16} m^{-3}$. Both values are consistent with temperatures and densities regularly seen in ALEXIS. It should also be noted that we have repeated this calculation for other temperature values with results that show little difference from those in Figure 4.5. For our analysis, we defined the time step to be one tenth the time associated with the largest rate coefficient in our dataset, for a time step of 3.11×10^{-5} s. We also defined a steady-state for the ALEXIS plasma as the time when the variance of the matrix defined by the [ground:1s5:1s3] metastables was less than 1×10^{-10}. We assume that these low values of the variance indicate the convergence of the solution. Our calculations continues after this steady state time is reached. The results are shown in Box 4.4.4.

Metastable steady state values for ALEXIS.

Time step 3.1×10^{-5} s

Steps 272

Time to steady state 0.0085 s

We can see that ALEXIS reaches a steady state, as defined in the previous paragraph, by ≈ 8.5 ms. In all likelihood we can assume a steady state much sooner, at around 4 ms,

due to the plateau observed in the plot. This is much longer than the anticipated residence time of the neutral Ar atoms in the plasma. Any ions would be removed quickly, as shown in the introduction, but the neutrals would simply bounce off the walls until they exit the chamber. Thus, one might expect the metastable populations to be at their steady state values. However, a synthetic spectrum generated under these assumptions does not produce good agreement with the observed spectral line intensities. This will be investigated in the remainder of this chapter.

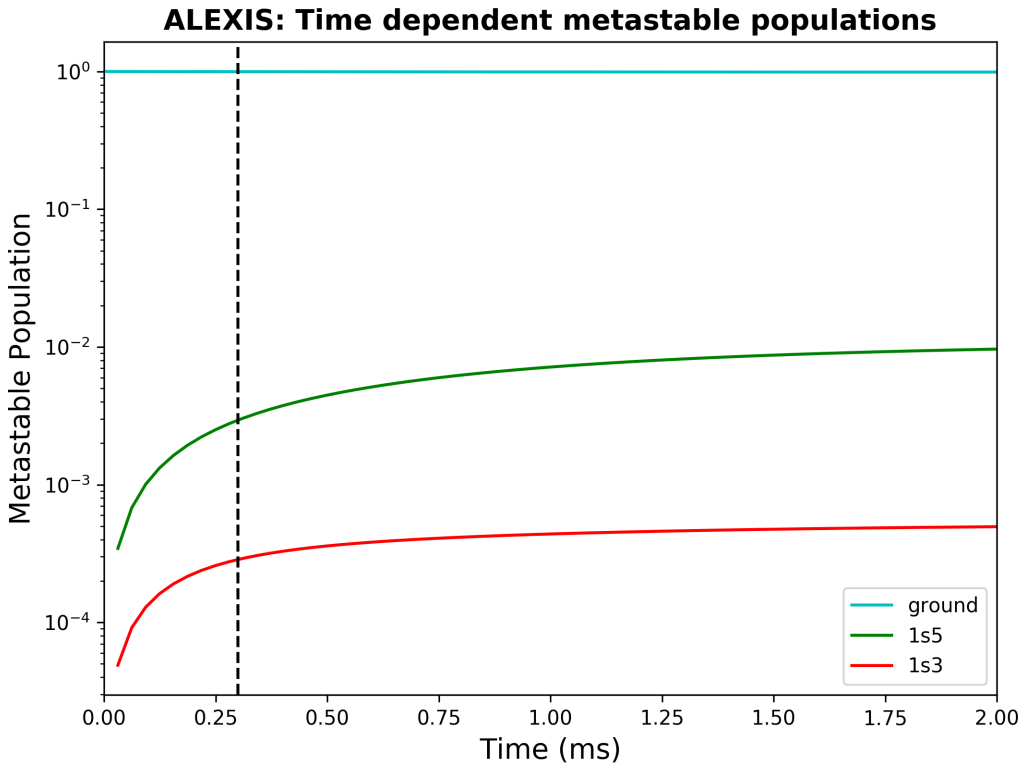

Figure 4.5: Time dependent metastable population densities for neutral argon at equilibrium. The dashed vertical line represents the limit for thermal neutral argon atoms to travel the radial distance of $\approx$ 4 cm from the center of the ALEXIS plasma to the plasma boundary. For this plot we choose $T_e \approx 5eV$; $N_e \approx 1 \times 10^{16} m^{-3}$.

Figure 4.6 shows the ratio of the ground state to the 1s3 metastable as a function of time. From the plot, we can see that the ground:1s3 metastable ratio drops to about 5000 almost instantaneously, and by about 0.4 ms (or roughly 13 time steps) falls below 3000,

until it reaches its steady state value of ≈ 1900 at around 8 ms. Room temperature neutral argon, moving at thermal speeds in a collisionless plasma would take $\approx 3.0 \times 10^{-4}$ s to travel the approximately 5 cm radial distance from the center of ALEXIS to the chamber wall. This roughly corresponds to index 10 in our time step array, for which the ground:1s3 metastable fraction is ≈ 3000. We take this as the upper limit, reflecting the possibility that collisions with the walls drives the metastable states down to the ground state. For the lower limit we use the steady state value of ≈ 2000. From this we conclude that the ground:1s3 metastable ratio in ALEXIS is in the range 3000:1 – 2000:1 during normal operation.

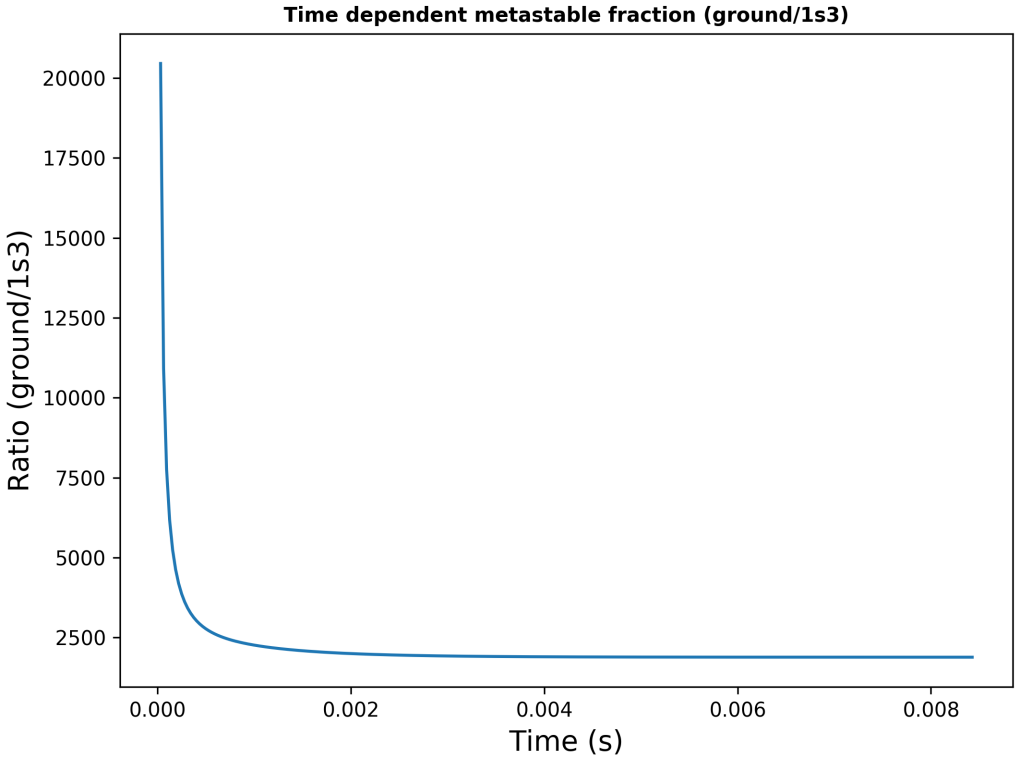

Figure 4.6: The ratio of the ground to 1s3 metastable as a function of time.

As previously stated, we believe that the 1s5:1s3 metastable fraction will dominate the temperature dependence of the line ratios in ALEXIS. In Figure 4.7 we plot this ratio as a function of time, assuming the same temperature and density as in Figure 4.5.

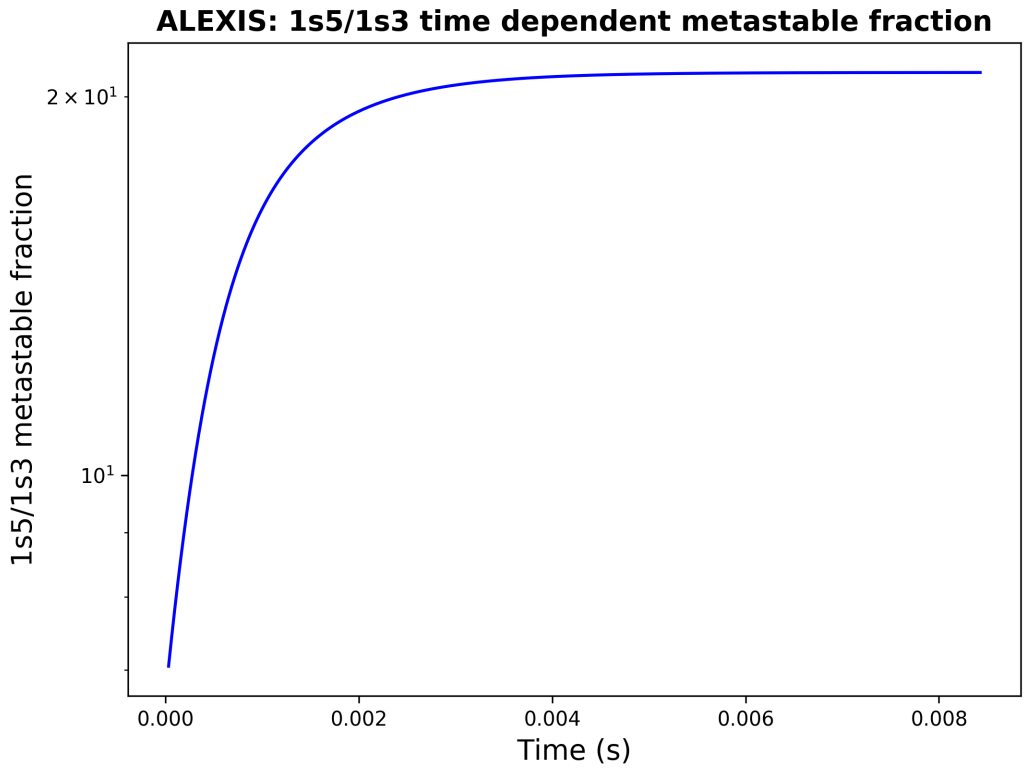

Figure 4.7: The ratio of the 1s5 to 1s3 metastables as a function of time.

We observe that this fraction plateaus at around 4 ms, and that the steady state value of this ratio is ≈ 20.1. We note significant variation in this plot for times less than 4 ms. Ratios less than this steady state value would place ALEXIS within the time dependent range of this curve, and could be used to assess the resident lifetime of excited neutrals in ALEXIS. This will be demonstrated in the next subsection.

4.4.5 Determining the metastable fraction in ALEXIS.

In the two previous subsections, we make the observation that the ratio of the 1s3 and 1s5 metastable populations in ALEXIS is both temperature and time dependent. In this subsection, we determine the metastable fraction in ALEXIS using a combination of experimental temperature and line ratio measurements, by comparing to their theoretical counterparts using PEC's calculated from our excitation data, using ADAS 208.

As described at the end of Section 4.4, we have chosen to focus on the spectral line ratios $\frac{763.5\ nm}{826.5\ nm}$, and $\frac{763.5\ nm}{852.1\ nm}$ for our temperature analysis of ALEXIS. We would like to point out some similarities between the lines at 826.5 and 852.1 nm, using the data in Table 4.3: 1) They have similar NIST relative strengths, 2) they share identical lower levels and core configurations 4s $^2[1/2]^o$ $(J = 1)$, 3) their upper levels only differ in the value of K, with $K = 1/2$ for the line at 826.5 nm, and $K = 3/2$ for the line at 852.1 nm, and 4) neither are core changing transitions. In light of this, it is probably not surprising that their temperature dependent behavior is similar in most respects. In the sections that follow we detail our metastable determination using the 763.5/852.1 line ratio. The reader should be aware that we have repeated this analysis for the 763.5/826.5 ratio, with no significant differences from the results that follow.

Our basic algorithm for the determination of the metastable fraction in ALEXIS is shown in Box 4.4.5.

Basic algorithm to determine metastable fractions in ALEXIS.

1. Assume a ground/1s3 metastable fraction of 2000:1.
2. Create an linear array of 300 potential 1s5/1s3 metastable fractions, from 0 to 30. In our code this is called the *mscale* array.
3. Determine the 763.5/852.1 average line ratio and electron temperature from experimental observations for each of the 46 data runs saved for post-processing.
4. For each ratio in the mscale array, find the *metastable fraction of best fit*, that is, the metastable fraction that produces theoretical line ratios that most closely match observed temperatures for that data run.

Figure 4.8 shows the results from analyzing one of our data runs collected from ALEXIS. The upper left plot shows a radial temperature profile from ALEXIS, and the upper right a radial density profile. The average temperature /density is displayed in each plot's legend. The plot at the bottom of the figure displays the weighted PEC ratio, using the metastable fraction of best fit, as determined using the algorithm from the above Box. We also show the experimentally determined average temperature as a vertical yellow line. The two horizontal lines in the plot show the experimentally measured line ratio $\frac{763.5\ nm}{852.1\ nm}$, and the theoretical line ratio corresponding to the experimental average temperature, using our interpolated weighted PEC array for the metastable fraction of best fit. Using this method we are able to match experimentally observed line ratios very closely for all 43 data runs.

Figure 4.9 shows the resulting 1s5:1s3 metastable fractions of best fit for all 43 data runs. As can be seen in the plot, correlation is extremely strong, with R^2 coefficient of 0.96.

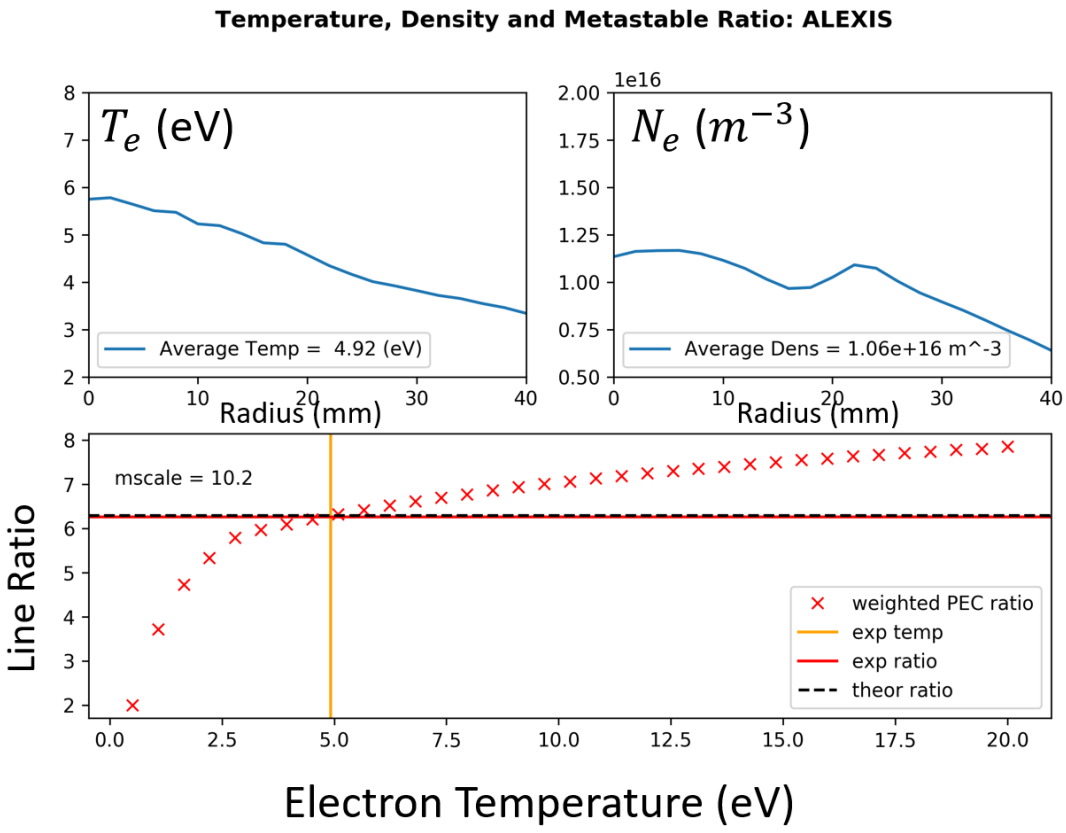

Figure 4.8: The theoretical *metastable fraction of best fit* is determined by looping over 300 possible metastable fractions, and comparing the resulting line ratio for experimental temperatures / line ratios observed in ALEXIS.

Using a linear fit to the plotted data allows us to model metastable fractions in ALEXIS using the measured line ratio $\frac{763.5\ nm}{852.1\ nm}$ with the following formula:

$$M_{frac} = 2.8603 * Ratio_{(\frac{763.5\ nm}{852.1\ nm})} - 7.8244 \tag{4.5}$$

We will use this in the next subsection to determine electron temperatures in ALEXIS using line ratios. To our knowledge, this is the first time a working relative metastable population density diagnostic for neutral argon from line ratios has been successfully demonstrated.

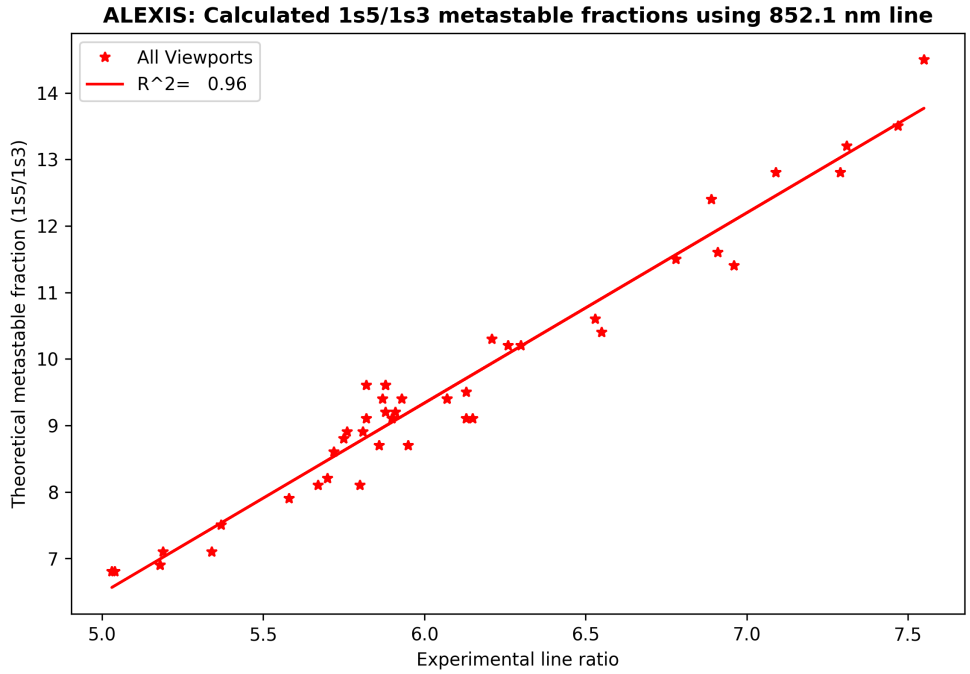

Figure 4.9: 1s5:1s3 theoretically calculated metastable fractions for all 43 data runs in ALEXIS using the line at 852 nm, plotted vs. the experimentally measured line ratios.

For completeness, we have repeated the analysis in this subsection for all 43 data runs, using the $\frac{763.5\ nm}{826.5\ nm}$ line ratio. The results were remarkably similar. A linear fit to the resulting metastable fractions of best fit had $R^2 = 0.92$, as opposed to $R^2 = 0.96$ for the $\frac{763.5\ nm}{852.1\ nm}$ ratio. Metastable fractions covered the same approximate range, with similar values as presented in Figure 4.10. We make the claim that either line could be used to diagnose the 1s3:1s5

metastable fraction. From this point forward, we choose to focus on the line ratio using the 852.1 nm line. Figure 4.10 shows results using the 826.5 nm line.

One important result from these two figures is we can now estimate how long neutral particles are within the plasma bulk, by comparing measured metastable fractions with the time dependent line ratio data shown in Figure 4.7. From Figure 4.9, we see that metastable fractions in ALEXIS have an mean value of $\approx 6.5 \pm 1.625$. Room temperature neutral argon has a thermal speed of ≈ 400 m/s. From Figure 4.7, this corresponds to a time of ≈ 0.2 ms. This time corresponds to a radial distance of approximately 5 cm, which matches the radial dimensions of our vacuum chamber. It would seem likely, then, that the primary limiting factor for the 1s5:1s3 metastable ratio is the radial scale length of ALEXIS.

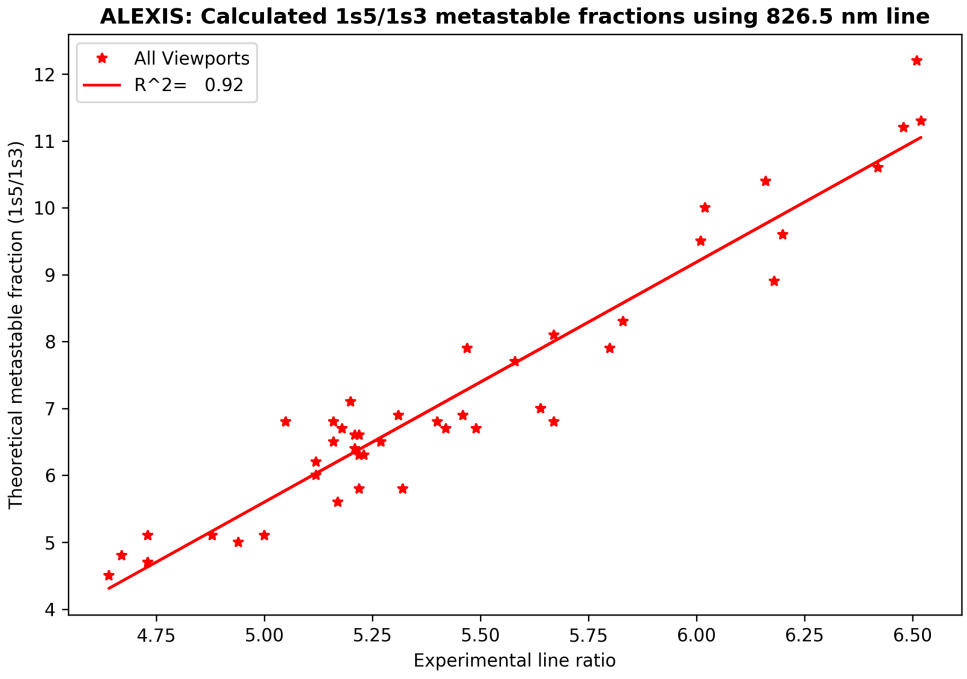

Figure 4.10: 1s5:1s3 theoretically calculated metastable fractions for all 43 data runs in ALEXIS using the line at 826.1 nm, plotted vs. the experimentally measured line ratios.

Now that we have successfully determined the metastable fraction in ALEXIS for a given data run, we can attempt to model the spectral emission from the experiment using

synthetic spectra built from weighted PEC's for the four distinct, strong lines in Table 4.5, using the following method:

Basic algorithm for creating synthetic spectra from weighted PEC's.

1. Determine the metastable fraction for a data run by calculating the $\frac{763.5\ nm}{852.1\ nm}$ line ratio from experimental data using the algorithm previously described.

2. Use this metastable ratio in Equation 4.5 to create weighted PEC's from the adf04 file.

3. Model spectral emission in ALEXIS by instrument broadening and adjusting these lines for index of refraction. For comparison, we normalize both spectra to the line height observed at 763.5 nm.

Using the algorithm outlined above, we have created synthetic emission lines for the four strong lines in Table 4.5. The result is plotted in Figure 4.11.

The excellent agreement with observation shown in this figure is not arbitrary or singular. We observe similar results for all 43 data runs. We believe this confirms the validity of our method, and the accuracy of the atomic dataset.

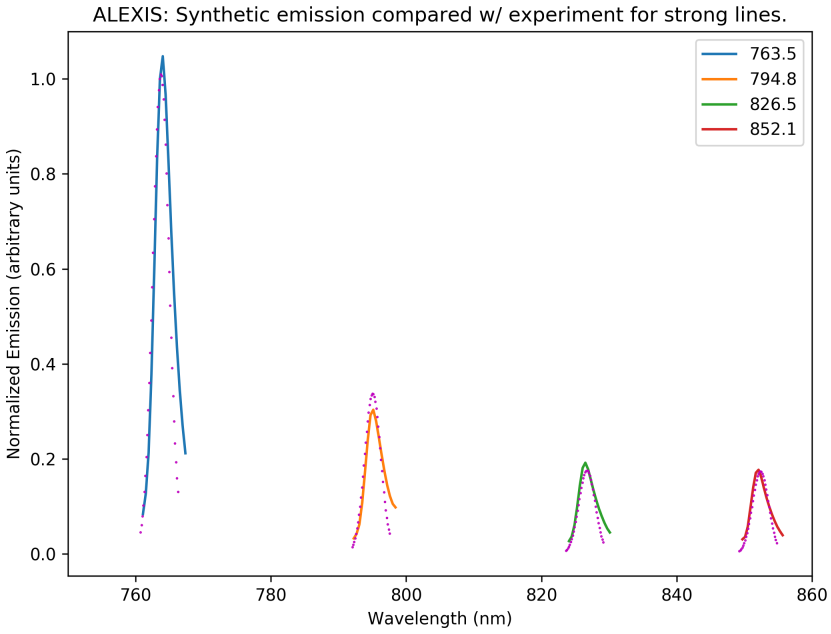

Figure 4.11: Synthetic emission compared with experimental observations for the four strong, distinct lines observed in ALEXIS.

4.5 Development of a working temperature diagnostic using spectral line ratios.

We now have a method to diagnose metastable fractions is ALEXIS, and can use metastable weighted PEC's to plot the response of line ratios as a function of electron temperature. From previous sections, we note that the line ratios $\frac{763.5\ nm}{826.5\ nm}$, and $\frac{763.5\ nm}{852.1\ nm}$ are predicted to be sensitive to temperature, but not density. Our process for determining electron temperature is then:

Algorithm to determine electron temperature from experimentally measured line ratios.

1. For the measured line ratio $\frac{763.5\ nm}{852.1\ nm}$, assume a steady state value for the ground:1s5 metastable fraction.

2. Calculate the 1s5:1s3 metastable fraction using the formula:

$$M_{frac} = 2.8603 * Ratio_{(\frac{763.5\ nm}{852.1\ nm})} - 7.8244$$

3. Use the metastable fractions in Items 1 and 2 to construct a line ratio vs. temperature plot, using interpolated temperatures and metastable weighted PEC's

4. Find the nearest temperature corresponding to the measured line ratio in Item 3.

Using the algorithm outlined above, we have calculated theoretical average electron temperatures from experimentally measured line heights for all 43 data runs. The results are shown in Figure 4.12.

In the plot, you can see that predicted temperatures all fall within experimental error bars for measurements taken with the ALEXIS double probe. We recognize that the relatively large error bars on our probe data make it difficult to draw extensive conclusions about the behavior of the experimental temperature data. Further, these theoretical temperatures seem to act in a smooth and predictable manner, demonstrated by the quadratic fit plotted as an orange line. We would note that we have repeated this analysis for the line ratio $\frac{763.5\ nm}{826.5\ nm}$, with similar results.

As a result of the data plotted in Figure 4.12, we now believe that we have a working model for temperatures in the ALEXIS plasma as a function of the temperature sensitive line ratio $\frac{763.5\ nm}{852.1\ nm}$ valid in the approximate T_e range 2–10 eV.

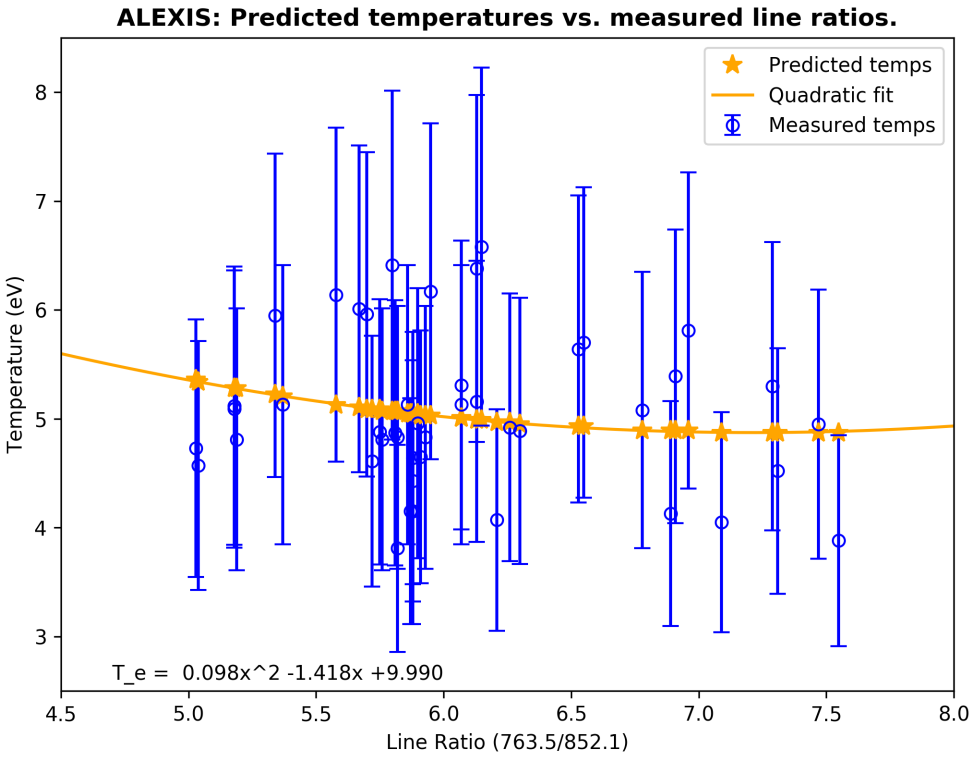

Figure 4.12: Experimental temperature measurements in ALEXIS, with error bars of 25 %. The orange stars are our predicted temperatures corresponding to the experimentally determined line ratios. The smooth curve is the result of a quadratic curve fit.

Temperatures in ALEXIS as a function of the line ratio $\frac{763.5\ nm}{852.1\ nm}$.

- $$T_e = 0.098 * Ratio^2 - 1.416 * Ratio + 9.990$$

We also believe that the methods for determining electron temperatures from line heights, using theoretical PEC's, can be extended to other low temperature argon plasma experiments. We intend to further test these methods on the Magnetized Dusty Plasma eXperiment (MDPX) at Auburn University. We also intend to collaborate with colleagues at West Virginia University, in order to test these methods on the LEIA and CHEWIE plasma experiments. These last two examples will allow us the opportunity to test our methods on a wider variety of plasma conditions.

4.6 Dependence of metastable fraction on electron density.

As a further check on our interpretation, that changes in the $\frac{763.5\ nm}{852.1\ nm}$ line ratio are reflecting changes in the metastable populations and that the metastable population is driven by electron collisions in the time-frame between the neutrals colliding with the vessel walls, it is instructive to plot our synthetic line ratios vs the measured electron density in the plasma. While we do not expect that metastable fractions are dependent on electron density, the varying response of the line ratios as a function of density could potentially lead to density dependent line ratios. Note that no assumption on the electron density was made in our diagnosed metastable fraction. The strong dependence on electron density shown in Figure 4.13 is as one might expect from our time-dependent metastable population modelling. If one increases the electron density, there are more excitations per second from the ground to the metastable state, resulting in a higher metastable population before the neutral hits the wall. If one is not close to the steady state value, this dependence upon electron density will be almost linear, something also observed in Figure 4.13.

Note that in determining the metastable population in the plasma, we have also determined the electron density. With the current diagnostic this required Langmuir probe measurements to calibrate the metastable fraction to the electron density. If one knew sufficient information about the neutral Ar density and temperature, it should be possible to determine the electron density directly from the measured metastable fraction. That is, one could use the set of time-dependent ionization balance curves, along with a measured metastable fraction, to fit the electron density that would produce the measured metastable fraction.

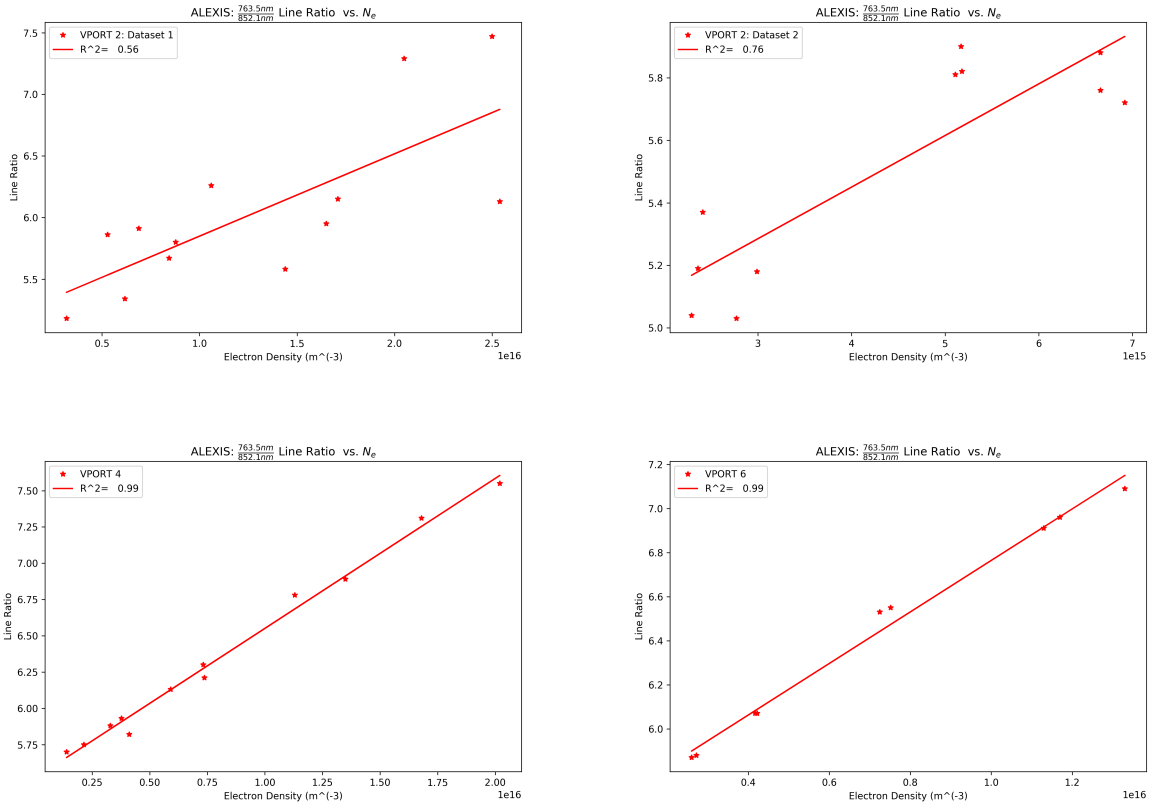

Figure 4.13: Metastable fraction vs electron density in ALEXIS fr all 43 data runs, separated by viewport and collection date. The top left plot displays data collected at viewport 2. The top right displays data from viewport 2 from a different collection date. The bottom left plot shows data collected from viewport 4. The bottom right plot is the data collected from viewport 6.

4.7 Summary.

We have used our new neutral Ar atomic data to investigate the metastable populations within the ALEXIS plasma, using 4 spectral lines we have determined to be good candidates for analysis. These lines are listed in Table 4.5. We have been able to determine the relative metastable populations within ALEXIS, and our calculated values (ranging from $\approx 7 - 14$) are in agreement with those measured by Piech et al. We determine these relative metastable population densities by optimizing the fit of theoretical line ratios vs experimentally measured temperature data, using an optimization parameter we call the *metastable fraction of best fit*. An example of one such optimization is presented in Figure 4.8, where the metastable fraction of best fit is simply labelled "mscale". This metastable information can also be used to determine the electron density in the plasma, and via some line ratio studies can be used to determine the electron temperature.

In the future, we hope to extend the analysis presented in this chapter to a wider variety of low temperature argon plasmas. We have plans to analyze plasmas at both Auburn University (MDPX) and West Virginia University (CHEWIE, LEIA) using the methods described in this work. We also hope to extend out model to include non-Maxwellian electron distribution functions. Acquiring data with higher resolved spectrometers could possibly allow for further work on density diagnostics. Finally, we hope to develop a more robust model that would allow for a completely *ab initio* temperature diagnostic, without the need for experimental data to determine metastable fractions from line heights.

Chapter 5

Conclusions, summary, future work.

5.1 Summary.

There is a demonstrated need for low temperature non-invasive plasma diagnostic techniques in the laboratory, medical, industrial, and dusty plasma communities. Argon plasmas are common in each of these areas. To this end, we have developed methods and techniques using a new atomic dataset for neutral argon which allows us to determine metastable fractions in the ALEXIS experiment, a low temperature neutral dominated plasma located at Auburn University in Alabama. We have compared the resulting metastable fractions for the 1s5:1s3 metastables to existing literature [66], and found good agreement for our results.

We are able to use the resulting metastable fractions to predict electron temperatures in ALEXIS using the line ratios at $\frac{763.5nm}{852.1nm}$, and $\frac{763.5nm}{826.5nm}$. We have compared the predicted temperatures from our model to Langmuir probe data collected from 43 data runs conducted on the ALEXIS experiment. These data runs represent a variety of plasma conditions. Because our spectrometer collects data along a radial line of sight, our predicted results are compared to electron temperatures averaged from successive radial measurements from the center to the edge of the plasma. Our predicted temperatures match their experimentally measured counterparts within the estimated error of the double Langmuir probe values.

In the following sections we recap the conclusions from Chapters 2, 3, and 4. The final section of this chapter presents a brief discussion of future work.

5.2 Conclusions: Electron impact excitation of neutral argon.

We have calculated direct, cascade, and apparent cross-sections for excitation from the ground and long-lived metastable states of neutral argon into all levels of the $2p$ manifold. We focus on the $2p$ manifold because of the ready availability of experimental data for comparison, but it should be noted that it is possible to calculate direct cross-sections for all transitions in our dataset, which includes spectroscopic levels up to $5p$ (not a Paschen designation, here we mean $n = 5, l = 1$), and cascade and apparent cross-sections for any transition whose cascade contribution can be well approximated by radiation from the remaining levels in our dataset above its upper level.

The agreement between our data and the data of previous authors is generally very good. Our ground-state data tends to agree well with the ground-state excitation data of Chutjian and Cartwright, and Hoshino *et al.*. We also are able to predict many of the qualitative features of the direct and cascade cross-sections described by Chilton *et al.*. We concur with previous authors that the Chilton data may overestimate the peak values of the cross-sections, potentially due to errors in the absolute calibration of their equipment.

We also show excellent agreement with the direct theoretical metastable cross-sections of Bartschat and Zeman. While our data tends to agree with the general shape and qualitative features of the experimental metastable apparent cross-section data of Piech *et al.*, our data disagrees with Piech's estimation of the cascade contribution. We find that the contribution from radiative cascades to the apparent cross-section is much greater than previously estimated.

5.3 Conclusions: Dielectronic recombination of low charge states of argon.

In response to a need for fully-level resolved DR rate coefficients in the fusion, astrophysical, laboratory, and industrial plasma modelling community, we have performed LS-coupling and (Breit-Pauli) intermediate coupling calculations of DR rate coefficients and cross sections for

Ar^+ through to Ar^{4+}. We anticipate that these new rates could be used in conjunction with results from the DR Project data [4] to provide a comprehensive set of accurate rate coefficients for argon (Ar^+—Ar^{17+}). This is especially appropriate for use with massive gas injection (MGI) experiments, currently being investigated as a primary method for the safe mitigation of dangerous plasma disruptions in large scale fusion reactors such as ITER and JET [54]. A complete, comprehensive set of rate coefficients is necessary for MGI, where it is expected that a noble gas such as argon will become fully ionized in less than 10 ms [69, 71]. These coefficients will also be useful in the modeling of plasmas that are dominated by neutrals or low charge species of argon, as can arise from numerous environments where the temperature and/or density is low, or the confinement time is short.

In general, we observe significant differences between our DR data and previously published, non-level-resolved rates. For higher temperatures ($>$ 10 eV), and low charge states (i.e. Ar^+, Ar^{2+}), our rates are almost an order of magnitude greater than those of Mazzotta, and one to two orders of magnitude less than the CADW results of Loch [57]. For more highly charged systems (i.e. $Ar^{3+}$and above), across the same energy range, our rates agree more closely with those previously published, though significant differences still exist. The higher results produced by the CADW method have been observed before in Li-like systems for cases where the autoionization and radiative rates for a given nl are close in magnitude [42]. Due to the largely semi-empirical nature of Mazzotta's data, the current discrepancies are not unexpected.

Also of interest in our data are the results for metastable initial levels in the recombining ion. For example, for the case of Ar^+, the ground level DR rate coefficient contains a sizeable fine-structure DR contribution at low temperatures, while the metastable rate coefficient does not, dropping off dramatically at low temperature (see Figure 3.3 of chapter 3).

We have tabulated our results in the form of both ADAS standard *adf09* data files and fitting coefficients in the style of Mazzotta [59], listed in Appendix A. We plan to submit our DR rate coefficients for inclusion in the DR project, as well as the ADAS database [73]. To

our knowledge, our new rates represent the only level resolved DR rate coefficients for Ar^{+}—Ar^{4+} to date, and therefore offer a significant improvement to rates published previously, and should be the best rates for these ion stages currently available. The DR data in the *adf09* files are also final state and metastable resolved, allowing generalised collisional-radiative modelling to be performed.

Using our new DR rates, we have calculated the equilibrium fractional abundance of argon for the first five ion stages of argon. We have compared this result to that calculated from rates published in previous works, and found significant differences. The largest differences are for the temperature of peak abundance of Ar^{2+} under equilibrium conditions, and it may be that such a difference can be tested from astrophysical observations.

5.4 Conclusions: A GCR Model for low temperature, neutral dominated argon plasmas.

We have used our atomic impact excitation data to investigate the metastable populations within the ALEXIS plasma, using 4 spectral lines we have determined to be good candidates for analysis. These lines are listed in Table 4.5. We have been able to determine the relative metastable populations within ALEXIS, and our calculated values (ranging from $\approx 7 - 14$) are in agreement with those measured by Piech et al. We determine these relative metastable population densities by optimizing the fit of theoretical line ratios vs experimentally measured temperature data, using an optimization parameter we call the *metastable fraction of best fit*. Repeating this procedure for all 43 data runs has allowed us to determine a simple, linear relationship between measured line ratios and metastable fractions in ALEXIS. We believe this method can be extended to other low-temperature argon plasmas for use a metastable fraction diagnostic.

We are able to use the *metastable cross coupling coefficients* calculated by ADAS 208 to investigate the time-dependence of the metastable fractions for low temperature neutral argon plasmas. Knowing the metastable fractions in ALEXIS allows us to theoretically

model the 4 strong lines listed in Table 4.5 by building synthetic spectra from metastable weighted PEC's. We have modeled the data in all 43 data runs with very good agreement with experiment. We believe this benchmark serves to validate the accuracy of our approach. An example is shown in Figure 5.1. The figure displays experimental line emission for the four strong lines believed to be good candidates for optical diagnostics, as detailed in Section 4.3. We overplot the corresponding synthetic line emission.

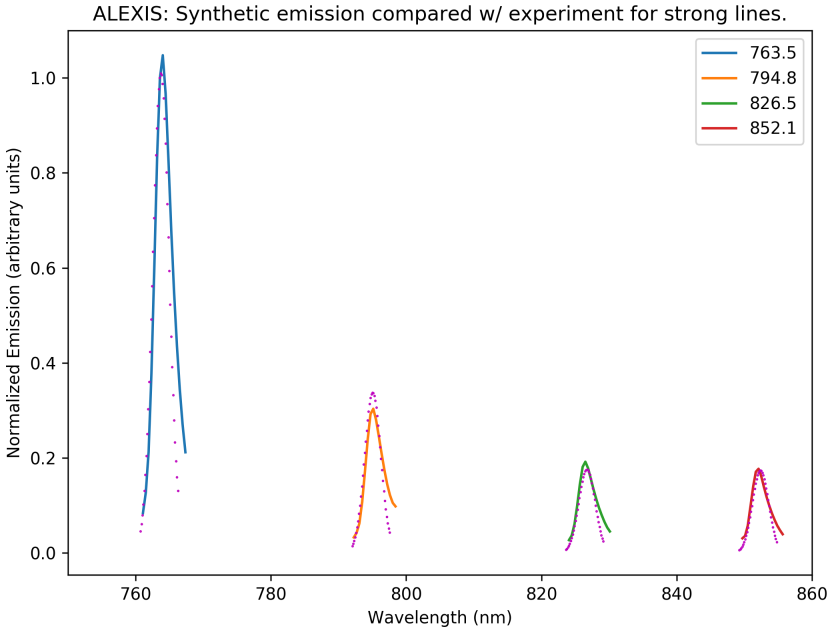

Figure 5.1: Benchmarking our results. The plot shown here displays experimental experimental measurement of the four strong lines in ALEXIS, with an overplot of their synthetic counterparts. The close agreement serves to validate our results.

Using the synthetic line heights, we have developed a temperature model for ALEXIS, with which we can predict electron temperatures from the experimentally measured line ratio $\frac{763.5\ nm}{852.1\ nm}$. This is detailed in Section 4.5. We have also observed a strong linear dependence between metastable fraction and electron density, and hope that this can be used to develop optical density diagnostics in the future.

5.5 Future work.

In the future, we hope to extend our diagnostic methods to a wider variety of low temperature argon plasmas. Investigating the impact of non-Maxwellian electron energy distribution functions is another avenue for future efforts. Acquiring data with higher resolved spectrometers could possibly allow for further work on density diagnostics. Finally, we hope to develop a more robust model that would allow for a completely *ab-initio* determination of metastable fractions. This would allow for completely theoretical temperature / density line ratio diagnostic techniques, without the need for experimental temperature and density measurements to develop an initial model. However, the spectral diagnostic approach of this work could be easily imported to other laboratory plasmas. First the metastable fraction of best fit would be determined, as in Figure 5.1, with Langmuir probe measurements used to provide the initial estimate of the temperature and density in the model. Once this has been completed, any metastable fraction can be diagnosed without the need of the probe measurements, and a set of strong spectral lines used to non-invasively diagnose the electron temperature and density in the plasma.

References

[1] Sh. A. Abdel-Naby, D Nikolić, T. W. Gorczyca, K. T. Korista, and N. R. Badnell. Dielectronic recombination data for dynamic finite-density plasmas XIV. The aluminum isoelectronic sequence. *Astronomy and Astrophysics*, 537, 2012.

[2] Z. Altun, A. Yumak, and N R Badnell. Dielectronic recombination data for dynamic finite-density plasmas. XI. The sodium isoelectronic sequence. *Astronomy and Astrophysics*, 447:1165–1174, 2006.

[3] I Arnold, E Thomas, S D Loch, S Abdel-Naby, and C P Ballance. The dielectronic recombination of Ar + Ar 4+. *Journal of Physics B: Atomic, Molecular and Optical Physics*, 48(17):175005, sep 2015.

[4] N R Badnell. Partial and total DR rate coefficients. `http://amdpp.phys.strath.ac.uk/tamoc/DATA/DR/`.

[5] N R Badnell. Dielectronic recombination of Fe 13+ : benchmarking the M-shell. *Journal of Physics B: Atomic, Molecular and Optical Physics*, 39(23):4825–4852, dec 2006.

[6] N R Badnell. A Breit Pauli distorted wave implementation for autostructure. *Computer Physics Communications*, 182(7):1528–1535, 2011.

[7] N R Badnell, M G O'Mullane, H P Summers, Z Altun, M A Bautista, J Colgan, T W Gorczyca, D M Mitnik, M S Pindzola, and O\ Zatsarinny. Dielectronic recombination data for dynamic finite-density plasmas I. Goals and methodology. *Astronomy and Astrophysics*, 412(3):14, dec 2003.

[8] NR Badnell. Dielectronic recombination of Fe22+ and Fe21+. *Journal of Physics B: Atomic and Molecular Physics*, 19:3827–3835, 1986.

[9] C P Ballance and D C Griffin. An R -matrix with pseudo states calculation of electron-impact excitation in Ar. *Journal of Physics B: Atomic, Molecular and Optical Physics*, 41(6):065201, mar 2008.

[10] Connor Ballance. *An Easy Introduction to GASP*, 2007.

[11] K. Bartschat and V. Zeman. Electron-impact excitation from the (3pˆ{5}4s) metastable states of argon. *Physical Review A*, 59(4):R2552–R2554, apr 1999.

[12] D R Bates and A E Kingston. Collisional-radiative recombination at low temperatures and densities. *Proceedings of the Physical Society*, 83(1):43, 1964.

[13] D. R. Bates, A. E. Kingston, and R. W. P. McWhirter. Recombination between electrons and atomic ions. i. optically thin plasmas. *Proceedings of the Royal Society of London A: Mathematical, Physical and Engineering Sciences*, 267(1330):297–312, 1962.

[14] M. A. Bautista and N. R. Badnell. Dielectronic recombination data for dynamic finite-density plasmas XII. The helium isoelectronic sequence. *Astronomy and Astrophysics*, 466(2):755–762, may 2007.

[15] Keith A. Berrington, Werner B. Eissner, and Patrick H. Norrington. RMATRX1: Belfast atomic R-matrix codes. *Computer Physics Communications*, 92(2-3):290–420, dec 1995.

[16] John B Boffard, R O Jung, Chun C Lin, L E Aneskavich, and A E Wendt. Argon 420.1419.8 nm emission line ratio for measuring plasma effective electron temperatures. *Journal of Physics D: Applied Physics*, 45(4):045201, feb 2012.

[17] John B Boffard, R O Jung, Chun C Lin, L E Aneskavich, and A E Wendt. Argon 420.1419.8nm emission line ratio for measuring plasma effective electron temperatures. *Journal of Physics D: Applied Physics*, 45(4):045201, 2012.

[18] John B. Boffard, Garrett A. Piech, Mark F. Gehrke, L. W. Anderson, and Chun C. Lin. Measurement of electron-impact excitation cross sections out of metastable levels

of argon and comparison with ground-state excitation. *Physical Review A*, 59(4):2749–2763, apr 1999.

[19] R. F. Boivin, J. L. Kline, and E. E. Scime. Electron temperature measurement by a helium line intensity ratio method in helicon plasmas. *Physics of Plasmas*, 8(12):5303–5314, 2001.

[20] S. A. Bozhenkov, M Lehnen, K H Finken, M W Jakubowski, R C Wolf, R Jaspers, M Kantor, O V Marchuk, E Uzgel, G Van Wassenhove, O Zimmermann, and D Reiter. Generation and suppression of runaway electrons in disruption mitigation experiments in TEXTOR. *Plasma Physics and Controlled Fusion*, 50(10), oct 2008.

[21] A Burgess. Coulomb integrals: tables and sum rules. *Journal of Physics B: Atomic and Molecular Physics*, 7(12):L364–L367, aug 1974.

[22] Alan Burgess. Delectronic Recombination and the Temperature of the Solar Corona. *The Astrophysical Journal*, 139:776–780, 1964.

[23] P. G. Burke, A Hibbert, and W D Robb. Electron scattering by complex atoms. *Journal of Physics B: Atomic and Molecular Physics*, 153, 1971.

[24] P.G. Burke and W.D. Robb. The R-Matrix Theory of Atomic Processes. *Advances in Atomic and Molecular Physics*, 11:143–214, 1976.

[25] Jen-Shih Chang. The inadequate reference electrode, a widespread source of error in plasma probe measurements. *Journal of Physics D: Applied Physics*, 6(14):304, sep 1973.

[26] Francis F Chen. *Langmuir Probe Diagnostics*, 2003.

[27] J. Chilton, John Boffard, R. Schappe, and Chun Lin. Measurement of electron-impact excitation into the 3pˆ{5}4p levels of argon using Fourier-transform spectroscopy. *Physical Review A*, 57(1):267–277, jan 1998.

[28] J. Ethan Chilton and Chun C. Lin. Measurement of electron-impact excitation into the 3 p 5 3 d and 3 p 5 5 s levels of argon using Fourier-transform spectroscopy. *Physical Review A*, 60(5):3712–3721, nov 1999.

[29] A. Chutjian and D. C. Cartwright. Electron-impact excitation of electronic states in argon at incident energies between 16 and 100 eV. *Physical Review A*, 23(5):2178–2193, may 1981.

[30] A. M. Dubois, I. Arnold, E. Thomas, E. Tejero, and W. E. Amatucci. Electron-ion hybrid instability experiment upgrades to the Auburn Linear Experiment for Instability Studies. *Review of Scientific Instruments*, 84(4):043503, apr 2013.

[31] A M DuBois, A C Eadon, and E Thomas. Suppression of drift waves in a linear magnetized plasma column. *Physics of Plasmas*, 19(7):072102, 2012.

[32] Ami M. DuBois, Edward Thomas, William E. Amatucci, and Gurudas Ganguli. Experimental characterization of broadband electrostatic noise due to plasma compression. *Journal of Geophysical Research: Space Physics*, 119(7):5624–5637, jul 2014.

[33] Ami Marie Dubois. Laboratory Investigation of the Dynamics of Shear Flows in a Plasma Boundary Layer. *AU Theses and Dissertations*, 2013.

[34] A C Eadon, E Tejero, A DuBois, and E Thomas. Upgrades to the Auburn linear experiment for instability studies. *The Review of scientific instruments*, 82(6):063511, jun 2011.

[35] Ashley Christopher Eadon. *Modifiction of Flow and Flow Driven Instabilities in ALEXIS*. PhD thesis, Auburn University, 2011.

[36] D. A. Verner & G. J. Ferland. Atomic data for astrophysics. i. radiative recombination rates for h-like, he-like, li-like and na-like ions over a broad range of temperature., 1996.

[37] A. R. Filipelli, Chun C. Lin, L.W. Anderson, and J.W. McConkey. *Cross Section Data*, volume 33 of *Advances In Atomic, Molecular, and Optical Physics*. Elsevier, 1994.

[38] Vuskovic L Filipovic D M, Marinkovic B P, Pejcev V. Electron-impact excitation of argon : I . The 4s [2. *Journal of Physics B: Atomic, Molecular and Optical Physics*, 677, 2000.

[39] T W Gorczyca and N R Badnell. Photoionization - excitation of helium using an R - matrix with pseudostates method. *Journal of Physics B: Atomic, Molecular and Optical Physics*, 30(17):3897–3911, sep 1997.

[40] Hans R. Griem. *Principles of Plasma Spectroscopy*. Cambridge Monographs on Plasma Physics. Cambridge University Press, 1997.

[41] D. C. Griffin, M. S. Pindzola, and N. R. Badnell. Low-energy total and differential cross sections for the electron-impact excitation of Si 2 + and Ar 6 +. *Physical Review A*, 47(4):2871–2880, apr 1993.

[42] D. C. Griffin, M. S. Pindzola, and C. Bottcher. Distorted-wave calculations of dielectronic recombination cross sections in the Li isoelectronic sequence. *Physical Review A*, 31(2):568–575, feb 1985.

[43] M. F. Gu. Dielectronic Recombination Rate Coefficients for H-like through Ne-like Isosequences of Mg, Si, S, Ar, Ca, Fe, and Ni. *The Astrophysical Journal*, 590(2):1131–1140, jun 2003.

[44] E.M. Hollmann, T.C. Jernigan, P.B. Parks, J.A. Boedo, T.E. Evans, M. Groth, D.A. Humphreys, A.N. James, M.J. Lanctot, D. Nishijima, D.L. Rudakov, H.A. Scott, E.J. Strait, M.A. Van Zeeland, J.C. Wesley, W.P. West, W. Wu, and J.H. Yu. Measurements of injected impurity assimilation during massive gas injection experiments in DIII-D. *Nuclear Fusion*, 48(11), nov 2008.

[45] M. Hoshino, H. Murai, H. Kato, Y. Itikawa, M.J. Brunger, and H. Tanaka. Resolution of a significant discrepancy in the electron impact excitation of the 3s[3/2]1 and 3s[1/2]1 low-lying electronic states in neon. *Chemical Physics Letters*, 585:33–36, 2013.

[46] Ian Hutchinson. *Principles of Plasma Diagnostics*. Cambridge University Press, 2009.

[47] R.K. Janev, D.E. Post, W.D. Langer, K. Evans, D.B. Heifetz, and J.C. Weisheit. Survey of atomic processes in edge plasmas. *Journal of Nuclear Materials*, 121:10–16, may 1984.

[48] R. O. Jung, John B. Boffard, L. W. Anderson, and Chun C. Lin. Excitation into 3 p 5 5 p levels from the metastable levels of Ar. *Physical Review A*, 75(5):052707, may 2007.

[49] F. P. Keenan, F. C. McKenna, K. L. Bell, C. A. Ramsbottom, A. W. Wickstead, L. H. Aller, and S. Hyung. Nebular and Auroral Emission Lines of [Ar iv] in the Optical Spectra of Planetary Nebulae. *The Astrophysical Journal*, 487(1):457–462, sep 1997.

[50] M A Khakoo, P Vandeventer, J G Childers, I Kanik, C J Fontes, K Bartschat, V Zeman, D H Madison, S Saxena, R Srivastava, and a D Stauffer. Electron impact excitation of the argon 3p 5 4s configuration: differential cross-sections and cross-section ratios. *Journal of Physics B: Atomic, Molecular and Optical Physics*, 37(1):247–281, jan 2004.

[51] A. Kramida and Yu Ralchenko. NIST Atomic Spectra Database Levels Form, 2014.

[52] M. Landini and B. C. Monsignori Fossi. A simple formula for the total dielectronic recombination coefficient. *Solar Physics*, 20(2):322–331, nov 1971.

[53] Irving Langmuir and H. M. Mott-Smith. Studies of Electric Discharges in Gases at Low Pressures. *Gen. Elec. Rev.*, 27:449, 538, 616, 762, 810, 1924.

[54] M. Lehnen, A. Alonso, G. Arnoux, N. Baumgarten, S.A. Bozhenkov, S. Brezinsek, M. Brix, T. Eich, S.N. Gerasimov, A. Huber, S. Jachmich, U. Kruezi, P.D. Morgan, V.V. Plyusnin, C. Reux, V. Riccardo, G. Sergienko, and M.F. Stamp. Disruption mitigation by massive gas injection in JET. *Nuclear Fusion*, 51(12):123010, dec 2011.

[55] Stephen Lepp. Atomic and Molecular Processes in the Early Universe. *AIP Conference Proceedings*, 770(1):393–398, may 2005.

[56] DongLin Liu, XiaoPing Li, Kai Xie, ZhiWei Liu, and MingXu Shao. Analysis of double-probe characteristics in low-frequency gas discharges and its improvement. *Review of Scientific Instruments*, 86(1):013504, jan 2015.

[57] S. D. Loch, Sh A. Abdel-Naby, C. P. Ballance, and M. S. Pindzola. Electron-impact ionization and recombination of M -shell atomic ions in the argon isonuclear sequence. *Physical Review A - Atomic, Molecular, and Optical Physics*, 76(2), aug 2007.

[58] Katharina Lodders. The Solar Argon Abundance. *The Astrophysical Journal*, 674(1):607–611, feb 2008.

[59] P Mazzotta, G Mazzitelli, S Colafrancesco, and N Vittorio. Ionization balance for optically thin plasmas: Rate coefficients for all atoms and ions of the elements H to Ni. *Astronomy and Astrophysics Supplement Series*, 133(3):403–409, dec 1998.

[60] H C Meng, P Greve, H J Kunze, and T Schmidt. Experimental rate coefficients for dielectronic recombination and ionization of Ar viii to Ar xii. *Physical Review A*, 31(5):3276–3281, 1985.

[61] A L Merts, R D Cowan, and N H Magee. The Calculated Power Output from a Thin Iron Seeded Plasma. *LANL Internal Report*, LA-6220-MS, 1976.

[62] D. M. Mitnik and N. R. Badnell. Dielectronic recombination data for dynamic finite-density plasmas VIII. The nitrogen isoelectronic sequence. *Astronomy and Astrophysics*, 425(3):1153–1159, oct 2004.

[63] H. M. Mott-Smith and Irving Langmuir. The Theory of Collectors in Gaseous Discharges. *Physical Review*, 28(4):727–763, oct 1926.

[64] G Pautasso, D Coster, T Eich, J C Fuchs, O Gruber, A Gude, A Herrmann, V Igochine, C Konz, B Kurzan, K Lackner, T Lunt, M Maraschеck, A Mlynek, B Reiter, V Rohde, Y Zhang, X Bonnin, M Beck, and G Prausner. Disruption studies in ASDEX Upgrade in view of ITER. *Plasma Physics and Controlled Fusion*, 51(12):124056, dec 2009.

[65] A. Jonathan Pearce. The role of atomic excited states in laboratory plasmas and a study in fine structure diagnostics for far infra-red astrophysical observations. *Auburn University Electronic Theses and Dissertations*, dec 2016.

[66] Garrett A. Piech, John B. Boffard, Mark F. Gehrke, L. W. Anderson, and Chun C. Lin. Measurement of Cross Sections for Electron Excitation out of the Metastable Levels of Argon. *Physical Review Letters*, 81(2):309–312, jul 1998.

[67] N.R. Pindzola, M.S. Badnell and D.C. Griffin. Validity of the independent-processes and isolated-resonance approximations for electron-ion recombination. *Physical Review A*, 1992.

[68] A. Pospieszczyk. *High-Temperature Plasma Edge Diagnostics*, pages 135–161. Springer Berlin Heidelberg, Berlin, Heidelberg, 2005.

[69] R. Raman, T. R. Jarboe, B. A. Nelson, S. P. Gerhardt, W. S. Lay, and G. J. Plunkett. Design and operation of a fast electromagnetic inductive massive gas injection valve for NSTX-U. *Review of Scientific Instruments*, 85(11), nov 2014.

[70] J. C. Raymond and N. S. Brickhouse. Atomic Processes in Astrophysics. *Astrophysics and Space Science*, 237(1-2):321–340, nov 1996.

[71] C. Reux, J. Bucalossi, F. Saint-Laurent, C. Gil, P. Moreau, and P. Maget. Experimental study of disruption mitigation using massive injection of noble gases on Tore Supra. *Nuclear Fusion*, 50(9), sep 2010.

[72] J. M. Shull and M. Van Steenberg. The ionization equilibrium of astrophysically abundant elements. *The Astrophysical Journal Supplement Series*, 48:95–107, jan 1982.

[73] H P Summers. The ADAS user manual, version 2.6. `http://www.adas.ac.uk`, 2004.

[74] H P Summers, W J Dickson, M G O'Mullane, N R Badnell, A D Whiteford, D H Brooks, J Lang, S D Loch, and D C Griffin. Ionization state, excited populations and emission of impurities in dynamic finite density plasmas: I. The generalized collisionalradiative model for light elements. *Plasma Physics and Controlled Fusion*, 48(2):263–293, feb 2006.

[75] Edward Thomas, Ashley Eadon, and Edwynn A. Wallace. Suppression of low frequency plasma instabilities in a magnetized plasma column. *Physics of Plasmas*, 12(4):042109, apr 2005.

[76] A.J. Thornton, K.J. Gibson, I.T. Chapman, J.R. Harrison, A. Kirk, S.W. Lisgo, M. Lehnen, R. Martin, R. Scannell, and A. Cullen. Plasma profile evolution during disruption mitigation via massive gas injection on MAST. *Nuclear Fusion*, 52(6), jun 2012.

[77] Edwynn Wallace, Edward Thomas, Ashley Eadon, and Jon David Jackson. Design and initial operation of the Auburn Linear Experiment for Instability Studies: A new plasma experiment for studying shear driven flows. *Review of Scientific Instruments*, 75(12):5160, 2004.

[78] D.G. Whyte, R. Granetz, M. Bakhtiari, V. Izzo, T. Jernigan, J. Terry, M. Reinke, and B. Lipschultz. Disruption mitigation on Alcator C-Mod using high-pressure gas injection: Experiments and modeling toward ITER. *Journal of Nuclear Materials*, 363-365:1160–1167, jun 2007.

[79] E. P. Wigner and L. Eisenbud. Higher Angular Momenta and Long Range Interaction in Resonance Reactions. *Physical Review*, 72(1):29–41, jul 1947.

[80] O. Zatsarinny, T. W. Gorczyca, J. Fu, K. T. Korista, N. R. Badnell, D. W. Savin, Z. Altun, A. Yumak, N. R. Badnell, J. Colgan, M. S. Pindzola, O. Zatsarinny, T. W. Gorczyca, K. T. Korista, N. R. Badnell, D. W. Savin, Z. Altun, A. Yumak, N. R. Badnell, S. D. Loch, M. S. Pindzola, D. M. Mitnik, and N. R. Badnell. Dielectronic recombination data for dynamic finite-density plasmas. *Astronomy and Astrophysics*, 425(3):1153–1159, mar 2004.

[81] O. Zatsarinny, T. W. Gorczyca, K. Korista, N. R. Badnell, and D. W. Savin. Dielectronic recombination data for dynamic finite-density plasmas VII. The neon isoelectronic sequence. *Astronomy and Astrophysics*, 426(2):699–705, nov 2004.

[82] Oleg Zatsarinny, Yang Wang, and Klaus Bartschat. Electron-impact excitation of argon at intermediate energies. *Physical Review A - Atomic, Molecular, and Optical Physics*, 89(2):022706, feb 2014.

Appendix A

Magnetic fields in ALEXIS.

A.1 Magnetic fields in ALEXIS

The following three tables map out the magnetic field in ALEXIS at the viewports 2, 4, and 6. All spectroscopic and probe based measurements given in this dissertation were taken at one of these three ports. All the values in these tables correspond to a measurement taken at the center of the ALEXIS vacuum chamber ($r = 0$ cm).

Table A.1: The magnetic field in ALEXIS at viewport 2 in Gauss, as a function of the current in chamber and source power supplies.

	Current: Small Power Supply (Amps)																
Current : Large Power Supply (Amps)	**0**	**20**	**30**	**40**	**50**	**60**	**70**	**80**	**90**	**100**	**120**	**140**	**160**	**180**	**200**	**225**	**250**
20	70.1	70.3	70.7	70.7	70.7	70.7	70.9	71.1	71.4	71.5	71.8	71.9	72.4	72.8	72.8	73.6	
30	102.6	102.8	103.2	103.2	103.2	103.2	103.4	103.6	103.9	104.0	104.3	104.4	104.9	105.3	105.3	106.1	
40	135.5	135.7	136.1	136.1	136.1	136.1	136.3	136.5	136.8	136.9	137.2	137.3	137.8	138.2	138.2	139.0	
50	168.4	168.6	169.0	169.0	169.0	169.0	169.2	169.4	169.7	169.8	170.1	170.2	170.7	171.1	171.1	171.9	
60	201.5	201.7	202.1	202.1	202.1	202.1	202.3	202.5	202.8	202.9	203.2	203.3	203.8	204.2	204.2	205.0	
70	234.0	234.2	234.6	234.6	234.6	234.6	234.8	235.0	235.3	235.4	235.7	235.8	236.3	236.7	236.7	237.5	
80	266.3	266.5	266.9	266.9	266.9	266.9	267.1	267.3	267.6	267.7	268.0	268.1	268.6	269.0	269.0	269.8	
90	299.3	299.5	299.9	299.9	299.9	299.9	300.1	300.3	300.6	300.7	301.0	301.1	301.6	302.0	302.0	302.8	
100	331.6	331.8	332.2	332.2	332.2	332.2	332.4	332.6	332.9	333.0	333.3	333.4	333.9	334.3	334.3	335.1	
120	397.9	398.1	398.5	398.5	398.5	398.5	398.7	398.9	399.2	399.3	399.6	399.7	400.2	400.6	400.6	401.4	
140	463.3	463.5	463.9	463.9	463.9	463.9	464.1	464.3	464.6	464.7	465.0	465.1	465.6	466.0	466.0	466.8	
160	529.3	529.5	529.9	529.9	529.9	529.9	530.1	530.3	530.6	530.7	531.0	531.1	531.6	532.0	532.0	532.8	
180	595.3	595.5	595.9	595.9	595.9	595.9	596.1	596.3	596.6	596.7	597.0	597.1	597.6	598.0	598.0	598.8	
200	660.6	660.8	661.2	661.2	661.2	661.2	661.4	661.6	661.9	662.0	662.3	662.4	662.9	663.3	663.3	664.1	
225	743.4	743.6	744.0	744.0	744.0	744.0	744.2	744.4	744.7	744.8	745.1	745.2	745.7	746.1	746.1	746.9	
250	825.8	826.0	826.4	826.4	826.4	826.4	826.6	826.8	827.1	827.2	827.5	827.6	828.1	828.5	828.5	829.3	

Table A.2: The magnetic field in ALEXIS at viewport 4 in Gauss, as a function of the current in the chamber and source power supplies.

	Current: Small Power Supply (Amps)																
Current : Large Power Supply (Amps)	**0**	**20**	**30**	**40**	**50**	**60**	**70**	**80**	**90**	**100**	**120**	**140**	**160**	**180**	**200**	**225**	**250**
20	69.3	69.3	69.3	69.3	69.3	69.3	69.3	69.5	69.9	69.9	69.9	69.9	69.9	70.0	70.0	70.3	
30	101.3	101.3	101.3	101.3	101.3	101.3	101.3	101.5	101.9	101.9	101.9	101.9	101.9	102.0	102.0	102.3	
40	133.4	133.4	133.4	133.4	133.4	133.4	133.4	133.6	134.0	134.0	134.0	134.0	134.0	134.1	134.1	134.4	
50	165.5	165.5	165.5	165.5	165.5	165.5	165.5	165.7	166.1	166.1	166.1	166.1	166.1	166.2	166.2	166.5	
60	197.9	197.9	197.9	197.9	197.9	197.9	197.9	198.1	198.5	198.5	198.5	198.5	198.5	198.6	198.6	198.9	
70	229.5	229.5	229.5	229.5	229.5	229.5	229.5	229.7	230.1	230.1	230.1	230.1	230.1	230.2	230.2	230.5	
80	261.4	261.4	261.4	261.4	261.4	261.4	261.4	261.6	262.0	262.0	262.0	262.0	262.0	262.1	262.1	262.4	
90	293.5	293.5	293.5	293.5	293.5	293.5	293.5	293.7	294.1	294.1	294.1	294.1	294.1	294.2	294.2	294.5	
100	325.3	325.3	325.3	325.3	325.3	325.3	325.3	325.5	325.9	325.9	325.9	325.9	325.9	326.0	326.0	326.3	
120	389.8	389.8	389.8	389.8	389.8	389.8	389.8	390.0	390.4	390.4	390.4	390.4	390.4	390.5	390.5	390.8	
140	454.0	454.0	454.0	454.0	454.0	454.0	454.0	454.2	454.6	454.6	454.6	454.6	454.6	454.7	454.7	455.0	
160	518.3	518.3	518.3	518.3	518.3	518.3	518.3	518.5	518.9	518.9	518.9	518.9	518.9	519.0	519.0	519.3	
180	582.3	582.3	582.3	582.3	582.3	582.3	582.3	582.5	582.9	582.9	582.9	582.9	582.9	583.0	583.0	583.3	
200	646.4	646.4	646.4	646.4	646.4	646.4	646.4	646.6	647.0	647.0	647.0	647.0	647.0	647.1	647.1	647.4	
225	726.8	726.8	726.8	726.8	726.8	726.8	726.8	727.0	727.4	727.4	727.4	727.4	727.4	727.5	727.5	727.8	
250	807.0	807.0	807.0	807.0	807.0	807.0	807.0	807.2	807.6	807.6	807.6	807.6	807.6	807.7	807.7	808.0	

Table A.3: The magnetic field in ALEXIS at viewport 6 in Gauss, as a function of the current in the chamber and source power supplies.

	Current: Small Power Supply (Amps)																
Current : Large Power Supply (Amps)	**0**	**20**	**30**	**40**	**50**	**60**	**70**	**80**	**90**	**100**	**120**	**140**	**160**	**180**	**200**	**225**	**250**
	20	69.3	69.3	69.3	69.3	69.3	69.3	69.3	69.5	69.9	69.9	69.9	69.9	69.9	70.0	70.00	70.3
	30	101.3	101.3	101.3	101.3	101.3	101.3	101.3	101.5	101.9	101.9	101.9	101.9	101.9	102.0	102.00	102.3
	40	133.4	133.4	133.4	133.4	133.4	133.4	133.4	133.6	134.0	134.0	134.0	134.0	134.0	134.1	134.10	134.4
	50	165.5	165.5	165.5	165.5	165.5	165.5	165.5	165.7	166.1	166.1	166.1	166.1	166.1	166.2	166.20	166.5
	60	197.9	197.9	197.9	197.9	197.9	197.9	197.9	198.1	198.5	198.5	198.5	198.5	198.5	198.6	198.60	198.9
	70	229.5	229.5	229.5	229.5	229.5	229.5	229.5	229.7	230.1	230.1	230.1	230.1	230.1	230.2	230.20	230.5
	80	261.4	261.4	261.4	261.4	261.4	261.4	261.4	261.6	262.0	262.0	262.0	262.0	262.0	262.1	262.10	262.4
	90	293.5	293.5	293.5	293.5	293.5	293.5	293.5	293.7	294.1	294.1	294.1	294.1	294.1	294.2	294.20	294.5
	100	325.3	325.3	325.3	325.3	325.3	325.3	325.3	325.5	325.9	325.9	325.9	325.9	325.9	326.0	326.00	326.3
	120	389.8	389.8	389.8	389.8	389.8	389.8	389.8	390.0	390.4	390.4	390.4	390.4	390.4	390.5	390.50	390.8
	140	454.0	454.0	454.0	454.0	454.0	454.0	454.0	454.2	454.6	454.6	454.6	454.6	454.6	454.7	454.70	455.0
	160	518.3	518.3	518.3	518.3	518.3	518.3	518.3	518.5	518.9	518.9	518.9	518.9	518.9	519.0	519.00	519.3
	180	582.3	582.3	582.3	582.3	582.3	582.3	582.3	582.5	582.9	582.9	582.9	582.9	582.9	583.0	583.00	583.3
	200	646.4	646.4	646.4	646.4	646.4	646.4	646.4	646.6	647.0	647.0	647.0	647.0	647.0	647.1	647.10	647.4
	225	726.8	726.8	726.8	726.8	726.8	726.8	726.8	727.0	727.4	727.4	727.4	727.4	727.4	727.5	727.50	727.8
	250	807.0	807.0	807.0	807.0	807.0	807.0	807.0	807.2	807.6	807.6	807.6	807.6	807.6	807.7	807.70	808.0

Appendix B

DR Fitting Coefficients.

Table B.1: Level-resolved fitting coefficients for all metastable states residing in the ground state term for each ion stage, in accordance with the formula: $\hat{\alpha}_d = \frac{1}{T^{\frac{3}{2}} \sum_i c_i \exp(\frac{E_i}{T})}\ cm^3 s^{-1}$. These coefficients are valid for temperatures greater than $1{\times}10^{-2}$ eV. For all ion stages the ground level is given first.

Ar^+		$i=1$	$i=2$	$i=3$	$i=4$	$i=5$	$i=6$	$i=7$
$^2P^o_{\frac{3}{2}}$	c_i	1.0983E-14	2.6689E-14	-6.0158E-15	9.0790E-12	7.8787E-10	7.4331E-10	**
	E_i	1.5273E-02	1.3541E-01	4.6362E-01	1.0846E+01	2.0307E+01	2.6388E+01	**
$^2P^o_{\frac{1}{2}}$	c_i	7.4775E-12	2.2403E-11	5.5900E-10	1.6735E-09	4.2855E-09	-5.2560E-09	**
	E_i	1.2879E+01	1.4182E+01	1.9480E+01	3.1527E+01	2.9611E+01	3.0708E+01	**
Ar^{2+}		$i=1$	$i=2$	$i=3$	$i=4$	$i=5$	$i=6$	$i=7$
$^3P_2$	c_i	2.3518E-13	8.5594E-13	6.0556E-13	3.8477E-12	4.1757E-10	7.9994E-09	**
	E_i	1.8934E-02	1.0078E-01	2.9404E-01	1.4112E+00	1.6058E+01	2.7302E+01	**
$^3P_1$	c_i	1.2900E-13	2.7459E-13	3.3577E-12	9.7089E-12	7.1249E-10	5.5821E-09	**
	E_i	2.2065E-02	9.2978E-02	1.0973E+00	6.2188E+00	1.9142E+00	2.7414E+01	**
$^3P_0$	c_i	1.4604E-13	3.6477E-14	3.7968E-13	3.8427E-12	3.3904E-10	4.6877E-09	**
	E_i	2.2260E-02	7.1580E-02	5.0116E-01	1.3002E+04	1.6183E+01	2.7000E+01	**
$^1D_2$	c_i	2.2885E-14	8.6547E-15	3.4268E-13	7.7442E-12	4.3990E-10	3.0671E-09	2.9595E-09
	E_i	1.1561E-01	2.5727E-01	1.1408E+00	8.2856E+00	1.8904E+01	2.4229E+01	2.7293E+01
$^1S_0$	c_i	5.1567E-14	1.0411E-13	2.8288E-12	1.4064E-10	1.0129E-09	2.4454E-09	**
	E_i	5.1902E+00	5.5638E+00	7.4569E+00	1.0347E+01	1.9783E+01	2.4349E+01	**
Ar^{3+}	$i=1$	$i=2$	$i=3$	$i=4$	$i=5$	$i=6$	$i=7$	
$^4S^o_{\frac{3}{2}}$	c_i	2.4638E-12	1.6639E-11	1.1359E-10	4.7037E-10	4.8077E-09	5.8236E-08	**
	E_i	6.9544E-02	1.7083E-01	5.4765E-01	1.6831E+00	1.2356E+01	2.8135E+01	**
$^2D^o_{\frac{3}{2}}$	c_i	3.80E-011	-3.80E-011	7.61E-011	1.78E-010	2.08E-009	8.36E-009	2.86E-010
	E_i	1.7128E-03	3.2988E-01	4.4731E-01	2.4927E+00	1.1499E+01	2.4331E+01	5.2811E+01
$^2D^o_{\frac{5}{2}}$	c_i	6.2668E-13	3.4592E-12	2.6115E-11	1.2430E-10	1.1704E-09	8.0403E-09	2.1772E-09
	E_i	3.1243E-02	1.9811E-01	6.5257E-01	1.9300E+00	8.8931E+00	2.1375E+01	3.4095E+01
$^2P^o_{\frac{1}{2}}$	c_i	4.1376E-12	8.3143E-12	4.8110E-12	5.1680E-11	7.2868E-10	4.8085E-09	2.3306E-09
	E_i	8.5443E-03	1.3361E-01	3.6940E-01	1.3981E+00	6.9227E+00	1.7941E+01	3.0174E+01
$^2P^o_{\frac{3}{2}}$	c_i	3.6918E-12	8.5537E-12	2.2188E-11	4.7454E-11	7.9794E-10	6.1916E-09	1.5594E

	E_i	3.8871E-02	1.3170E-01	5.7974E-01	1.7251E+00	7.0394E+00	1.9361E+01	3.3996E+01
Ar^{4+}		$i=1$	$i=2$	$i=3$	$i=4$	$i=5$	$i=6$	$i=7$
$^3P_0$	c_i	4.1437E-11	1.4879E-10	3.0398E-09	-2.9118E-09	2.5038E-09	2.0319E-08	**
	E_i	2.0993E-02	9.6851E-02	2.7122E+00	2.7846E+00	1.5655E+01	2.7789E+01	**
$^3P_1$	c_i	2.4891E-11	3.0131E-11	7.5872E-11	1.1255E-10	2.9087E-09	1.7628E-09	**
	E_i	3.0274E-02	1.0503E-01	8.8362E-01	3.4583E+00	1.6876E+01	2.7727E+01	**
$^3P_2$	c_i	1.5550E-12	8.9377E-12	1.7896E-11	9.9536E-11	1.3781E-09	3.6532E-09	1.4515E-08
	E_i	1.4455E-02	1.1839E-01	3.2250E-01	1.1490E+00	5.1091E+00	1.8336E+01	2.7648E+01
$^1D_2$	c_i	5.5443E-13	9.6954E-13	5.3626E-12	1.1512E-10	1.1812E-09	4.3213E-09	9.3596E-11
	E_i	3.2151E-01	4.2359E-01	1.2912E+00	6.6792E+00	1.5924E+01	2.5221E+01	4.4734E+01
$^5S_2^o$	c_i	6.2195E-14	1.5485E-12	2.1155E-12	5.3028E-11	9.5122E-10	1.7018E-09	3.9862E-12
	E_i	1.2048E-01	2.6344E-01	8.7096E-01	4.9045E+00	1.2609E+01	2.2800E+01	1.4859E+02
$^3D_1^o$	c_i	3.6351E-14	7.6817E-12	9.5989E-12	1.3338E-10	5.1928E-10	8.3712E-10	6.2000E-12
	E_i	3.9321E-02	2.0088E-01	6.9298E-01	3.3271E+00	9.2379E+00	1.6742E-09	8.2839E+01
Ar^{5+}		$i=1$	$i=2$	$i=3$	$i=4$	$i=5$	$i=6$	$i=7$
$^2P^o_{\frac{1}{2}}$	c_i	6.7355E-12	4.8557E-12	1.8319E-12	1.5839E-10	9.0394E-10	1.3519E-08	2.5038E-08
	E_i	7.9759E-02	1.7551E-01	3.1290E-01	2.8034E+00	9.0606E+00	1.9003E+01	2.6649E+01
$^2P^o_{\frac{3}{2}}$	c_i	1.1999E-12	2.3998E-12	6.8235E-11	2.6798E-10	8.4794E-09	2.2078E-08	**
	E_i	7.3349E-01	8.3225E-01	2.0813E+00	4.4133E+00	1.6042E+01	2.5453E+01	**
$^4P_{\frac{1}{2}}$	c_i	2.1245E-12	3.3521E-12	3.7110E-11	3.0653E-10	7.0075E-10	7.0075E-10	2.3608E-10
	E_i	2.7781E-02	1.1183E-01	9.0300E-01	3.4942E+00	1.0323E+01	1.0323E+01	2.0573E+01
$^4P_{\frac{3}{2}}$	c_i	3.0380E-13	1.0337E-12	2.2454E-11	6.8157E-11	4.3269E-10	1.3501E-09	9.1917E-11
	E_i	4.6529E-02	1.5615E-01	7.1917E-01	2.0110E+00	4.9299E+00	1.1570E+01	2.5144E+01
$^4P_{\frac{5}{2}}$	c_i	2.8096E-13	2.2550E-12	1.6130E-11	7.8012E-11	3.9719E-10	1.2517E-09	1.2732E-10
	E_i	1.1706E-01	2.2493E-01	6.3597E-01	1.9865E+00	5.0063E+00	1.1177E+01	2.2990E+01

Appendix C

Creating usable GCR Data.

Getting the code. The codes referenced in this section (with the exception of the FORTRAN utility code `sortadf04.f`) are maintained by Connor Ballance. For access to these codes, plus a much more detailed review of their usage, please visit `connorb.freeshell.org`.

The FORTRAN utility code `sortadf04.f` (used to insert non-dipole rates into an ADF04 file) is freely available on github under an MIT license at `https://github.com/AUAMO/atomic_data_codes`.

The R-Matrix codes used to generate the collisional rate coefficients usually result in very large data files, labeled as "OMEGA" files, containing the collision strengths. The GCR codes require excitation rate coefficients, generated from these collision strengths. For example, the result of the R-Matrix excitation calculation performed by Connor Ballance is a neutral argon OMEGA file that is $\approx$ 1.2GB in size. We will also use this ADF04 file to calculate branching ratios for the purpose of determining the cascade contribution to excitation cross-sections, which we will compare to experimental data observed by the Wisconsin group, as detailed in Chapter 3. This appendix describes the process of converting an OMEGA file into an ADF04 file.

To accomplish this, we can start by recognizing that while there are 450 levels in the R-Matrix calculation, only 57 of these levels represent spectroscopic orbitals. The remaining levels are Laguerre pseudo-orbitals used to represent high lying Rydberg states and the energy continuum, and are used to increase the accuracy of our calculation by considering the interaction between target states and the continuum. However, they do not represent

bound states, and it is not necessary to include them for purposes of calculating cross-sections, branching ratios, PEC's, etc. Therefore, a significant reduction in file size can be accomplished by simply removing the atomic data for the 393 levels that are not bound states. This is accomplished by the FORTRAN utility code `omgred.f`. The resulting output is an OMEGA file that has been reduced to the specified number of levels.

Our R-Matrix excitation calculation only includes dipole rates; we will use AUTOSTRUCTURE to calculate the non-dipole radiative rates. Our final adf04 file will result from combining the dipole and non-dipole rates resulting from the R-Matrix and AUTOSTRUCTRURE calculations, respectively, using the FORTRAN utility code `sortadf04.f`. First, however, we must reorder the OMEGA file to match the AUTOSTRUCTURE energy order. This is accomplished by the utlity code `omorder.f`, which requires the input file `dord`. Here is a simple example `dord` file:

```
&OMORDER ELAS='NO' &END


1   1
2   8
...
...
6   7
7   6
8   2
```

After a short namelist (the ELAS flag turns elastic collisions on or off), the file is simply two columns. Column 1 is the original position of the energy level, column two is its new position. In this example, levels 2 and 8 have been swapped, along with levels 6 and 7. In this way the energies of the omega file can be reordered to match those from AUTOSTRUCTURE. `omorder.f` takes an OMEGA file and a dord file as input, and returns a reordered OMEGA file.

Now that we have an OMEGA file that is in the same energy order as AUTOSTRUCTURE, we can use the utility code `adasexj.f` to create an adf04 file from our OMEGA file. `adasexj.f` takes an OMEGA file and input file adasexjin as input, and returns an adf04 data file suitable for use with ADAS. Here is an example adasexjin.

```
&ADASEX NLEVS=57  FIPOT=127110.0 IEL='Ar' NUMTMP=12 IRDTMP=1 MXTMP=1 ielas=-1 &END
1.00+03 2.00+03 5.00+03 1.00+04 2.00+04 3.00+04 4.00+04 6.00+04 8.00+04 1.00+05 1.50+05
1 1S2 2S2 2P6 3S2 3P6                (1)0( 0.0)               0.0000
2 1S2 2S2 2P6 3S2 3P5 4S1            (3)1( 2.0)           93143.7600
3 1S2 2S2 2P6 3S2 3P5 4S1            (3)1( 1.0)           93750.5978
4 1S2 2S2 2P6 3S2 3P5 4S1            (3)1( 0.0)           94553.6652
5 1S2 2S2 2P6 3S2 3P5 4S1            (1)1( 1.0)           95399.8276
6 1S2 2S2 2P6 3S2 3P5 4P1            (3)0( 1.0)          104102.0990
...
...
56 1S2 2S2 2P6 3S2 3P5 4F1            (1)3( 3.0)          120249.8760
57 1S2 2S2 2P6 3S2 3P5 4F1            (3)3( 4.0)          120249.9140
```

Row 1 is a namelist used to control various flags in the `adasexj.f` code. Row 2 is a list of energies whose number must match the NUMTMP flag in the previous row. These two rows are followed by a list of configurations and corresponding energies that can be found at the bottom of the "olg" data file that results from an AUTOSTRUCTURE run.

At this point, non-dipole rates can be included using the utility code `sortadf04.f`. This code takes two adf04 files as input and returns an adf04 file that merges the non-dipole rates from the first into the second. As a final step, we then shift the values for all of the energies to their NIST equivalents for spectroscopic accuracy, effectively fixing the position of any emission lines from a resulting synthetic spectrum. The result is a 57 level adf04 file that includes non-dipole rates and contains NIST accurate energy levels, suitable for use by ADAS208.

The flow chart in Figure C.1 illustrates the process detailed in this appendix.

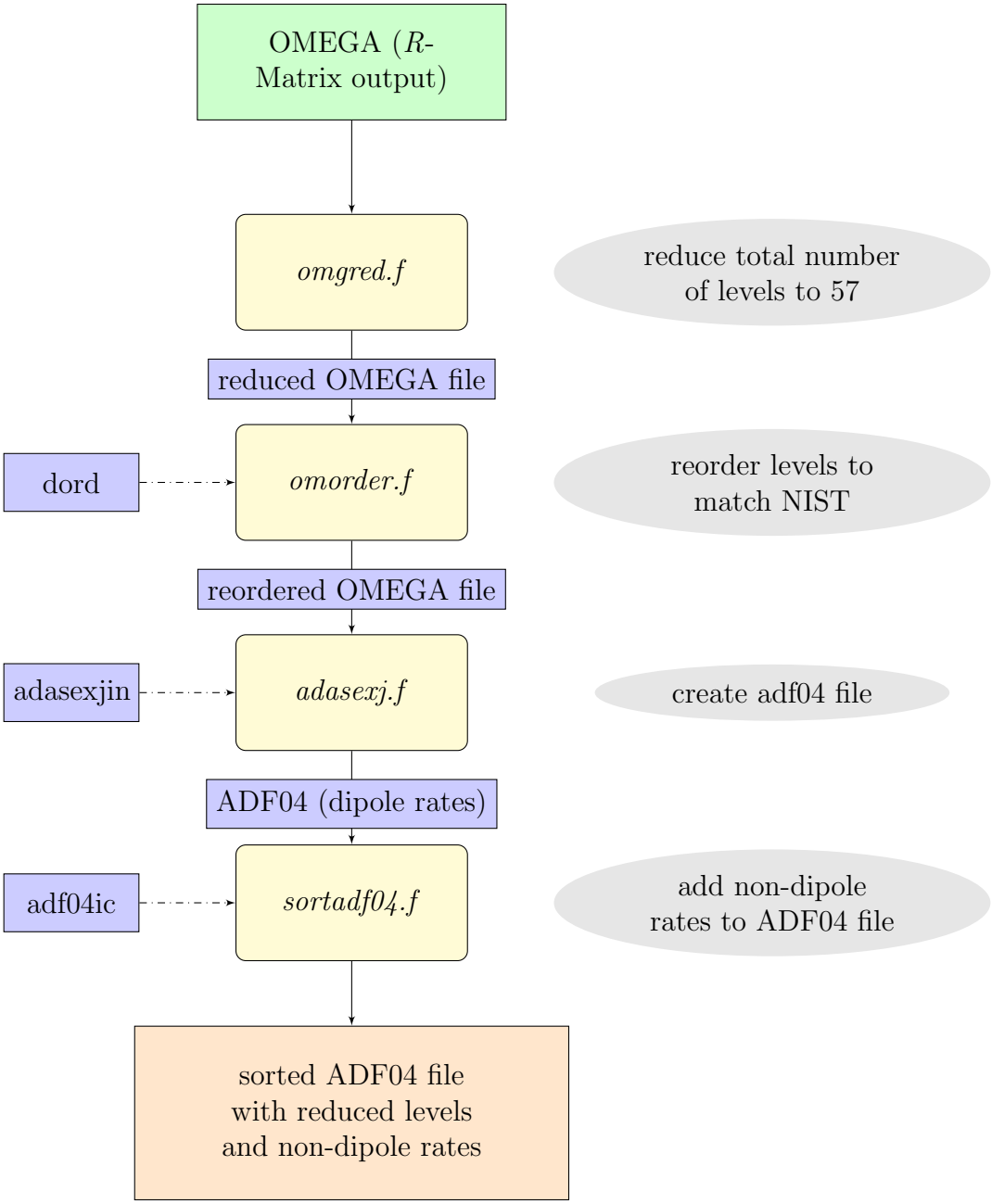

Figure C.1: Flow chart for creating GCR data from R-Matrix output.

Appendix D

Chapter 2 Codes (ELEX).

Beyond the R-Matrix utility codes discussed in Appendix B, Chapter 3 uses code developed and maintained by the author to calculate *branching fractions* for neutral argon excitation cross-sections. These branching fractions are then used to determine the contribution of cascade cross-sections from an upper level k to a lower level i. As detailed in Chapter 2, the cascade contribution can be described by:

$$Q_{ki}^{cas} = Br_{ki} * Q_{ki}^{opt} \tag{D.1}$$

where Br is the *branching fraction*, and is determined from Einstein A-values using:

$$Br_{ki} = \frac{A_{ki}}{\sum_{j<k} A_{kj}} \tag{D.2}$$

where it is understood that the sum over j is taken over all possible values $\neq k$. For example, in a system with only three levels and corresponding A-Values A_{21}, A_{31}, and A_{32}, the branching fraction Br_{31} would be written as $\frac{A_{31}}{A_{21}+A_{31}+A_{32}}$.

The code used to determine these branching fractions is `brat.py`. `brat.py` is written in python3 and makes use of a FORTRAN subroutine developed with the help of Connor Ballance. It also utilizes a python3 utility script developed by the author to read data from a standard ADAS ADF04 data file, named `read_adf04.py`. The code is freely available under the MIT license, and can be found at: `https://github.com/AUAMO/atomic_data_codes` (look in the subfolder "brat").

`brat.py` was designed specifically for this project, and is not guaranteed to work without modification for any other purpose than that described in this appendix.

Installing the Dependencies.

- A quick but not necessarily complete list of dependencies for brat.py include python3, python3-numpy, python3-dev, python3-matplotlib, gfortran, gcc, and the aforementioned `read_adf04.py`. With the exception of `read_adf04.py`, these are all readily available through standard Linux package management channels. The appropriate command to install these in a Debian based linux distribution (such as Ubuntu) would be:

```
sudo apt-get install python3 python3-numpy python3-dev
python3-matplotlib gfortran  gcc
```

- For Windows 7/8 it is likely best to install a complete scientific Python distribution (such as the excellent one provided by Anaconda and found at: `continuum.io/downloads`), and to install the gnu compiler suite provided by mingw or cygwin. For Windows 10 it is recommended to use the Windows Subsystem for Linux (WSL) environment, which provides a complete Ubuntu userspace with native Windows file system access. This is also known as "Bash on Ubuntu on Windows".

- For Mac OS the recommended Python 3 libraries can be installed using Anaconda (same as Windows) while the necessary gnu compilers can be obtained using homebrew or some other appropriate method. This is left to the user. The author does not use this platform, and has no further insight.

- **It should be noted that the recommended OS is Linux (any variety), or the WSL environment packaged with Windows 10, as these are the platforms used to develop and test the codes.**

`brat.py` requires that the files "omega", "adf04", `branch.for`, "read_adf04.py", and "paschen.dat" are in the same directory. These files are all provided in the github repository. "omega" is the reduced and reordered omega file, with non-dipole rates included, used in Chapter 2 to create the impact excitation cross-sections. It is used here for the same purpose. "adf04" is our NIST shifted ADF04 file. `branch.for` is the FORTRAN subroutine used to extract cross-section information from the file "omega". "read_adf04.py" contains the python function used to extract data from the ADAS ADF04 file. Finally, "paschen.dat" is used for labeling the levels and writing out files with appropriate filenames. It contains an ordered list of the levels in our ADF04 data file, complete with associated energies and configuration information.

Prior to using `brat.py`, the user must compile the FORTRAN subroutine `branch.for` using f2py3, via the following command: `f2py3 -c branch.for -m branch` . This creates a python shared object named `branch.so` (plus a bunch of other files) in the same directory as `brat.py`.

Once the python shared object branch.so has been created using f2py3, the user can run `brat.py` by typing: `python3 brat.py` at a bash command prompt. The user is then prompted to enter the lower level index number, the upper level index number, and the metastable index. In all cases the metastable index is the same as the initial level, making this step somewhat redundant. The upper and lower levels are indexed by the ADF04 file, and listed both in "adf04" and "paschen.dat". As a quick example, to calculate the cascade and direct excitation cross sections for excitation from the 1s5 metastable to the 2p9 excited state of neutral argon, the user would enter 2 for the lower level index, 9 for the upper level index, and 2 for the metastable index.

`brat.py` outputs three separate files:

Data output: brat.py

1. cross-section data file with naming format:

   `<lower-level>_<upper-level>_<delta-j>.dat`

   This file contains data on four columns in the following order: Electron Temperature (eV), Total Cross-Section, Direct Cross-Section, Cascade Cross-Section. Column 2 is the sum of Column 3 and 4.

2. plot with naming format:

   `<lower-level>_<upper-level>_<delta-j>.png`

   A plot of the data from item 1, with the total cross-section in red, direct cross-section in blue, and cascade cross-section in green.

3. condensed branching fraction data file with naming format:

   `bcon_<lower-index>_<upper-index>_<lower-level>_<upper-level>.dat`

   This data file is a condensed list of the total branching fractions out of levels between the lower and upper levels given at the input prompt. Branching fractions less than 1e-10 are disregarded. This floor can be adjusted using the variable ZZERO in `brat.py`.

For all three files, lower and upper levels are given in Paschen notations, and the lower and upper indices are the index numbers in the ADF04 file. Both are listed in "paschen.dat".

Appendix E

Chapter 3 Codes (DR).

The primary code used for the generation of DR rate coefficients in Chapter 2 is AUTOSTRUCTURE. AUTOSTRUCTURE is developed and maintained by Nigel Badnell of the University of Strathclyde. More information about the code (including detailed instructions as to its usage, licensing information, etc...) can be found here: `http://amdpp.phys.strath.ac.uk/autos/`

Appendix F

Chapter 4 Codes (GCR).

F.1 Foreword

All the codes in this appendix are "pure Python" (with one exception, see next section), meaning that they only require Python3 and Python3 libraries to run. The required libraries are either included or available through standard package management channels, either directly using Linux package management (through a standalone distro or through the Windows subsystem for Linux environment bundled with Windows 10), or by using the Python package management system "pip". On all three major platforms (Windows, Linux, or Mac OS), it is sufficient to install Python3 using the Anaconda Scientific Python distribution found at: `continuum.io/Downloads` and installing peakutils using the following command at the Anaconda command prompt:

```
pip install peakutils
```

The user should note that if they choose to install Python3 and the required libraries through standard Linux package management, the list of required dependencies is much longer. A good start is to type (on Debian based distros):

```
sudo apt-get install python3 python3-dev python3-scipy python3-matplotlib
python3-setuptools python3-pip
```

at the command line. After the command completes the user can then type:

```
sudo pip3 install astropy peakutils
```

to install the packages not included in standard package management channels. It is likely that this will still not be sufficient to run all codes, and that other packages will need to be installed either with apt-get or pip as needed.

As in Appendix D, all the codes covered here are specific to neutral argon and the ALEXIS experiment. However, it is the intent of the author to make these codes available in order to be adapted as needed for other projects. The basic functions (i.e. reading in an ADF04 file, generating weighted PEC's, creating synthetic spectra, etc....) have applications beyond those specific to this project, and it is the hope of the author that these routines can be adapted for diagnosing a wide variety of plasmas, including plasmas created from gases besides argon.

The purpose of the code provided in this appendix is to demonstrate the basic functions and techniques used to create the data and plots in Chapter 4. They are not, however, complete versions of the same code used in this work. Instead, this appendix is intended as a presentation of the building blocks (the Python functions) used to create those codes.

All the code in this section is developed and maintained by the author and freely available under the MIT license

F.2 pec_fits_dat.pro

`pec_fits_dat.pro` is an IDL program (script?) that generates a .fits data file containing metastable resolved PEC's on a 2D temperature and density grid. This grid can be changed by the user. There is no input. The output defaults to `pec_dat.fits`. `pec_fits_dat.pro` requires both IDL and ADAS. Licenses for either of these development environments are relatively cost-prohibitive for the individual user, though many universities provide access to one or both. In the future, the author plans to include a variety of PEC data files covering a range of temperature and densities, included in the same github repo as the code covered in this appendix. `pec_fits_dat.pro` also requires the free NASA IDL subroutine

writefits.pro. This is provided, in the same directory as pec_fits_dat.pro. Both can be found at https.github.com/AUAMO/atomic_data_codes/gcr/pec_fits_dat.

To run pec_fits_dat.pro, the user simply launches IDL (either through the workbench or command line) and runs the script. The output is automatically created in the same directory.

F.3 pec_208.py

pec_208.py is a script in Python3 that loads a .fits data file output by pec_fits_dat.pro and imports the PEC information into numpy arrays. It creates arrays for electron temperature, density, wavelengths, and the PEC's themselves. This is a fairly simple script. The user is prompted for a desired wavelength, and the script searches for the nearest PEC corresponding to the user input. It then creates 3D surface plots, one for each metastable, displaying PEC vs a 2D meshgrid of temperature and density. The code can be found here: https.github.com/AUAMO/atomic_data_codes/gcr/pec_208.

Though the code is pretty short and simple, it introduces two things that are used frequently throughout most of the other scripts presented in this section. The first is a way to import .fits data from the output generated by pec_fits_dat.pro:

```
# Import .fits data into numpy arrays.
from astropy.io import fits
hdulist = fits.open('pec_dat_650_950_lowdens.fits')


# Create numpy arrays from the pages in the .fits file
pec_temps = hdulist[0].data       # The array of temps in eV
n_meta = hdulist[1].data          # Array listing the metastable #
pec_dens = hdulist[2].data        # Density array
```

```
pec_wave = hdulist[3].data        # Wavelengths corresponiding to each PEC
pec_pec = hdulist[4].data.T       # 3-D array containing all PEC's
```

In the example above the data file is the one included on github.

The second important piece of code introduced by `pec_208.py` is a python snippet found at some point by the author on Stack Overflow that returns the nearest value and its index from a numpy array. The following snippet returns the nearest value and index for a PEC indexed by the "wavelist" variable:

```
# Function to find the nearest value in an array.
# Returns value and index.
def find_nearest(array, value):
    idx = (np.abs(array - value)).argmin()
    return idx, array[idx]
indx, wavelength = find_nearest(wavelist[:,1], linenum)
```

It should be noted that the surface plots in `pec208.py` require matplotlib > version 0.99, and a recent version of python3-six. The default matplotlib and python3-six packages provided by Ubuntu 16.04 do not meet this requirement, and the script will crash on Ubuntu systems using these default packages. This can be avoided in one of two ways: 1) install the Anaconda Python3 distribution (works on all platforms), which includes updated versions of matplotlib and most of the other scientific python packages. 2) On Ubuntu (or Bash on Ubuntu on Windows), upgrade matplotlib and python3-six using pip3. This means running some variation of the following commands, assuming you have already installed the Ubuntu package python3-pip:

```
sudo apt-get remove python3-matplotlib python3-six
sudo apt-get autoremove
```

```
sudo pip3 install matplotlib six
sudo apt-get install python3-tk
```

Again, the recommended fix is simply to install Anaconda (`continuum.io/Downloads`), especially for beginning Python users.

F.4 qcd_solver

As described in Chapter 4, ADAS208 outputs a file labeled qcd.pass, which contains metastable coupling coefficients (QCD's). `qcd_solver.py` is a Python 3 library containing some useful functions for solving the GCR matrix using these QCD's, and determining how neutral argon metastable populations evolve in time. Its only dependency is numpy. The `qcd_solver.py` library is freely available under an MIT license and can be found at `https:github.com/AUAMO/atomic_data_codes/gcr/qcd_solver`. It contains the following functions:

F.4.1 qcd_reader

Similar to `read_adf04`, `qcd_reader` is a function designed to populate numpy arrays from an ADAS data file. By default it reads data from the file `qcd208.pass`. The function requires the arguments (filename, nmeta) in the format (string, int), where filename is the file to be opened and nmeta is the number of metastables present in the file. An example of how to call this function is: `pop_1s3_matrix = qcd_reader('\verb`qcd208.pass—', nmeta)— , which would return the data from file `qcd208.pass`, with three metastables, into the numpy array pop_1s3_matrix. It is used primarily as in internal subroutine in other functions in this library.

F.4.2 qcd_plotter

Displays 3D surface plots for each metastable's QCD's. It requires the same arguments as `qcd_reader` and can be called by simply adding `qcd_plotter('\verb`qcd208.pass—', nmeta)— to a Python 3 script, or by typing this command into a Python3 or IPython3 console after importing the `qcd_solver` library. It should be noted that this function creates plots for all QCD's in the GCR matrix, which for a three metastable system includes six total plots for the QCD's $Q_{21}, Q_{31}, Q_{12}, Q_{32}, Q_{13}, Q_{23}$.

F.4.3 qcd_eq_solver

Can be used to determine the relative metastable populations at equilibrium. This functions calls internally to generate numpy data arrays from `qcd208.pass`, and solves the time independent GCR QCD matrix. It requires the (filename, nmeta) arguments as the previous two functions.

F.4.4 qcd_td_solver

For a given temperature and density, chosen to match desired plasma conditions, `qcd_td_solver` solves the GCR matrix in a time dependent fashion by assuming that at $t = 0$ the populations of the excited metastables (for argon these are 1s3, 1s5) are zero (i.e. all the atoms are in the ground state). It then determines a suitable time step based on the QCD values stored in `qcd208.pass`' and propagates this solution forward unitl the solution converges. The condition for this convergence is set to be when the variance of the time dependent population matrix is $<$ 1e-10. The output can then be plotted to determine the time dependent evolution of the metastable populations for a specific temperature and density. `qcd_td_solver` requires the arguments (filename, nmeta, t_indx, d_indx) in the format (string, int, int, int). It returns the time dependent population matrix and an array of time steps. It can be called using:

```
t_matrix, td_pop_matrix = qcd_td_solver('\verb|qcd208.pass|', \
                          nmeta = 3, t_indx = 8,  d_indx = 4)
```

F.4.5 Example script to demonstrate qcd_solver.py

The script `ar_qcd_analysis.py` is shown below and included in the github repo containing the `qcd_solver.py` library. It can be run from the command line by typing

```
python3 qcd_solver.py
```

In addition `ar_qcd_analysis.py` makes use of Python "cells" (denoted by (`# %%`), as used by the scientific development environment Spyder, which is installed by default if using Anaconda and can be installed in Ubuntu with the command `sudo apt-get install spyder3` or with pip using `sudo pip3 install spyder`. Spyder allows users to run scripts (and cells) interactively, and is in many ways similar to a MatLAB or IDL Workbench environment.

```
# ar_qcd_analysis.py
# Script to determine equilibrium and time-dependent \
# relative metastable populations for neutral argon \
# using the qcd_solver library.


# %%
import numpy as np
import matplotlib.pyplot as plt


# all the magic is contained the the qcd_solver library
from qcd_solver import *
# %% Create QCD array for equilibrium conditions.
dens_array, temp_array, pop_grd_matrix, pop_1s5_matrix, \
pop_1s3_matrix = qcd_eq_solver('\verb|qcd208.pass|', 3)
```

```
pop1 = pop_grd_matrix[0:25] / pop_1s3_matrix[0:25]
pop2 = pop_grd_matrix[0:25] / pop_1s5_matrix[0:25]
pop3 = pop_1s5_matrix[0:25] / pop_1s3_matrix[0:25]
# %% Create a time dependent QCD array for ALEXIS \
#    relevant temperature and density.
t_matrix, td_pop_matrix = qcd_td_solver('\verb|qcd208.pass|',
nmeta = 3, t_indx = 8,  d_indx = 4)
# %% Surface plot the QCD's
qcd_plotter('\verb|qcd208.pass|', 3)
# %% Plot the time dependent Populations.
fig1 = plt.figure(figsize=(8, 6), facecolor='white')
plt.semilogy(t_matrix, td_pop_matrix[0,:], 'c', label="ground")
plt.semilogy(t_matrix, td_pop_matrix[1,:], 'g', label="1s5")
plt.semilogy(t_matrix, td_pop_matrix[2,:], 'r', label="1s3")

plt.title("ALEXIS: Time dependent metastable populations", \
weight = 'bold', fontsize=14)
plt.xlabel("Time (s)", fontsize=14)
plt.ylabel(r"Rate Coefficient $(cm^3 * s)^{-3}$", fontsize=14)

plt.legend(loc=4)
plt.savefig("td_pop.png", dpi=300)
plt.show(fig1)
print("Plot output saved to td_pop.png")
# %% Plot the time time dependent metastable fractions..
ratio_mat = np.divide(td_pop_matrix[1,1:], \
```

```
td_pop_matrix[2,1:])


grd_ratio_mat =np.divide(td_pop_matrix[0,1:], \
td_pop_matrix[2,1:])
fig2 = plt.figure(figsize=(8, 6), facecolor='white')
plt.semilogy(t_matrix[1:], grd_ratio_mat, label = 'ground/1s3')
plt.semilogy(t_matrix[1:], ratio_mat, label = '1s3 / 1s5')
plt.title("Time dependent metastable fractions", \
weight='bold', fontsize=10)
plt.xlabel("Time (s)", fontsize=14)
plt.ylabel("Ratio", fontsize=14)
plt.legend(loc=1)
plt.savefig("td_meta_fracs.png", dpi=300)
plt.show(fig2)
print("Plot output saved to td_meta_fracs.png")
# %%
def qcd_temp_plot(d_indx):
import matplotlib.pyplot as plt
fig3 = plt.figure(figsize=(8, 6), facecolor='white')
plt.plot(temp_array,  pop_1s5_matrix[:,d_indx], 'g', label = '1s5')
plt.plot(temp_array,  pop_1s3_matrix[:,d_indx], 'r', label = '1s3')
plt.title('Temperature Response of QCD\'s')
plt.ylabel('Temperature (eV)')
plt.legend(loc=1)
plt.savefig('qcd_temp_respnse.png', dpi=300)
plt.show(fig3)
```

```
print("Plot output saved to qcd_temp_response.png")

qcd_temp_plot(3)5
```

F.5 Optical Emission Spectroscopy codes (OES_lib.py).

Foreword: All the examples contained in this section are designed to diagnose plasma parameters using data collected in the ALEXIS experiment. These codes are made freely available at `https://github.com/AUAMO/atomic_data_codes/gcr/ar_OES` under an MIT license. These are provided with the intent that they can be adapted for use with other plasmas, or that future researchers on ALEXIS can continue to use these codes for future efforts.

Most of the code provided is contained in the Python 3 library `OES_lib.py`. In addition to all the functions outlined in the previous section, this library contains the following functions:

F.5.1 retrieve_ALEXIS_data

When called, `retrieve_ALEXIS_data` prompts the user to select an ALEXIS data file from the directory `spect_dir`, which is also the functions' only argument. This function carries out all the analysis necessary on the collected double probe and spectrometer data and returns the filename, a temperature and density data array (numpy array), an array of average temperatures and densities for each data run in the data file, an array of wavelengths that are common to all collected spectra, an array of all collected spectral intensities, and an array of average spectra for each data run in the file. The function can be called like this:

```
filename, temp_dens_data, temp_dens_av, wavelengths, spect_array, \
spect_mean = retrieve_ALEXIS_data(spect_dir)
```

The user then selects a data file from directory either the BC1A, BC1C, or BC1E directories, which are all inside the DATA directory located in the same folder as `OES_lib.py`. The

names of the data directories reflect the spectrometer and viewport used to collect the data. The data in BC1A was collected with the Black Comet (BC) spectrometer at viewport 6 on ALEXIS, BC1C data was collected with the Black Comet at viewport 4, BC1E data was collected with the Black Comet at viewport 2.

F.5.2 get_spect_ratio

The function `get_spect_ratio` has the arguments (wavelengths, spect, wl_low, wl_high), where wavelengths is a numpy array of the spectrometer wavelengths, spect is a numpy array of spectral intensities of the same size as wavelengths, wl_low is the wavelength of the lower line in the ratio, and wl_high is the wavelength of the upper line. `get_spect_ratio` returns (ratio), which is simply the ratio of the two lines: lower/upper.

`get_spect_ratio` can be called thus:

```
ratio= get_spect_ratio(wavelengths, spect_mean, 763.5, 852.1)
```

The above example will return the ratio $\frac{I_{763.5}}{I_{852.1}}$.

F.5.3 get_meta_scale

The function `get_meta_scale` has the arguments (temp, ratio, lval, uval), where temp is the average electron temperature T_e from a a double probe data sweep, ratio is the line ratio from a spectral array for the two lines in question, lval is the wavelength of the lower line, and uval is the wavelength of the upper line.

`get_meta_scale` works by creating a test array of 300 potential metastable ratios, linearly spaced between 0 and 30, for the 1s5:1s3 relative metastable populations. It assumes that the ground:1s3 ratio is 2000:1, for reasons detailed in Chapter 4. It creates weighted PEC's for each metastable ratio in the m_scale array and then interpolates the array using a cubic spline method onto a temperature grid of 1000 linearly spaced points. For each of these 300 ratios, it compares the weighted temperature and line ratio values generated by the

theoretical PEC output to their experimentally measured counterparts. The theoretically determined line ratio that produces a theoretical temperature that most closely matches the experimental measurement is then returned. We call this the "metastable of best fit".

The function `get_meta_scale` returns (m_indx, mscale[m_indx], pec_temps, pec_scaled_array[m_indx], flux_lam, flux). m_indx is the array index of the metastable of best fit, mscale[m_indx] is the 1s5:1s3 metastable ratio corresponding to index m_scale, pec_temps is an array of electron temperatures correspondng to the output from ADAS208, pec_scaled_array[m_indx] is weighted PEC array created using m_scale, flux_lam is an array containing wavelengths matching an instrument broadened version of a theoretical spectrum created from the weighted PEC's, and flux is an array containing the instrument broadened intensities to match flux_lam.

The function `get_meta_scale` can be called like this:

```
meta_indx, meta_scale, pec_temps, pec_array, flux_lam, flux = \
get_meta_scale(temp_av, ratio, 763.5, 852.1)5
```

which would return a data array as described above matching the "metastable of best fit" using the experimentally measured line ratio 763.5:852.1.

F.5.4 Example script to demonstrate OES_lib.py

Finally, we have provided an example script called `\ar_OES_diagnostics_763_852.py`, which calls the functions in this section and plots the weighted PEC output for the 763.5:852.1 line ratio. Using line ratio vs. electron temperature plots created from "metastable of best fit" weighted PEC's for all the data collected from ALEXIS is how we have generated the mathematical models for determining electron temperatures from experimentally measured line ratios detailed in Chapter 4. We provide a copy of the example script `\ar_OES_diagnostics_763_852.py` below. This script can be run from the command prompt or in an interactive Python environment such as Spyder.

```
# ar_oes_diagnostics_763_852.py
# script to demonstarate functions within the Python 3 library
# OES_lib.py

# %%  Open an appropriate ALEXIS data file and import temp,
#     dens and spectral data.
import numpy as np
import matplotlib.pyplot as plt
from OES_lib import *
spect_dir = './DATA'

# %% Retrieve data from an ALEXIS data file. When prompted navigate to \
#    either the BC1A, BC1C, or BC1E directory located within the \
#    directory "DATA"

filename, temp_dens_data, temp_dens_av, wavelengths, spect_array, \
spect_mean = retrieve_ALEXIS_data(spect_dir)

temp_av = np.sqrt(np.mean(np.square(temp_dens_data[1, 0:15])))
dens_av = np.sqrt(np.mean(np.square(temp_dens_data[2, 0:15])))
temp_min = np.max(temp_dens_data[1, 0:15])
temp_max = np.min(temp_dens_data[1, 0:15])

# Find the ratio of the 763 / 852 nm lines using the get_spect_ratios \
# function from OES_lib.py.
ratio= get_spect_ratio(wavelengths, spect_mean, 763.5, 852.1)
```

```
limit = 16
temp_av = np.sqrt(np.mean(np.square(temp_dens_data[1, 0:limit])))
dens_av = np.sqrt(np.mean(np.square(temp_dens_data[2, 0:limit])))
temp_min = np.max(temp_dens_data[1, 0:limit])
temp_max = np.min(temp_dens_data[1, 0:limit])

meta_indx, meta_scale, pec_temps, pec_array, flux_lam, flux = \
get_meta_scale(temp_av, ratio, 763.5, 852.1)

# %% Plot the Average Temp, Density, and Weighted PEC's for the \
#    metastable of best fit
pec_x = np.linspace(0.5, 20, 1000)
from scipy.interpolate import interp1d
terp = interp1d(pec_temps, pec_array, kind='cubic')
pec_fit = terp(pec_x)
indx, av_temp = find_nearest(pec_x, temp_av)
theor_ratio = pec_fit[indx]

fig = plt.subplots(2, 2, figsize=(9, 6))
plt.subplot(221)
label = "Average Temp = {:5.2f} (eV)".format(temp_av)
plt.plot(temp_dens_data[0, :], temp_dens_data[1, :], label=label)
plt.ylim(2,8)
plt.xlim(0,40)
plt.legend(loc=3)
plt.subplot(222)
```

```
label = "Average Dens = {:5.2e} m^-3".format(dens_av)
plt.plot(temp_dens_data[0, :], temp_dens_data[2, :], label=label)
plt.legend(loc=3)
plt.subplot(212)
m_label='mscale = ' + str(meta_scale)
plt.text(0.1,7, m_label, size=10)
plt.plot(pec_temps, pec_array, 'rx', label='weighted PEC ratio')
plt.axvline(temp_av, color="orange", label="exp temp")
plt.axhline(ratio, color='red', label="exp ratio")
plt.axhline(theor_ratio, color='k', ls='--', label="theor ratio")
plt.legend(loc=4)
plt.suptitle('Temperature, Density and Metastable Ratio: ALEXIS', \
weight = 'bold')
plt.savefig("theor_mfrac.png", dpi=300)
plt.show()


# %% Create synthetic emission spectra for strong lines and
#    compare to ALEXIS.
line_array=np.array([763.5, 794.8, 826.5, 852.1])
gscale = 2000
y0 = flux[0] * gscale
y1 = flux[1] * meta_scale
y2 = flux[2] * 1.
flux_sum = (y0 + y1 + y2)
flux_windx, flux_walue = find_nearest(flux_lam, 763.5)
spect_windx, spect_value = find_nearest(wavelengths, 763.5)
fig1 = plt.figure(figsize=(8,6), facecolor="white")
```

```
for i in range(4):
ylabel = str(line_array[i])
def find_nearest(array, value):
idx = (np.abs(array-value)).argmin()
return idx, array[idx]
flux_indx, flux_value = find_nearest(flux_lam, line_array[i])
spect_indx, spect_value = find_nearest(wavelengths,\
line_array[i])
flux_sum = flux_sum / (flux_sum[flux_indx])
plt.plot(wavelengths[spect_indx-6: spect_indx+10], \
spect_mean[spect_indx-6:spect_indx+10] / \
spect_mean[spect_windx], label = ylabel)
plt.plot(flux_lam[flux_indx-20:flux_indx+20],\
flux_sum[flux_indx-20:flux_indx+20] / \
flux_sum[flux_windx], 'm.', ms=2)
plt.title("ALEXIS: Synthetic emission compared w/ experiment \
for strong lines.")
plt.legend(loc=1)
plt.xlabel("Wavelength (nm)")
plt.ylabel("Normalized Emission (arbitrary units)")
plt.xlim(750, 860)
plt.savefig("syn_spect.png", dpi=300)
plt.show(fig1)
```